A new detergent-free approach to solubilize membrane proteins to maintain their native environment



Juan Francisco Bada Juarez

University College

University of Oxford

Thesis submitted to the Board of the Medical Sciences Division in partial fulfillment of the requirements for the degree of

Doctor of Philosophy

Trinity term 2018

Abstract

Biophysical characterisation of membrane receptors in their native environment is essential for drug development, as lipid removal may affect conformational freedom and ligand binding. Membrane proteins are commonly solubilised with detergent for structural and functional studies, although the resulting micelles may be polydisperse, prone to aggregation and occlude of the binding site. Recently a hydrolysed copolymer of styrene and maleic acid (SMA) has been shown to be highly effective in extracting membrane proteins from native membranes without the use of detergent and the resulting coin-shaped nanoparticles, called Lipodisq (or SMALPs) are suitable for use in a wide range of biophysical methodologies.

Here we have been able to purify and characterize a range of membrane proteins from their native environment including bacteriorhodopsin (bR), archaerhodopsin 3 (AR3), Dopamine receptor 1 (D1, a human GPCR) and EcMATE (a bacterial transporter) using size-exclusion and affinity chromatography, circular dichroism and dynamic light scattering. Microscale thermophoresis and radio-ligand binding have been used to assess the activity of the different proteins. These nanoparticles have further allowed us to characterize the oligomeric state and to identify native ligands by native mass spectrometry.

The crystal structure of AR3 was obtained in the absence of detergent directly from its native membrane and its structure was solved to 1.3 Å resolution, where post-translational modifications, such as the pyroglutamate residue (PCA) at the N-terminus of AR3, and several side-chain rotamers are resolved for some key residues in the proton translocation channel as well as multiple water molecules. Some of the water molecules have partial occupancy within the extracellular-facing half channel, consistent with the existing FTIR data. Native mass spectrometry with Lipodisq has characterised the post-translational modifications carried by the protein. Moreover, a first structural study of the AR3 photointermediates using time-resolved XFEL crystallography has been performed.

Lipodisq nanoparticles were used to study the lipid and protein composition of *C. elegans* by comparing the wild-type N2 worm to a mutant strain (*agmo-1*), which lacks for an important enzyme in the lipid biosynthesis.

Finally, Lipodisqs have been evaluated as a drug delivery agent for Doxorubicin, a potent anti-tumour drug, which is commercially available as the PEGylated liposomal formulation Doxil. Previous work on the delivery of the drug to intracellular

compartments of HeLa cells followed by confocal microscopy and IC_{50} measurements show that, unlike in the case of encapsulated systems, there is no decrease in *in vitro* efficacy over the water-solubilised form of the drug. Here the fluorescent derivative of the SMA polymer has been synthesised and its biodistribution followed *in vivo*.

Acknowledgements

Firstly, I would like to thank Professor Anthony Watts for supporting this DPhil and the work presented thereafter. I particularly would like to express my gratitude for his support, freedom to develop my own ideas and his critical thinking and giving me the opportunity to study in Oxford.

I especially would like to thank Dr Peter Judge for the time spent for now more than 4 years since I started as a Master student from EPFL and I really want to express my gratitude for his patience, the great discussions about science and other subjects, the time spent in Diamond and long days in SACLA, for his advices and his optimism for the projects underdone during my thesis. I also have to thank him for being one of the proof-reader of this thesis. Thanks Peter!

This work would not have been possible without some people from the Watts lab and their daily support and friendship. I especially want to thank Dr Patricia Dijkman for teaching and introducing me to purify membrane proteins and about different other lab techniques. Gracias por todo Patricia! I also have to thank Dr Rosana Reis Thevenot and Dr Juan Carlos Munoz Garcia for their help and support in the D1 project, taking time to teach me many basic lab techniques. Thank for the good times spent in the lab, it was really great! I also would like to say a big 'thank you' to Javier Vinals, for which we have spent a lot of time purifying AR3 for crystallography and even more time talking about football or other sports! Gracias Javi por la ayuda y por ser tan buena persona! Special thanks also to Peter Fisher, for his general help around the lab and to Claudia Cassidy for being so efficient and crazy!

My thanks go to the many students I have supervised or co-supervised during my time in the lab: Charles Davies, Arisu Shigeta, Stephanie Gover, Soumia Zeghida, Alice Hart, Clare Kai Cimperman and Constanze Cavalier for their help in the lab. Thank you all!

A project cannot be carried on without the help of excellent collaborations and and in this case I would like to thank: Benjamin Brocco, Dr Juliette Devos, Dr Ralf

Schweins, Dr Michael Haertlein and Prof. Trevor Forsythe from the ILL (Grenoble, France) for the neutron scattering work; Dr Holger Kramer for assisting with the MALDI work carried out in this thesis; Dominic Hewitt, Kin Hoi, Dr Hsin-Yung Yen, Dr Jonathan Hopper and Prof. Carol V. Robinson for the native mass spectrometry work presented in this thesis; Dr Andrew Harper and Dr Steve Tonge from Malvern Cosmeceutics for providing the SMA polymer; Dr Agata Butryn, Dr Danny Axford and Dr Allen Orville for their help during the XFEL beamtime; James Birch for preparing the samples for XFEL and synchrotron data collection; Dr Isabel Moraes for being so patient in introducing me to membrane protein crystallization as well as the participation to several beamtimes in Diamond Light Source (Harwell, UK) and SACLA (Hyogo, Japan); Dr Delia O'Rourke and Prof. Jonathan Hodgkin for providing *C. elegans* samples and expertise in the field of *C. elegans* and finally to the Sandvig group in Norway for the biodistribution studies of the Dox-Lipodisq samples.

Lastly, I would like to say a big thank you for my friends for being there during this DPhil!

J'aimerais également dire un immense merci à toute ma famille, tout spécialement à mes parents et à ma soeur, pour leur soutien inconditionnel dans les moments difficiles durant toutes ces années d'études en Suisse et à l'étranger, qui ont été, bien malgré moi, très longues... mais très enrichissantes au niveau personnel et professionnel! On sait tous que ça n'a pas été facile, alors merci beaucoup pour votre soutien, vous êtes les meilleurs!

List of publications and presented work

List of publications in preparation

1. **J. F. Bada Juarez**, P. J. Judge, A. J. Harper, S. R. Tonge and A. Watts. Working title: **From Polymer Chemistry to Structural Biology: The Development of SMA and Related Amphipathic Polymers for Membrane Protein Extraction and Solubilisation**, *Submitted*

2. **J. F. Bada Juarez**, P. J. Judge, J. Vinals, D. Axford, A. Butryn, P. Aller, A. M. Orville, J. Birch, D. Sherrell, J. Beale, R. Owen, I. Moraes and A. Watts. Working title: **Detergent-free crystal structures of the dark-adapted Archaerhodopsin 3**, PDB 6GUX deposited August 2018 *In preparation*

3. **J. F. Bada Juarez**, K. Hoi, H.Y. Yen, J.T.S. Hopper, J. Devos, R. Schweins, M. Haertlein, P. J. Judge, V. T. Forsyth, C. V. Robinson and A. Watts. Working title: **Native mass spectrometry on Lipodisq nanoparticles using microbial rhodopsin as model proteins** *In preparation*

4. **J. F. Bada Juarez**, P. J. Judge, J. Vinals, D. Axford, A. Butryn, P. Aller, A. M. Orville, J. Birch, D. Sherrell, J. Beale, R. Owen, E. Nango, T. Nakane, R. Tanake, S. Iwata, I. Moraes and A. Watts. Working title: **Study of the photocycle of Archaerhodopsin 3 using time-resolved serial femtosecond crystallography.** *In preparation*

5. **J. F. Bada Juarez**, D. O'Rourke, P. J. Judge, J. Hodgkin and A. Watts. Working title: **Lipodisqs for eukaryotic lipodomics with retention of viability: infection resistance linked to C.elegans cuticle components** *Submitted*

6. **J. F. Bada Juarez**, P. J. Judge, T.G. Iversen, M. L. Torgersen, K. Sandvig and A. Watts. Working title: **Lipodisq nanoparticles as a new drug delivery platform** *In preparation*

7. **J. F. Bada Juarez**, J.C. Munoz Garcia, R. I. Reis Thevenot and A. Watts. Working title: **Native extraction, purification and characterization of a**

low-expressing neuronal human GPCR *In preparation*

Oral and poster presentations

Oral presentations at the following meetings:

- EBSA Biophysics Course on Membrane Biophysics and Lipid Protein Interactions in Montpellier, France (2014)
- Departmental Annual Recess of Biochemistry, University of Oxford, UK (2017)
- British Biophysical Society meeting in Southampton, UK (2018)

Posters presented at the following conferences:

- British Biophysical Society meeting in Liverpool, UK (2016) *Awarded poster prize*
- 19^{th} IUPAB congress and 11^{th} EBSA congress in Edinburgh, UK (2017)
- British Biophysical Society meeting in Southampton, UK (2018)

Contents

List of Figures **ix**

List of Tables **x**

List of Abbreviations **xi**

1 Introduction **1**

1.1 Biological membranes . . . 1

1.1.1 Lipids . . . 2

1.1.1.1 Classes of lipids . . . 3

1.1.1.2 Lipid phases . . . 5

1.1.1.3 Lipid asymmetry . . . 7

1.1.1.4 Lipid signalling . . . 9

1.1.1.5 Lipid-protein interactions . . . 10

1.1.1.6 Homeostasis and diseases . . . 12

1.2 Membrane proteins . . . 12

1.2.1 Microbial rhodopsins . . . 12

1.2.1.1 The retinal binding pocket of microbial rhodopsins 14

1.2.1.2 Potential applications of photoreceptors . . . 16

1.2.1.3 Mammalian rhodopsins . . . 18

1.2.2 Transporters . . . 19

1.2.3 Receptors . . . 21

1.3 Reconstitution of membrane proteins . . . 23

1.3.1 Liposomes . . . 25

1.3.2 Amphipols . . . 26

1.3.3 Bicelles . . . 28

1.3.4 Nanodiscs . . . 28

1.3.5 Other discoidal membrane mimetics . . . 30

1.4 Methods to visualize lipid-protein interactions . . . 30

1.4.1 Detergent-free extraction of membrane proteins using a hydrolysed co-polymer of styrene and maleic acid (SMA) . . . 30

1.4.1.1 Polymers available . . . 31

1.4.1.2 SMA 31
1.4.1.3 SMA-derivatives 33
1.4.1.4 Mechanism of formation of SMALPs 34
1.4.1.5 SMA as a tool to solubilize membrane proteins from biological membranes 35
1.4.2 Mass spectrometry technique 38
1.4.2.1 Native mass spectrometry (nano-ESI mass spectrometry, nMS) 39
1.5 Aims of this thesis 47

2 Bacteriorhodopsin as a model system to explore the capabilities of Lipodisqs for native mass spectrometry of membrane proteins. 49
2.1 Introduction 49
2.1.1 Bacteriorhodopsin (bR) 49
2.1.2 Small-angle neutron scattering (SANS) 52
2.1.3 Aims 53
2.2 Materials and methods 53
2.2.1 SMA hydrolysis 53
2.2.2 Bacteriorhodopsin expression and purification 54
2.2.3 Bacteriorhodopsin expression and purification in presence of nicotine 54
2.2.4 Addition of retinal after nicotine bR expression 55
2.2.5 bR ^{2}H, ^{15}N and ^{13}C labelled 55
2.2.6 Incorporation into Lipodisqs 55
2.2.7 Size-exclusion chromatography 56
2.2.8 UV-Vis spectroscopy 56
2.2.9 Dynamic Light Scattering (DLS) 56
2.2.10 Circular dichroism (CD) 56
2.2.11 Small angle neutron scattering (SANS) 57
2.2.12 Electron microscopy (EM) 57
2.2.13 Native mass spectrometry (nMS) 57
2.2.14 Thin layer chromatography (TLC) 58
2.3 Results and discussion 58
2.3.1 Preparation of bR-Lipodisqs 58
2.3.2 Biophysical characterisation of the bR-Lipodisq complex . . 60
2.3.3 Small-angle neutron scattering (SANS) experiments 64
2.3.4 Native mass spectrometry experiment using Lipodisq 70
2.3.5 Bacteriorhodopsin with nicotine treatment 74
2.3.6 Further identification of low molecular weight adducts 77
2.4 Conclusions 80

3 Detergent-free extraction of membrane proteins: the case of a transporter in *E. coli* and a human GPCR from human embryonic kidney (HEK) cells 82
3.1 Introduction . . . 82
3.1.1 Multidrug and toxic compound extrusion transporter (MATE) 82
3.1.2 Dopamine receptor 1 (D1) . . . 86
3.1.3 Microscale thermophoresis (MST) . . . 90
3.1.4 Aims . . . 91
3.2 Materials and methods . . . 91
3.2.1 Expression and membrane isolation of EcMATE . . . 91
3.2.2 Expression and membrane isolation of D1 . . . 92
3.2.3 Lipodisq formation and purification . . . 93
3.2.4 Circular dichroism (CD) . . . 93
3.2.5 Microscale thermophoresis (MST) . . . 94
3.2.6 Ligand binding on D1 Lipodisq samples . . . 94
3.2.7 Proteomics experiments . . . 95
3.2.8 Western Blot . . . 95
3.2.9 Native mass spectrometry . . . 96
3.3 Results and discussion . . . 96
3.3.1 Protein extraction and purification . . . 96
3.3.2 Proteomics of D1 . . . 100
3.3.3 Structural characterisation of the protein incorporated in Lipodisq . . . 101
3.3.4 Radioactive and non-radioactive ligand binding assays . . . 102
3.3.4.1 EcMATE Lipodisq . . . 102
3.3.4.2 D1 Lipodisq . . . 104
3.3.5 Native mass spectrometry . . . 106
3.3.5.1 EcMATE Lipodisq . . . 106
3.3.5.2 D1 Lipodisq . . . 111
3.4 Conclusions . . . 113

4 Structure of archaerhodopsin 3 in a detergent-free environment. From expression to high resolution crystal structure. 115
4.1 Introduction . . . 115
4.1.1 Archaerhodopsin 3 (AR3) . . . 115
4.1.2 Membrane protein crystallography . . . 121
4.1.3 XFEL and time-resolved serial femtosecond crystallography . 122
4.1.4 Aims . . . 124
4.2 Materials and methods . . . 125

4.2.1 Expression and purification of AR3 . . . 125
4.2.2 Delipidation of the protein . . . 125
4.2.3 UV-Vis spectroscopy . . . 126
4.2.4 Dynamic light scattering . . . 126
4.2.5 Electron microscopy (EM) . . . 126
4.2.6 Circular dichroism (CD) . . . 126
4.2.7 Lipodisq preparation . . . 127
4.2.8 Native mass spectrometry . . . 127
4.2.9 LCP preparation and crystallization screens . . . 127
4.2.10 Data collection on synchrotron radiation experiments at Diamond and XFEL experiment . . . 128
4.3 Results and discussion . . . 128
4.3.1 Expression and purification . . . 128
4.3.2 Characterization of the claret membrane . . . 128
4.3.3 nMS of AR3 Lipodisq . . . 132
4.3.4 AR3 crystallisation from the claret membrane . . . 134
4.3.5 Crystal structure analysis . . . 137
4.3.6 Crystallisation of AR3 from Lipodisq nanoparticles . . . 146
4.3.7 Time-resolved serial femtosecond crystallography . . . 147
4.4 Conclusions . . . 151

5 SMA as a complementary tool to study of the protein and lipid composition of the cuticle of *C. elegans* 153
5.1 Introduction . . . 153
5.1.1 *C. elegans* . . . 153
5.1.2 Matrix-Assisted Laser Desorption/Ionization time-of-flight mass spectrometry (MALDI-TOF-MS) . . . 156
5.1.3 Aims . . . 160
5.2 Materials and methods . . . 161
5.2.1 *C. elegans* culture . . . 161
5.2.2 Formation of Lipodisq . . . 161
5.2.3 Proteomics . . . 161
5.2.4 Lipids extraction from Lipodisq . . . 162
5.2.5 Thin layer chromatography . . . 162
5.2.6 Matrix assisted laser desorption ionization mass spectrometry (MALDI-MS) . . . 163
5.3 Results and discussion . . . 163
5.4 Conclusions . . . 171

6 Lipodisq nanoparticles as a new drug delivery platform 173
6.1 Introduction . . . 173
6.1.1 Doxorubicin as a model drug for lipid-based drug-delivery . 174
6.1.2 Aims . . . 176
6.2 Materials and methods . . . 177
6.2.1 Drug incorporation to Lipodisq . . . 177
6.2.2 Synthesis of SMA-SH . . . 177
6.2.3 Conjugation of fluorescent dye to SMA-SH (SMA-SH-A) . . 178
6.2.4 Purification of SMA-SH-A . . . 178
6.2.5 Size exclusion chromatography . . . 178
6.2.6 UV-Vis spectroscopy . . . 178
6.2.7 Fluorescence quenching experiments . . . 179
6.2.8 Size determination using dynamic light scattering . . . 179
6.2.9 Biodistribution experiments in mice . . . 179
6.3 Results and discussion . . . 180
6.3.1 Synthesis and purification of SMA-SH-A . . . 180
6.3.2 Incorporation of doxorubicin in SMA-SH-A Lipodisq . . . 182
6.3.3 Fluorescence quenching . . . 184
6.3.4 Biodistribution experiments . . . 187
6.3.5 Conclusions . . . 189

7 Conclusions 191

Appendices

A Appendix 197
A.1 SDS-PAGE . . . 197
A.2 Western Blot . . . 197
A.3 Silver stain . . . 197
A.4 Coomassie staining . . . 198
A.5 BCA assay . . . 198
A.6 Calibration curve for size-exclusion chromatography . . . 198
A.7 Trace metal solution . . . 198
A.8 Data collection at synchrotron . . . 199
A.9 Data collection for XFEL . . . 199
A.10 Distances between the retinal Schiff base and several amino acids . 200

References 201

List of Figures

1.1 Representation of biological membrane 2
1.2 Different phospholipid classes shown protonated. 3
1.3 Hydrogen bonding between lipids 5
1.4 Lipid phase diagram 6
1.5 Lipids involved in asymmetry 8
1.6 Signalling pathway of PI lipids 10
1.7 Hydrophobic mismatch 11
1.8 Retinal isomerization and microbial rhodopsins 13
1.9 Amino acids important for bacteriorhodopsin 15
1.10 Photocycle of bacteriorhodopsin 16
1.11 Biotechnological applications of bR 17
1.12 The six steps to optogenetics 18
1.13 Proteins involved in transport of molecule across the membrane . . 20
1.14 Different types of transporter 20
1.15 GPCR involvement in physiological processes 21
1.16 GPCR signalling pathways 22
1.17 Common detergents used for MPs and detergent phase diagram . . 23
1.18 Platforms for membrane proteins study 25
1.19 Different amphipols illustrated 27
1.20 Membrane protein incorporation in Nanodisc 29
1.21 SMA polymer 32
1.22 Different alternatives to SMA 33
1.23 Mechanism of formation of Lipodisq 35
1.24 Purification of membrane protein using SMA 36
1.25 Cryo-EM structure using SMALPs 38
1.26 nano-ESI and Orbitrap illustration 40
1.27 Signal conversion in Orbitrap mass analyser 41
1.28 Collisional energy in native mass spectrometry 42
1.29 Principle of ion-mobility mass spectrometry illustrated 44
1.30 Crucial importance of a lipid in the formation of a dimer 45
1.31 Native mass spectrometry of Nanodisc 47

2.1 Representation of the purple membrane of *Halobacterium salinarum* 50
2.2 Typical archaeal ether lipids 51
2.3 AFM picture of the purple membrane 52
2.4 SANS contrast match explanation 53
2.5 Purification of bR 59
2.6 Formation of bR DMPC Lipodisq 60
2.7 DLS measurement of the purple membrane and Lipodisqs 61
2.8 SEC profile of bR DMPC Lipodisq 62
2.9 UV-Vis spectra of bR in PM and Lipodisq 63
2.10 CD spectra of bR in PM and Lipodisq 64
2.11 Contrast match point of ^{2}H-bR 65
2.12 SANS curves obtained for Lipodisq 66
2.13 Lipodisq seen as a cylinder 66
2.14 Scattering curve for Lipodisq with deuterated bR 69
2.15 EM pictures from Lipodisq after SANS 70
2.16 Energy ramp of bR DMPC Lipodisq for nMS 71
2.17 Native mass spectrometry bR DMPC Lipodisq 72
2.18 Sequence of bacteriorhodopsin with PTMs 73
2.19 Retinal biosynthesis pathway 75
2.20 bR purification of the nicotine treated cells 75
2.21 nMS spectra of bR treated with nicotine 76
2.22 Biosynthesis of the S-TGD lipids 78
2.23 TLC of the lipid extracted from the bR DMPC Lipodisq 79

3.1 Crystal structure of PfMATE 83
3.2 Structure of NorM with different ligands 84
3.3 Crystal structure of PfMATE in two distinct conformations 85
3.4 Dopamine receptor structure 87
3.5 Signalling pathways of dopamine receptors 88
3.6 Crystal contacts of the D2 receptor 89
3.7 Principle of microscale thermophoresis 90
3.8 Overview of how to form Lipodisq from membranes 96
3.9 Size exclusion profile before IMAC 98
3.10 Purification of EcMATE and D1 Lipodisq 99
3.11 Western blot of EcMATE and D1 100
3.12 CD of EcMATE with ligands 101
3.13 TeV cleavage of EcMATE-GFP Lipodisq 103
3.14 MST binding data for EcMATE Lipodisq 104
3.15 Radio-ligand binding data for D1 Lipodisq 105
3.16 nMS spectra of EcMATE from membranes 106

3.17 Purification of the EcMATE DMPC supplemented Lipodisq 108
3.18 nMS spectra of the DMPC EcMATE Lipodisq 108
3.19 Purification of the EcMATE from PG deficient membranes 109
3.20 nMS spectra of the EcMATE PG deficient Lipodisq 110
3.21 nMS spectra of the D1 Lipodisq 111
3.22 Sequence of D1 with PTMs 113

4.1 Sequence alignment of AR3 with bR and other ARs 116
4.2 Structure of AR2 with bacterioruberin 116
4.3 Photocurrent produced by microbial rhodopsins 117
4.4 Proteins used in optogenetics 118
4.5 AR3 photocycle 119
4.6 Tuning of the absorption spectra by mutations 120
4.7 MD simulation of XFEL pulse 122
4.8 Setup fo SFX experiments 123
4.9 AR3 purification 129
4.10 EM picture of the proteoliposomes from the claret membrane 130
4.11 Absorption spectra and SEC profile of AR3 130
4.12 CD spectra of AR3 131
4.13 nMS spectra of AR3 DMPC Lipodisq 132
4.14 Maturation pathway of AR3 133
4.15 Crystallization of AR3 136
4.16 AR3 crystal structure 137
4.17 Pyroglutamate at the N-terminus 138
4.18 Unresolved C-terminus 138
4.19 Retinal Schiff base with electron density 139
4.20 The pentameric arrangement of the AR3 and bR in the light- and dark-adapted state 141
4.21 Arg82, Glu194 and Glu204 hydrogen bond network 142
4.22 Light- and dark-adapted structure of bacteriorhodopsin 143
4.23 N-terminus omega loop 144
4.24 N-terminus omega loop with lipid electron density 145
4.25 Lipid electron density 145
4.26 Crystallization of AR3 DMPC Lipodisq 146
4.27 Crystals for XFEL 147
4.28 Schematic setup used for the XFEL experiment 148
4.29 Picture of the setup used in SACLA 149
4.30 Asp85 and water movement in the XFEL setup 150

5.1 *C. elegans* picture on NGM plates 154

5.2 Different component of the surface coat 155
5.3 MALDI-MS process illustrated 158
5.4 Linear TOF mass analyser 159
5.5 Reflectron TOF mass analyser 160
5.6 Worms before and after addition of SMA 164
5.7 DLS data of the Lipodisqs from the wild-type and mutant strain of *C. elegans* 164
5.8 SDS-PAGE of the protein extracted 165
5.9 TLC plates from the mutant strain 167
5.10 MALDI-MS spectra of the lipids 168

6.1 Doxorubicin and its mechanism of action 175
6.2 Doxil 176
6.3 Chemical reaction to form SMA-SH 181
6.4 TLC to purify SMA-SH-A 182
6.5 DLS of the SMA-SH-A Lipodisq 182
6.6 DLS of the SMA-SH-A Doxorubicin Lipodisq 183
6.7 Doxorubicin fluorescence affected by solvent 185
6.8 Doxorubicin fluorescence quenching 185
6.9 Doxorubicin fluorescence peak ratio 186
6.10 Fluorescence imaging of mice 188

List of Tables

1.1 Lipid content in different organisms 5

2.1 DLS measurement of bR in purple membrane and in Lipodisq . . . 61
2.2 Summary of the samples studied by SANS 68
2.3 Results of the lipids identified from the LipidMAPS online database 79

3.1 Peptides identified from proteomics experiments for D1 100

4.1 DLS measurement of claret and purple membrane 129
4.2 Comparison of the distances between the retinal and a few amino acids obtained by x-ray crystallography and NMR 140
4.3 Comparison of amino acids in the retinal pocket 144

5.1 DLS data of the Lipodisq from the wild-type and mutant strain . . 165
5.2 Lipids identified by TLC 167
5.3 Lipids identified by MALDI-MS 170
5.4 Abbreviations for lipids identified from LipidMAPS online database 171

6.1 Fluorescence ratio for the Dox SMA-SH-A Lipodisqs 187

List of Abbreviations

ABC . . . . . ATP-binding cassette

ADHD . . . . Adult attention deficit disorder

ADP . . . . . Adenosine diphosphate

AFM . . . . . Atomic force microscopy

AGMO . . . . Alkylglycerol monooxygenase

AO . . . . . Archae-opsin

Apols . . . . . Amphipols

AP . . . . . Alkaline phosphatase

AR . . . . . Archaerhodopsin

ASR . . . . . *Anabaena* sensory rhodopsin

ATP . . . . . Adenosine triphosphate

BCA . . . . . Bicinchoninic acid

BME . . . . . β-mercaptoethanol

BO . . . . . Bacterio-opsin

BPG . . . . . Biphosphatidylglycerol

bR . . . . . Bacteriorhodopsin

cAMP . . . . . Cyclic adenosine monophosphate

Cb . . . . . Cerebrosides

CCS . . . . . Collision cross section

CD . . . . . Circular dichroism

CE . . . . . Collisional energy

Ce . . . . . Ceramides

CHAPS . . . . 3-[(3-cholamidopropyl)dimethylammonio]-1-propanesulfonate

CHAPSO . . . 3-([3-cholamidopropyl]dimethylammonio)-2-hydroxy-1-propanesulfonate

ChR . . . . . Channelrhodopsin

CID . . . . . Collision induced dissociation

CL . . . . . Cardiolipin

CMC . . . . . Critical micellar concentration

CNS . . . . . Central nervous system

CNT . . . . . Carbon nanotube

cryo-EM . . . Electron cryomicroscopy

CTAB . . . . . Cetyl trimethylammonium bromide

cwEPR . . . . Continuous wave electron paramagnetic resonance

DAG . . . . . Diacylglycerol

ddH_2O . . . . Double distilled water

DDM . . . . . n-dodecyl-β-D-maltoside

DGDG . . . . Digalactosyldiacylglycerol

DHAP 2-acetyl-1,3-dihydroxybenzene

DHB . . . . . 2,5-dihydroxybenzoic acid

DHPC 1,2-dihexanoyl-*sn*-glycero-3-phosphocholine

DIBMA . . . . Diisobutylene maleic acid polymer

DLS . . . . . Dynamic light scattering

DMF . . . . . Dimethylformamide

DMPC 1,2-dimyristoyl-*sn*-glycero-3-phosphocholine

DNA . . . . . Deoxyribonucleic acid

Dox . . . . . Doxorubicin

DRs . . . . . Dopamine receptors

DTT . . . . . Dithiothreitol

ECL . . . . . Enhanced chemiluminescence

E. coli . . . . . *Escherichia coli*

EDTA . . . . . Ethylenediaminetetraacetic acid

EPR . . . . . Enhanced permeability retention

ER . . . . . Endoplasmic reticulum

ESI . . . . . Electrospray ionisation

Fab . . . . . Fragment antibody

FBS . . . . . Fetal bovine serum

FT-ICR . . . . Fourier-transform ion cyclotron resonance

FT-IR . . . . . Fourier-transform infrared spectroscopy

GDP . . . . . Guanosine diphosphate

GFP . . . . . Green fluorescent protein

GPCR . . . . . G-protein-coupled receptor

GTP . . . . . Guanosine triphosphate

GUV . . . . . Giant unilamellar vesicles

HEK . . . . . Human embryonic kidney

HR . . . . . Halorhodopsin

IC_{50} . . . . . Half maximal inhibitory concentration

IMAC . . . . . Ion metal affinity chromatography

IM-MS . . . . Ion-mobility mass spectrometry

IP3 . . . . . Inositol triphosphate

K_D . . . . . Dissociation constant

LacCer . . . . Lactosyl ceramides

LB . . . . . Luria-Bertani medium

LC-MS/MS . Liquid chromatography tandem mass spectrometry

LCP . . . . . Lipidic cubic phase

LHC II . . . . Light-harvesting complex II

LogP . . . . . Partition coefficient

LPC . . . . . Lyso-glycerophosphatidylcholine

LPG . . . . . Lyso-glycerophosphatidylglycerol

LPIP . . . . . Lyso-phosphatidylinositol-monophosphate

LPS . . . . . Lyso-glycerophosphatidylserine

LUV . . . . . Large unilamellar vesicles

LPE . . . . . Lyso-glycerophosphatidylethanolamine

m/z . . . . . Mass-to-charge ratio

MATE . . . . . Multidrug and toxin extrusion protein

mAU . . . . . Milli absorbance unit

MALDI-TOF Matrix assisted laser desorption ionisation time-of-flight

MD . . . . . Molecular dynamics

MIPC . . . . . Mannosyl-phosphatidylinositol-ceramides

M(IP)$_2$C . . . Mannosyl-di-phosphatidylinositol-ceramides

MLV . . . . . Multilamellar vesicles

MO . . . . . Monoolein

MP . . . . . Membrane protein

MS . . . . . Mass spectrometry

MSP . . . . . Membrane scaffold protein

MST . . . . . Microscale thermophoresis

MWCO . . . . Molecular weight cut-off

NaR . . . . . Sodium pumping rhodopsin

nESI . . . . . nano-Electrospray ionisation

NMR . . . . . Nuclear magnetic resonance

nMS . . . . . Native mass spectrometry

NSAID . . . . Nonsteroidal anti-inflammatory drug

NpHR . . . . . *Natronomonas pharaonis* Halorhodopsin

NGM . . . . . Nematode growth medium

OG . . . . . n-octyl-β-D-glucopyranoside

OP50 . . . . . *E. coli* strain for nematode maintenance

pA . . . . . picoAmps

PA . . . . . Phosphatidic acid

PBS . . . . . Phosphate buffer

PC . . . . . Glycerophosphatidylcholine

PCA . . . . . Pyroglutamate

PE . . . . . Glycerophosphatidylethanolamine

PEG . . . . . Polyethylene glycol

PG . . . . . Glycerophosphatidylglycerol

PGP-ME . . . 2,3-di-O-phytanyl-*sn*-glycero-1-phospho-(3'-*sn*-glycerol-1'-methyl phosphate)

PI . . . . . Glycerophosphatidylinositol

Pi . . . . . Inorganic phosphate

PIP$_2$ . . . . . Phosphatidylinositol biphosphate

PM . . . . . Purple membrane

PMF . . . . . Protein mass fingerprint

PMME . . . . Phosphatidyl-*N*-monomethylethanolamine

POPC 1-palmitoyl-2-oleoyl-*sn*-glycero-3-phosphocholine

PR . . . . . Proteorhodopsin

PS . . . . . Glycerophosphatidylserine

PTM . . . . . Post-translational modifications

PVDF . . . . . Polyvinylidene difluoride

R6G . . . . . Rhodamine 6G

RF . . . . . Radio frequency

$\mathbf{R_f}$ . . . . . Retention factor

$\mathbf{R_g}$ . . . . . Radius of gyration

S-DGD . . . . Sulfo-digalactosyldiacylglycerol

S-TGD . . . . Sulfo-trigalactosyldiacylglycerol

SANS . . . . . Small angle neutron scattering

SDS . . . . . Sodium dodecyl sulfate

SDS-PAGE . . Sodium dodecyl sulfate polyacrylamide gel electrophoresis

SEC . . . . . Size-exclusion chromatography

σ . . . . . Root mean square deviation of electron density

SGA . . . . . Sulfonylgalactose

SM . . . . . Sphingomyelin

SMA . . . . . Styrene maleic acid polymer

SMA-SH . . . Styrene maleic acid thiol conjugated polymer

SMA-SH-A . . Styrene maleic acid Alexa dye conjugated

SMALP . . . . Styrene-maleic acid lipid particle

SMAnh . . . . Styrene maleic anhydride polymer

SMX . . . . . Serial millisecond crystallography

SR . . . . . Sensory rhodopsin

SRCD . . . . . Synchrotron radiation circular dichroism

ssNMR . . . . Solid-state nuclear magnetic resonance

SUV . . . . . Small unilamellar vesicles

SQDG . . . . . Sulfoquinovosyldiacylglycerol

T4L T4-Lysozyme

TCEP . . . . . Tris(2-carboxyethyl)phosphine

TEM . . . . . Transmission electron microscopy

TeV . . . . . Tobacco etch virus

TG . . . . . Tri(acyl)glycerols

TGF-β . . . . . Transforming growth factor β

TLC . . . . . Thin layer chromatography

TM . . . . . Transmembrane

T_m . . . . . Melting temperature

TOF . . . . . Time-of-flight

TR-SFX . . . Time-resolved serial femtosecond x-ray crystallography

UV . . . . . Ultraviolet

UV-Vis . . . . Ultraviolet-Visible spectroscopy

v/v . . . . . Volume to volume ratio

WE . . . . . Wax ester

w/v . . . . . Weight to volume ratio

w/w . . . . . Weight to weight ratio

XFEL . . . . . X-ray free electron laser crystallography

1 Introduction

1.1 Biological membranes

All cells are surrounded by membranes, which form a semi-permeable barrier between the external environment and the cytoplasm. Its composition (lipids, small molecules and proteins) varies from organisms to organism [1–3], cell to cell [2, 4, 5] and even within organelles [6, 7], and their study is challenging due to their complexity. As an example, 5% of the eukaryotic genome encodes thousands of lipids [8] and more than 30% encodes membrane proteins [9]. The main components of the membrane are lipids, which spontaneously form a bilayer structure and provide a stable hydrophobic environment for membrane proteins and other hydrophobic molecules such as cholesterol [10]. The hydrophobic interior renders impossible the passive passage of polar molecules, ions or other hydrophilic molecules [11]. The fluid-mosaic model, states that the biological membrane is a two-dimensional solution of amphipathic proteins within a fluid bilayer solvent, where mobility rely on the strength of non-covalent molecular interactions within the membrane [12]. In this model, interactions between lipids and membrane proteins are either weak, non-specific interactions (e.g. van der Waals forces) or strong specific interaction between the polar headgroups of lipids. Also, in this model, lipids and membrane proteins have independent dynamics within the bilayer.

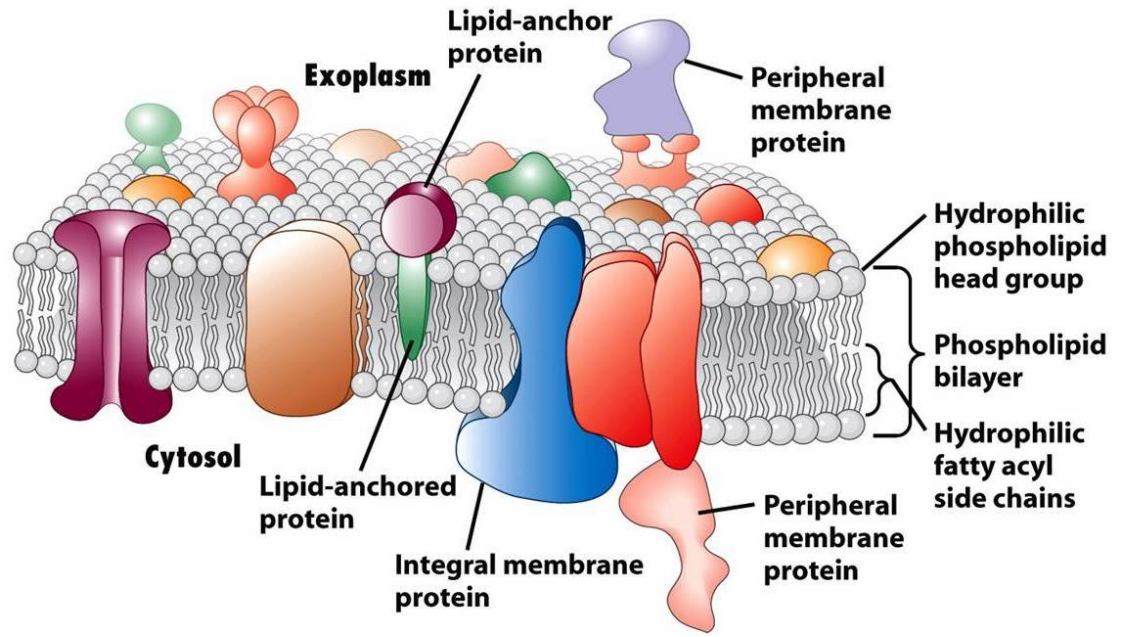


Figure 1.1: Representation of biological membrane. Lipids form a bilayer where different modes of insertion of membrane protein are illustrated. Adapted from [10]

1.1.1 Lipids

The word 'lipid' is derived from the Greek *lipos*, meaning fat. In most membranes, lipids are the major components by number. They are amphipathic molecules, with a hydrophobic tail and a hydrophilic head which usually contains a phosphate group [6]. They can constitute up to 50% of the mass of most animal cell membranes, numbering approximately 10^9 lipid molecules in one eukaryotic cell membrane [10]. Their roles are diverse, from inducing curvature [13, 14] facilitating vesicle budding and formation [15] and in some cases also have some impact on protein structure and function [11, 16–18], energy storage [19], cell signalling [20] or post-translational modification of proteins [21, 22].

The core amphipathic structure of a typical membrane lipid exhibits a wide diversity of different chemical structure with different headgroups or different length tails of hydrocarbons. Moreover, the compositional diversity can be noticed in different organisms, between and within cells of the same organism [23]. Both confer specific and unique properties on lipids giving rise to specific environment and

affect the combined comportment of lipids in membranes between themselves (lipid-lipid interaction) [6, 23] and other component of the membrane (lipid-protein interaction [24, 25]).

1.1.1.1 Classes of lipids

The main lipids found in a typical cell membrane are phospholipids and sterols [6]. Glycerol-3-phosphate forms the backbone of glycerophospholipids, to which a phosphate-containing polar head is attached (via a phospho-ester bond) two hydrophobic tails (hydrocarbon chains of same or different length) attached to the backbone via an ester bond (in most organisms) [11]. The main lipid headgroups found in eukaryotes are phosphatidylcholine (PC), phosphatidylethanolamine (PE), phosphatidylinositol (PI), phosphatidylserine (PS), phosphatidylglycerol (PG) and phosphatidic acid (PA) as showin in Figure 1.2.

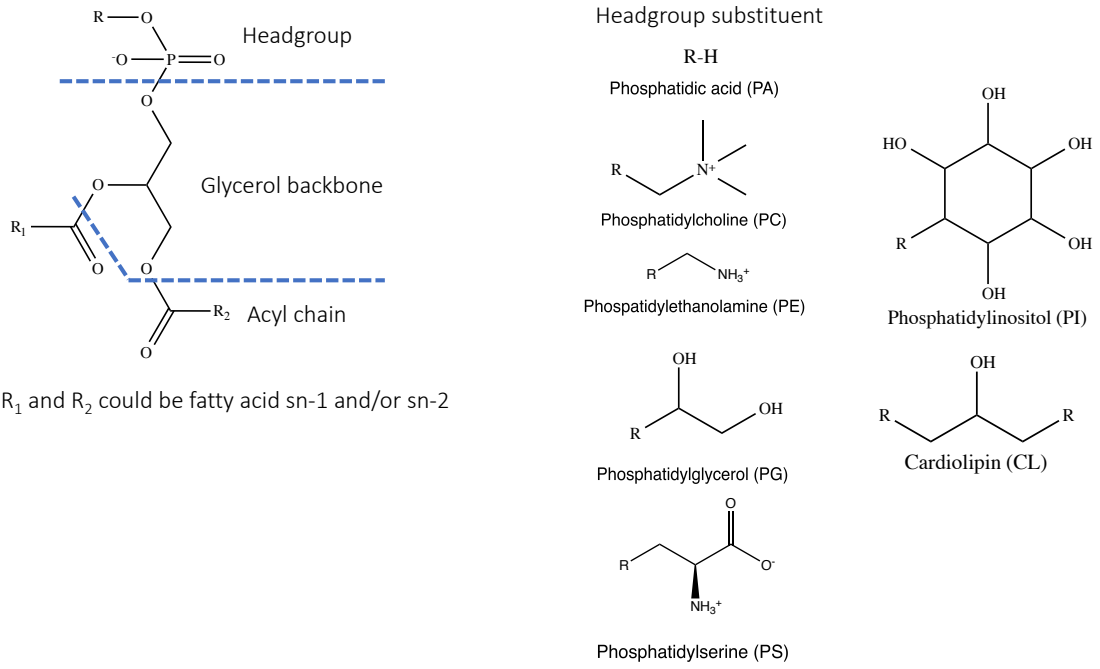


Figure 1.2: Different phospholipid classes shown protonated.

Phospholipids can be classified by their headgroups into two main categories, anionic (PA, PG, PS, PI, CL) and zwitterionic (PC, PE), leading to different physical and mechanical properties of the membranes. The lipid tails have also some

importance as they contribute to membrane flexibility and regulate thickness and lateral pressure [13, 23, 26]. Usually for PC-type lipids, at least one unsaturated bond in the hydrophobic chain is observed, permitting the membrane to be fluid at physiological temperatures and helping to obtain a cylindrical packing within the membrane [11]. PE lipids, due to their small headgroup and ability to H-bond directly to other lipids, adopt a conical conformation, which helps in membrane deformation, inducing curvature or helping in fusion processes [27]. PS lipids are key signalling messengers for apoptosis, as these lipids are usually found in the intracellular leaflet of the bilayer. Their exposure to the extracellular side of the membrane, leads to macrophage signalling and degradation of cells [28, 29]. PI lipids, with their inositol group, which can be phosphorylated at up to three different positions, are key to several signalling pathways and can act as primary and secondary messengers depending on the pattern of phosphorylation present on the inositol group [24, 25].

Other types of lipids can be found in the membrane such as sphingolipids. They are made from a sphingosine backbone (two hydroxyl groups and one amino group) which differs from glycerol (bearing three hydroxyl groups), and they can exhibit single or double acyl chain with one of the chain linked by an amide bond to the backbone. Sphingomyelin is a major component of mammalian cells and has a choline headgroup with usually saturated or *trans*-unsaturated acyl chains, permitting them to adopt a taller and thinner cylindrical shape than similar glycerophospholipids [30]. Moreover, the chemical properties of the headgroup of sphingolipids, where both hydrogen bond acceptor and donor groups are present, compared to glycerophospholipids where only an acceptor group is present, making them prone to form a tighter structure within the membrane due to more extensive hydrogen bonding network [31] as shown in Figure 1.3. A direct impact can be observed on membranes formed from sphingolipids, which have a higher melting temperature [32].

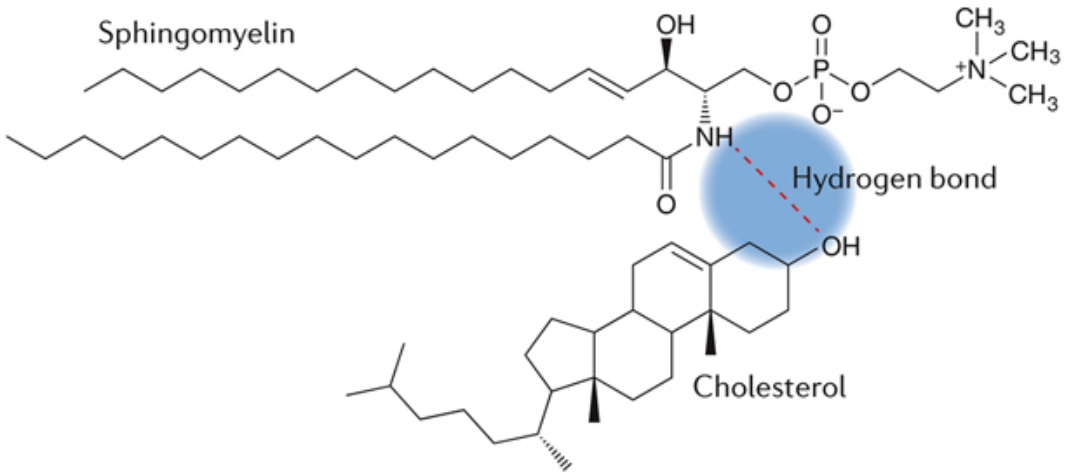


Figure 1.3: Hydrogen bonding between sphingolipid and cholesterol, reproduced from [23]

Diversity of lipid composition is key as different lipids will modulate activity of some proteins, curvature or dynamics within the component of the membrane [11, 33]. An overview of different membranes from different organisms and from different organelles is presented in the Table 1.1. Not only is the headgroup composition different, but acyl chain length and the number of double bonds per chain may vary. Acyl chains containing 16 to 24 carbons and up to 6 unsaturated bonds are predominantly found in natural membranes [34].

Content (in percent)	PC	PE	PI	PS	PG	SM	Cardiolipin	Other	Sterol (mol/mol ratio)
Human embryonic kidney (HEK) cells [35]	36	16	7	18	3	11	-	9	0.24
Endoplasmic reticulum [10]	40	17	-	5	-	5	-	27	0.06
***Escherichia coli*[10]**	-	70-80	-	-	15-20	-	5	-	-
***Sf9* insect cells [36]**	35	36	23	-	-	-	4	2	0.04
***C. elegans* (N2 wild type) [37]**	54	36	5	5	-	-	-	-	<0.01

Table 1.1: Table showing the content of lipids in several organisms

1.1.1.2 Lipid phases

Different polymorphic phases can exist for lipid bilayers, which are dependent on the melting point temperature (T_m) of the lipid due its chemical composition [38] as shown in Figure 1.4. The melting temperature of lipids depends on both the headgroup and the acyl chains, the longer the carbon chain is, the higher the T_m [7]. Double bond addition to the acyl chain decreases the melting temperature as van der

Waals interactions are reduced [2, 7]. Headgroups also play a role as explained earlier as they can promote tighter packing for PE lipids than PC for instance [39, 40].

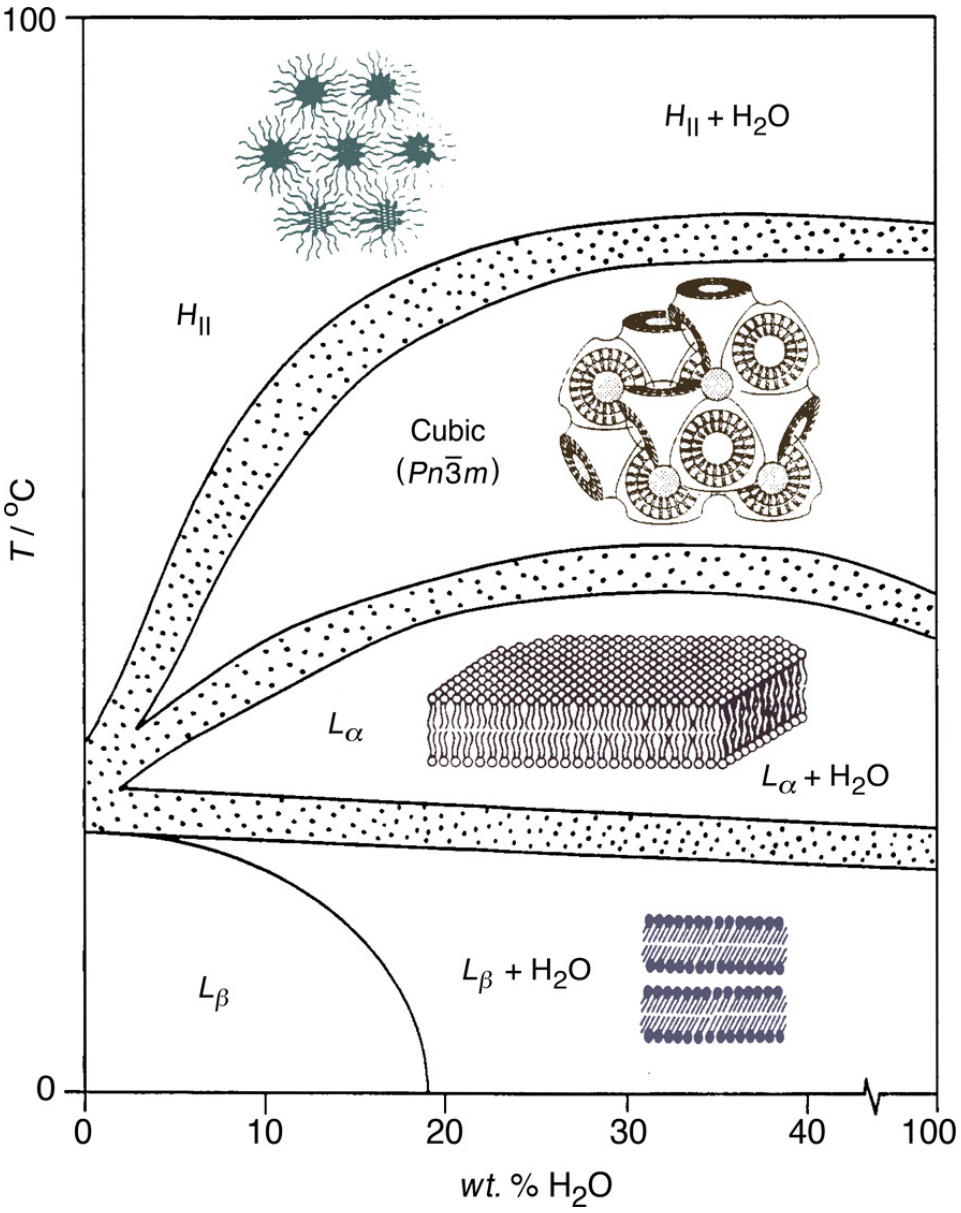


Figure 1.4: Lipid phase diagram. Gel phase (L_β) represent a phase where lipid motion is restricted. In lamellar phase (or liquid crystalline phase, L_α), lipids are less ordered, and motion is less restricted than in L_β. Cubic and hexagonal phase appeared at higher temperature. Dashed zones represent phase transition (reproduced from [40]).

Organisation and motion of the lipid can be influenced by the phase in which the lipid resides at a given temperature. Model membrane have been used for the study of lipid phase using one lipid or a lipid mixture. It has been observed

that below the T_m of the lipid, called the gel phase, the lipid motion is restricted, and lipids are highly ordered. Upon temperature increase, the lipid starts to order less and above the T_m of the lipid, a liquid crystalline phase appears [6]. Intermediate states and therefore co-existence of both phases have been studied extensively in the literature and could account for the formation of specific lipid domains *in vivo* and *in vitro* [23, 41] that could have some important structural and functional implications for membrane proteins. Their existence usually correlates with some high sterol content in the membrane which can induce phase-separation and microdomains formation. These transient domains are small (10-20 nm width) and have been imaged recently in live cells thanks to super-resolution microscopes. Domain formation is dependant not only on lipid-lipid interactions, but also on lipid-protein and protein-protein interactions [23, 42]. This accounts in variation of composition (segregation of certain lipids) and affects key properties of the membrane such as fluidity and membrane shape.

The phase transition for lipids is a multiparametric process which can be best described by a phase diagram (Figure 1.4). Further to the gel and lamellar phase, the cubic phase has some relevance in the field of protein crystallography with the use of lipidic cubic phase (LCP) [43–45], which has facilitated the strong growth in membrane protein structures deposited in the protein data bank in the past few years (from 50 structures deposited up to 2008 and now more than 200 structures available) [46].

1.1.1.3 Lipid asymmetry

Biological membranes have an asymmetric distribution of lipid types between the two leaflets. Membrane asymmetry appears to be important for for biological processes such as apoptosis [47], stability of the membrane [48] and maintaining the membrane potential [49].

Different lipid types can cross through the bilayer between leaflets (flipping of lipids) at different rates, which depends on their charge, size and headgroup properties. As an example, PC and sphingolipid usually have slow flipping rate

(hours to days) compared to ceramides or sterols for which their flipping rates is much faster (seconds) [50, 51]. In eukaryotic membranes, the outer leaflet is usually rich in PC and sphingolipids and the inner leaflet enriched in PS and PE lipids [52, 53].

Neutron scattering experiments using model membrane have demonstrated that certain component such as cholesterol have a completely different flipping rate [54] compared to other lipids. Nevertheless, the authors claimed that the difference attributed here is certainly due to the chemical tags used for the experiments. Even though, they claim that cholesterol is actively transported across the bilayer due to the experimental slow rate observed.

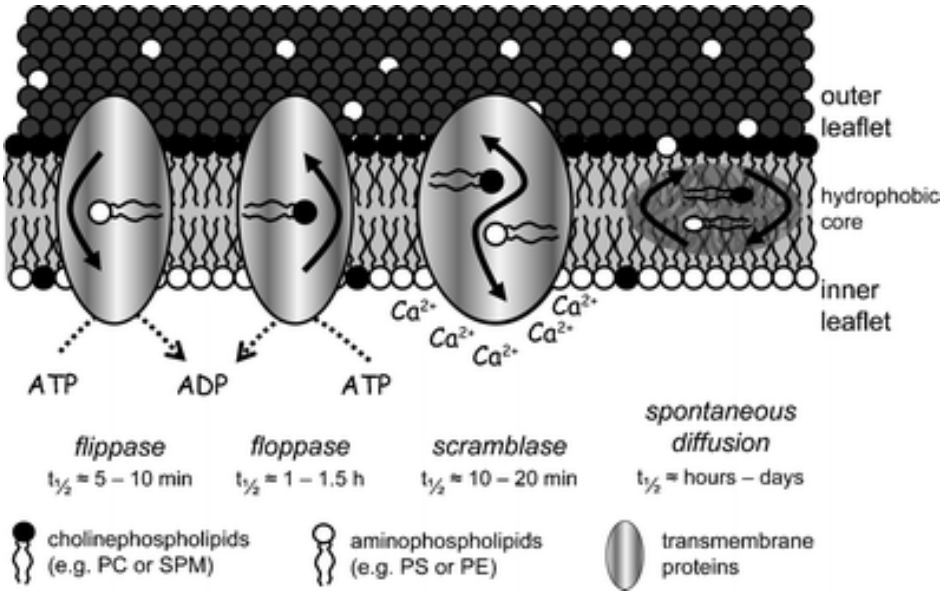


Figure 1.5: Different types of protein involved in determining membrane asymmetry (reproduced from [55]).

Another determinant for lipid asymmetry is the presence (or absence) of specific transporters which helps the translocation of lipids across the membrane (Figure 1.5). For eukaryotes, two different ATP-depending translocases and a Ca^{2+}-dependant scramblase play a major role in translocating and redistributing lipids within the bilayer [56, 57]. ATP-binding cassette (ABC) transporter moves lipids from the inner to the outer leaflet, whereas an aminophospholipid translocase moves some specific

lipid towards the inner leaflet [58, 59]. Strong specificity towards PS and PE lipids for the translocase protein leads to the lipid asymmetric distribution mentioned above.

Last but not least, Ca^{2+}-dependent scramblase protein, allows non-specific bidirectional transport of lipids, disrupting asymmetry [60]. This causes the PS lipid to accumulate on the outer leaflet, triggering macrophage signalling and apoptosis of the cell [28, 29]. Lipid flip-flop could also occur without the need for any kind of enzymes and as it is difficult to produce such asymmetric membrane *in vitro* [61].

Asymmetry is also very important for membrane protein function. Some negatively charged lipids in the inner leaflet, help to approximate and orientate enzymes towards the membrane. Some specific lipids are also known to help in maintaining essential structural roles or to be essential co-factors for protein activity (such as PS lipids for ATPase) [62].

1.1.1.4 Lipid signalling

In addition to their mechanical and structural roles in biological membranes, lipids may also act as signalling molecules. Hydrophobic and headgroup components could be hydrolysed and each employed as either first or second messengers within the lipid bilayer, for recruitment of other proteins or within the cytoplasm with the detachment of hydrophilic headgroup [20]. Phosphatidylinositol lipids (PI), especially with mono-, bi- or tri-phosphate groups in the inositol moiety, play a key role in cellular signalling [63, 64] as depicted in Figure 1.6. Misregulation of phospholipase in the cells, may lead to apoptosis, as a large amount of lipid is hydrolysed, giving rise to differences in mechanical and physical properties of the membrane [65–67]. Nevertheless, a high transient local concentration of lipids is required to perform signalling via the membrane [68].

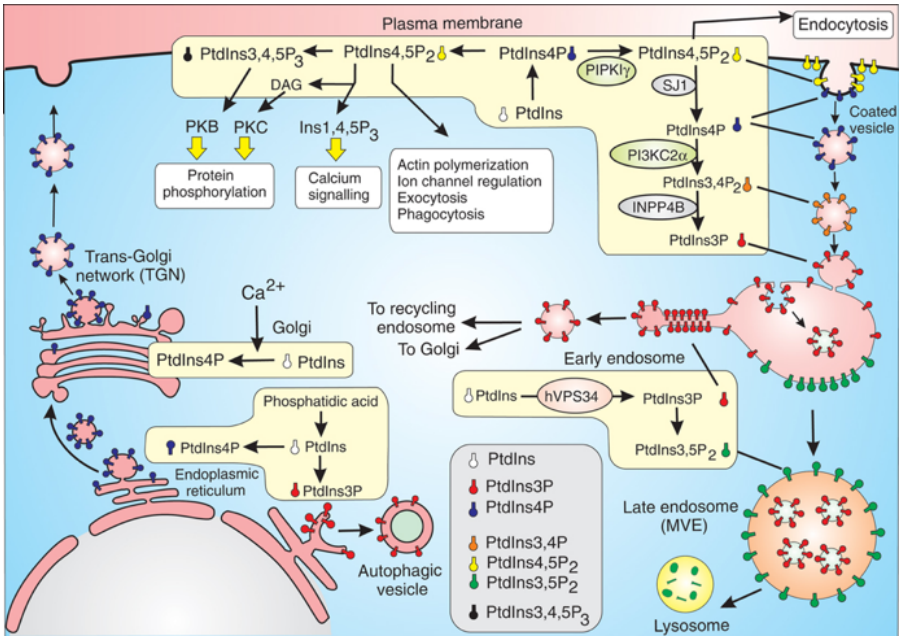


Figure 1.6: Signalling pathway of PI lipids in cells (reproduced from [69]).

1.1.1.5 Lipid-protein interactions

Several membrane proteins are functionally modulated by the presence of certain lipids [70]. Several examples in the literature can be found where lipids have an influence on the oligomeric state of the protein as for rhodopsin [71, 72], on ligand binding [73] or as allosteric modulator [74] for GPCRs [35].

Annular lipids are lipids that are in close proximity and have a stronger interaction with the protein, but are still able to exchange with the bulk lipids. This has been demonstrated mainly by electron paramagnetic resonance spectroscopy (EPR) and NMR [75, 76].

Finally, it has been suggested that non-annular lipids are tightly bound to the protein, either at the interface or inside, and are often described as lipid cofactors [77]. X-ray crystallography [27, 75] together with the development of native mass spectrometry [74, 78], have drawn the attention to this kind of different lipid interactions and their influence on the structure and activity of membrane proteins. Indeed, membrane proteins tend to have some clefts or narrow grooves, in between α-helices, in their outer surface, where lipids can be accommodated [79–81].

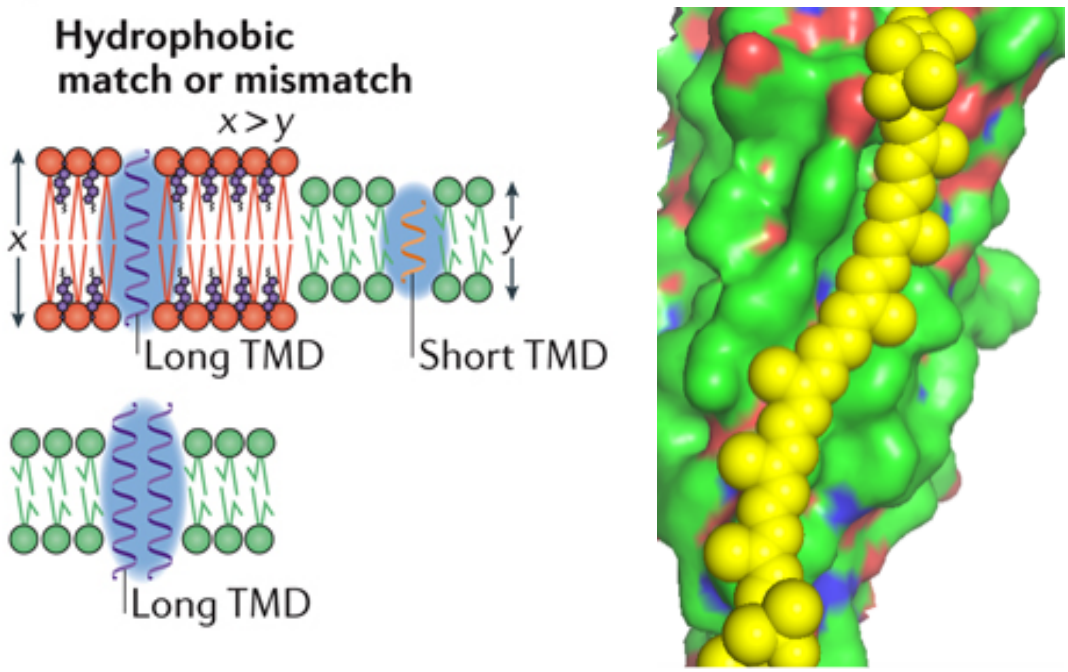


Figure 1.7: Hydrophobic mismatch illustrated from [23], where longer trans-membrane domain (TMD) need longer lipids to accommodate in the membrane. Right: Archaerhodopsin 2 structure (PDB:2Z55, green) where a small molecule (bacterioruberin, in yellow) is intercalated in between alpha helices.

Due to their chemical diversity, lipids can also have an impact on the diffusion rate or the thickness of the bilayer. Hydrophobic mismatch [40, 82, 83], where some of the hydrophobic part of a lipid or protein is exposed to the hydrophilic environment due for example to a difference in acyl chain length between lipids, can cause the lipid or the protein to tilt or rotate within the bilayer to reduce its exposure to solvent (Figure 1.7). Such observations have been reported for different proteins such as rhodopsin [40] (where the protein can be locked in a state depending on the bilayer thickness), for mechanosensitive channels [84] and for ion channels [85].

Headgroup interactions could also make an important contribution. Examples include the difference of hydrogen bonding or effect of curvature due to PE lipids or charge state due to PS or PG could also influence interactions between lipids and proteins [86].

1.1.1.6 Homeostasis and diseases

Misregulation of lipids, mainly due to mutations in proteins involved in their biosynthesis, can lead to several severe diseases such as Sjögren-Larsson syndrome, a neurological and skin disease caused by a mutation in a protein regulating the degradation of sphingolipids [87]. Changes in lipid composition could also be a sign of a disease state. A few examples involve the increase of ceramide lipids in Alzheimers and diabetes or changes in acyl chains of phospholipid could be found in some cancer cells [4, 88, 89]. Moreover, lipids could serve as biomarkers to differentiate healthy from diseased cells [11].

1.2 Membrane proteins

Membrane proteins, encoded by up to 30% of the genome of most organisms [90] are of great pharmaceutical interest and close to 60% of commercially available drugs target membrane proteins [91]. Membrane proteins perform several key roles in the cells such as receptors between the cytoplasm and the external environment, transport of ions and hydrophilic molecules or perform enzymatic reactions close to the membrane. Structure determination of membrane proteins is still a challenging task and is a key milestone to understand their mechanism of action and to design better drugs [92].

Classification of membrane proteins is based on their incorporation in the bilayer and could be either transmembrane (fully inserted), surface bound (partially inserted) or anchored to the membrane via lipid(s) [93]. For the purpose of this thesis, we will mainly focus on integral membrane proteins of three different sub-groups of membrane proteins, being microbial rhodopsins, transporters and receptors.

1.2.1 Microbial rhodopsins

Retinal-containing photoreceptors are present in all phyla of life and the microbial rhodopsin family contains more than 7,000 different proteins, which can be found in different organisms throughout the oceans, in plants or in soils [94]. They share

two main structural features, being folded as seven transmembrane helices which form a pocket where a chromophore, retinal (vitamin A), is covalently bound to the protein via a Schiff base linkage to a lysine residue located in the helix G and is able to photoisomerize and perform different processes of light conversion to intra- or intercellular signalling, to survival and adaptation to the environment [95, 96] (Figure 1.8). The position of helix A which is variable, and that the B-C loop is the longest and conformationally different loop, are some structural features observed in microbial rhodopsins [95, 97]. Their functional unit is a monomer, but their oligomeric assembly in specialized and highly-ordered membranes differs between organisms, from dimer (sensory rhodopsin) [98], trimer (bacteriorhodopsin) [99], pentamer or even hexamer in proteorhodopsin [100].

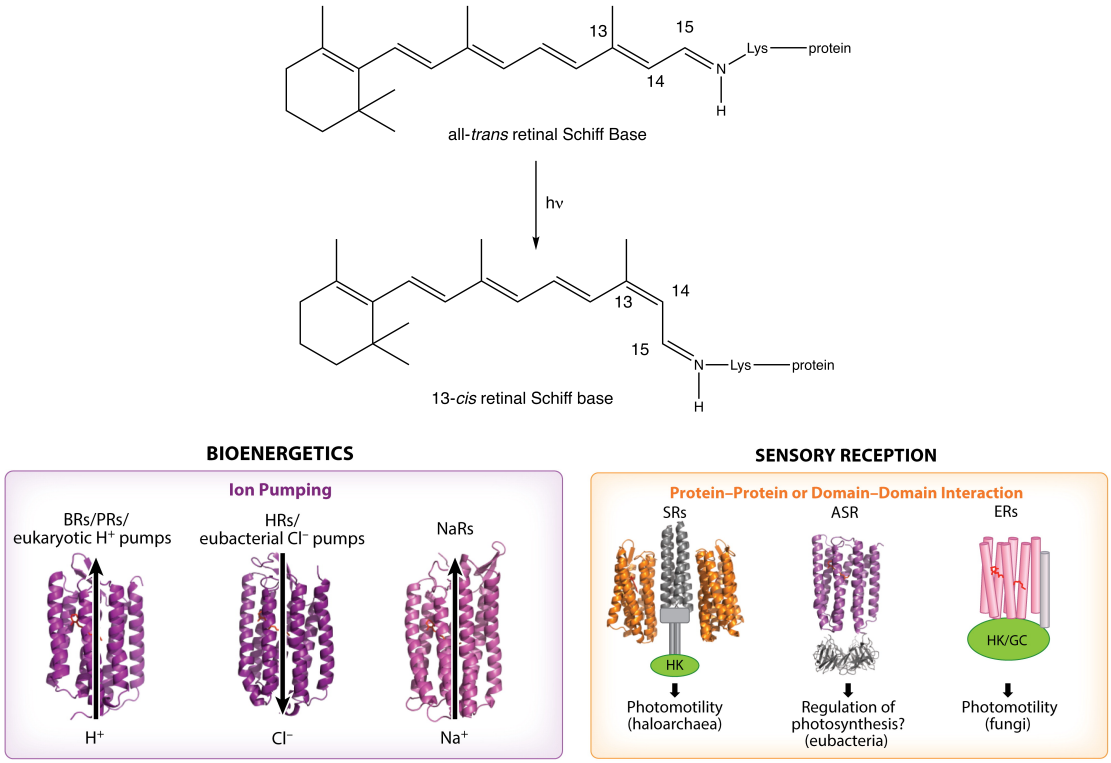


Figure 1.8: Left: Retinal isomerization when illuminated. Right: Different types of microbial rhodopsins (adapted from [94]).

Microbial rhodopsins are categorized by their biological functions, the first being energy transduction, which converts light energy into an electrochemical potential

difference, by translocating H^+, Na^+ or Cl^- across the cell membrane [94](Figure 1.8). Examples of such proteins are halorhodopsin, proteorhodopsin, channelrhodopsin, bacteriorhodopsin or archaerhodopsin for which more detailed descriptions will be provided in chapter 4. The second group are photosensory receptors which use light 'to sense' the external environment and regulate several cellular processes. Examples of such proteins includes sensory rhodopsin I or *Anabaena* sensory rhodopsin [101, 102]. Signalling processes for sensory rhodopsin covers different range from protein-protein interactions, to interactions of cytoplasmic domain with soluble proteins, enzymatically or eventually by passive ion channel conduction [95].

1.2.1.1 The retinal binding pocket of microbial rhodopsins

The aldehyde form of vitamin A, which is synthesized from β-carotene, is used to capture light [103]. Retinal binding to the protein via the Schiff base linkage to a lysine residue, converting the opsin to rhodopsin, enables the protein to adopt its conformation as shown by folding-unfolding experiments [104]. Even though loops, interfacial regions, arrangement of different side chains or distribution of internal could vary, the retinal pocket is highly conserved between rhodopsins [105]. Amino acids location and orientation have strong implications such as W86 and W182, which enable photoisomerization of the retinal and can serve as mechanical transducers to dissipate the energy stored upon deformation of the retinal to the protein, permitting the protein to adopt different photocycle conformations [95, 106]. Other residues such as Y185, R82, K216, D85 and D212 play important roles in maintaining the hydrogen bonding networks [107, 108](Figure 1.9).

Different mutations in these amino acids lead to the protein function to be altered. As an example, the well-known D85N mutation which blocks the proton transfer in bacteriorhodopsin [109], or D85T which converts the bR in a chloride pump [110]. FT-IR, X-ray crystallography and computational methods have shown the importance for protein function of the water molecules located close to the retinal Schiff base [111–114].

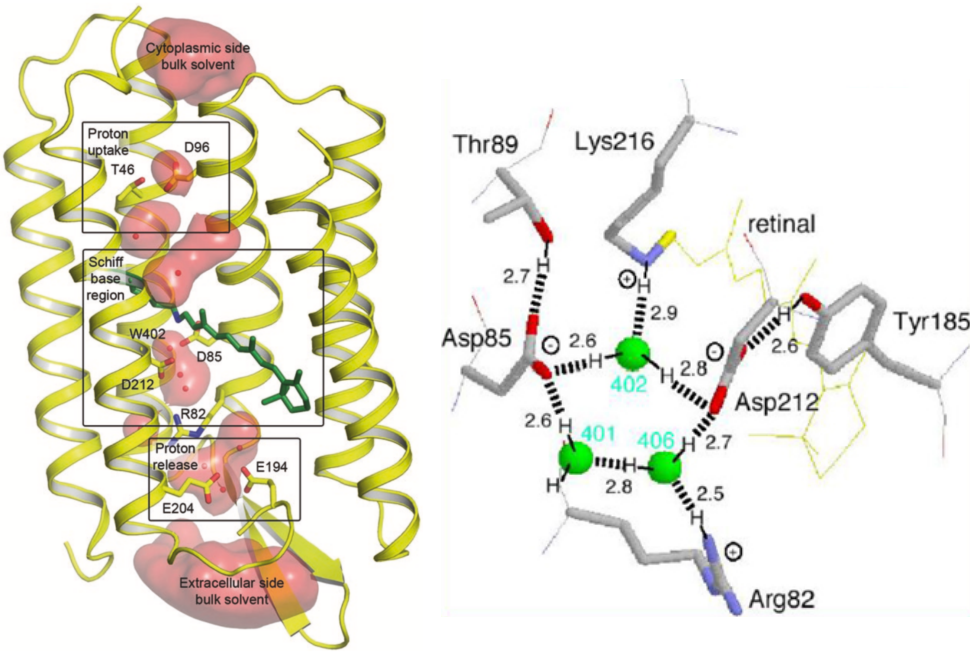


Figure 1.9: Left: Amino acids involved in the proton translocation mechanism (adapted from [97]) Right: Pentameric arrangement in bR involving amino acids and water molecules in the retinal pocket (reproduced from [115]).

The environment of the retinal moiety determines the absorbance spectrum of the protein, which can be tuned to yield different batho- or hypsochromic shifts by changing the surrounding amino acid residues [116, 117]. Upon illumination, retinal undergoes a photoisomerisation from its all-*trans* configuration to 13-*cis* in microbial rhodopsin (Figure 1.8), which differs from mammalian rhodopsin (11-*cis* to all-*trans*), triggering a cyclic reaction called the photocycle, which procedes via different photointermediates mediating the transport of ions across the channel. The bacteriorhodopsin photocycle is presented in Figure 1.10 [118, 119]. Typically, 6 different states are observed for bR, starting with the K state and ending with the O state, which thermally re-isomerises to the ground state conformation. These photointermediates differ in their kinetic stability and all have different protonation and isomeric states. The shortest lived step in the photocycle is the K state, where the all-*trans* Schiff base retinal is isomerized to 13-*cis* retinal on the

femtosecond timescales after light illumination and the slowest step is the formation of ground state from the O state, which occurs on the millisecond timescale. Several intermediates have been identified by the combination of several techniques such as site-directed mutagenesis, solid-state NMR, (time-resolved) crystallography, molecular dynamics and spectroscopy [120, 121].

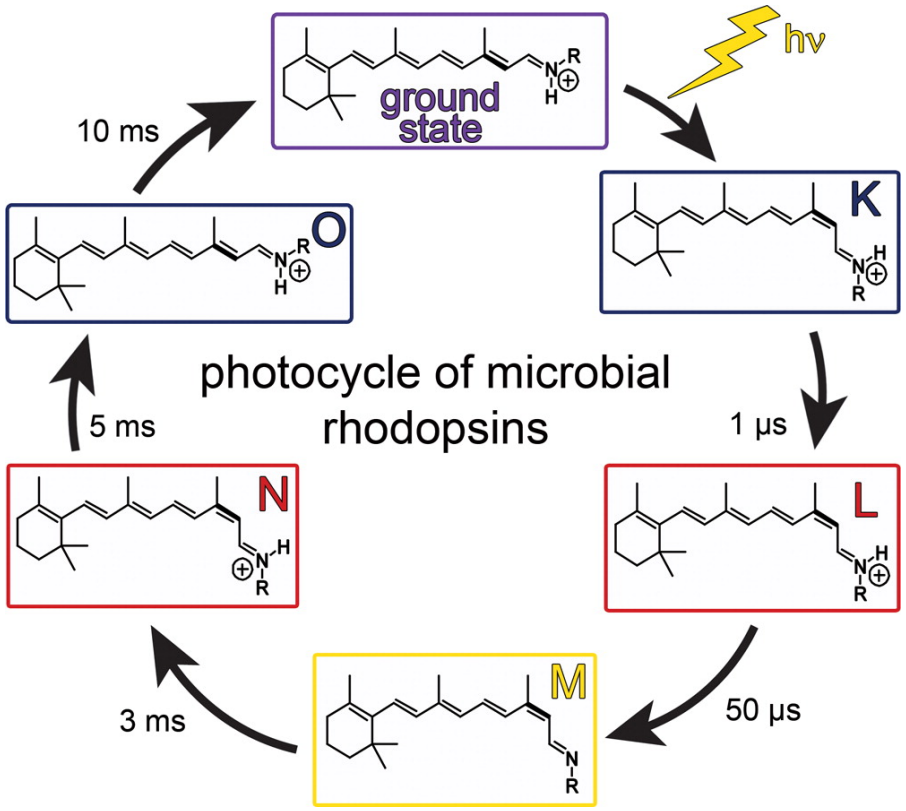


Figure 1.10: Photocycle of bR showing isomeric and protonation state of the retinal. L, M, N states are blue-shifted compared to the ground state (reproduced from [95])

1.2.1.2 Potential applications of photoreceptors

Since the discovery of bacteriorhodopsin in 1971 [122], several other microbial rhodopsins have been identified in other extremophiles; they are robust and stable proteins under extreme conditions such as high temperature, acidic pH or high salt concentration.

The development of several biophysical techniques such as x-ray crystallography or cryo-EM, FTIR, Raman, solution and solid-state NMR, EPR, AFM, crystallization or computational methods have benefited from microbial rhodopsins as

model systems [95]. They have notably helped in the development of membrane mimics, notably Nanodiscs [123] and Lipodisq [124], where bR was the first protein to be incorporated in these two nano-platforms.

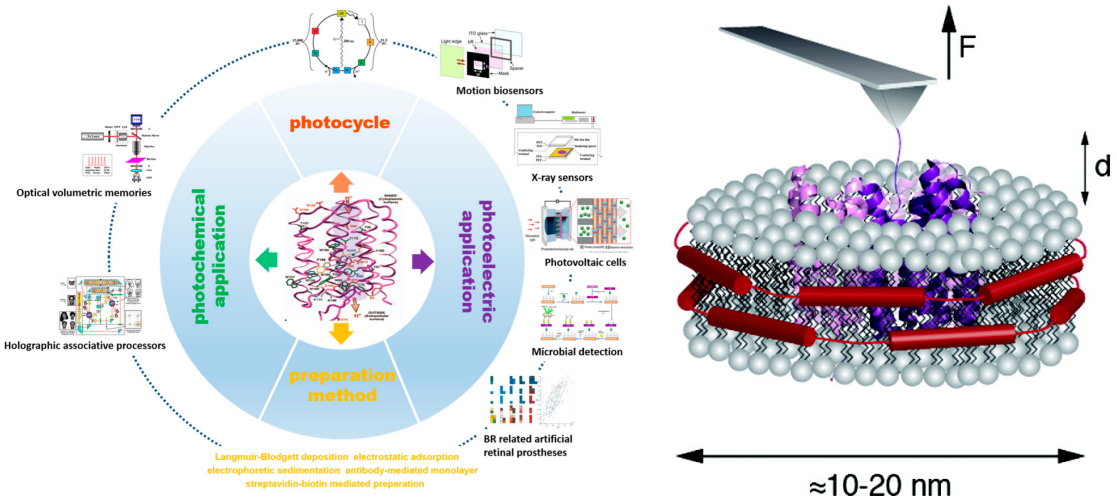


Figure 1.11: Left: Biotechnological applications of bR (reproduced from [125]) Right: AFM of bR embedded in POPC Nanodiscs to demonstrate that protein folding could be studied in Nanodiscs (adapted from [126]).

Mutants of bacteriorhodopsin and other microbial rhodopsins have been used in several other applications implicated in current generation such as potential dye-sensitized solar cells, as a bioelectronics device for memory storage or as biosensors [127] (see Figure 1.11). Channelrhodopsin, a light-gated cation channel found in algae, has opened the field of optogenetics (Figure 1.12) in which light is used to trigger depolarization or hyperpolarization of neuronal cells [128]. Optogenetics, a technique chosen by Nature Methods in 2010 as '*Method of the year*' and by Science as '*Breakthrough of the decade*' is a technique that uses light to control cells in living organisms. To do so, light-sensitive proteins are needed and microbial rhodopsins are the proteins of choice. In neurons the excitation is performed by light-gated channelrhodopsins and silencing by another light-gated halorhodopsins (chloride ions) [129, 130]. Recently archaerhodopsins (AR1 and AR3) have been used as new powerful and multiple-wavelength silencing proteins of neural activity [131, 132]. AR proteins are indeed able to produce very high currents (several hundreds

of pA, compared to bacteriorhodopsin) and thus are able to nearly perform 100% silencing of neurons. Compared to halorohodopsins, which remain inactive for few minutes after illumination, AR spontaneously recover within seconds. Therefore, the atomistic understanding of the mechanism of ion translocation by microbial rhodopsins is of crucial importance.

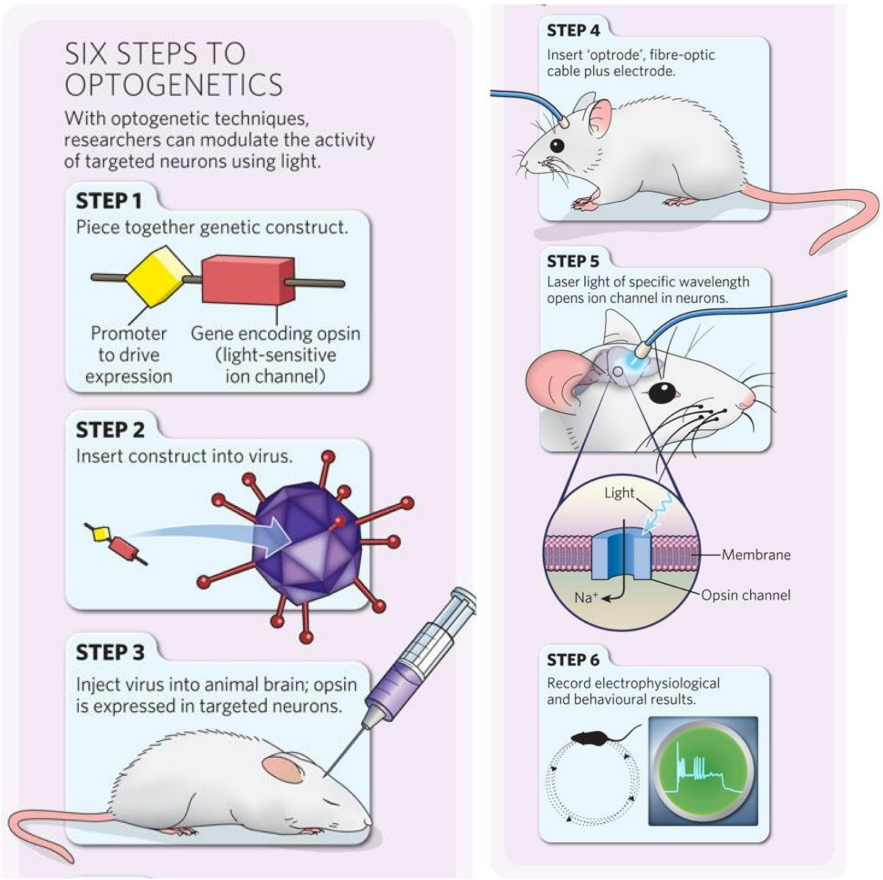


Figure 1.12: The six steps to optogenetics (adapted from [133]).

1.2.1.3 Mammalian rhodopsins

Briefly, mammalian rhodopsins display same structural similarities, with the same retinal Schiff base linkage but belong to the G-protein-coupled receptor (GPCR) family. Upon light activation, the retinal (in *cis* conformation) isomerizes irrevocably to the trans conformation, which triggers the exchange of GDP for GTP and protein conformational changes and activate a phototransduction cascades (via G_t, a transducin G-protein, found exclusively in retina rods and cones) [134]. The

signalling process ends once arrestin binds to rhodopsin, the protein is internalized, and the *trans*-retinal moiety is exchanged for a new *cis*-retinal molecule [135]. A different series of events is also observed but the protein does not spontaneously reform the ground-state, therefore the term photocycle is usually not used.

1.2.2 Transporters

Ions or other small hydrophilic molecules cannot cross biological membranes unaided. Permeability of the membrane is dependent on different factors such as hydrophobicity, charge and size of the solute molecule. Gases, ethanol, water and urea can diffuse across the membrane but sugars or ions cannot due to their hydrophilic character or charge state [136]. Nature has evolved to provide molecules or ions with poor membrane permeability, a pathway within the membrane via transporters, which are generally specific towards one molecule or closely related ones. They operate via two different modes, active or passive transport. In active transport, molecules move towards their concentration gradient requiring energy either from ATP hydrolysis or from an electrochemical gradient. Facilitated diffusion (passive transport) is the process where molecules or ions cross the membrane down to their concentration gradient, spontaneously, without any requirement of energy coupled transporter.

Transporters (Figure 1.14) permit the movement of ions, molecules (such as lactose) or amino acids through the bilayer against their concentration gradient. Co-transport of ions such as potassium, chloride or sodium is performed through the coupling of a thermodynamic favourable movement of one ion in one direction with another ion which is non-thermodynamically favoured [137]. Example of such co-transport are the Na^+/glucose symporter to help in the concentration of glucose in nephritic cells or the Na^+/Ca^{2+} antiporter responsible of maintain a low calcium concentration in cardiac cells [138].

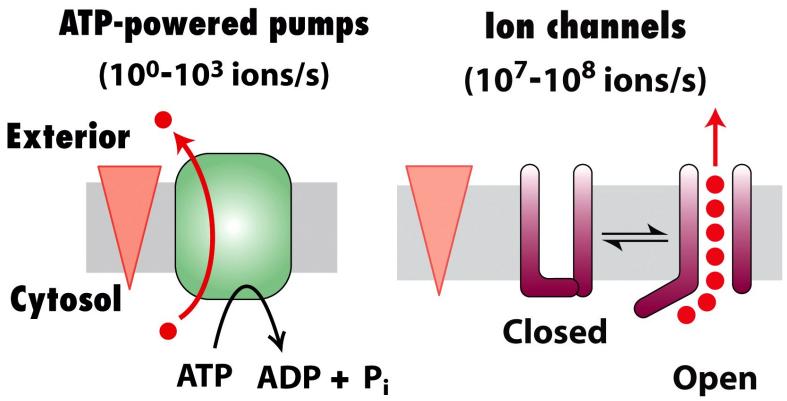


Figure 1.13: Schematic representation of different types of proteins permitting the movement of molecules across the membrane (adapted from [138])

Channel proteins (Figure 1.13), such as aquaporins or ion channels, can transport ions or small molecule such as water down to their concentration gradient a process commonly known as facilitated diffusion [139]. They are involved in maintaining the membrane potential and are prominent in neuronal cells for example.

ATP-driven transport (Figure 1.13), uses the hydrolysis of ATP to move molecules against their concentration gradient (commonly named as active transport). As an example, ATP-binding cassettes (ABC transporter) regulate the export of hydrophobic molecules from the cytoplasm via hydrolysis of ATP [140]. They are implicated in bacteria and cancer cell multidrug resistance. The role of bacterial ABC transporters is basically exporting antibiotic molecules, whereas in eukaryotes, P-glycoprotein (P-gp) is actively exporting anti-cancer drugs such as paclitaxel or doxorubicin, reducing the potency of the drug [141].

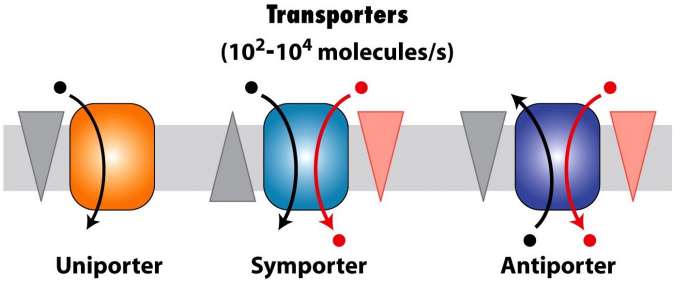


Figure 1.14: Different types of transporter illustrated. (adapted from [138])

1.2.3 Receptors

Receptors are transmembrane proteins, with a buried or water exposed ligand-binding site, which may face either the cytoplasmic or extra-cellular environment. Upon binding of the ligand, the receptor undergoes conformational changes that trigger the activation of a transducer or secondary messenger [142].

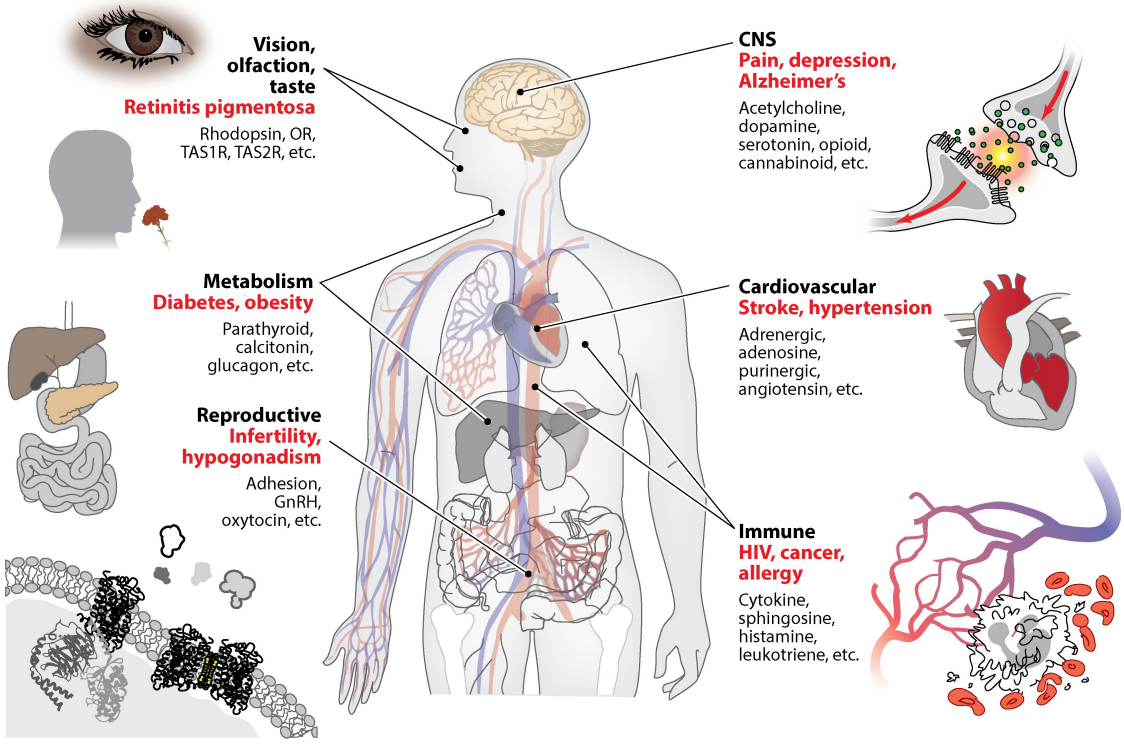


Figure 1.15: GPCRs are involved in many physiological processes (in black) and pathologies (in red) (reproduced from [143])

G-protein coupled receptors are seven transmembrane protein receptors and are the largest family of protein receptors in humans accounting for approximately 1% of the genome [144]. Lefkowitz and Kobilka won the 2012 Nobel Prize in chemistry for their pioneering work on GPCRs [145]. They are the most studied class of receptor, due to their implication in several signalling pathways and are pharmaceutical targets [146] (Figure 1.15). Ligands such as hormones, peptides, neurotransmitters, ions, photons, lipids or odorants can trigger GPCR signalling [147]. They can be divided in different class (A to F), based on sequence similarities, even though they

differ significantly in their extracellular N-terminal domain. Class A (rhodopsin-like) is the most prominent class, containing more than 700 receptors [148]. Other classes are based on sequence and signalling similarities. Ligand binding to GPCRs, induces a conformational change to the protein, especially to the cytoplasmic-facing part, which can therefore easily bind the G-proteins [134, 149].

G-proteins, for which another Nobel prize in 1994 was awarded for their discovery, are heterotrimeric proteins, containing α, β and γ subunits [150] (Figure 1.16). Subunit α, which is responsible to bind GTP and can carry post-translational modification such as myristoylation or palmitoylation, and β subunits are forming the major part of the G-protein and these are the subunits which direct contact with the GPCR [151]. γ subunits possess an extended alpha helical shape and can be prenylated. These PTMs permits the G-proteins to be in close contact to the membrane. Once bound to the GPCR, the subunits dissociate into G_α and $G_{\beta\gamma}$, which separately trigger other proteins such as phospholipases, adenylate cyclase or phosphodiesterase [152].

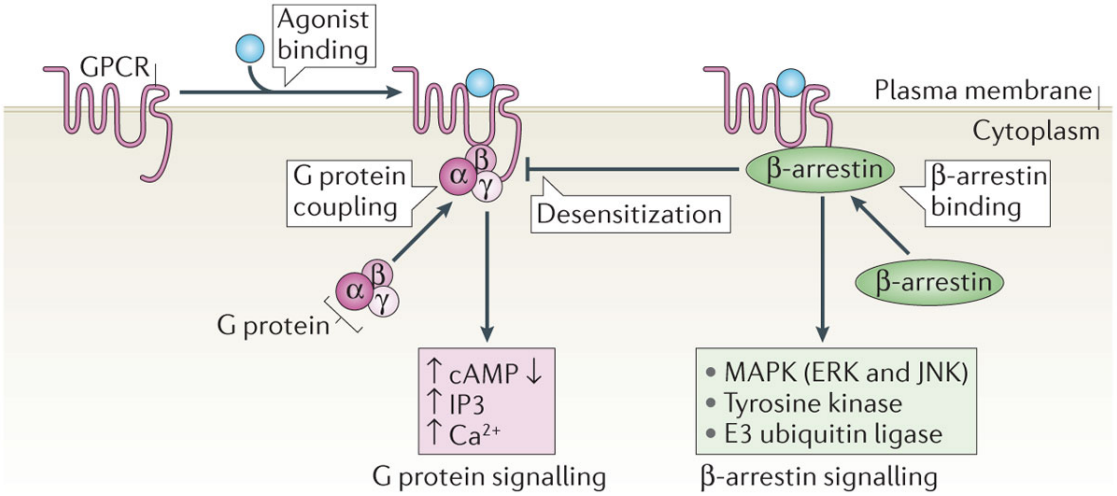


Figure 1.16: Binding of ligand induces conformational changes in the G-protein-coupled receptor (GPCR) to activate it. The different signalling pathways are illustrated (reproduced from [153])

There are several types of G_α subunit, classified on the basis of their sequence and mode of action: G_t, transducin G-protein, is found in the retina [154], G_s, which

signalling is performed via adenylyl cyclase or G_i, which inhibit the adenylyl cyclase pathway. All three types affect the intracellular concentration of cAMP [155, 156].

1.3 Reconstitution of membrane proteins

Membrane proteins are generally studied using detergent-solubilized biological membranes [157, 158]. Detergents (or surfactants, surface active molecules) are compounds which exhibit amphipathic properties, usually with a long hydrophobic carbon chain with a hydrophilic polar head [159](Figure 1.17). Their role is to extract proteins from the membrane by lowering the surface tension of the bilayer and solubilizing lipids and proteins. Micelles are spherical aggregates of detergent molecules and are formed above a critical concentration (critical micellar concentration, CMC), for which the inner core is hydrophobic, and the outer core is hydrophilic. Micelle formation is dependent on temperature, concentration of detergent and ionic strength of the solution. As lipids, detergents can be described by a phase diagram [160].

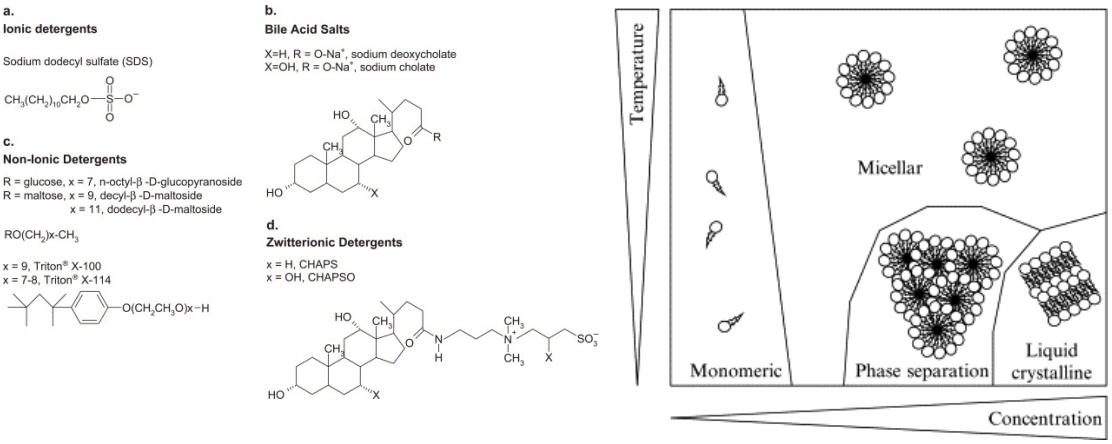


Figure 1.17: Left: Different types of detergent used for membrane protein studies. (reproduced from [159]). Right: A simplified phase diagram of a glycosidic detergent, where the transition from monomeric molecule to micelle assembly is named as the critical micellar concentration (CMC) (reproduced from [161])

For membrane protein extraction, the use of detergents above their CMC is critical (Figure 1.17). The amount of detergent plays another role in ensuring

enough detergent molecules are present to solubilize the vast majority of proteins present in the membrane [162]. To perform this task, several types of detergents are now commercially available, either from synthetic or natural sources, which can be classified by their headgroup properties. Ionic detergents, such as SDS or CTAB, routinely used for gel electrophoresis or DNA isolation, are categorized as harsh detergents as they usually denature proteins, whereas zwitterionic or neutral detergents have milder effects on protein structure and activity [161]. The choice of detergent depends strongly on the downstream applications. For example, Triton-type detergents could have some negative impact on circular dichroism spectroscopy due to their aromatic ring [163]. For NMR, special lipid-mimetic detergents have been developed to reduce the motion of the protein and therefore maintain sample heterogeneity while in solution [164, 165]. Finally, crystallization of membrane proteins in detergents is a difficult task to achieve as the presence of lipids and detergents adds another level of complexity to the crystallisation screening and due to the typical high salt and extreme pH used, tend to phase-separate impeding nucleation and formation of protein crystals [166].

Experiments on detergent-solubilized proteins have played a fundamental role in helping to understand the structure and activity of membrane proteins. Nevertheless, micelles are poor membrane mimetics as a loss of lateral pressure is experienced compared to a bilayer environment [167]. Moreover, detergents may remove or perturb the annular lipids of the protein, which can have a direct influence on protein function [168]. The pursuit for a detergent that maintains protein function and structure is a time-consuming and expensive task, as no single detergent is appropriate for all membrane proteins [169]. High concentrations of detergent may result in the occlusion of binding sites or denaturation of hydrophobic binding domains. Other binding partners may have non-specific interactions with micelles, reducing their effective concentration and effects on the protein [170].

Due to the limitations of detergent-solubilised samples, new membrane mimetics which more accurately reflect the native cell membrane have been developed, which can be classified into two different groups, the non-lipid-based mimetics which

includes detergent and amphipols and a lipid-based groups including liposomes, bicelles, Nanodiscs, SMALPs and Salipro discs (Figure 1.18). Except for the Lipodisq (SMALPs) preparation, the first step requires the use of a detergent-solubilized membrane protein.

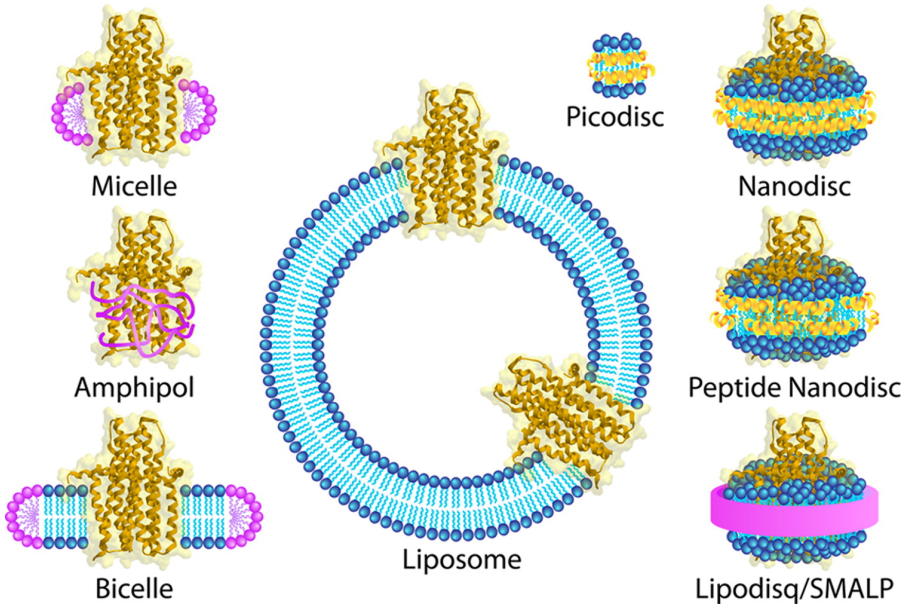


Figure 1.18: Different platforms to study membrane proteins. Amphipols and detergent have no lipid-scaffold and are mimicking lipid environment. Liposomes, bicelles, Picodisc and (Peptide-)Nanodisc are lipid-based scaffolds, where membrane proteins are first solubilized in detergent prior to their reconstitution. Lipodisq/SMALPs is a detergent-free method to extract membrane proteins directly from their expression host membrane. Reproduced from [78]

1.3.1 Liposomes

Liposomes are spherical lipid compartments formed upon addition of an aqueous solution to either as a lipid powder or from a solvent dried film. Multilamellar vesicles are the lipids compartments composed by multiple layer of lipid bilayers (comparable to a Russian Matryoshka Doll structure) and their formation arises upon simple mixing of lipid with an aqueous buffer [171]. Their size is approximately 0.2-10 μm. Because of their big size and multiple layers, which are not ideal for proteins to reconstitute, smaller vesicles are formed by simply sonicating the sample. The resulting small unilamellar vesicles (SUV) are characterized by their small

size (between 20-50 nm) and highly curved shape, into which protein incorporation is difficult [172, 173].

Extrusion of a lipid suspension using polycarbonate filters is commonly used instead of sonication, because the size of the lipid vesicles can be varied by changing the pore size of the polycarbonate filter [174]. During extrusion, large unilamellar vesicles (LUV) are formed (size up to 1 μm) and they are the preferred lipid platform for protein reconstitution because their curvature and lipid composition resembles native biological membranes more closely, mimicking the lateral pressure exerted in native membranes. They are the preferred reconstitution platform for ion channels or transporters as liposomes can enclose an aqueous environment that differs from the external solution. Liposomes have been used to show protein activity for amino acid transporters [175] or potassium channels [176].

Finally, the giant unilamellar vesicles (GUV), which can be formed by electroformation or by controlled dehydration of a lipid film, are usually used for microscopy or electrophysiological experiments (patch-clamp) because due to their size (up to 100 μm) they can accommodate microelectrodes and are suitable for imaging, but due to their high scattering in spectroscopic experiments and fragility, they are not commonly used for other biophysical methods [177].

1.3.2 Amphipols

Amphipols (Apols) are amphipathic polymers consisting of alternating hydrophilic and hydrophobic units and are categorized as surfactants (Figure 1.19). They were developed in the early 90's and were originally developed for biophysical methods to increase the stability of membrane proteins compared to detergents [178]. The hydrophobic part of the protein is covered by a thin layer of amphipathic polymer. Three or four polymers chain self-assemble around the membrane protein and provide a hydrophobic environment different from detergents, where both sides of the protein are accessible. Amphipols are flexible to accommodate the irregular shape of the protein and to possess close spacing between hydrophobic groups in the polymer in order to prevent formation of loops. The polymer chain size

typically varies between 4 and 60 kDa, but most of them fall in the 10 kDa range [179]. As detergents, they exhibit different properties based on their charge and backbone chain length as Figure 1.19 shows.

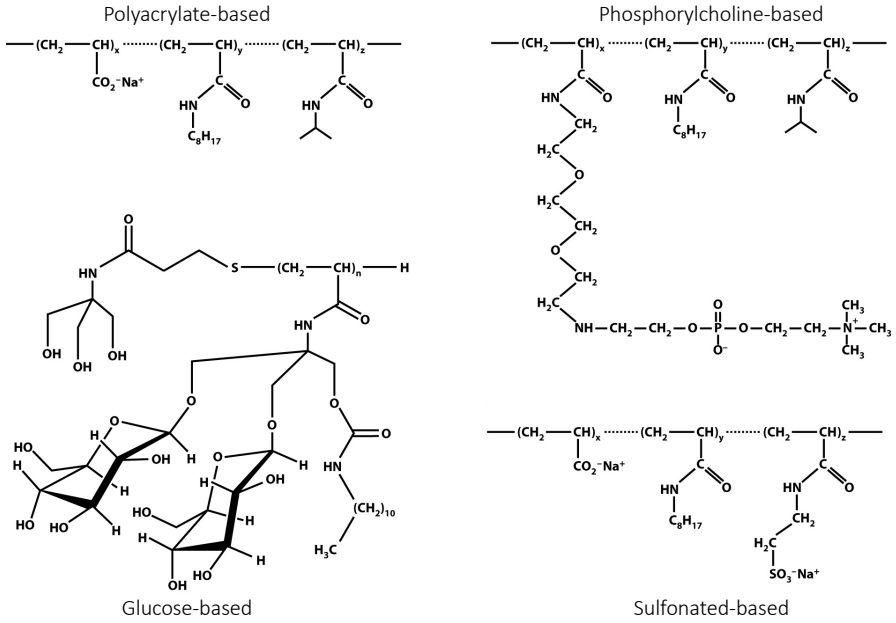


Figure 1.19: Different structures of the most used amphipols for membrane proteins studies represented. (reproduced from [179])

Amphipols are generally not able to solubilize membrane proteins directly from a host membrane and so proteins are generally extracted using a mix of membrane with detergent and amphipols. Several proteins have been able to be reconstituted and studied as amphipols, which have been re-designed over the years with multiple Apols now available, that do not interfere with biophysical methods such as CD or NMR. Bacteriorhodopsin, GPCRs and other membrane proteins such DAGK have shown to be able to perform ligand binding or G-protein binding, but at slower rate as observed for detergent-solubilized membrane proteins due to the polymer shielding the membrane protein. As in detergent, the lateral pressure provided by lipid in the bilayer is considerably reduced, which has some impact on protein stability and activity.

Considerable efforts have been made to use Apols to crystallise membrane proteins, but so far this method has succeeded for only a few proteins [180]. TEM

and cryo-EM have also been applied to membrane proteins in Apols, for which low resolution structures of macromolecular complexes have been obtained. Some other applications to Apols have been developed such as being a suitable platform to perform cell-free expression of membrane proteins or used as vectors for delivery of insoluble peptides *in vivo*. Globally, they offer a much more stable environment than detergent, but with the same limitations as detergent concerning ligand binding or protein-protein interactions.

1.3.3 Bicelles

Bicelles are coin-shaped nanoparticle formed by mixture of long (DMPC) and short (DHPC) chain phospholipids or by long chain phospholipid mixed with particular detergent such as CHAPS(O) in defined ratio [181, 182]. The short chain phospholipid (or detergent) will form a belt to cover the long hydrophobic chain of the phospholipid. Unlike liposomes, both sides are easily accessible once the protein is reconstituted, which make them suitable system for studying protein-protein interaction upon activation of the proteins. The size of the bicelle can be controlled by changing the lipid:lipid or lipid:detergent ratio [183]. Several proteins have been reconstituted in bicelles. DAGK has shown to perform comparable activity in detergent or liposomes, being able to conserve its enzymatic activity [184]. EmrE, a multidrug resistance transporter from *E. coli*, exhibits drug binding once reconstituted in bicelles in different lipid compositions [185].

Bicelles have been widely used for NMR, as upon a certain concentration, they tend to align with the magnetic field. They have been also for membrane protein crystallization and for drug delivery. The main drawback of bicelles is the variability of their size, which changes upon dilution of bicelles in solution.

1.3.4 Nanodiscs

A modified sequence of the human Apolipoprotein A1, called MSP, once in contact with a certain amount of lipids is able to form discoidal bilayer of approximately

10 nm diameter [186, 187]. Several MSP proteins have been designed by mutagenesis to accommodate bigger protein complexes and to produce Nanodiscs of different sizes [188].

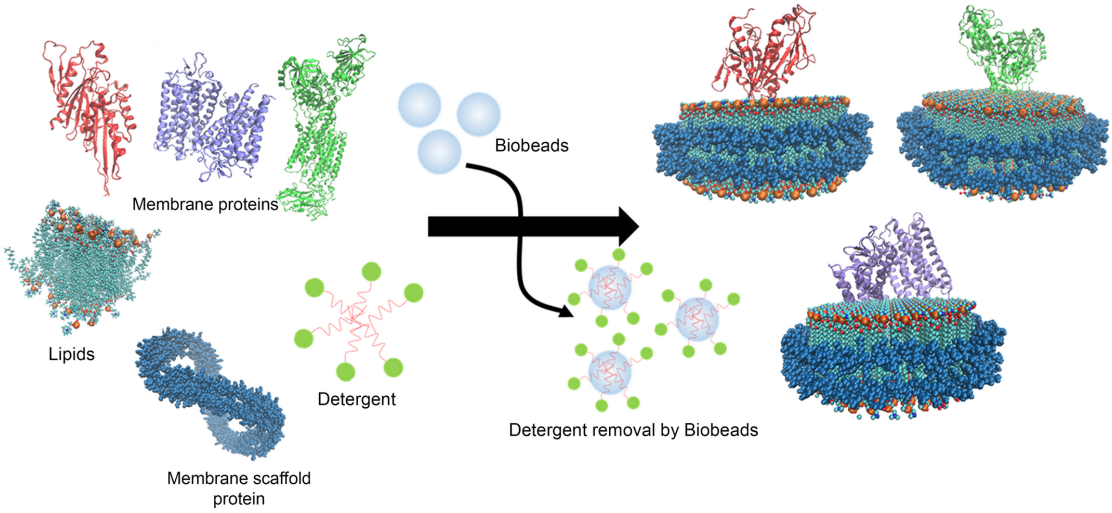


Figure 1.20: Membrane protein incorporation in Nanodisc. Membrane protein in detergent is mixed with lipid and membrane scaffold protein (MSP). Biobeads are added in order to remove detergent and Nanodiscs are formed after the concentration of detergent is below its CMC. (reproduced from [189])

Detergent-solubilized membrane proteins were soon incorporated into Nanodiscs. Their formation relies by simply adding the lipid and the MSP protein in the presence of Biobeads to remove excess detergent in a protein-dependent defined ratio [123](Figure 1.20). Their use to show functional activity and signalling have been proven not only by the fact that today more than 550 publications but also due to the compatibility of the nano-platform to carry several biophysical techniques such as chromatography, X-ray crystallography, cryo-EM, NMR and spectroscopy. Nanodiscs are preferred in most cases as they offer a similar environment to a native membrane [188].

Proteins cannot be incorporated into MSP Nanodisc directly from their native environment, therefore a detergent step is necessary to purify the protein, in which some important molecules, lipids and oligomeric state are lost [190]. The size of Nanodiscs is not flexible enough to accommodate large macrocomplexes and

some protein-protein interactions may occur between the reconstituted protein and the MSP protein.

1.3.5 Other discoidal membrane mimetics

Peptide-Nanodiscs could also be formed by the addition of mimetic peptide fragments of the apo-A1 protein. Several monomeric peptides have been designed and had the ability of modulate the nanodiscs diameter from 9 to 15 nm, but their stability and protein incorporation are still under investigation [191].

Recently, a new lipid bilayer mimetic has been developed called Salipro (also called Picodisc). They rely on saposin A, a protein involved in lipid transport, which can form in presence of lipid and protein lipid nanoparticle [192]. They have the ability to adapt their size to the incorporated protein, with only few lipids surrounding the protein, forming a minimal lipid-protein nanoparticle [193]. To date, only human Saposin A has been exploited, but as for the MSP, we should expect several mutants to be generated as other saposin proteins might have preference for certain lipid or protein class. As for Nanodiscs, different parameters when the protein is reconstituted should be taken into account such as lipid, lipid-protein ratio, incubation time and temperature [192]. Protein-loaded discs from lipid-protein discs may easily be separated by size-exclusion chromatography, compared to Nanodiscs, which size is mainly governed by the MSP belt for integral membrane proteins [193]. Their potential for membrane protein determination by cryo-EM has been recently shown [193, 194] as well as their potential to study structure, dynamics and ligands or protein interactions by solution NMR.

1.4 Methods to visualize lipid-protein interactions

1.4.1 Detergent-free extraction of membrane proteins using a hydrolysed co-polymer of styrene and maleic acid (SMA)

In the previous section, several discoidal platforms for membrane protein reconstitution were reviewed. Their common feature, was that all of them use detergent

at least for the first steps of the reconstitution process. Detergents have some detrimental effects on membrane protein as previously described as they destabilize and distort structure and affect protein activity. The pursuit of a tool which would avoid detergent solubilisation of membranes has been unravelled by the discovery of a polymer composed of styrene and maleic acid which is able to assemble in an amphipathic hypercoiled structure able to extract small patches of lipid bilayer [195, 196]. The advantage of this technique is that the resulting nanoparticles provide a membrane-like environment for the embedded proteins.

The aim of this section is to shortly review the use of hypercoiled polymer, such as SMA or derivatives, which can easily extract and purify membrane proteins from their native environment without the use of detergent. These nanoparticles have been commonly called SMALPs [197], standing for Styrene-Maleic Acid Lipid Particles or Lipodisq [124].

1.4.1.1 Polymers available

1.4.1.2 SMA

SMA polymer (Figure 1.21) is synthesized from styrene and maleic anhydride monomer units in a defined ratio by radical polymerisation reaction [198]. Synthesis of SMA is performed by a radical reaction where both maleic anhydride and styrene molecules are mixed together continuously in order to prevent heterogeneity of the polymer. Nevertheless, non-homogeneous samples are obtained, varying in length and composition [198]. SMA is formed by simple hydrolysis of the maleic anhydride giving rise to the maleic acid. The ratio of styrene to maleic acid may vary from 1:1 to 4:1, resulting in polymers that have physico-chemical properties such as different solubility, pK_a or molecular weight (from 7.5 kDa to 10 kDa).

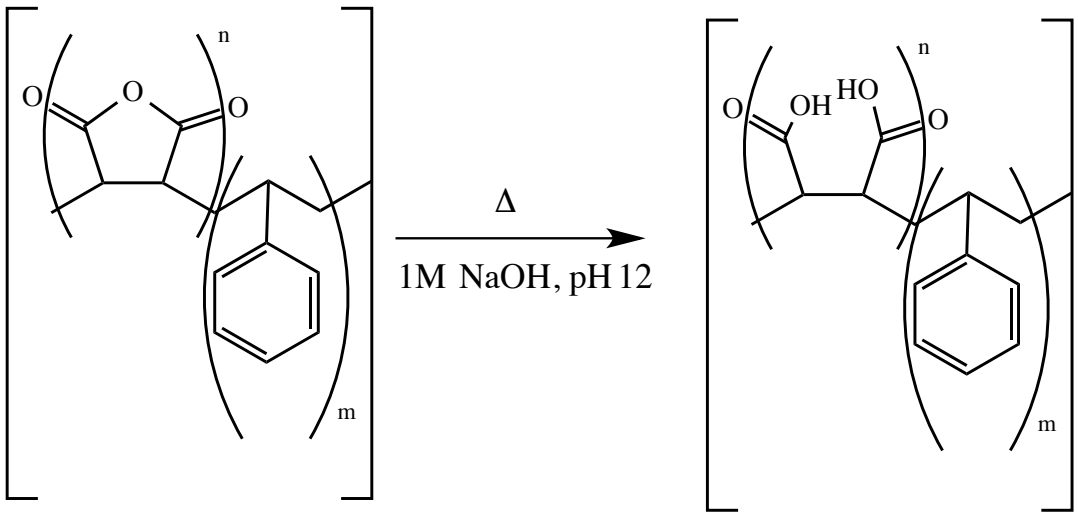


Figure 1.21: SMA polymer hydrolysis, where a single unit (square bracket) is represented. Maleic anhydride is hydrolysed into maleic acid at high temperature in alkaline environment. Ratio of styrene (m) to maleic acid (n) can vary from 2:1 up to 4:1.

SMA polymers were first used for drug delivery carrier, where drugs were conjugated via the acetate group in the maleic acid moiety [199]. It was discovered that SMA has the ability of forming small discoidal nanoparticles when combined with lipid (10 nm diameter). Malvern Cosmeceutics first patented the use of SMA for multiple applications such as drug delivery or solubilisation of lipid bilayers for extraction of membrane proteins [200]. From then, different polymers have emerged carrying different ratio styrene to maleic acid and different lengths as Xiran-type polymers produced by Total Cray Valley (SMALPs) or SMA by Malvern Cosmeceutics (Lipodisq) [201].

SMA solubility depends strongly on pH and concentration of divalent cations. Indeed, hydrophobicity of the polymer not only depends on the ratio between the styrene and maleic acid but strongly on the pK_a of the different maleic moieties in the SMA, which ranges from 6 to 10, depending itself on the number of surrounding styrene groups [195]. Indeed, pH values below 6 show a decrease of solubility of SMA in solution, as all the carboxylate groups are protonated (Figure 1.21). At pH above the pK_a of the carboxylate groups, electrostatic repulsion prevails over the

hydrophobic effect and permits the SMA to adopt the typical random coil already observed by Tighe and Tonge [196] for other polymers.

Divalent cations such as Mg^{2+} or Ca^{2+} are chelated by the carboxylate groups and the polymer precipitates. Concentration of such ions in solutions for which precipitation is observed vary from polymer to polymer, with a threshold of 1 mM X^{2+}. Lastly, the solubility of SMA depends strongly on ionic strength of the solution used as demonstrated by Scheidelaar and colleagues [195].

1.4.1.3 SMA-derivatives

Several other polymers have been developed during the years for diverse applications (Figure 1.22). SMASH, a polymer carrying a thiol groups enables conjugation of the polymer to maleimide dyes or different affinity tags, has been used for FRET or fluorescence microscopy [202]. To overcome the problem of the presence of divalent cations or low pH, zwitterionic polymers have been synthesised, in which phosphocholine groups are substituted for the maleic group. They seem to form more homogenous samples around 10-30 nm diameters. SMA-EA [203], which is a SMA derivative where the carboxylic groups is conjugated by an ethanolamine molecule offers another alternative to SMA. The size of the nanoparticles (between 10-50 nm) and its resistance towards high salt concentration, presence of divalent cations, high temperature and low pH made them an attractive new polymer for which some NMR and EPR studies have been performed. Alignment of SMA-EA large discs to magnetic field can be achieved by the addition of Yb^{3+} ions and allows the tilt angles of transmembrane helices to be studied by solid state NMR. [201].

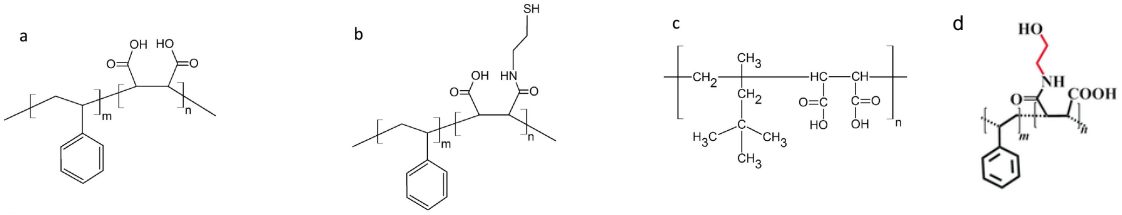


Figure 1.22: Different types of SMA. a) SMA, b) SMA-SH, c) DIBMA, d) SMA-EA (adapted from [201, 203])

DIBMA, a polymer composed of diisobutylene instead of styrene, which is a BASF byproduct known as Sokalan CP9, can produce discs of approximately 12 to 30 nm diameter [204]. They are less efficient in terms of disc formation, but unlike SMA, they do not absorb UV light and are therefore useful for CD and UV-Vis spectroscopy. Compared to SMA, DIBMA tolerates high concentrations of divalent cations.

1.4.1.4 Mechanism of formation of SMALPs

The formation of the SMALPs (Figure 1.23) consists of three steps which have been studied using turbidity measurement by Scheidelaar and colleagues [195]. The first step is the deposition of the SMA polymer on top of the lipid bilayer, which can be modulated by the presence of anionic lipids such as PG which repel the polymer and hinder deposition. Increasing the ionic strength of the solution would promote the deposition of the polymer, shielding charges and reducing charge-charge interactions. The second step is the insertion of the polymer into the hydrophobic core, which is strongly dependent on the lipid packing. Indeed, membrane fluidity, lateral pressure and bilayer thickness have an impact on the insertion of the polymer as tight packing or thick membrane have detrimental effect on SMA insertion. Gel phase lipids are much more difficult to solubilize as demonstrated by Swainsbury and colleagues [205]. The last step is the formation of lipid discs by solubilizing the lipid present in the lipid bilayer. When SMA is in excess, the solubilisation process strongly depends on the second step as a large enthalpic penalty for the charge buried and the formation of the SMA-nanoparticles is therefore favoured [198]. Last but not least, SMA shows no preference for certain lipids, as demonstrated by the solubilisation of a lipid mixture of *E. coli* inner membrane shows the same composition of lipid before and after SMA addition [195].

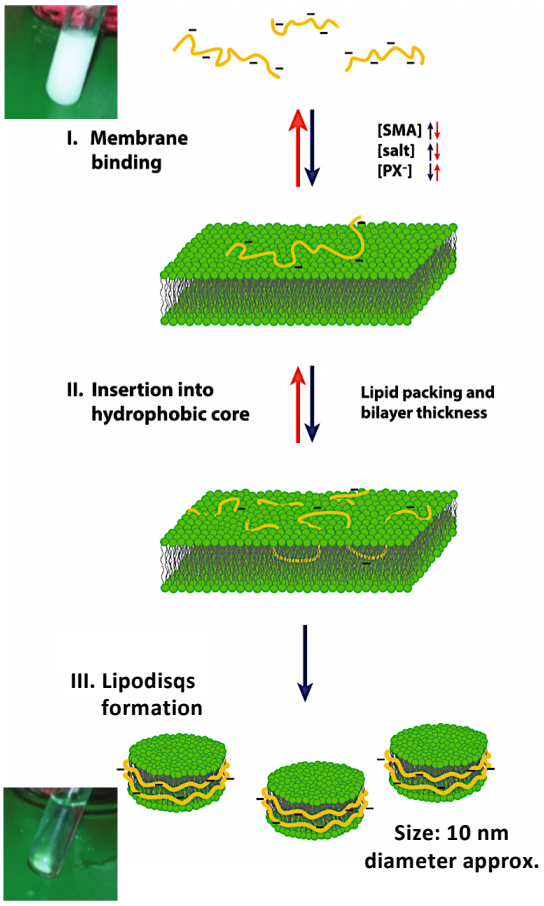


Figure 1.23: Proposed mechanism of formation of Lipodisq, which is dependant of different factors such as concentration of polymer, salt and negatively charged lipids and lipid packing (adapted from [198]).

1.4.1.5 SMA as a tool to solubilize membrane proteins from biological membranes

Not only is the SMA polymer able to solubilize pure lipid membranes, it has been possible to extract membrane proteins from biological membranes using standard purification methods (Figure 1.24).

Proteins from different host organisms such as bacteria [206], archaea [207], yeast [208], insect [209] and human cells [209]. Bacteriorhodopsin, 27 kDa, has been incorporated from a DMPC-supplemented native membrane for biophysical characterization [124]. Other membrane proteins have been incorporated from a single alpha helix peptide to a huge macro-complex such as holo-translocon [210] or cytochrome c oxidase [208]. These proteins have been either isolated from their

natural source in which they are abundant or recombinantly expressed. Some difficulties in the formation of Lipodisq or SMALPs could arise due to the tight lipid packing around membrane proteins or the high protein-lipid ratio in the native membrane. A simple solution to help in solubilizing such membrane is to supplement the membrane with PC lipids which helps to untighten the natural lipid environment and therefore improves the yield of SMA-discs [195].

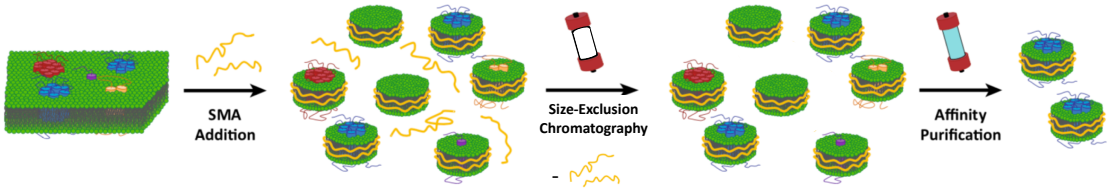


Figure 1.24: Schematic representation of how to purify membrane proteins using SMA. First, SMA is added to the host membrane, which form proteo-Lipodisq. Excess of SMA is removed via SEC and finally proteo-Lipodisq are purified via IMAC (adapted from [198]).

Purification of such proteo-SMALPs (Figure 1.24) could be achieved by size exclusion chromatography if the protein purified is easily separated by size from other proteins present and if the protein expressed is abundant, e.g. cytochrome c oxidase and bacteriorhodopsin. Recombinant proteins bearing a His-Tag incorporated in SMALPs can be purified by standard Ni^{2+} immobilized metal affinity chromatography (IMAC). Purification of proteo-SMALPs requires the removal of excess polymer by size-exclusion chromatography, as the excess polymer could obstruct the binding of the His-Tag to the Ni^{2+} column [198]. To date, only one group has used the FLAG tag [211] to purify a human nucleoside transporter. It is expected that other tags could be used using standard protocol established for Nanodiscs for example and would complement the existing purification techniques.

Comparison of the stability of proteins embedded in SMALPs with those solubilized in detergent reveals that a higher activity is maintained over larger periods. Because proteins are surrounded by lipids, they are in a less dynamic environment compared to detergent micelles therefore reducing flexibility and improving stability and storage potential significantly. Several examples have

been studied in the literature such as GPCRs, transporters and macro-complex for which SMALPs have demonstrated being a better scaffold to study proteins [212]. Cycles of freeze-thaw, long-storage at low temperature or temperature-dependence experiments of receptor in SMALP and detergent have been compared, with the nanoparticles being more efficient in maintaining protein activity than detergent [213, 214].

The lipid composition of certain tissues and the lipid environment of membrane proteins have been studied using either thin layer chromatography or mass spectrometry-based methods (lipidomics) [215]. Circular dichroism has enabled the study of folding and thermo-stability of protein in SMALPs. (Pulsed-)EPR and NMR study of ion channels and other transporters have been performed and show an enhancement in signal compared to other lipid platforms such as liposomes [124, 216]. Compared to Nanodiscs, no significant change is observed but the fact that SMA preserves the native environment of the proteins is seen here as an advantage. Ligand binding experiments using both radioactive and fluorescent probes have been used successfully for a number of receptor including GPCRs [209, 217] and ABC transporters [214].

Recently, bacteriorhodopsin has been crystallized from SMALPs using LCP, although the time needed for crystal formation was months [218]. Some structures have been solved combining cryo-EM and SMA such as AcrB (resolution 30 Å) [219] and complex III (resolution 3.2 Å) [220] (Figure 1.25).

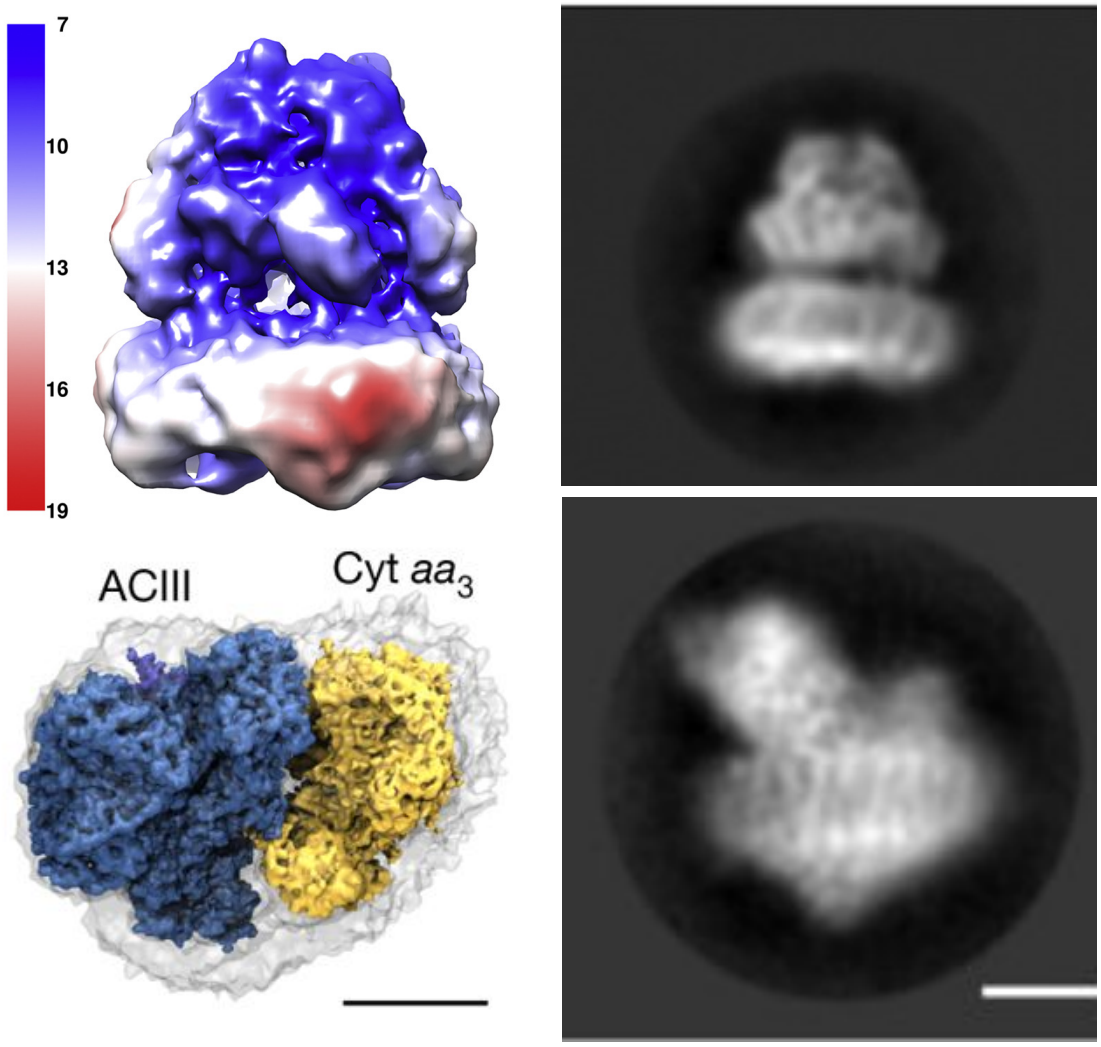


Figure 1.25: Top: AcrB 2D class average images yielding an 8 Å resolution cryo-EM structure (resolution colour are blue for high resolution and red for low resolution) (adapted from [219]). Bottom: 2D class average images yielding an 3 Å resolution cryo-EM structure ACIII-cyt aa3 supercomplex in Lipodisq (scale bar 50 Å, adapted from [220])

1.4.2 Mass spectrometry technique

Mass spectrometry has become an important analytical tool for biology since the discovery of matrix-assisted laser desorption/ionization (MALDI) and electrospray ionization (ESI) in the 1980s and for which both ionization techniques have promoted their inventors, Koichi Tanaka and John Fenn to receive the Nobel prize in Chemistry in 2002. Methods including collision-induced dissociation (CID) have enabled the characterization of more than 250,000 organic molecules deposited in a public

databank, which is now routinely used in analytical sciences [221]. Discovery of ESI and MALDI MS techniques have enabled the ionization of large biomolecules such as proteins and peptides to be transferred intact and at least singly charged in the gas phase. In this work, we will mainly focus on MALDI-TOF MS and nano-ESI MS for the study of membrane proteins as it has been shown to preserve native structure in the gas phase.

Mass spectrometers are typically composed of an ion source, a low-resolution mass analyser, a collision cell and a high-resolution mass analyser [222]. Ion sources help in the production of charged species and usually preserve the integrity of molecules. To focus the ions and remove neutral species, a quadrupole or ion trap is usually used, after which the ions enter the collision cell to be fragmented or further activated in order to remove remaining water or buffer molecules present. Finally, the ions are directed towards the detector, which could be of several types, such as time of flight (TOF) [223], Orbitrap, or Fourier-transform ion cyclotron resonance (FT-ICR) [224]. All of which are able to isotopically resolve the mass of small peptides (up to 50 amino acids and charge up to 7) [222]. The resulting signal is transformed into a mass spectrum where the mass to charge (m/z) ratio is plotted against the intensity of ions. The mass of the molecules is then deduced depending on the ionization techniques. If fragmentations have been performed, the structure of the molecule can be assessed (for small molecules) or if employed with large biomolecules, the sequence of the protein can be obtained.

1.4.2.1 Native mass spectrometry (nano-ESI mass spectrometry, nMS)

The pursuit of a MS technique which retains the native conformation of proteins immediately prior to entry into the gas phase, has been achieved by nano-ESI MS, which is performed in solution under non-denaturing conditions (Figure 1.26).

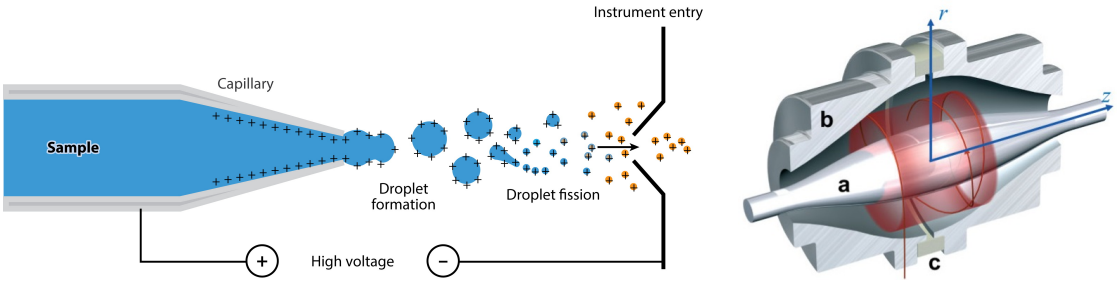


Figure 1.26: Left: Electrospray ionization process where droplets are formed, yielding different charge states of the protein (reproduced from [225]). Right: Orbitrap detector composed of inner electrode (a), outer electrode (b) and insulator (c). Ions are injected perpendicular to the z axis (reproduced from [226])

The instrumentation used here is different from MALDI as the sample is directly sprayed via a conducting gold-coated capillary. The sample is first dissolved in a volatile buffer, such as ammonium acetate, to facilitate the desolvation of the sample in vacuum and to reduce the possibility of formation of protein-buffer adduct [227]. Once sprayed, the sample is ionized and dispersed into small droplets which evaporate as they enter the instrument yielding proteins that bear multiple charges compared to MALDI-MS [228]. Smaller droplets (up to 10 orders of magnitude smaller) require less harsh conditions for evaporation, therefore, the native fold of the protein is more likely to be maintained [225]. Samples consumption is low as the flow rates used for nano-ESI are in order of nl/min (only few μL of samples are required for a single experiment) [229]. After being sprayed, collision cell parameters have to be carefully controlled to ensure that the sample is kept intact in the gas phase [230]. Control of the pressure within the instrument helps to maintain the internal energy of the ions (drastically reduced due to the change of pressure), to dissociate molecules still in contact with the protein and finally to ensure the formation of a condensed ion beam which is important for detection. CID experiments occur in a collision cells, which are compartments where inert gas molecules are injected at a certain pressure to help in the dissociation of water or other molecules in close contact with the protein [231, 232]. Therefore, they improve the signal of the protein as they get rid of the remaining molecules stuck on their surface.

The Orbitrap mass analyser (Figure 1.26) used for nESI MS experiments achieves higher resolution than TOF detectors for larger macromolecule complexes. Orbitraps are ion-trap detectors for which ions are injected inside a spindle-like electrode and are placed in orbit around the electrode in a frequency proportional to their m/z ratio [225]. The central electrode is brought to an alternating voltage from opposite polarity of the ions. Movement of the ions around the coil can be decomposed in two different motions, circular and axial, for which the frequency can be used to measure the mass. The equation for the axial movement is given by the following equations and is independent of any initial parameters [233].

$$z(t) = z_0 cos(\omega t) + \sqrt{\frac{2E_z}{k}} sin(\omega t)$$

$$\omega = \sqrt{\frac{kq}{m}}$$

Indeed, the movement of the ions generates an induced current which is detected and converted by Fourier transform in frequency spectra and afterwards in mass spectra using the previous equation (Figure 1.27). Orbitrap mass analysers are a cheap and low maintenance alternative to FT-ICR with the same accuracy and high resolving power for low m/z ions [234]. They are able to analyse intact protein complexes in their native state. High resolution could be enhanced by adapting the Orbitrap RF current and by better desolvation in the source as achieved by Hopper and Laganowsky [230, 235].

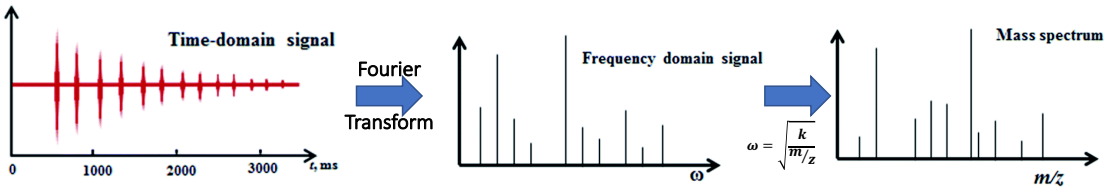


Figure 1.27: Signal conversion in Orbitrap mass analyser (adapted from [236])

At first, it was believed that the free detergent molecules bound to the surface of membrane proteins would suppress ionization and would render mass spectrometry on membrane proteins in detergent impossible [237]. But thanks to the work of

Barrera and Robinson, the protein $BtuC_2D_2$ in excess of detergent (2x CMC) was characterized [238]. In that work, the protein was dissociated from detergent micelles using high voltage (collisional energy of 200 V in a CID cell) before being detected (Figure 1.28). It has been shown that micelles in vacuum act as a protecting scaffold and play a key role of transferring the protein to the gas phase. Indeed, as CE voltage is increased, detergent micelles in the gas phase are ejected by pairs, therefore shrinking the detergent micelles (termed 'detergent evaporation') to finally release the naked protein similarly as in the desolvation process for soluble proteins [239]. The less detergent present around the protein, the narrower would the peak be in the MS spectra. For soluble proteins, peaks are generally broad as they still carry some residual buffer or water molecules which cannot be removed without affecting protein conformation [229, 240, 241].

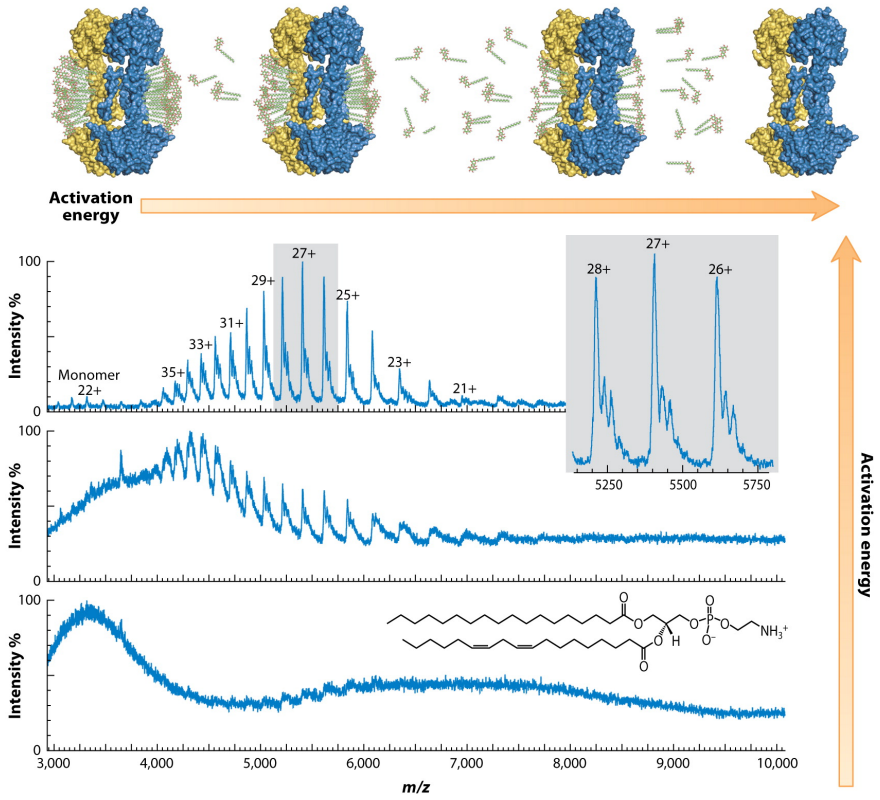


Figure 1.28: Increase of activation energy (also called collisional energy (CE)) leads to protein loosing detergent molecules and better resolved mass spectra (adapted from [242]).

For membrane proteins, the use of high voltage, even higher than those accessible using by commercial instruments (>200V), help in removing the remaining detergent molecules on the surface of the protein, therefore, reducing peak broadening [229]. Nowadays it is still a challenging task and most of the commercial instruments have been modified to perform such experiments. It is also well known that certain types of detergent favour strong interactions with proteins (such as DDM), leading to broad peaks in the MS spectra even at high voltage. The quality of a mass spectrum is also dependant on the membrane protein studied. The charge observed for membrane proteins is usually low (between 3-15, depending on the size of protein studied) compared to soluble proteins as usually fewer charged amino acids are exposed to solvent in membrane proteins [243, 244]. Nevertheless, lower charge states also indicate that the protein is in a compact conformation which has been speculated to preserve the native conformation of the protein [225].

It has been observed that at higher CE, peaks become narrower, but some new conformations of the proteins can be observed, as revealed by ion-mobility MS (IM-MS) measurement for an ABC transporter [245]. IM-MS is comparable to an electrophoresis experiment but happening in the gas phase (Figure 1.29). Ions are separated by their mobility in a gas-filled drift cell and are accelerated by a low electric field until they reach a constant speed (drift velocity) due to the friction experienced [240, 246]. The drift time, which is the time an ion spends in the gas-filled cell, is proportional to the size and therefore to the collisional cross section (CCS), which can be calculated from the crystallographic structure of a protein or *in silico* [244]. Different conformations or oligomeric assembly could then be observed within a same m/z value. It can be used also to assess if protein conformation is altered due to the binding of small molecules such as ligands or lipids for membrane proteins. The gating mechanism of the mechanosensitive channel of large conductance (MscL) has been unravelled thanks to IM-MS, showing that several steps are needed before the complete opening of the channel [247]. Therefore IM-MS is a new robust tool that could be very useful to assess if the native conformation of proteins is conserved in the gas phase.

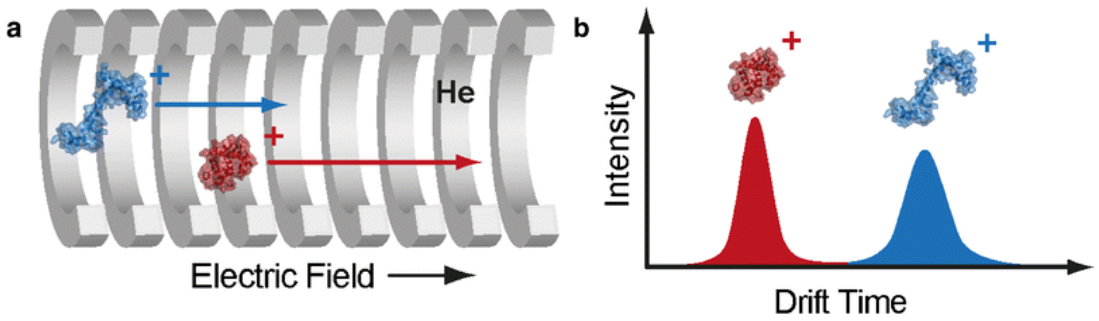


Figure 1.29: Principle of ion-mobility mass spectrometry. Bigger molecules (or slightly elongated molecules) are retained in the tube and give rise to different drift time (similar to gel electrophoresis experiments but in gas phase) (reproduced from [248]).

Since the study of $BtuC_2D_2$, several other membrane proteins such as transporters [249, 250], ion channels [74], GPCRs [251] and receptors [74, 242] have been studied in detergent by MS. The role of lipids as stabilizing molecules has been demonstrated in a few examples but more especially in the ammonium channel (AmtB) [249]. PG (a negatively charged lipid) was suggested to form a strong interaction with the protein by nMS and once the protein was crystallized in presence of such lipid, it has been shown to interact specifically in one of the loops of the protein. Recently, it has even been demonstrated that certain class of lipid act as allosteric modulator for this protein [252]. Other studies on lipid-protein interactions by nMS have been performed on MscL and Aquaporin Z showing that specific lipids have an important role for the function of the protein [74] and stability of the oligomeric state [253]. Recently, nMS data in combination with MD simulation have been able to show that lipids influence the oligomeric state of the protein [250] (Figure 1.30).

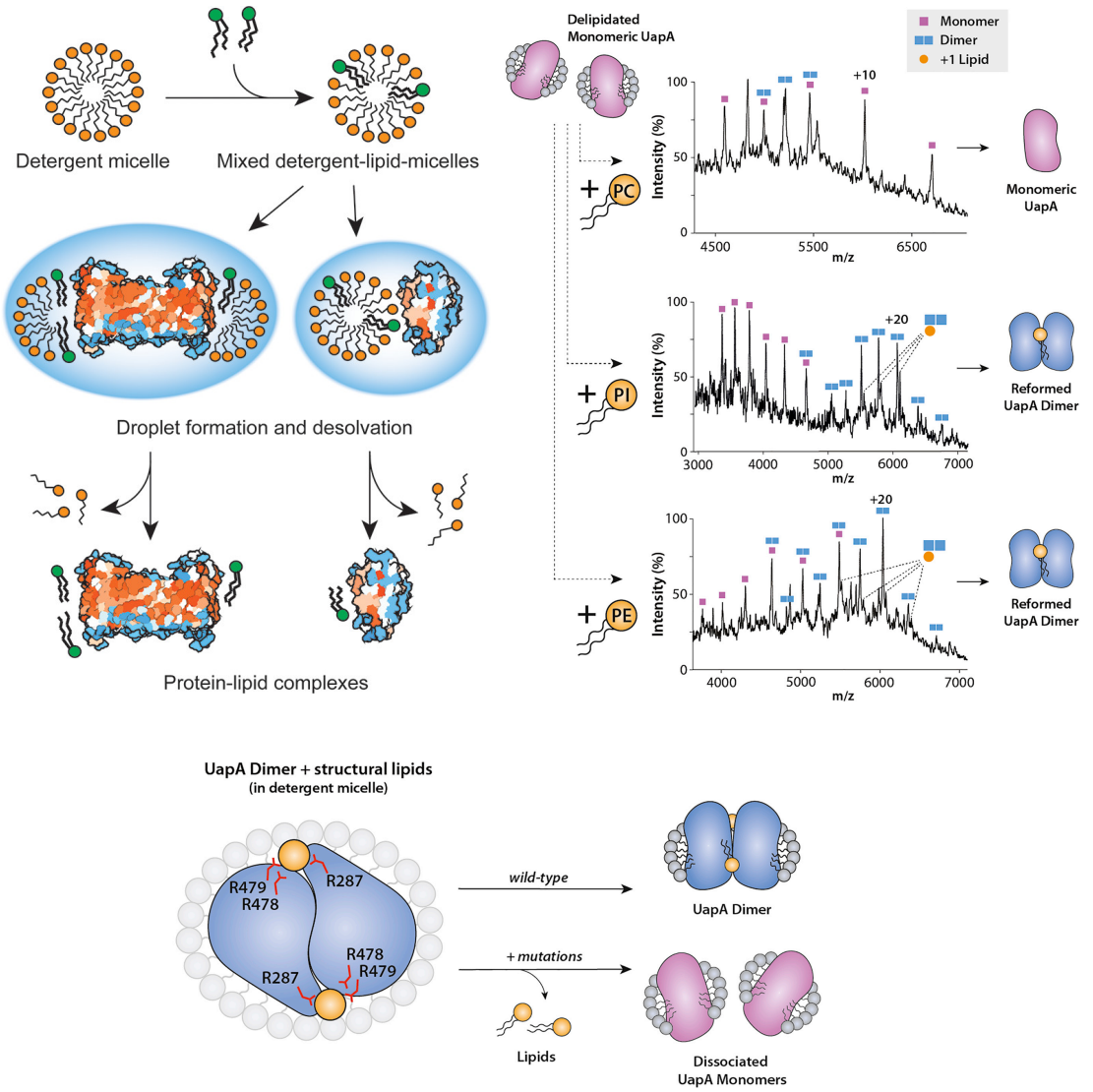


Figure 1.30: Example of how lipid have a crucial importance for the formation of a dimer using nMS and site-directed mutagenesis. First, lipids are titrated back to the sample via mixed micelle-detergent and incubated with the protein of interest. Several lipids were screened, and the formation of the homodimer was only observed with PE and PI lipid-types. Identification of the binding site of the lipid have been identified using site-directed mutagenesis (adapted from [250, 254]).

As described earlier, detergents can have detrimental role for membrane proteins and poorly represent the native lipidic environment. Therefore, several other platforms have been developed to reconstruct the native environment of the membrane including amphipols, bicelles, liposomes and Nanodiscs. For mass spectrometry, such platforms have been tested to show how membrane proteins

behave compared to detergents.

For amphipols, IM-MS experiments suggest that the polymers maintain the native protein conformation, but that the interaction between the protein and the polymer is strong and requires very high energy to dissociate, making nMS experiments difficult [235]. Preservation of the oligomeric state could also be difficult as observed for DgaK by Hopper and colleagues. As for detergent, the energy to dissociate the polymer from the protein is protein-dependent. Interestingly, amphipols have also shown the ability to keep some bound lipids in the gas phase, reaffirming the theory that certain lipids could be important for structural and/or functional role of the protein.

Bicelles, the size of which is sensitive to change of concentrations and for which only certain type of lipids can be used, have also shown to conserve compact conformation for membrane proteins and have been successfully analysed by nMS. Hopper and colleagues showed that the native oligomeric assembly of DgaK was conserved whereas it was partially lost in amphipols [235].

Lastly, Nanodiscs, which are bilayer nanoparticles encircled by two copies of MSP protein in a defined diameter of approximately 10 nm diameter, have attracted most of the studies of membrane protein as the lipid composition could easily be changed and homogeneous sample can be prepared compared to bicelles. In contrast to other platforms, very high CE voltage (300-400 V) is required to dissociate the protein embedded in Nanodiscs [235, 255] (Figure 1.31). Also, the mass spectra obtained are difficult to interpret. Whereas at low m/z ratio lipid monomer and other assembly can be observed, at high m/z ratio the peaks overlap due to the different lipid adduct possible, complicating the assignment of the peaks [78]. Fortunately, as the mass of the lipid is known, the spectra can be interpreted using a probability-based deconvolution algorithm developed by the Robinson group, called Universal Deconvolution (UniDec) [256]. Using this algorithm, Marty and colleagues performed IM-MS on the Nanodisc sample and found that the nanoparticle was still intact at low CE voltages (0-100 V) with a CCS corresponding to a discoidal particle, which start to dissociate above 100 V [78]. A few proteins were incorporated in

Nanodiscs and analysed by nMS. Proteins in Nanodiscs such as AmtB or Aquaporin Z have been successfully analysed and have been shown to have the expected oligomeric state. The lipid content of Nanodiscs is polydisperse and heterogeneous, rendering the assignment of the peaks difficult.

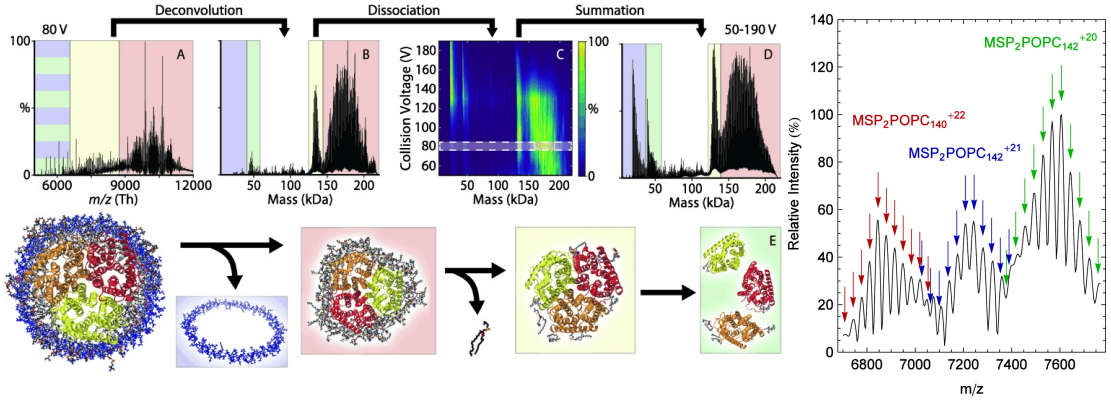


Figure 1.31: Left: Native mass spectrometry spectra of AmtB in POPC Nanodiscs. From raw acquisition data to final deconvoluted spectra using UniDec algorithm. (reproduced from [256]). Right: Peak of empty POPC Nanodisc showing the complexity of the mass spectra (reproduced from [255]).

1.5 Aims of this thesis

Unfortunately, all the previously mentioned methods for nMS of membrane proteins employ detergent solubilisation in a first step, which has the potential to disrupt lipid-protein and protein-protein interactions. A new method such as Lipodisq, which captures protein-lipid and protein-protein interactions intact from the membrane, shows promising alternative to the use of detergents. In this thesis, we will explore the capabilities of the Lipodisq for native mass spectrometry, first, using bacteriorhodopsin as a model protein to observe oligomeric state and post-translational modifications. Full characterization of the protein incorporation in Lipodisq is performed using chromatographic methods, CD, electron microscopy, neutron scattering, UV-Vis spectroscopy and native mass spectrometry (Chapter 2).

In Chapter 3, we focus on the study of two other membrane proteins, EcMATE a bacterial transporter and Dopamine receptor 1 (D1), a human GPCR, both of which

are expressed in their native organism. Biophysical and biochemical characterization have been performed prior to native mass spectrometry experiments. We expect to identify new lipid-protein and protein-protein interactions. As heterogeneity could cause some problems for assignment of nMS spectra, a different method has been tested in this thesis to try to obtain homogenous sample in both protein and lipid composition.

Chapter 4 is dedicated to archaerhodopsin 3 (AR3), which is a microbial rhodopsin with close similarity to bacteriorhodopsin. It is purified from its native organism (archaeal source) and biophysically characterized in a detergent-free environment. As no crystal structure of AR3 is available, different x-ray crystallography techniques are used in this thesis to obtain an atomistic structure, including lipidic cubic phase (LCP) and Lipodisq and combination of both techniques. First insights of the photocycle of AR3 are studied using the novel x-ray free electron laser crystallography using time-resolved serial femtosecond crystallography (TR-SFX XFEL).

Chapter 5 is focused on using the SMA polymer to perform lipidomics and proteomics on two strains of *C. elegans*, one of which is known to express ether-linked lipids. Extraction of lipid is performed using SMA and compared to conventional organic extraction. Lipids are identified by thin layer chromatography (headgroup) and MALDI-TOF mass spectrometry in combination with LipidMaps for identification.

Lipodisq as a novel drug carrier is assessed in Chapter 6, where SMA is fluorescently-labelled and doxorubicin, a well-known anti-cancer drug is incorporated in DMPC Lipodisq. Fluorescence and DLS experiments are used to assess if the drug is incorporated in the Lipodisq. *In vivo* experiments are presented for the first time showing the biodistribution of the SMA.

General conclusions and proposed future work are presented in Chapter 7.

2

Bacteriorhodopsin as a model system to explore the capabilities of Lipodisqs for native mass spectrometry of membrane proteins.

2.1 Introduction

2.1.1 Bacteriorhodopsin (bR)

Microbial and animal rhodopsins are used as model proteins for biophysical experimental methods because of their stability, robustness and easy expression and purification protocols [95]. The first microbial rhodopsin to be discovered was bacteriorhodopsin (bR), a 27 kDa protein expressed in the purple membrane (PM) of the extremophile *Halobacterium salinarum* [122] (Figure 2.1). The expression of the protein usually yields several tens of milligrams of pure protein per litre of culture and the purification is easily performed via differential centrifugation (sucrose gradient) following cell lysis.

The purple membrane, where the protein is expressed, is a highly crystalline membrane (2D lattice) made of specific lipids and where the only protein present is bacteriorhodopsin (Figure 2.1). The protein is trimeric *in vivo*, where 24 lipids surround the protein and six lipids are positioned within the trimer. The purple

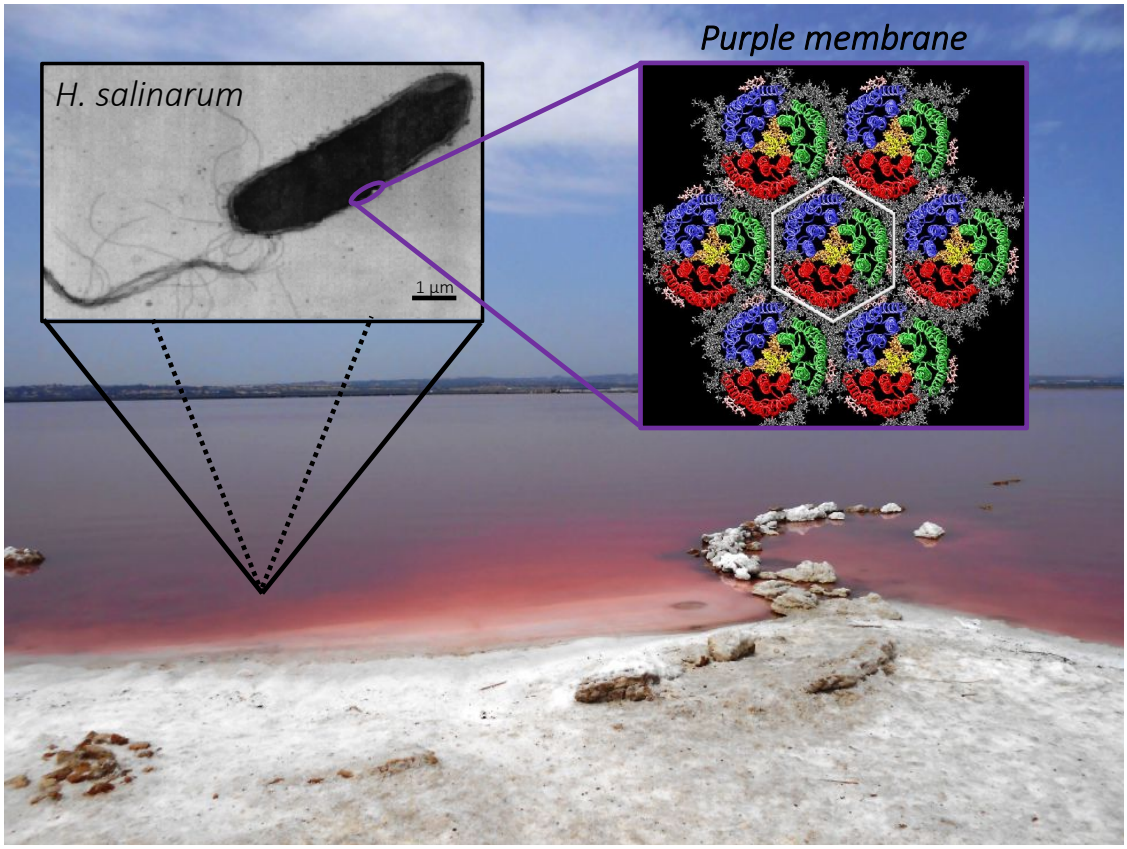


Figure 2.1: Typical salt lake where *Halobacterium salinarum* is growing (picture from Torrevieja lake in Spain (image taken from [257])). *H. salinarum* and a representation of the purple membrane are pictured, where bR is its trimeric assembly. (scale is 1 μm, adapted from [258])

membrane contains ether-linked lipids (also called archaeol lipids, (Figure 2.2)) which are highly bound to the protein even after detergent-treatment (as shown by several crystal structures and some mass spectrometry experiments [259]). Ether-linked lipids are more resistant to chemical and biological degradation compared to ester-linked lipids commonly found in eukaryotes. Bacteriorhodopsin (bR) is therefore embedded in a very robust environment, resistant to light exposure and to thermal [260] and chemical fluctuations (protein is active down to very low pH) [94, 95]. Other molecules such as squalene or derivatives of beta-carotene (carotenoids) can also be found in the PM and are thought to have a protective role as antioxidant molecules [261].

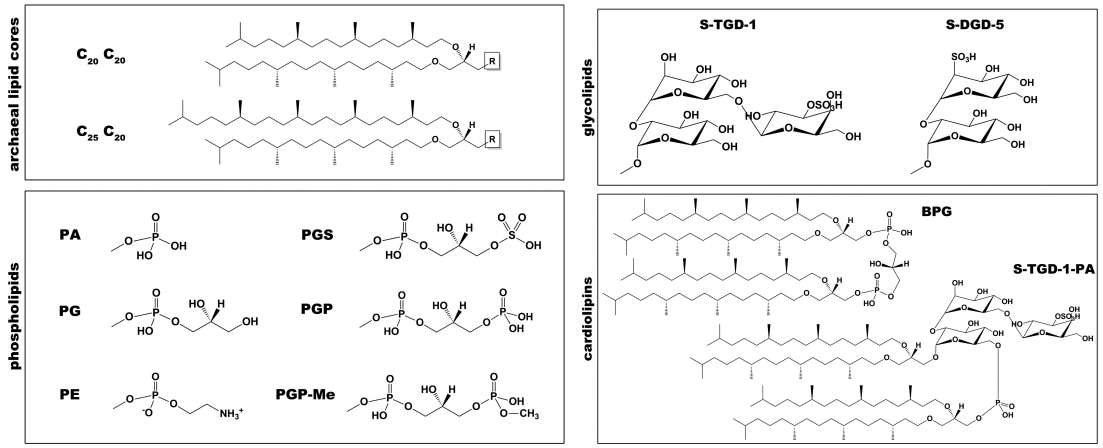


Figure 2.2: Typical archaeal ether lipids (archaeol). Typical lipid chains and headgroups found in *Halobacterium salinarum* (adapted from [262]).

bR harvests energy from light via the retinal molecule (vitamin A aldehyde) which is covalently bound to the protein by a Schiff base linkage to a lysine residue (K216). Once photons are absorbed, the protein undergoes a cycle of conformational changes, in which the pK_a values of different residues and the retinal change enabling proton translocation across the membrane [95, 105]. bR was the first membrane protein to have its structure solved, initially by electron microscopy to 7 Å resolution showing the seven transmembrane helices and the trimeric arrangement of the protein [263] and a few years later to 3.5 Å resolution [264]. Due to its close similarity to GPCRs, bR was used as a model structure for 7-TM receptors. Later, higher resolution X-ray crystals structure of the ground state and photocycle intermediates have identified the proton translocation mechanism [119]. Today, there are more than 130 structures in the protein database using different techniques of crystallisation [119] (bicelles [265], LCP [266, 267] or SMALP [218] as examples) or different biophysical techniques such as solution or solid state NMR, Cryo-EM, X-Ray crystallography (synchrotron and the novel XFEL technology [268, 269]) and from different protein mutations or trapped photo-intermediates at low temperature [119, 270].

The oligomeric form of bR has been discussed in literature and it has been demonstrated that the monomer is a functional unit of the protein [95]. The monomer is less stable compared to the trimeric assembly and it has been suggested

that certain lipids or molecules could have an impact on the stability of the complex [271]. X-ray crystal structures have also confirmed the role of specific lipids in stabilizing the oligomers [272]. AFM and EM have been used to confirm the trimeric oligomeric state in purple membrane patches (Figure 2.3) [263, 273].

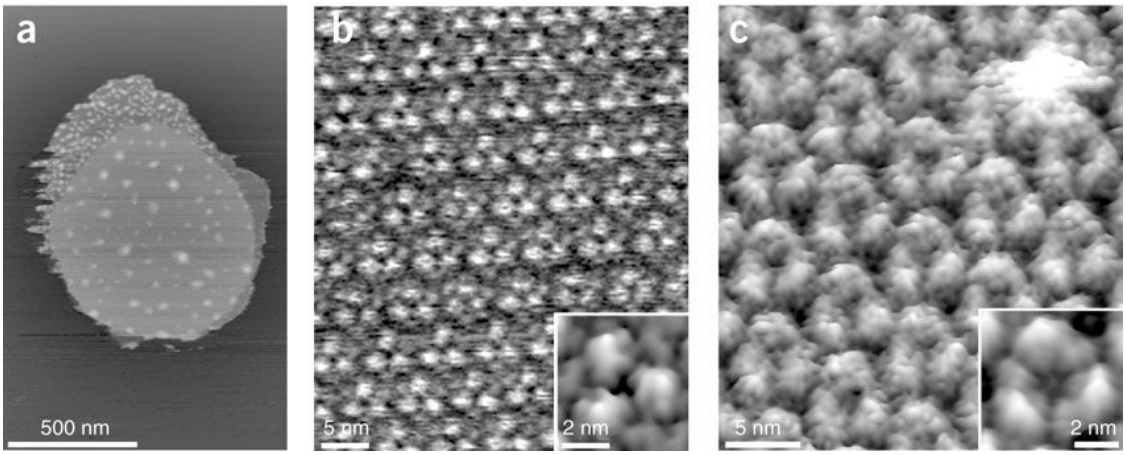


Figure 2.3: AFM picture of the purple membrane (a), extracellular side (b) and cytoplasmic surfaces confirming the oligomeric state of bR (reproduced from [273]).

Due to its robustness and spectral properties, bR and other rhodopsins have been involved in the development of different biophysical and biochemical methods and applications. Unfortunately, most of these techniques use detergent-solubilized protein, which disrupts the oligomeric state [274], alters the function of the protein [275] and removes some of the natural ligands present in the purple membrane [271].

2.1.2 Small-angle neutron scattering (SANS)

The use of deuterated molecules (or protein) in a non-deuterated environment for SANS, is comparable to the staining method used in electron microscopy and helps to enhance the contrast of particular structural features. In our case, we used deuterated lipids or protein in non-deuterated environment, and vice-versa, to study the shape and size of the different components of the Lipodisq. As shown in Figure 2.4, the protein gives low scattering intensity in a high content of D_2O, therefore similar to the one of the buffer. Consequently, the protein 'disappears' in 100% D_2O buffer, thus permitting the study of the other components of the Lipodisq,

such as the lipids and the SMA. Likewise, using a buffer with 100% H_2O, where the lipid and the SMA have the same scattering intensity (therefore 'invisible' in the experiment), enable the study of the deuterated protein in the Lipodisq.

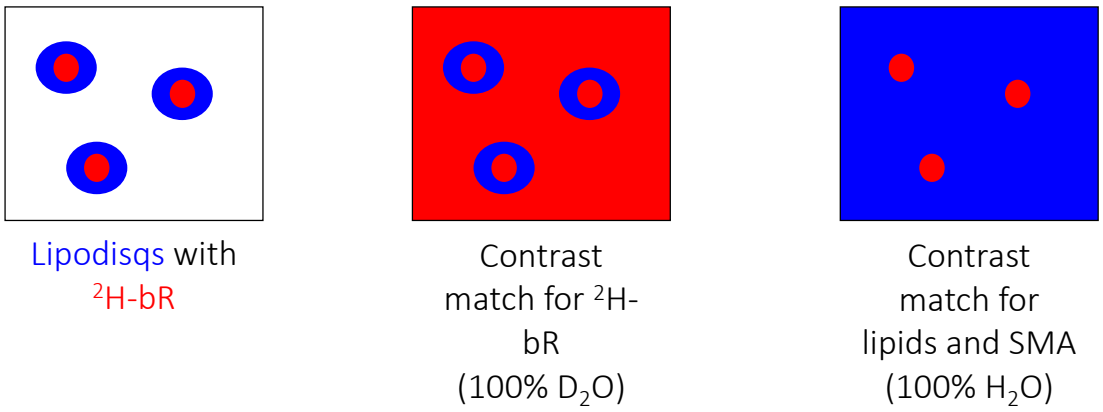


Figure 2.4: SANS Contrast matching . Use of deuterated molecules in a non-deuterated environment is comparable to the staining method used in electron microscopy and helps enhance the contrast of particular structural features.

2.1.3 Aims

Our aim in this chapter is to use bR reconstituted into detergent-free Lipodisq nanoparticles for native mass spectrometry. We expect to be able to observe lipids, small molecules and possible post-translational modifications of the protein. We will also characterize the protein incorporation into Lipodisq using biophysical methods including CD, SANS, SEC and UV-Vis spectroscopy to show that the protein retains its native properties in the Lipodisq environment.

2.2 Materials and methods

2.2.1 SMA hydrolysis

SMAnh (3:1) kindly provided by Malvern Cosmeceutics was hydrolysed by adding 1M NaOH solution (5% w/v final) (Fisher), heated at 80-90°C for 1-2 h. Solution goes from cloudy to clear yellow. 5 M HCl was then added to precipitate the

SMA, which was pelleted by centrifugation (2000g, 5 min, RT). Pellet was re-solubilised in water and was subjected to multiple washing and centrifugation steps (2000g, 5 minutes). Once washed, ddH_2O was added to the solution and dialysis was performed overnight in order to remove the excess of salt and to adjust the pH. At that stage, the SMA should be a clear yellowish solution and in order to further concentrate it, lyophilisation is performed. A white powder was collected and weighted. ddH_2O water or buffer was added to a final concentration of 125 mg/ml and pH adjusted to pH 8.

2.2.2 Bacteriorhodopsin expression and purification

Halobacterium salinarum starter cultures were inoculated in a modified Peptone medium (LP72, Oxoid) and cultured up to an OD_{600} of 1.8-2.0 (5-7 days). Conical flasks (2 L) each containing 500 mL of media were inoculated with 25 mL of starter culture. Growth was allowed to proceed at 37°C, 150 rpm under light illumination (30W LED white light) up to an OD_{600} of 2-2.1 (12-15 days). Cells were harvested by centrifugation (8000g, 30 min, 4°C). Pellets were resuspended in 20 mL of 4 M NaCl. DNase (2 mg) was added and stirred for 10 minutes at 4°C. The suspension was homogenized using a 10 mL homogenizer and dialysed overnight in 0.1 M NaCl. The membranes were centrifuged (50,000g, 1h, 4°C) and the pellet was resuspended in ddH_2O and applied to a sucrose gradient of three different layers (20%, 40% and 60% w/v sucrose). Sucrose gradient was centrifuged (110,000g, 16 h, 15°C). The purple layer was collected and dialysed against water in order to remove the excess of sucrose. The purple membrane was then centrifuged (40,000g, 45 min, 4°C) and the pellet resuspended in ddH_2O.

2.2.3 Bacteriorhodopsin expression and purification in presence of nicotine

bR cultures were expressed as previously, but nicotine was added at a final concentration of 1 mM to both the starter cultures and the 500 mL culture.

Purification and sucrose gradient were performed as described previously. The bottom orange layer was collected.

2.2.4 Addition of retinal after nicotine bR expression

bR cultures containing nicotine were expressed in presence of 1 mM retinal added to both the starter cultures and then to the 500 mL culture. At the end of the growth, all-*trans* retinal (Sigma) was added to obtain a final concentration of 5 μM and incubated (4h, 25°C), with occasional shaking under ambient light illumination. Purification by sucrose gradient ultracentrifugation was performed as mentioned previously. The bottom purple layer was collected.

2.2.5 bR ^{2}H, ^{15}N and ^{13}C labelled

Starter cultures were inoculated in a triple labelled media Celtone-CN and Celtone-N (Cambridge isotopes) in 70% D_2O and cultured up to an OD_{600} of 1.2-1.5 (5-7 days). Conical flasks (250 mL) each containing 100 mL of media were inoculated with 1 mL of starter culture. Growth was allowed to proceed at 37°C, 110 rpm up to an OD_{600} of 1.6-1.7 (12-14 days). Cells were harvested by centrifugation (7000g, 30 min) at 4°C. Pellets were resuspended in 20 mL of 4 M NaCl. DNase (2 mg, Sigma) was added and stirred (10 min, 4°C). Suspension was homogenized using a 10 mL homogenizer and dialysed overnight in 0.1 M NaCl. The membranes were centrifuged (60,000g, 1h, 4°C) and the pellet was resuspended in ddH_2O and applied to a sucrose gradient of three different layers (30%, 60% and 80% w/v sucrose). Sucrose gradient was centrifuged (110,000g, 16 h, 4°C). The purple layer was collected, and sucrose was removed by several rounds of dilution and centrifugation (60,000g, 45 min, 4°C). The pellet was resuspended in ddH_2O.

2.2.6 Incorporation into Lipodisqs

bR was incorporated into Lipodisqs as described previously with some changes outlined below [124].

Briefly, 4 mg of bR was pelleted (45,000g, 30 min, 4°C) and resuspended in 1 mL of 50 mM sodium phosphate and 200 mM NaCl buffer containing 20 mg of 1,2-dimyristoyl-*sn*-glycero-3-phosphocholine (DMPC) small unilamellar vesicles (SUVs) produced by the freeze/thaw and extrusion technique in a final protein/lipid molar ratio of 1:172. The solution was sonicated (30 min) in a bath sonicator with gentle heating (30-35°C). Styrene-maleic acid copolymer (25 mg, added as a solution in ddH_2O) was added to the vesicle membrane sample, and the solution incubated (42°C, 1 h). Samples were centrifuged (100,000g, 30 min, 15°C) in order to remove non-solubilized membrane and the supernatant collected.

2.2.7 Size-exclusion chromatography

Lipodisqs samples were applied to a Superdex Increase 200 10/300 GL column connected to an Akta Pure (GE Healthcare). The column was equilibrated with buffer for 2 column volumes and sample was applied at a flow rate of 0.5 mL/min. Protein was detected using a UV-detector at a wavelength of 280 nm and fractions were collected in 15 mL falcon tubes (Greiner). Purple fractions were collected and concentrated using a Vivaspin concentrator (Merck) and colourless fractions were discarded.

2.2.8 UV-Vis spectroscopy

Spectra were recorded on a Jasco V-630 instrument at different wavelengths in the visible range, using a 1 cm quartz cuvette and were blanked against buffer.

2.2.9 Dynamic Light Scattering (DLS)

Particle size was measured using a Malvern Zetasizer Nano S instrument in a disposable cuvette at 633 nm. The data was processed using Malvern Zetasizer software.

2.2.10 Circular dichroism (CD)

CD spectra were acquired with a Jasco J-815 Spectropolarimeter using a 1 mm cuvette. A wavelength range (185-240 nm) was selected to monitor secondary

structure of the proteins at ambient temperature. Concentration range used for measurements was adjusted between 0.01-0.1 mg/mL and the protein was diluted in low salt buffer in order to perform experiments. The data was analysed, and baseline corrected using the Spectra Manager software from Jasco. α, β and random coil content was calculated from the Dichroweb website [276] using the CDSSTR analysis programme [277] and the reference set SMP180 for membrane protein [278].

2.2.11 Small angle neutron scattering (SANS)

The size of the particles and the presence of the protein inside Lipodisq nanoparticles was determined at the Institute Laue-Langevin (Grenoble, France) on SANS beamline D11, using a monochromatic neutron beam with a wavelength of 6.0 Å. The detector was placed at 1.3 m, 7 m and 13 m from the sample to collect Q ranges of between 0.5 $Å^{-1}$ and 0.004 $Å^{-1}$. Samples were measured at room temperature in rectangular quartz cuvettes with a 1 mm path length (Hellma Analytics, Germany). Intensities were acquired for 2 min for each datapoint and contrasts of 100% H_2O and 100% D_2O were used. Buffer-exchange of the different samples was performed using P-30 Micro Bio-spin column (BioRad). The data were modelled using SASview software (DANSE, Tennessee, USA). Scattering length densities were calculated using the BSLDC website from ISIS [279] for the protein and lipids and polymer SLDs were determined using the SLD Calculator tool in SASview.

2.2.12 Electron microscopy (EM)

Images were recorded at the Institut de Biologie Structurale (Grenoble, France) using negative stain at different magnifications (30,000x, 49,000x and 68,000x). Images were analysed using Fiji/ImageJ.

2.2.13 Native mass spectrometry (nMS)

Native mass spectra were acquired using a Thermo Q-Exactive mass spectrometer (as described in [230]) in collaboration with the group of Prof. Carol Robinson (University of Oxford, UK). Experiments were carried using a gold coated needle

(home-made) at high sample concentration (50-200 μM) in a volatile buffer (usually ammonium acetate) and collisional energy voltage was applied in order to obtain a protein signal (from 10 V to 200 V). Data was analysed and deconvoluted using the UniDec algorithm [256].

2.2.14 Thin layer chromatography (TLC)

Lipids were extracted using Bligh and Dyer method, dried under nitrogen gas and solubilized in chloroform:methanol mixture (2:1 v/v). Samples were spotted onto a Merck Silica Gel 60 HPTLC plates (10 x 10 cm). Plates were developed with different mixture of methanol/chloroform/ammonium hydroxide (65:25:4 v/v/v) or chloroform/methanol/90% acetic acid (65:4:35 v/v/v) solvent systems ([280]). Lipid bands were visualized by spraying the plates with molybdenum blue and charred at 200°C. Retention factors (R_f) were calculated and reported for further determination of lipid headgroups.

2.3 Results and discussion

2.3.1 Preparation of bR-Lipodisqs

Expression of bacteriorhodopsin yields about 10 to 15 mg of pure protein per litre culture of *H. salinarum*. Purification, performed via sucrose gradient, produces a purple band between 40%-60% sucrose density with high purity as assessed by SDS-PAGE where a single band appeared around 17-20 kDa (Figure 2.5 and 2.6).

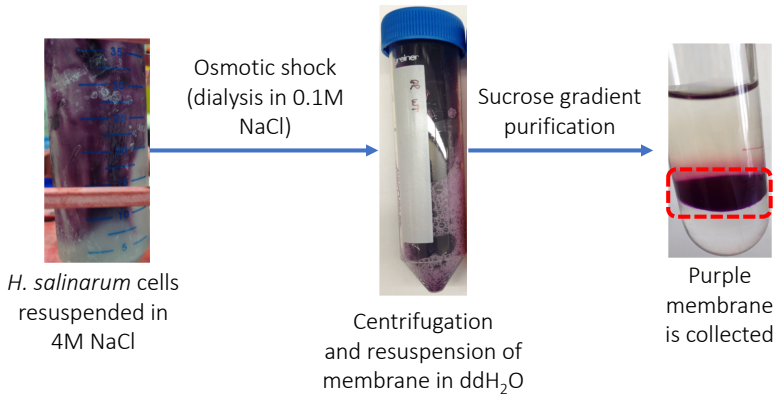


Figure 2.5: Purification of bacteriorhodopsin from *H. salinarum* cells. *H. salinarum* cells are lysed by osmotic shock. Membrane are collected, and purification is performed via sucrose gradient. Purple membrane appears as a single band between 40%-60% w/v of sucrose.

Detergent-free reconstitution of monomeric bR in DMPC liposomes was performed by forming LUVs, by extrusion of a DMPC solution (Figure 2.6)[124]. The lipid to protein ratio was chosen to incorporate 1 protein per Lipodisq, so the ratio used here was 172:1 (lipid to protein ratio), as used by Orwick and colleagues (in this group) for EPR and ssNMR experiments [124]. Conditions were controlled to ensure monomerization of the protein, including lipid:protein ratio, salt concentration and temperature [272, 281, 282]. The purple membrane was sonicated with the DMPC LUVs solution at moderate temperature (30°C-40°C) (Fig. 4). Sonication is performed to disrupt the crystalline environment of the purple membrane and to assist in the mixing of the DMPC LUVs with PM proteoliposomes to form bR-DMPC SUVs. Thereafter, the hydrolysed SMA polymer is added to the cloudy purple bR-DMPC SUVs to form the Lipodisqs. The amount of polymer added is 1:1.25 w/w polymer excess as described in the literature [124]. Indeed, the SMA concentration is crucial, as addition of a low amount of polymer will induce an incomplete solubilisation of the lipid present in solution, whereas an excess of polymer will cause the Lipodisq to shrink and be less inclined to accommodate protein inside the nanoparticle as observed previously [195].

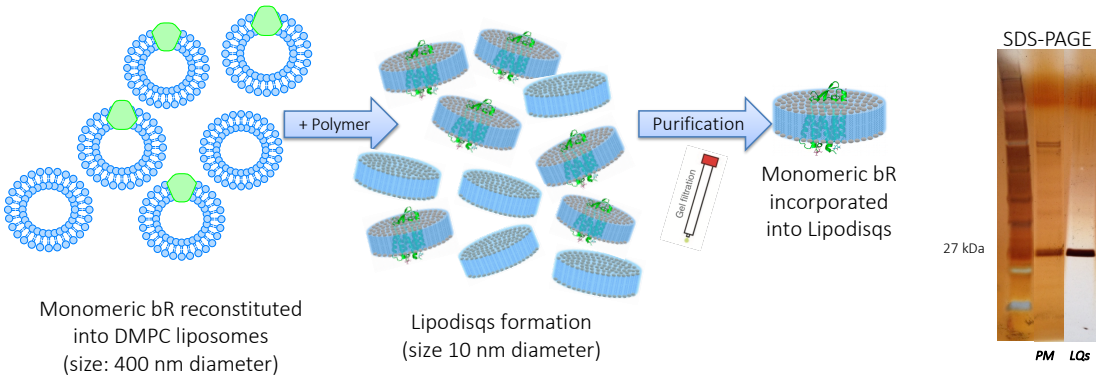


Figure 2.6: Left: Formation of bR Lipodisq from bR liposomes. Lipid protein ratio chosen as 1:172 as in [124]. Right: SDS-PAGE showing the purity of the bacteriorhodopsin in the purple membrane and once reconstituted in Lipodisq.

Another important parameter to be controlled is the temperature at which the proteoliposomes and SMA mixture is incubated (37°C-40°C in our case), since the polymer solubilises lipid molecules faster when the temperature of the solution is higher than the T_m of the lipid mixture [195, 198]. The temperature used here is higher than the T_m of the DMPC (23°C) but lower than the one for the purple membrane (70-75°C, [283]), but as the lipids are now mixed due to the sonication, the T_m of the lipid mixture should be close to DMPC as it is the dominant lipid after sonication.

2.3.2 Biophysical characterisation of the bR-Lipodisq complex

To assess if the SMA has been able to form Lipodisq containing bR, dynamic light scattering experiments were performed. As shown in Figure 2.7, bR-DMPC-Lipodisq and purple membrane proteoliposomes are compared (see Table 2.1). A drastic change of size between the PM and Lipodisq samples is observed, indicating that the SMA has successfully solubilised the PM, but this does not prove the protein has been incorporated inside discoidal nanoparticles.

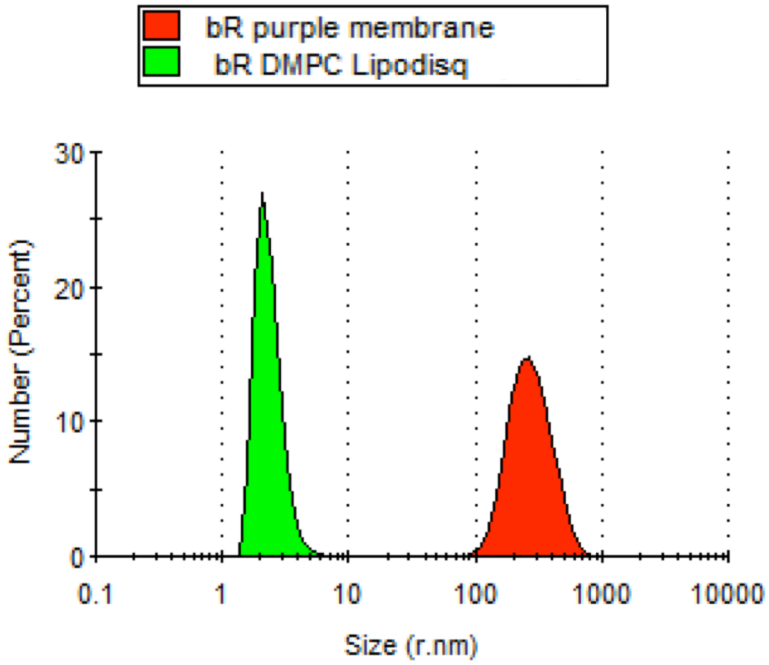


Figure 2.7: Dynamic light scattering measurement of the purple membrane and bR-DMPC-Lipodisq. A drastic change of size is observed when bR is reconstituted in DMPC-Lipodisq.

DLS measurement	**Radius [nm]**
bR in purple membrane	290 ± 129.3
bR DMPC Lipodisq	3.81 ± 0.7

Table 2.1: DLS measurement table showing the difference in size

Excess SMA must be removed prior to biophysical characterization. Excess of SMA could render the study of the protein in the Lipodisq difficult especially for techniques such as CD, where the styrene group strongly absorbs in the UV region. Size exclusion chromatography (Figure 2.8) has been used to separate Lipodisq from excess polymer. Effectively, Lipodisq, which is a 5-10 nm diameter, eluted as a 200 kDa globular protein (early elution, 9-12 mL) and the polymer, which is only 10 kDa, elutes later (19-21 mL).

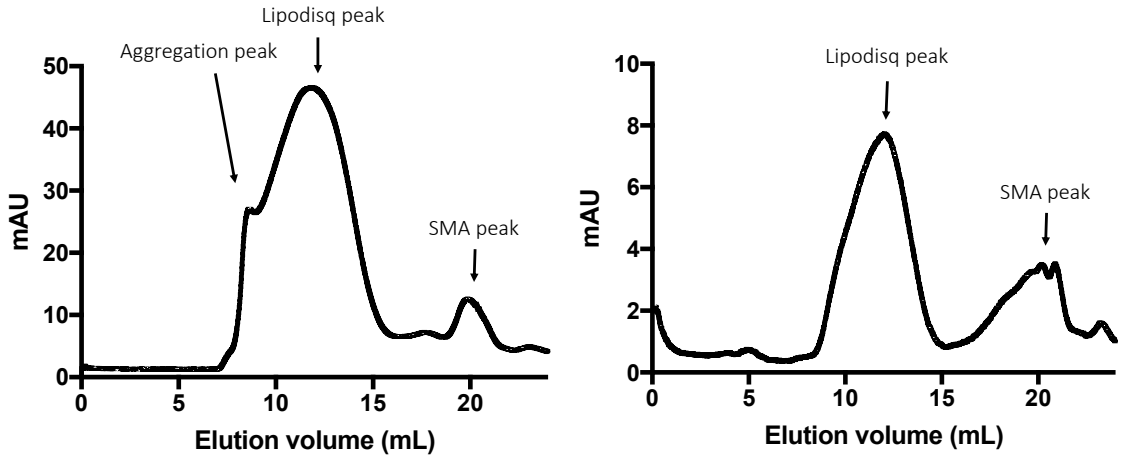


Figure 2.8: Left: Size exclusion profile of bR-DMPC-Lipodisq on a Superdex 200 Increase. Right: Empty Lipodisq on the same column. The profile is different as no aggregation peak is observed and elution of the Lipodisq is at 12 mL. Free SMA eluted at 20-22 mL.

The first peak observed on the chromatogram at 7-8 mL (Fig.2.8) is the aggregated peak and could be the non-incorporated bR still in the remaining (proteo)lipososomes, which SMA has not been able to solubilise or some protein aggregation. The elution volume, at which Lipodisq peaked, is around 11 mL and using the calibration curve (see Appendix A.1), we obtain an estimate of the particle size, in this case being between 5-10 nm diameter. The last peak eluting, at an elution volume of 20-24 mL, is the excess SMA. Using the calibration curve, we find that the SMA has an average molecular weight of 10 kDa, as expected from [284].

To further ensure that the protein was incorporated into Lipodisq, UV-Vis spectra of the early fractions were recorded. UV-Vis spectroscopy revealed a peak at 555 nm, a 10 nm blue shift compared to the purple membrane sample (Figure 2.9). Literature reports that the shift is due to a change of environment and a change of oligomeric state (from trimeric in the purple membrane to monomeric in Lipodisq) [285]. From the early fractions, a single band was observed by SDS-PAGE (Figure 2.6).

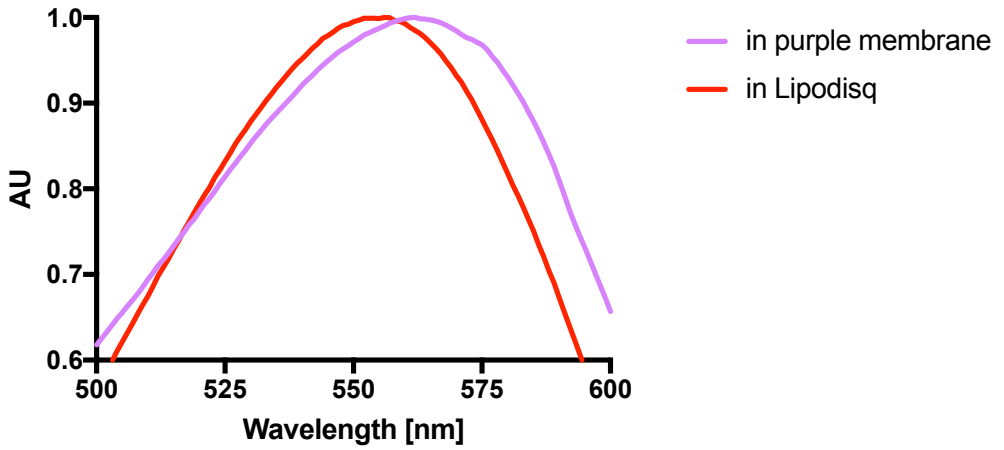


Figure 2.9: UV-Vis spectra of bR in purple membrane showing a shift to 555 nm when bR is incorporated in Lipodisq.

A control purification with protein-free lipid-only Lipodisq (empty Lipodisq) was performed and the elution volume obtained by size-exclusion was 12 mL, suggesting that Lipodisq nanoparticles without any protein are slightly smaller than those containing bR. The last elution peak (20 mL) was still observed (Figure 2.8). Unfortunately using SEC, separation of the proteo-Lipodisq from the empty Lipodisq is difficult, as the peak is broad due to the different length of the SMA forming slightly different size of Lipodisq. For the purpose of this chapter, no further attempt to remove the empty Lipodisq from the bR-DMPC-Lipodisq was made. Nevertheless, successful attempts of separating empty Lipodisq from bR-DMPC-Lipodisq was achieved using a sucrose gradient as performed by Bayburt and colleagues, who were attempting to separate monomeric bR-POPC-Nanodiscs from trimeric bR-POPC-Nanodiscs [286].

Circular dichroism was performed to check that the folded state of the protein was maintained once the protein was incorporated in Lipodisq (compared to the purple membrane). As seen in Figure 2.10, the secondary structure of the protein is conserved compared to the purple membrane. A small shift can be observed, and this is usually observed when the protein is in a lipid environment such as bicelles or liposomes as reported [287]. The shape of both spectra, with the typical 'double minima' between 200-230 nm, indicate that the protein is mainly α-helical

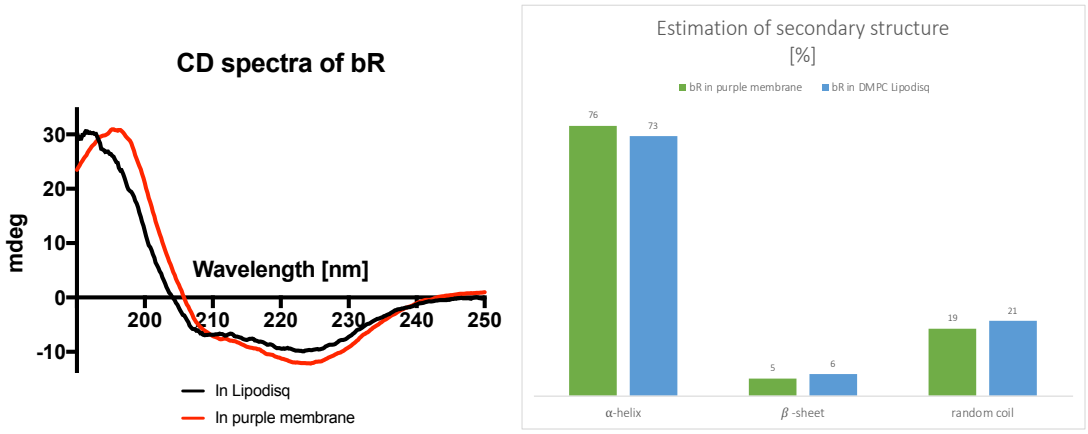


Figure 2.10: Left: Circular dichroism spectra of bR in purple membrane or Lipodisq (samples are at same concentration and the CD spectra was measured in three analytical replicates and mean values were taken for representation). Small shift in the Lipodisq spectra is due to the lipid scattering [287]. Right: Histogram showing the estimation of secondary structure from the CD spectra of bR in both the purple membrane and Lipodisq.

as expected from the crystal structure of bacteriorhodopsin. Moreover, estimation of the secondary structure from Dichroweb using the CDSSTR algorithm using the membrane protein set suggests similar α, β and random coil content in both in purple membrane and Lipodisq. This indicates that the protein is properly folded once incorporated in Lipodisq.

2.3.3 Small-angle neutron scattering (SANS) experiments

As a preliminary experiment (Figure 2.11), we have calculated the contrast match point of ^{2}H-bR by solubilizing the protein in different mixtures of H_2O/D_2O content and different scatter values (q values) were obtained. As seen in Figure 2.11, 95% D_2O and 100% D_2O give the lowest intensity for several scatter values. Therefore, all the experiments were performed in 100% H_2O where the protein is fully 'visible' and in 100% D_2O where the deuterated protein 'disappears'.

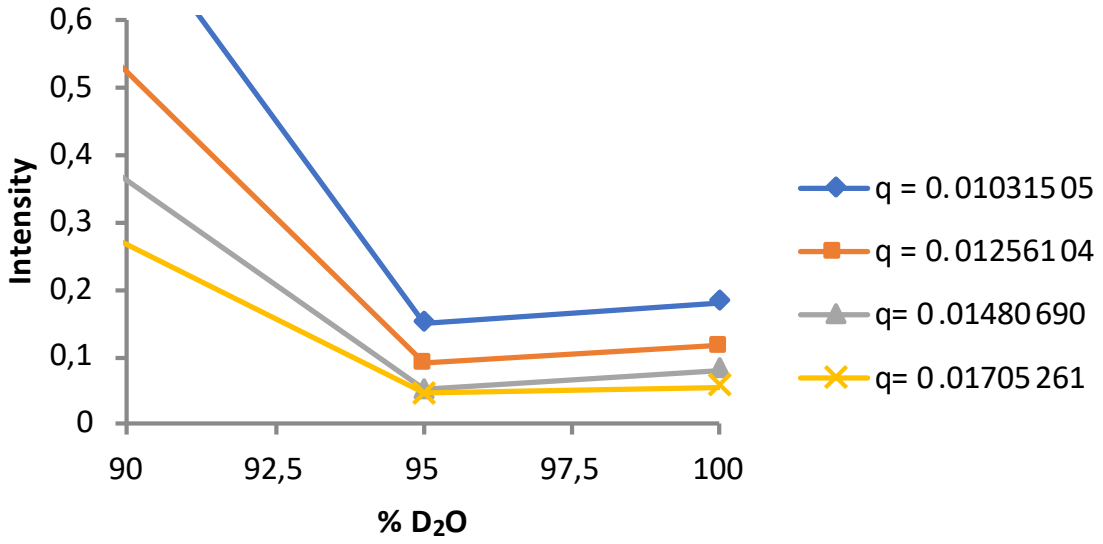


Figure 2.11: Contrast match point determination of ^{2}H-bR. As a preliminary experiment, we have calculated the contrast match point of ^{2}H-bR by solubilizing the protein in different mixtures of H_2O/D_2O content and using different scatter values (q values). All the experiments were performed in 100% H_2O where the protein is fully 'visible' and in 100% D_2O since the protein is giving low signal at 100% D_2O as shown here.

A dispersion of Lipodisqs containing ^{1}H-DMPC in H_2O buffer was used to determine the size of Lipodisq particles containing no protein. The scattering curve for this sample (Figure 2.12) was first analysed by a Guinier plot to extract the radius of gyration of the particles in both H_2O and D_2O buffer. Different ranges have been analysed in order to discard the contribution of the aggregates to the curve. The plot of the radius of gyration for range 1, shows values above 200 Å, indicating that this region should be discarded for later analysis, as this reflects some aggregation in both samples. For range 2, the radius of gyration for hydrogenated buffer sample is 31.7 ± 0.2 Å and in D_2O buffer is 77 ± 1.8 Å for range 2. If we consider the Lipodisq as a shallow cylinder (as reported by [214], see Figure 2.13), we can extract the radius and the length of the Lipodisq using the formula below [288]:

Cylinder with radius R and length L

$$R_g^2 = \frac{R^2}{2} + \frac{l^2}{12}$$

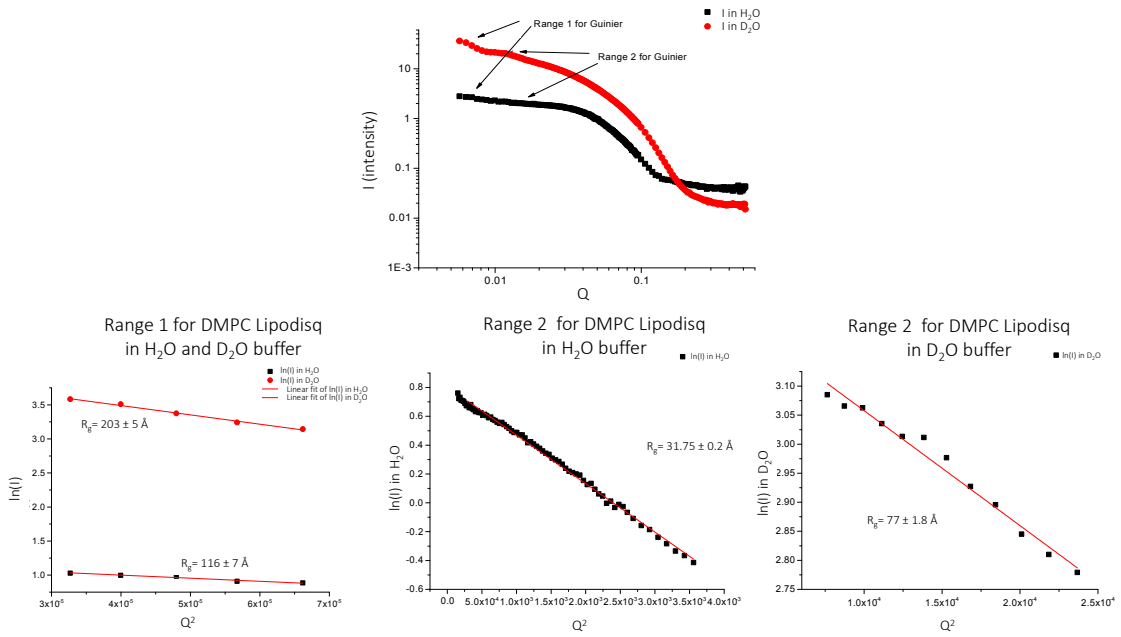


Figure 2.12: Neutron scattering curves from the Lipodisq containing no protein (empty Lipodisq) in deuterated and protonated buffer. Two different ranges for Guinier analysis are presented. Linear regression has been performed to extract the radius of gyration of the nanoparticles in both buffers. I: intensity, Q: scattering vector value

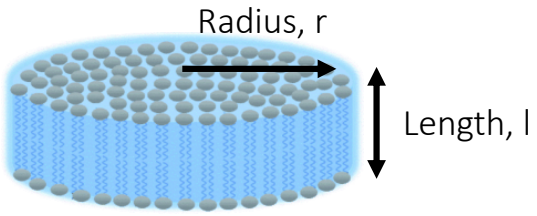


Figure 2.13: Lipodisq seen as a cylinder

Considering that the length of the Lipodisq is the width of a bilayer, approximately 4 nm, we obtain 4.3 ± 0.2 nm for the radius of the cylinder in H_2O buffer and 10.8 ± 0.4 nm in D_2O buffer. As DLS models the Lipodisqs as spherical nanoparticles, we can use the formula to extract the radius of a sphere which is given below:

$$R_g^2 = \frac{3}{5}R^2$$

The radii for the hydrogenated and deuterated buffer samples are 4.26 nm and

9.94 nm respectively, indicating already that the D_2O samples are not behaving as expected as their sizes are too big to be considered as Lipodisqs. This is confirmed by EM, where lipid patches bigger than the one found in hydrogenated buffer can be observed (Figure 2.15). Therefore, we decided to discard the samples in D_2O as these could not be considered as Lipodisq due to their size and shape observed by neutron scattering and EM.

After Guinier analysis, fitting of the scattering curves is performed using SASview. Different models were examined and assessed by their χ^2 values. The best model with the lowest χ^2 value, is a cylinder model with some polydispersity in the radius, which may arise as the SMA polymer can have different lengths and therefore could form different sizes of Lipodisq. The cylinder model is in agreement with some previous published data, showing similar size of the nanoparticles [214]. The results are summarized in Table 2.2.

Table 2.2: Summary of the size of the Lipodisq samples studied by SANS

	Sample	^{1}H-DMPC Lipodisq	^{1}H-DMPC Lipodisq	^{1}H-DMPC ^{2}H-bR Lipodisq	SMALPs [214]	Purple membrane from EM [263]
	Solvent	H_2O	D_2O	H_2O	Mix of H_2O and D_2O	-
	Model	Cylinder	Cylinder	Elliptical cylinder	Core shell cylinder	EM data
	Chi-square	0.77	6.2	3.88	Not reported	-
Lipid + SMA	Length [nm]	4.1 ± 0.2	3 ±0.1	-	2.6	4.5
	Small r [nm]	4.5 ± 0.1	13.1 ± 0.1	-	4.8	-
	Large r [nm]	-	-	-	5.8 (with SMA)	-
	Guinier R_g [nm]	3.2 ±0.1	7.7 ±0.2	2.8±0.1	-	-
bR	Length [nm]	-	-	3.5±0.3	-	5
	Small r [nm]	-	-	3.3±0.3	-	2.3
	Large r [nm]	-	-	5.3±0.2	-	4.2

An additional sample consisting of Lipodisqs containing ^{1}H-SMA, ^{1}H-DMPC, ^{2}H-bR in H_2O buffer was analysed by SANS to determine if the protein is properly incorporated in the Lipodisq (the scattering curve is shown in Figure 2.14). The data was successfully modelled (χ^2: 3.88) using an elliptical cylinder model, which correlates well with the data from the EM of bR in the purple membrane, suggesting that the protonated and deuterated lipids do not mix extensively within the core of the Lipodisq. This is consistent with the reported dynamics of the Lipodisq-embedded bacteriorhodopsin, which closely resembles that of protein in the native purple membrane [124].

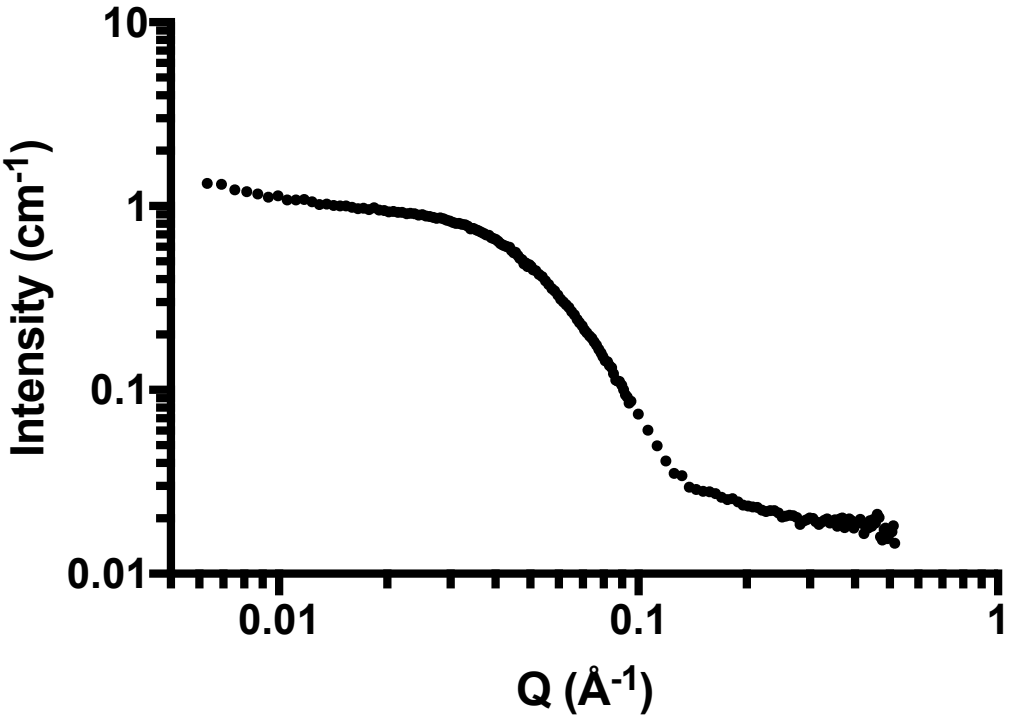


Figure 2.14: Scattering curve for ^{1}H-DMPC ^{2}H-bR in Lipodisq in hydrogenated buffer.

The morphology of the bR-Lipodisq by EM (Figure 2.15)can be described by rouleaux or stacks as previously observed for Nanodiscs [188] and SMALPs [289]. These stacks are an artefact resulting from the positively charged choline lipid headgroup which interact with the inorganic ions from the staining solution [289]. No aggregation or purple membrane patches can be observed, while the

empty Lipodisq do not form any stacks in our experiment, certainly due to a low concentration of empty Lipodisq for the EM experiment compared to the bR-DMPC Lipodisq sample, in agreement with the data discussed so far.

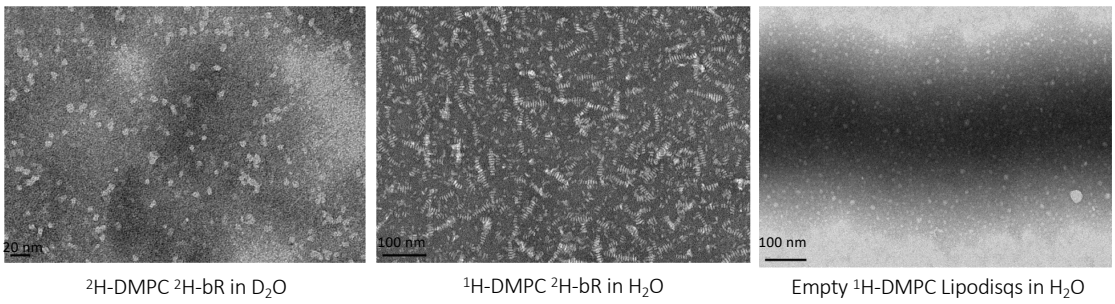


Figure 2.15: Electron microscopy pictures from different samples after SANS experiments. Lipodisq samples solubilized in D_2O buffer (left) did not exhibit the correct size and morphology. Samples containing protein form stacks (worm-like structure, middle picture). Lipodisq containing no protein (empty) are shown with the expected size and morphology (right). Scale bar is represented at the bottom left on each picture.

2.3.4 Native mass spectrometry experiment using Lipodisq

The data presented so far have informed us about Lipodisq shape (SANS), the folding of the protein (CD) and the protein environment (DLS and UV-Vis). Unfortunately, we do not have any data concerning the protein incorporated. We have some clues that the protein could potentially carry some endogenous lipids, as revealed by SANS experiments (Figure 2.14 and Table 2.2). We also have some indirect proof that the protein is in contact with DMPC and about its oligomeric state from the UV-Vis absorption spectra (Figure 2.9). Unfortunately, we do not have yet any data concerning post-translational modifications (PTMs) of the protein in Lipodisq as for bR in purple membrane, where some modifications such as truncations in the sequence and the presence of a non-standard amino acid are present. To further investigate the PTMs of the proteins and try to identify the lipids in close proximity with the protein, we decided to use native mass spectrometry, which has shown to be able to identify lipids, small molecules and PTMs for membrane protein in detergent and reconstituted in Nanodiscs [235].

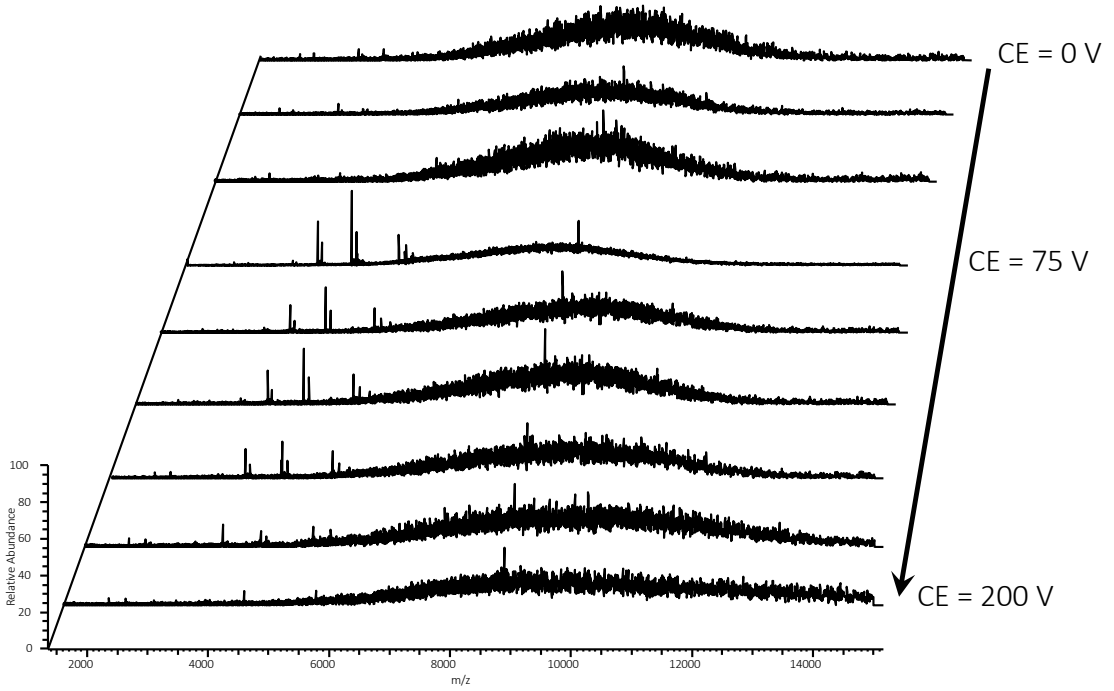


Figure 2.16: Energy ramp of bR-DMPC Lipodisq from low collisional energy (0 V) to high collisional energy (200 V). Protein signals (between 3,000 and 5,500 *m/z*) appear from 75 V, which is a quite low energy to observe protein peaks compared to Nanodisc or detergent samples. The hump between 6,000 *m/z* and 12,000 *m/z* is also observed in Nanodiscs samples and represent partial breakage of the Lipodisq with the protein bearing several lipids adducts (up to 100 lipids), which renders impossible the assignment of the peaks.

Mass spectra of bR-DMPC-Lipodisq are shown in Figure 2.16 using a collisional energy ramp from 0 V to 200 V, with protein peaks appearing at 75 V between 3,000 and 6,000 *m/z*, which is a low CE compared to Nanodiscs (protein peaks above 200 V) and some detergent samples (above 100 V). This voltage enables further analysis such as tandem MS, to identify possible adducts or molecules in close proximity to the protein. Such tandem MS experiments are difficult to perform on Nanodisc samples as the CE voltage used for such experiments is already very high. A 'hump' is observed between 6,000 *m/z* and 12,000 *m/z* also reported for Nanodisc samples, which represents the partial breakage of the Lipodisq with the protein bearing several lipids or molecules adducts (up to 100 lipids). Assignment of the peaks in the hump is impossible as these peaks cannot be fully resolved.

Figure 2.17 shows a zoom of a 5^+ mass charge series containing several peaks of different mass to charge ratio at a CE of 75 V. Using the UniDec algorithm [256], the mass of these peaks could be extracted. A mass corresponding to 27,048 Da is obtained, which is approximately 1 kDa lower than the expected mass from the full-length bacteriorhodopsin sequence (Uniprot P029452, 28,518 Da with retinal).

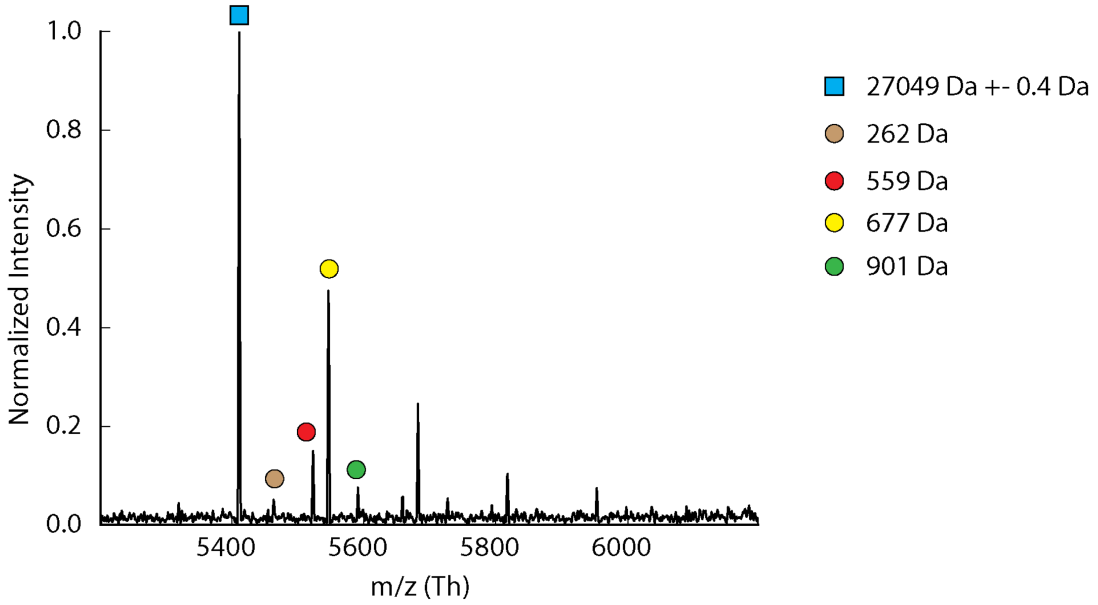


Figure 2.17: Native mass spectrum of bR DMPC Lipodisq. The 5^+ charge state is presented here where different adducts are present. Adduct of bR with DMPC lipid molecule confirms that the protein is really embedded in the Lipodisq.

Nevertheless, from this sequence, four post-translational modifications may be identified for bR expressed in *H. salinarum* (Figure 2.18). The first modification involves the cleavage of 13 residues at the N-terminus, which corresponds to a signal peptide. Secondly, the (incomplete) cleavage of an aspartate residue at the C-terminus is performed. A covalent modification is performed on bR by the formation of the Schiff base linkage between the retinal and the lysine-216 [290]. A last modification is achieved on the protein as the first amino acid residue (a glutamate) in the N-terminus cyclizes into a pyroglutamic acid (or pyrrolidine carboxylic acid, abbreviated PCA), as suggested in the literature [291]. PCA role in bR is not clear but it has been suggested that it mediates the interaction between

receptors and could be implied as a stabilizing agent against N-terminal degradation. Therefore, the final mass obtained is 27,049 Da (mature bR), which is identical to the mass obtained from early ESI mass spectrometry experiments [292] and our native mass spectrometry experiments.

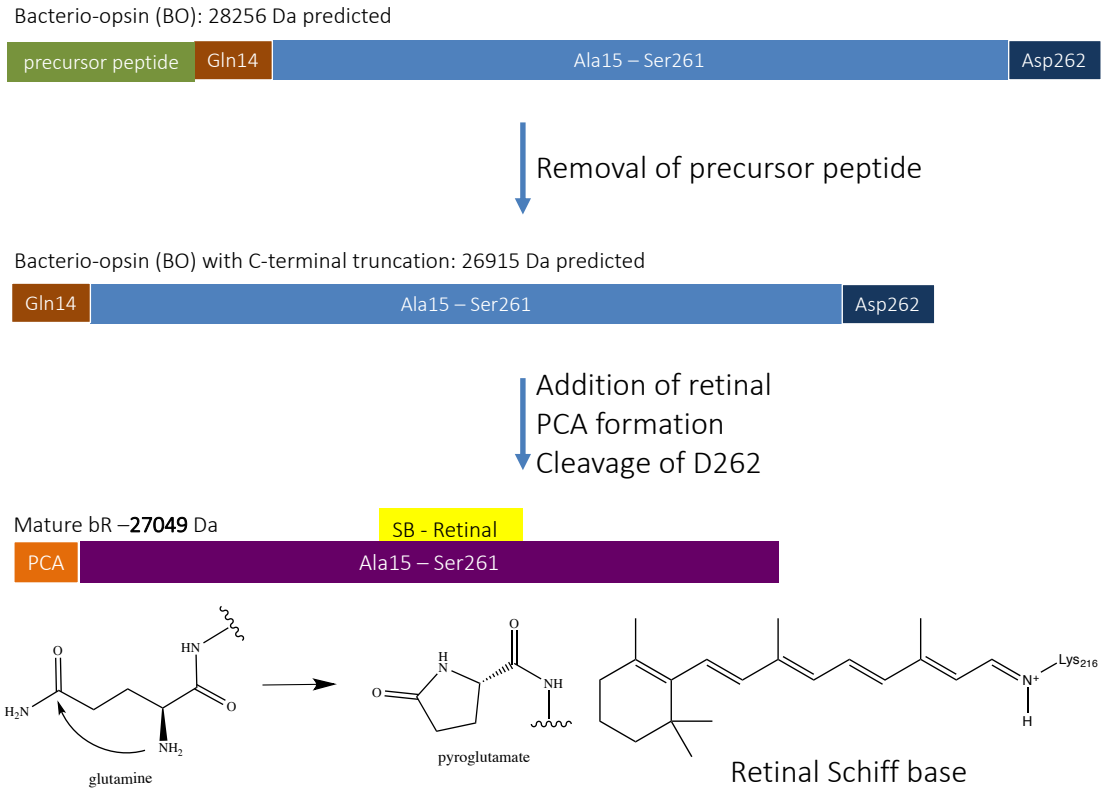


Figure 2.18: Top: Schematic representation of the sequence of bacteriorhodopsin with truncation and mass of the resulting sequence. Mature protein has a mass of 27,049 Da. Bottom: The pyroglutamate (left) and the retinal Schiff base (right) are shown.

The mass spectrometry experiments demonstrate that Lipodisq are able to incorporate bR in its native state without affecting either the primary sequence or post-translational modifications. The oligomeric state of the protein is confirmed by the nMS spectra as it reveals a mass corresponding to a monomeric bR, demonstrating that, as already suggested by the UV-Vis spectra and the SANS data, the monomeric reconstitution has been successful. Moreover, as Figure 2.17 shows, there are multiple peaks corresponding to different adducts, which indicate that different other molecules are in close proximity to the protein once reconstituted in

the Lipodisq and for which identification of such adducts have been attempted.

The 677 Da adduct is the exogenous DMPC lipid added to form the Lipodisq, implying that the protein is really embedded in the Lipodisq and that DMPC is able to accommodate bR as already suggested by the neutron scattering data (Figure 2.14). Another of the adducts, with a mass of 901 Da, has been identified as an ether-linked lipid (PGP-Me) found extensively in the purple membrane, which is the major lipid component in the PM and is suggested to have a stabilising role for the protein and PM and important for the activity of bR [283]. It can also be found in several crystal structures of bacteriorhodopsin (identified as 2DP in the PDB), demonstrating that some natural lipids from the purple membrane remain bound to the protein. It also shows that this lipid is in close proximity to the protein as already suggested by a few crystallographic structures [259] and by our neutron scattering data.

Some of the adducts observed could possibly be small molecules as their masses are close to some carotenoid pigments and lipids found in the purple membrane. The 262 Da mass adduct is close to the retinal molecule (284 Da) and the 559 Da mass adduct is close to a β-carotene (536 Da) molecules but quite a different mass from squalene (410 Da), another small molecule present in the purple membrane.

2.3.5 Bacteriorhodopsin with nicotine treatment

It is suggested that small molecules could be involved in the retinal biosynthesis pathway. Inhibition of this pathway was performed by adding nicotine in the media culture for bR growth (denoted bR +-). Nicotine addition results in accumulation of bacterio-opsin (BO) protein, which is the protein without any retinal covalently bound, affecting both the expression and the correct folding of the protein [104, 293]. Accumulation of BO inhibits the production of different other carotenoids (including bacterioruberin) as shown in Figure 2.19. Conversion of BO to bR could be performed by addition of retinal at the end of the growth (denoted by bR ++) as shown by Oesterhelt and colleagues [294].

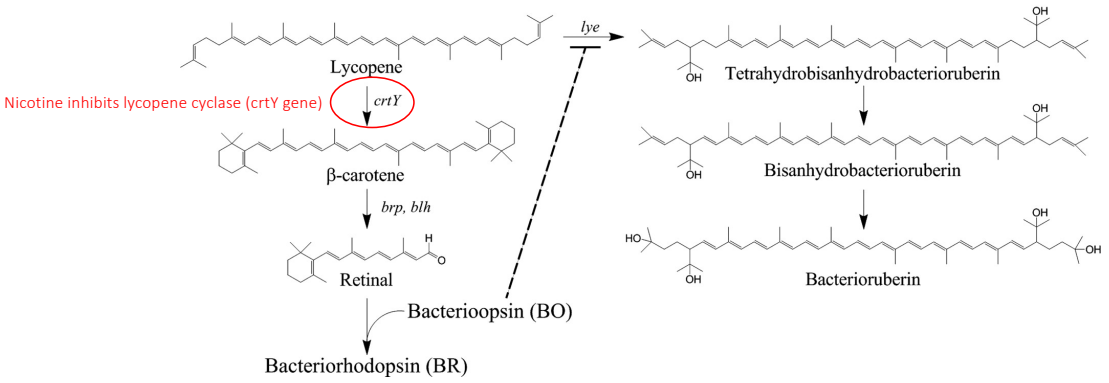


Figure 2.19: Retinal biosynthesis in *H. salinarum*. Nicotine inhibits the lycopene cyclase (*crtY* gene). Accumulation of BO inhibits bacterioruberin biosynthesis (represented by a dashed line). (adapted from [295])

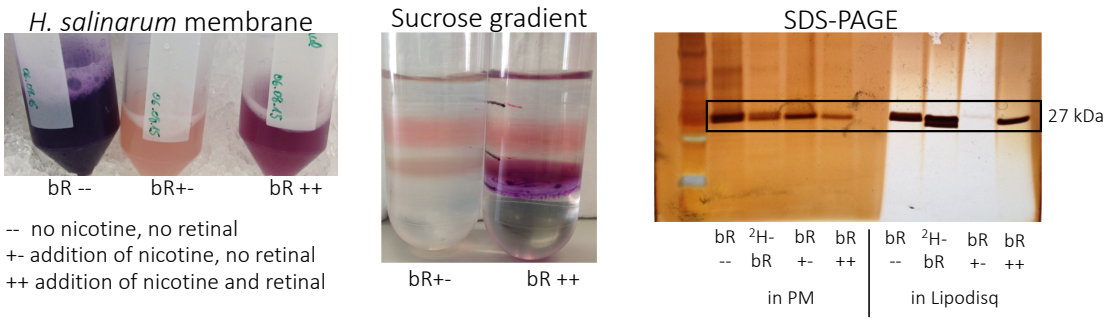


Figure 2.20: Addition of nicotine induces the *H. salinarum* to change colour. Sucrose gradient purification yields a different pattern for bR +- compared to non-nicotine samples (bR - -). SDS-PAGE (using silver stain) reveals that, even though the colour is different for the bR +-, protein is present in the purple membrane, while when reconstituted in the Lipodisq, a faint band could be observed, indicating a poor reconstitution in Lipodisq.

H. salinarum cells grown in presence of nicotine are yellow/orange in colour, but rapidly become purple after addition of retinal to the growth medium. The colour observed in the nicotine sample can be explained by the accumulation of lycopene as the retinal biosynthesis is stopped from lycopene to beta-carotene and the accumulation of bacterio-opsin inhibits the production of bacterioruberin, therefore making the lycopene molecule, a red molecule, to accumulate in the cells. But not only protein colour is affected, the amount of protein produced is drastically reduced, from 15 mg per litre of culture to 1 mg of protein per litre of culture. bR ++ sample will give rise to a yield in between with 10 mg of protein per litre of culture.

The different bR samples (bR ++, bR +-) were reconstituted in Lipodisq and were subjected to nMS. Protein reconstitution was achieved, except for the bR+- sample, which was poor as only a faint band was observed in SDS-PAGE gel as shown in Figure 2.20. This is most likely due to the fact that the protein, BO, in this case as no retinal is present, is not properly folded and did not reconstitute as well as bR.

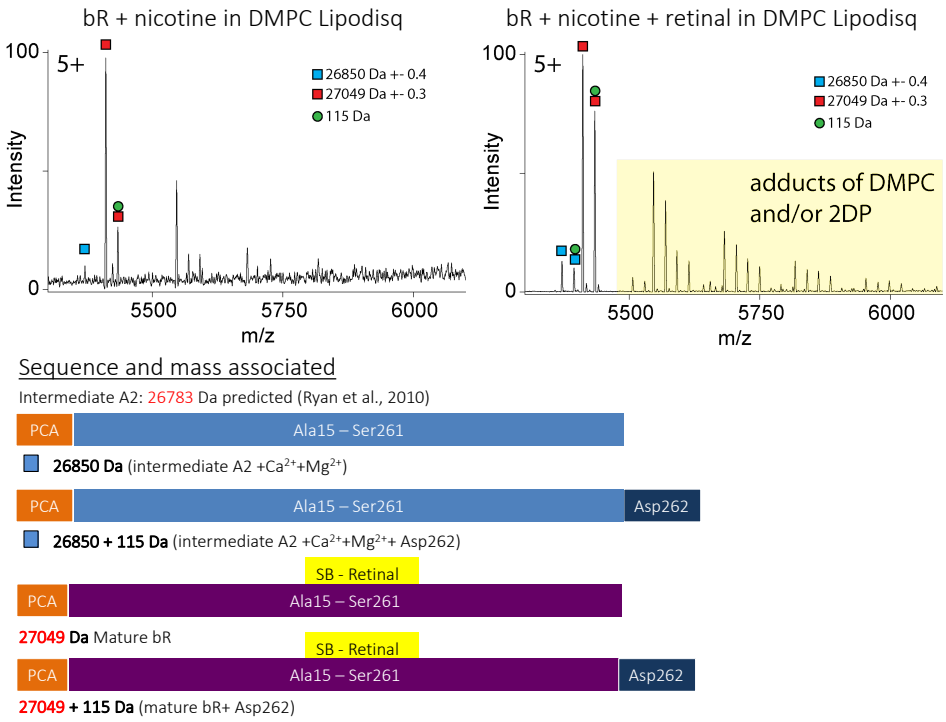


Figure 2.21: Top: Native mass spectrometry spectra from bR +- and bR ++ reconstituted in DMPC Lipodisq. Bottom: Sequence with modifications and calculated mass.

Figure 2.21 shows the nMS spectra obtained from the different bR +- and bR ++ samples. The mass obtained for bR is 27,049 Da, which is similar as the one observed before (Figure 2.16), and 26850 Da, which has been attributed to BO as it carries the same sequence as the mature protein but missing the retinal Schiff base and the addition of some Mg^{2+} and Ca^{2+} ions [296] compared to the 26,783 Da observed in ESI-MS by Ryan and colleagues [292]. These ions have been suggested to be present in bR in a total of 2 of Mg^{2+} and Ca^{2+} per bR molecule [296]. No adducts of 262 Da and 559 Da can be observed in both samples, where the only adducts are the lipid adducts, 2DP and DMPC, observed only for

the bR ++. For bR +-, no lipid signal was observed suggesting that 2DP could possibly help in the reconstitution in Lipodisq and helps, as already discussed in the literature, in the correct folding of the protein in the PM. Importantly, no adducts of 262 Da and 559 Da are observed, suggesting that these molecules could be involved in the retinal biosynthesis pathway.

2.3.6 Further identification of low molecular weight adducts

As no clear evidence that both adducts could be carotenoid molecules, another suggestion was studied. A molecule, such as myo-inositol (260 Da), is close to the mass observed and it has been demonstrated that myo-inositol lipids are involved in stress response (such as osmotic shock) and signalling in archaea. However, none of the bacteriorhodopsin structures deposited in the protein databank show any myo-inositol group present and no real proof of the existence of such molecules has been established to date.

When *Halobacterium* cells are disrupted by osmotic shock to purify bR (as performed in this study), the lipid composition of the PM changes. It has been reported that PM lipid composition is enriched by glycocardiolipin lipids such as sulfo-lipids (S-TGD), myo-inositol lipids and cardiolipin type archaeol lipids (BPG) [298–300]. A close look into the biosynthesis pathway of these lipids shows that a sulfonylgalactose (SGA) molecule is covalently linked to S-TGD lipid in the final step of the synthesis [297] (Figure 2.22). The mass of such molecule (261 Da) is close to the 262 Da adduct identified in Figure 2.17. Moreover, this molecule has been found in several structures of bR, which indicates a close contact between the molecule and the protein, similarly as in the nMS experiment, which suggests that SGA could be one of the small molecules which remains to be identified.

For the 559 Da adduct, we decided to search the mass in the lipid MAPS online database as the mass of the molecule could correspond to a low molecular weight lipid molecule. A list of several possible molecules is presented in Table 2.3. Interestingly, a molecule in the list is an ether-linked lipid, bearing a myo-inositol headgroup with a single acyl chain length of 16 carbons, which could mix with the DMPC

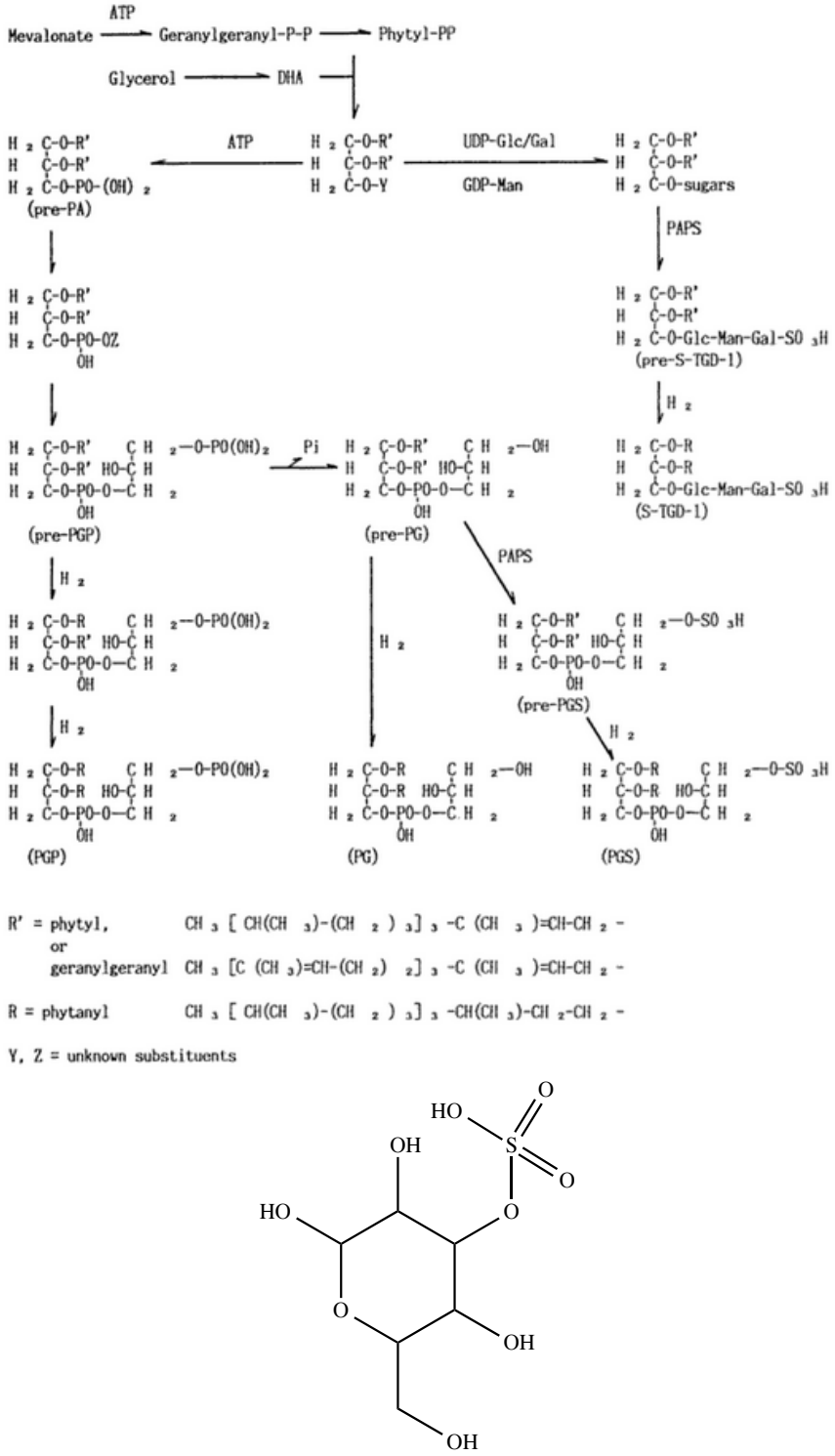


Figure 2.22: Top: Biosynthesis pathway of S-TGD lipids (Reproduced from[297]). Bottom: sulfonylgalactose molecule (SGA) with a molecular weight of 261 Da

lipid molecule present in the Lipodisq as suggested by the miscibility table from the Avanti website [301]. To further assess if a lyso-PE lipid is present in the bR-DMPC Lipodisq, thin layer chromatography was performed (Figure 2.23). Lipids were extracted from the Lipodisq using Bligh and Dyer method [302]. Different spots can be observed and lipid headgroup have been identified by their retention factor for a given solvent mixture. The results are summarized in Table 2.3 and Figure 2.23.

Table 2.3: Results from LipidMAPS online database for the 559 Da mass.

Input Mass	Matched Mass	Delta	Name	Ion
559	559.2878	.2878	LPI(15:0)	$[M+H]^+$
559	559.3030	.3030	LPG(22:5)	$[M+H]^+$
559	**559.3242**	**.3242**	**LPI(O-16:0)**	$\mathbf{[M+H]^+}$
559	559.3477	.3477	MGDG(20:2)	$[M+H]^+$
559	559.3758	.3758	LPA(27:3)	$[M+H]^+$
559	559.4357	.4357	DG(32:5)	$[M+H]^+$
559	558.4551	.5449	NAT(30:1)	$[M+H]^+$
559	559.5449	.5449	WE(38:3)	$[M+H]^+$
559	558.4517	.5483	CAR(28:5)	$[M+H]^+$
559	558.3918	.6082	CerP(d30:3)	$[M+H]^+$
559	558.3554	.6446	LPE(24:4)	$[M+H]^+$
559	558.2943	.7057	SHexSph(t18:1)	$[M+H]^+$

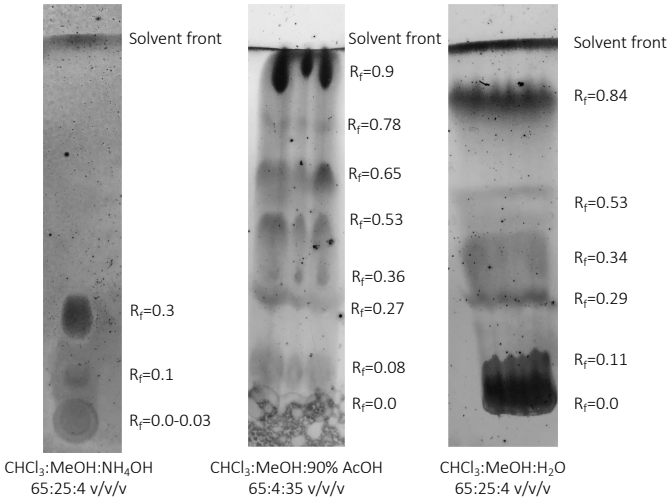


Figure 2.23: Thin layer chromatography of lipid extracted from DMPC-bR-Lipodisq by Bligh and Dyer method [302]. Retention factors are shown.

We found that the lipid component of the Lipodisq is composed of PC lipids, coming from the DMPC supplemented for the formation of the Lipodisq. PI and lyso-PI lipids are also present confirming that the LPI (O-16:0/0:0) lipid found in

the database could be present in the Lipodisq. Finally, some PGP-Me lipids (2DP, the 901 Da adduct) are also present in the Lipodisq as suggested from Figure 2.17. Other spots observed indicate that other lipids are present but are not observed in the nMS. This could be due to the fact that these lipids are present in the Lipodisq but not in close proximity with the protein, therefore not observed as adducts. Another possibility could be that during the breakage of the Lipodisq during the nMS experiment, these lipids dissociate at very low voltage from the protein as they do not have a strong interaction (such as PGP-Me lipid) with bR. Therefore, any peaks from these lipids were not observed in the nMS mass spectrum.

2.4 Conclusions

Here, it has been demonstrated that Lipodisq can be a suitable platform to study membrane proteins using a wide variety of biophysical techniques in a detergent-free environment. Incorporation of bR has shown some potential for the study of other membrane proteins as it has been possible to observe by CD (Figure 2.10) that the secondary structure of the protein hasn't been affected and that the protein is really embedded in a lipid discoidal nanoparticle of approximately 10 nm diameter as shown by SEC (Figure 2.8), DLS (Figure 2.7), SANS (Figure 2.12 and 2.14 and Table 2.2) and nMS (Figure 2.17).

Native mass spectrometry experiments have shown to behave better than Nanodisc samples as low CE voltage (Figure 2.16) can be used and no further deconvolution of the spectra is required. Furthermore, native mass spectrometry experiments have been able to demonstrate that post-translational modifications (Figure 2.18) can be conserved and identified when the protein is incorporated in a Lipodisq.

Finally, native lipids and small molecules, as shown by the different adducts in Figure 2.17, can be extracted from the membrane, implying the possibility of extracting membrane proteins with some of its native and naturally abundant lipids or ligands, compared to detergents, which are usually disrupting the close environment of the protein. Using bR-DMPC Lipodisq, we have demonstrated

that all the difficulties when working with detergents can be overcome and make the Lipodisq a suitable new tool to study membrane protein, as we are able to extract and retain the native environment, conformation and post-translational modifications of the protein.

3

Detergent-free extraction of membrane proteins: the case of a transporter in *E. coli* and a human GPCR from human embryonic kidney (HEK) cells

3.1 Introduction

3.1.1 Multidrug and toxic compound extrusion transporter (MATE)

Transporters import or export molecules to and from the cell through the plasma membrane. Multidrug and toxic compound extrusion (MATE) transporters can be found in all domains of life and they are involved in exporting different molecules such as cationic molecules, lipophilic substances, drugs or xenobiotics including anti-cancer drug molecules [303, 304]. MATE transporters also confer multidrug resistance against various antibiotics in bacteria[303]. In plants, MATE transporters export principally secondary metabolites such as flavonoids, nicotine or xenobiotics in order to protect the plant from external aggressions [303, 305] .

In humans, MATE transporters are expressed mainly in the kidney where they export cationic molecules such as acyclovir into the urine or bile using a proton gradient [306]. Inhibition of the protein can be achieved using antibiotics (such as

fluoroquinolene) and co-administration of antibiotics has been shown to enhance the effects of the drugs. Therefore, the concentration of a drug in the body can be regulated by these transporters. The cationic anti-cancer drug, oxaliplatin, which is a similar molecule to cisplatin, is a substrate for human MATE and is excreted quickly compared to cisplatin, explaining the low nephrotoxicity observed for oxaliplatin and its low potency, compared to cisplatin, as an anti-cancer drug [307] (Figure 3.1). As this last example shows, the need to understand the specificity and mechanism of transport is important to improve drug efficacy and design of new drugs. Up to now, several MATE crystal structures have been reported from different organisms, all having a common monomeric protein bearing 12 transmembrane helices with an intramolecular two-fold symmetry, named the N- and C-lobe [303, 306, 308] (Figure 3.1).

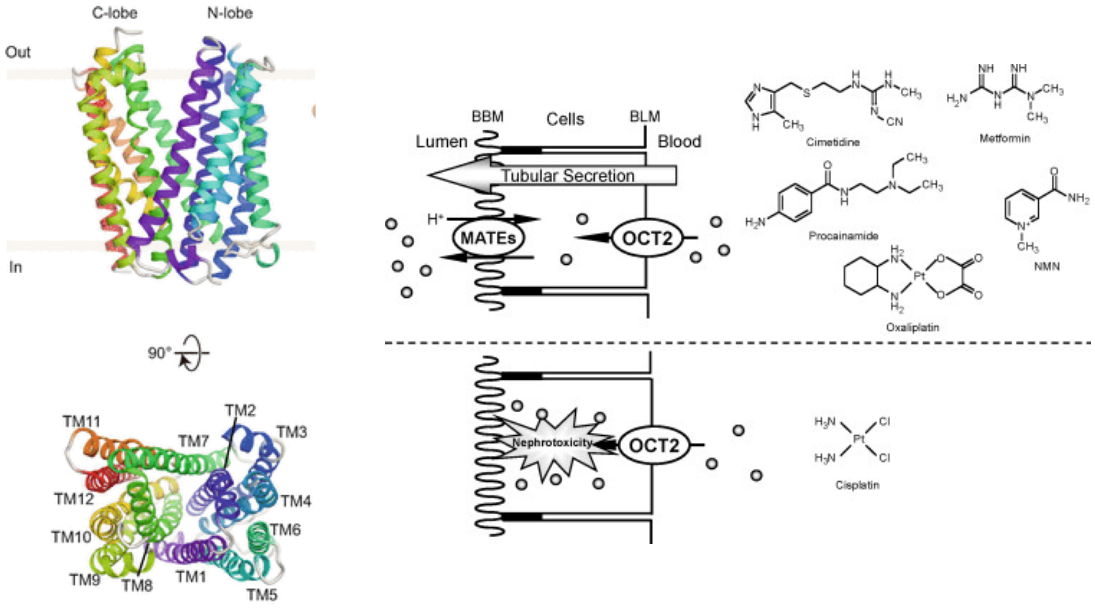


Figure 3.1: Left: Crystal structure of PfMATE (PDB:3VVN). Right: Schematic showing why cisplatin is nephrotoxic compared to oxaliplatin. Oxaliplatin is a substrate for human MATE and is excreted quickly compared to cisplatin, which accumulates since there is no MATE able to transport it across the membrane. (BLM: Basolateral membrane; BBM: brush-border membrane; OCT2: organic cation transporter 2, adapted from [309, 310])

NorM was one of the first MATE proteins identified and has been shown to mediate the resistance to multiple xenobiotics [303, 311]. Its structure has been

solved at 3.6 Å without and with ligand (Figure 3.2) revealing twelve α-helices and a large cation binding site cavity with high affinity for monovalent cation due to the negatively charged amino acids present in the pocket. It also shows that some acidic residues in both lobes are important for transport [311].

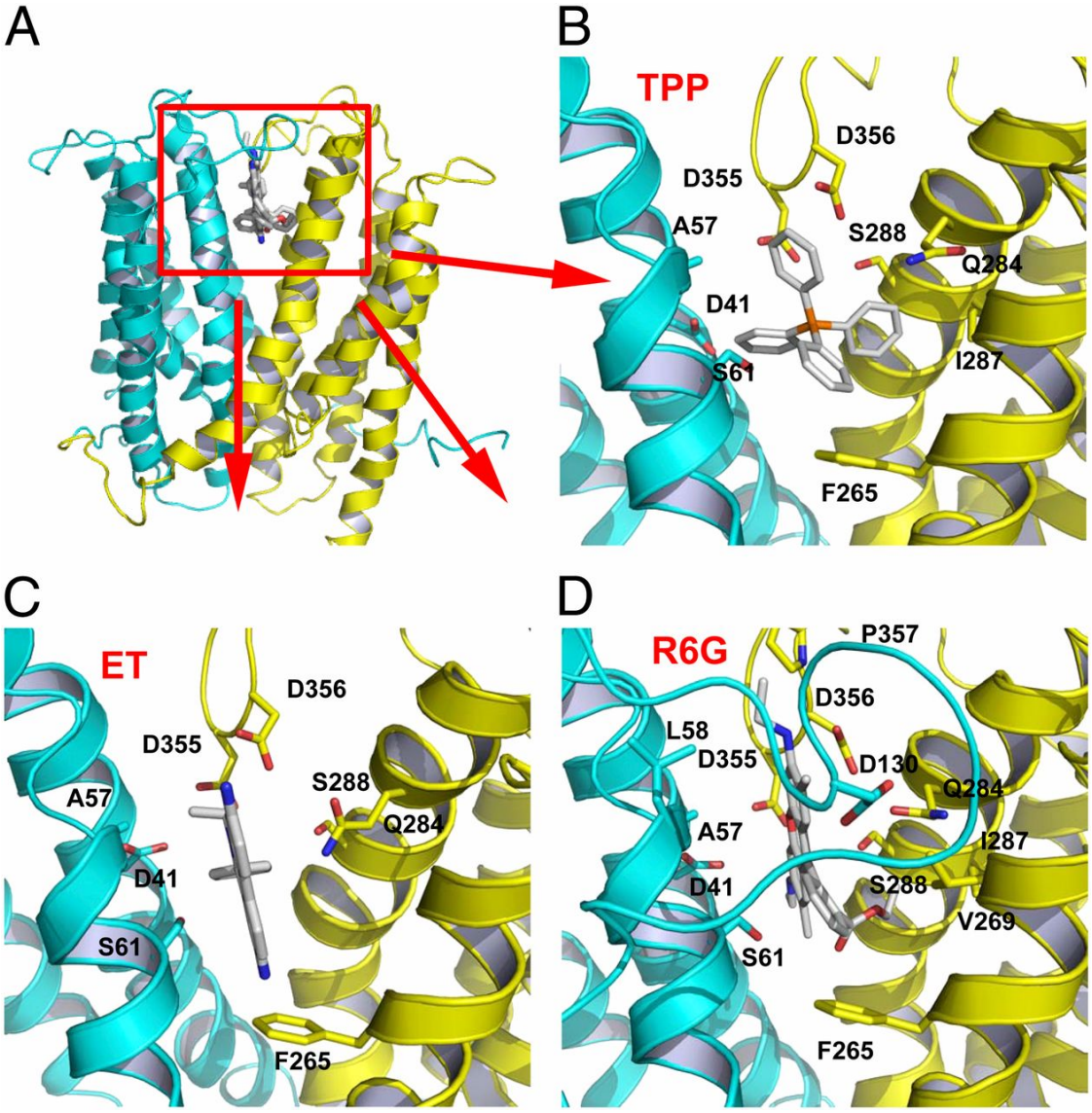


Figure 3.2: Structure of NorM where the binding pocket with the different ligands (ET: ethidium, TPP: triphenylphosphonium and R6G: rhodamine 6G) and amino acids implicated in the binding are shown (reproduced from [311])

Recently the crystal structure of *Pyrococcus furiosus* MATE (PfMATE), has been solved using macrocyclic peptides and an antibacterial drug as co-crystallization ligands [308, 309, 312] (Figure 3.3). The protein has the same topology as NorM

which shows a different distribution of acidic residues, located mainly in the N-lobe. Interestingly, the bending of the TM1 coupled to the protonation of the aspartate residues has been observed in the crystal structures, which could be important for the extrusion mechanism. Moreover, the inhibitory effects of the macrocyclic peptides are perfectly correlated with the location of these amino acids in the central cleft of the protein, which suggests that understanding this site will be important for the development of new inhibitors for MATE transporters [309].

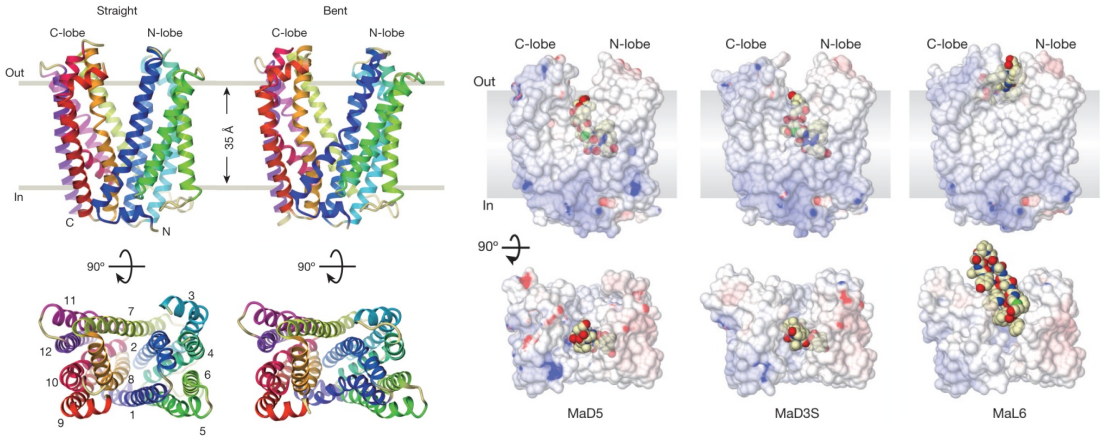


Figure 3.3: Left: Crystal structure of PfMATE where two conformations can be observed (straight and bent). TM1 and TM2 can be observed in two distinct conformations. Right: Surface model from the crystal structure of PfMATE with the macrocyclic peptides (MaD5, MaD3S and MaL6) in space filling model (adapted from [309]).

E. coli MATE (EcMATE) a homolog of PfMATE, has been chosen to study drug interactions in Lipodisq using native mass spectrometry and other biophysical techniques such as CD and microscale thermophoresis. Here, we want to demonstrate that once the protein is extracted from its natural environment using SMA, the protein activity and its secondary structure are maintained. Native mass spectrometry is able to identify some natural ligands, small molecules or specific lipids present, which could be important for the proper folding of the protein or its transport activity.

It has been recently suggested, for the AcrB protein that the ligand binds first to the outer surface of the lipid bilayer, close to the protein, and then diffuses laterally towards the protein before interacting with the transporter [313]. This

would imply that the lipid environment close to the protein plays an essential role in ligand binding and thus protein activity.

Several MATE transporters have been reported as monomers in crystallographic structures, whereas other transporters from different families such as EmrE, from the small multidrug resistance family, have been crystallized as a dimer in detergent [314]. The dimerization has been proposed as an artefact of crystallization due to an antiparallel dimer but has recently been demonstrated to occur within a specific lipid environment with, as yet, no physiological role demonstrated [315]. The structure of AcrB has been recently solved by cryo-EM using SMALPs, for which a dimer could be observed [219] (Figure 1.25). It has been demonstrated that the AcrB protein purified from detergent, is still carrying some lipids from the expression organism, indicating that some lipids could be important for the formation of the functional unit [219, 316]. Unfortunately, due to the low resolution for the SMALPs cryo-EM structure, none of these lipids could be identified.

In this chapter, we aim to extract and purify EcMATE using SMA from the native *E. coli* membrane to determine its oligomeric state, the possible small molecules or lipids bound to the protein to assess its activity using microscale thermophoresis (MST) and its secondary structure using circular dichroism.

3.1.2 Dopamine receptor 1 (D1)

As a second protein to study, we decided to use dopamine receptor 1, which is a G-protein-coupled receptor (GPCR). GPCRs are seven transmembrane proteins and constitute the largest class of cell surface receptors and comprise approximately 4% of the human genome [317]. Once activated by a ligand, GPCRs can couple to other proteins and generate a signalling cascade, which may depend on the ligand bound to the protein [318]. In humans, approximately 400 GPCRs have been identified to bind endogenous ligands and approximately 500 GPCRs are responsible for either olfaction or taste [319]. The heterogeneity of these GPCRs ensure the large recognition of several external stimuli such as taste, smell, light, pain or internal stimuli such as hormone secretion or neurotransmission [320, 321]. Due to their

implication in nearly all signalling events in the cells, they are of major interest to the pharmaceutical industry, with approximately 40% of all current marketed drugs acting as modulators of approximately 5% of known GPCRs [91].

Here we will focus on dopamine receptors (DRs) which are class A GPCRs, characterized by an extracellular N-terminus containing several conserved cysteine residues to stabilize the protein structure and a very long intracellular C-terminus [322] (Figure 3.4). The C-terminus is responsible for the different signalling events in the cell such as the phosphorylation which leads to internalization via the β-arrestin pathway [323–325]. These receptors are prominent in the central nervous system (CNS) and mediate several physiological functions such as voluntary movement, reward, hormonal regulation and hypertension [322, 324, 326]. Drugs targeting dopaminergic neurotransmission have been employed to treat several neurological and psychiatric disorders, including Huntington's and Parkinson's disease, schizophrenia, attention deficit hyperactivity disorder (ADHD) and Tourette's syndrome [327]. DRs are also used to study drug abuse or addiction [324].

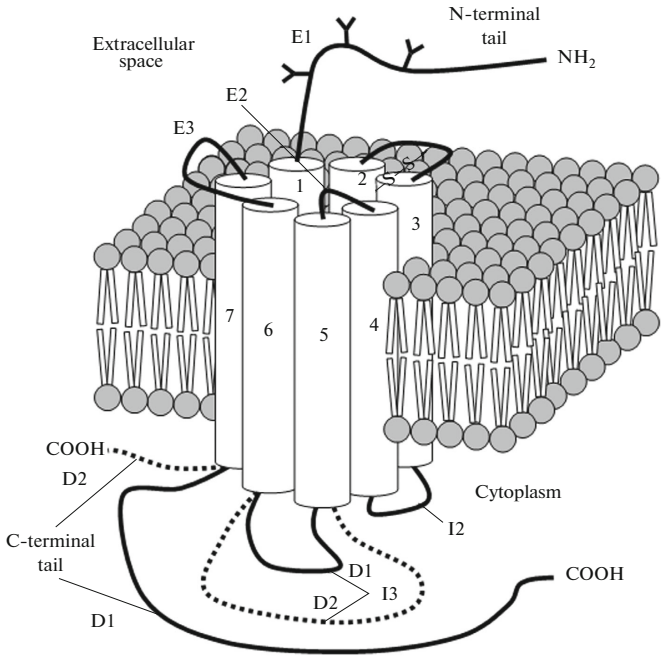


Figure 3.4: Structure of dopamine receptor (D1 and D2) where differences in intracellular loops and C-termini length are indicated (reproduced from [322])

DRs are divided into two subfamilies, D1 family (D1 and D5) and D2 family (D2, D3, D4) based on their ability to modulate intracellular concentrations of cAMP (Figure 3.5). They are thought to be present in the membrane as monomers but also homodimers, heterodimers or tetramers, demonstrated by fluorescence and bioluminescence experiments using both *in vivo* and *in vitro* models [322, 328–330] . As an example, the heteroligomerization of D1 and D2 receptor is thought to play a role in drug addiction phenomena by changing the signalling transduction cascades. These receptors can also hetero-oligomerize with other GPCRs such as the opioid, cannabinoid, histamine or neurotensin receptors, making difficult their study due to their broad range of interactions and potential signalling pathways [331–333].

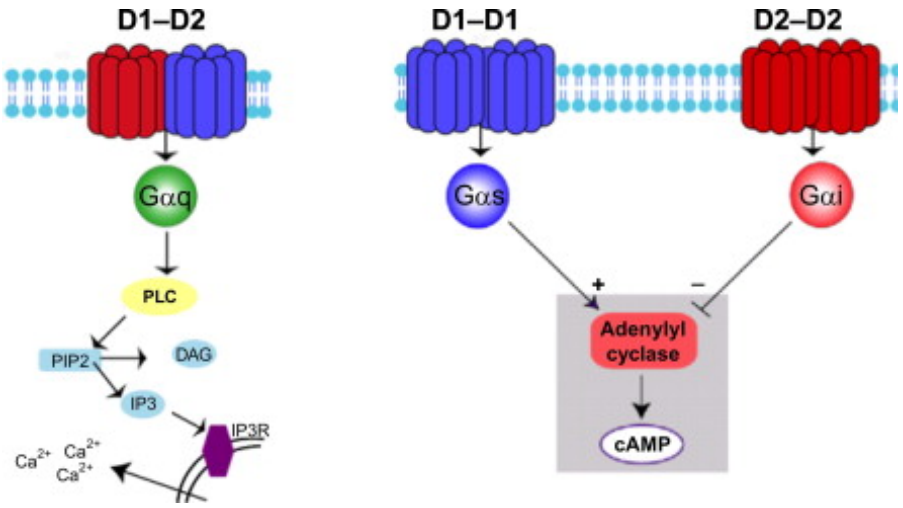


Figure 3.5: Different signalling pathways of dopamine receptors. D1-D2 heterodimers triggers signalling via G_{α}, here $G_{\alpha q}$) which leads to the activation of the the phospholipase C and IP3 receptor to release calcium (calcium signalling). Homodimers signal mainly via $G_{\alpha i}$ or $G_{\alpha s}$ (reproduced from [330]).

Although DRs have been extensively studied for nearly 40 years (discovery of the first dopamine receptor in 1975), only a few crystal structures have been published so far (from D3 [334], D4 [335] and D2 [336] recently) impeding the molecular understanding of ligand binding and therefore the development of more potent drugs or inhibitors.

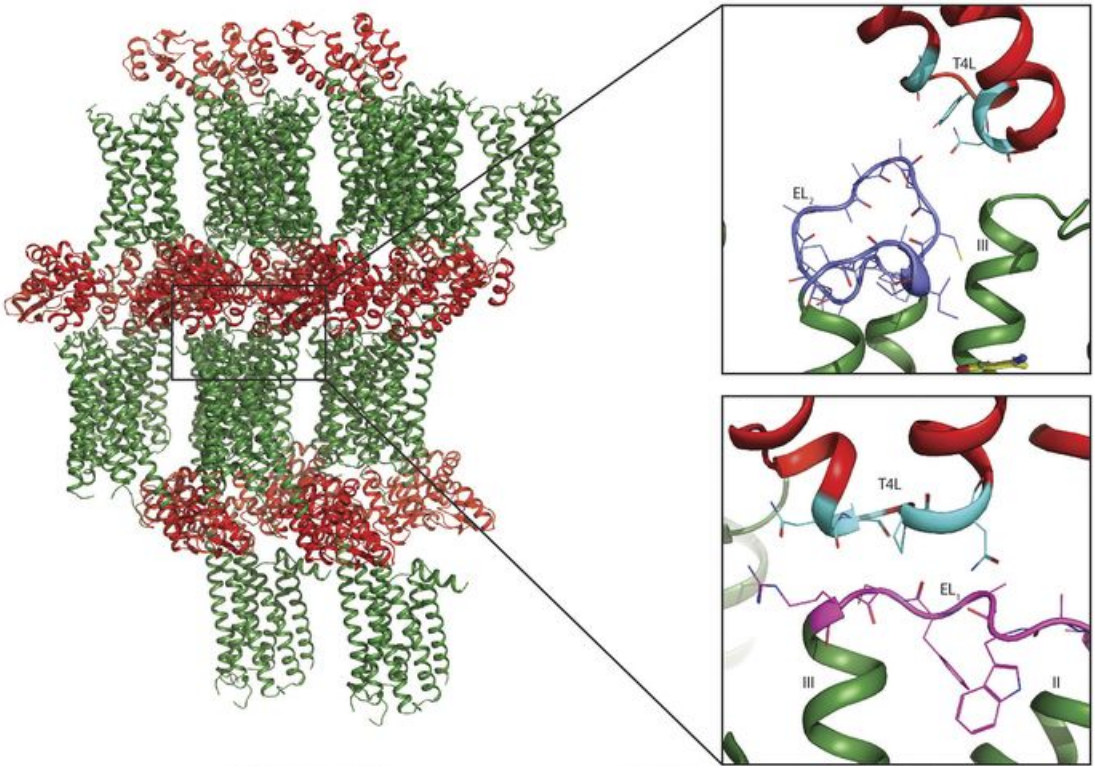


Figure 3.6: Packing of the D2 protein while in the crystal environment, where the T4 Lysozyme (T4L) is shown in red. Crystal contacts between D2 extracellular loop 2 (EL2), EL3 and T4L are depicted (adapted from [336]).

Indeed, the majority of the studies on DRs have been performed using in vitro models such as cell culture or animal tissues, but fewer studies have been performed using detergent, due to their poor stability. It is also challenging to express the functional receptor in sufficient amounts for biophysical characterization and crystallization. Several tricks have been developed throughout the years to help the expression of GPCR, including the change of the host expression organism (from bacterial to mammalian sources), introducing a soluble protein in the sequence to help the expression (by either adding a GFP-tag on one of the protein termini or introducing T4 Lysozyme in one of the loops of the protein to favour crystal contacts for crystallography, (Figure 3.6)) or mutations on the protein sequence in order to obtain a more robust protein (development of thermostabilized mutants) [337]. All these steps have usually detrimental effects on ligand binding or signalling.

3.1.3 Microscale thermophoresis (MST)

Microscale thermophoresis relies on detecting the change of thermophoresis using fluorescence as a reporter by applying an infrared laser, to heat a small area of the sample. Thermophoresis relies on the direct motion of molecules in a temperature gradient and is very sensitive to changes in size, conformation, charge and hydration shell of the molecules [338, 339]. The binding of the ligand to the protein will change the thermophoresis of the protein-ligand complex allowing, the affinity constant of the protein to be determined [339]. In our case, since the conformation of the protein is affected, we expect to observe a change in fluorescence upon the increase of the concentration of the ligand.

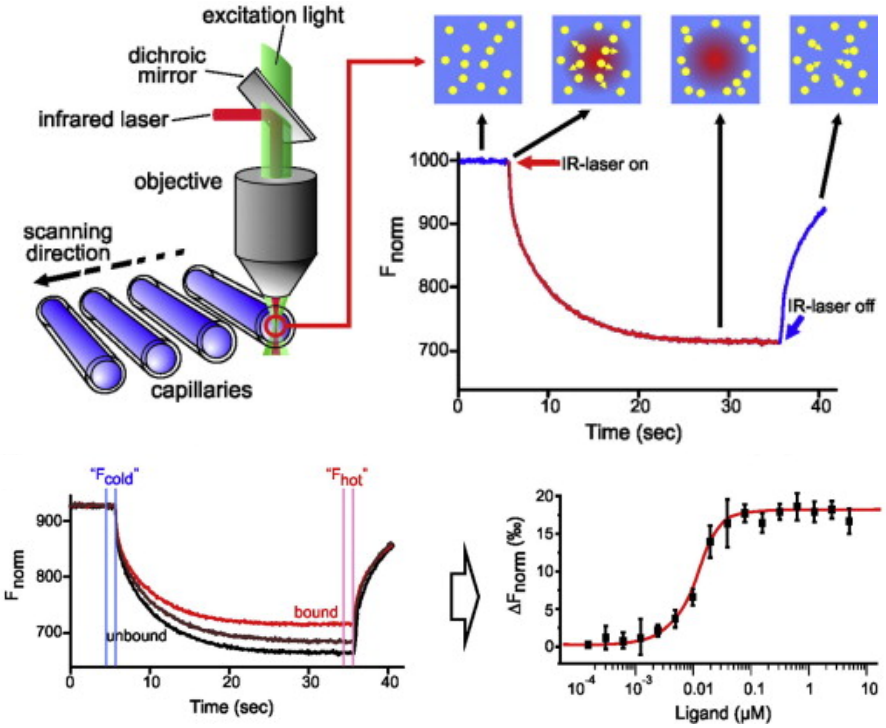


Figure 3.7: Principle of the microscale thermophoresis technique. The experiment is performed in capillaries where the thermophoresis is performed. Thermophoresis signal is changing upon ligand addition and can be plotted in a dose-response curve, from which the binding affinity can be deduced (adapted from [339] and [338]).

3.1.4 Aims

The use of a non-thermostabilized receptor expressed in a cell line, which has a makeup that is close to the native environment where the protein is usually expressed, and the possibility of keeping its environment intact, is of great interest.

Here, EcMATE in *E. coli* and D1 receptor expressed in HEK cells and with the use of the SMA polymer, we have been able to extract, purify and characterize the receptor using standard biophysical techniques such as circular dichroism, radioligand binding and microscale thermophoresis. Native mass spectrometry was used to try to resolve the oligomeric state of the protein and possible ligands bound to the protein. We aim to show that the Lipodisq is a robust platform for sensitive proteins such as GPCRs and transporters as they maintain the protein intact in its native lipid environment, which is crucial for protein activity.

3.2 Materials and methods

3.2.1 Expression and membrane isolation of EcMATE

EcMATE-GFP was expressed in the group of Prof. Carol Robinson, University of Oxford. Briefly, EcMATE-GFP plasmid was transformed into *E. coli* BL21 (DE3) Gold (Agilent). Several colonies were inoculated into 50 ml LB Miller (5 g yeast extract, 10 g peptone from casein, and 10 g sodium chloride per litre) and grown overnight at 37°C. One litre of LB in 2 litre shaker flasks was inoculated with 7 ml of overnight culture and grown at 37°C until the culture reached an OD_{600} between 0.6 to 0.8. Isopropyl β-D-1-thiogalactopyranoside (IPTG) was added to the culture at a final concentration of 0.5 mM and grown for 3 h at 37°C. Cells were collected by centrifugation (5000g, 10 min, 4°C). Cell pellets were resuspended in phosphate-buffered saline, pelleted by centrifugation (5000g, 10 min, 4°C). Cell pellets were thawed and resuspended at 20 ml per litre of culture in 20 mM Tris, 300 mM sodium chloride, pH 7.4 supplemented with a complete protease inhibitor tablet (Roche) and 5 mM β-mercaptoethanol (BME). The cell suspension was passed several times through an M-110 PS microfluidizer (Microfluidics) at

19,000 psi. Insoluble material was pelleted by centrifugation (20,000g, 25 min, 4°C). Membranes were pelleted by centrifugation (100,000g, 2h, 4°C). Membranes were resuspended in ice-cold 20 mM Tris, 100 mM sodium chloride, 20% glycerol, 5 mM BME, pH 7.4 and homogenized using a Potter-Elvehjem Teflon pestle and glass tube. Resuspended membranes were used either directly used for Lipodisq formation or flash frozen in liquid nitrogen and stored at -80°C.

3.2.2 Expression and membrane isolation of D1

Dopamine receptor 1 was expressed by UCB Celltech (Slough, UK). Briefly, all cells were cultured at 37°C in a humidified atmosphere of 5% CO_2. Cells were grown in DMEM F12+ GlutaMAX-I medium (GIBCO, Invitrogen, Merelbeke, Belgium) containing 10% fetal bovine serum (FBS) (BioWhittaker, Lonza, Verviers, Belgium), 400 μg/ml Geneticin (GIBCO, Invitrogen, Merelbeke, Belgium), 100 IU/ml Penicillin and 100 IU/ml Streptomycin (Pen-Strep solution, BioWhittaker, Lonza, Verviers, Belgium). HEK293f cells expressing the human dopamine receptor 1 were developed in house. Adherent cells were cultured in 176 cm^2 Petri dishes until confluent, and the medium removed. The cells were washed with 30 mL phosphate buffered saline (PBS) at 25°C and detached by incubation with 30 mL of 1 mM EDTA solution in PBS (pH 7.4) for 7 minutes at 37°C, and centrifuged (1500g, 10 min, 4°C). Membranes prepared using HEK283f cells (from 500 mL of culture) were resuspended in 3 mL of cold homogenization buffer (20 mM PBS pH 7.4, 2 mM EDTA, and 2 μL/mL of aprotinin, pepstatin and leupeptin protease inhibitors), and then dounce homogenize (100 strokes) on ice. The homogenate was centrifuged (1000g, 15 min, 4°C), and the resulting supernatant ultracentrifuged (40,000g, 1 h, 4°C). The resulting pellet was resuspended in buffer (50 mM NaH_2PO_4, 200 mM NaCl, pH 8 and 2 μL/mL of aprotinin, pepstatin and leupeptin protease inhibitors) using a 25-gauge needle (100 passes). The total concentration of protein was determined by BCA assay. Resuspended membranes were used either directly used for Lipodisq formation or flash frozen in liquid nitrogen and stored at -80°C.

3.2.3 Lipodisq formation and purification

Lipodisqs were formed by directly adding the copolymer (styrene-maleic acid, SMA) 3:1 pH 8 to the previously prepared membranes, at a membrane:SMA w/w ratio of 1:1.5. Sample was left to incubate (8 h, 4°C) in a rotating wheel in 50 mM NaH_2PO_4, 200 mM NaCl, pH 8. To remove non-solubilized membrane particles and any aggregated material, ultra-centrifugation was performed (100,000g, 40 min, 4°C) prior to size exclusion chromatography. The supernatant was subjected to SEC on a Superdex 200 Increase 10/300 GL (GE Healthcare) to remove excess polymer. Fractions from size exclusion chromatography (from 9 mL to 13 mL elution volume) were collected and applied to a 5 mL HisTrap HP (GE Healthcare) column previously equilibrated in binding buffer. Samples were recirculated through the column at 1.5-2 mL/min for 1-2 hours at 4°C. For elution, increasing concentration of imidazole in binding buffer were employed, using 2 column volumes per concentration gradient. Elution peak appeared between 50 to 500 mM imidazole. D1-Lipodisqs were concentrated and buffer-exchanged with PBS buffer to remove the imidazole, using a 100k MWCO Vivaspin20 tube (Greiner).

3.2.4 Circular dichroism (CD)

CD spectra were acquired with a Jasco J-815 Spectropolarimeter using a 1 mm cuvette. A wavelength range (185-240 nm) was selected to monitor secondary structure of the proteins at ambient temperature. Concentration range used for measurements was adjusted between 0.01-0.1 mg/mL and the protein was diluted in low salt buffer in order to perform experiments. Sample and ligands were left to incubate for 30 minutes at room temperature before spectra acquisition. The data was analysed, and baseline corrected using the Spectra Manager software from Jasco. α, β and random coil content was calculated from the Dichroweb website [276] using the CDSSTR analysis programme [277] and the reference set SMP180 for membrane protein [278].

3.2.5 Microscale thermophoresis (MST)

Microscale thermophoresis experiments were performed on a blue/red Monolith NT.115 instrument (NanoTemper Technologies). A typical experiment is carried using a dilution series (10-15 points) of the unlabelled binding partner. LoBind tubes were used to ensure minimal adsorption of the sample in the reaction tubes. Capillary scans were performed to ensure that fluorescence was constant (within ±10%) within the tubes. For EcMATE-Lipodisq experiments, the fluorescent labelled ligand was prepared in 20 mM PBS without NaCl and KCl at pH 7.4 at the desired concentration. Samples were incubated at room temperature for 30 minutes in buffer after which they were loaded into capillaries (Standard treated, NanoTemper Technologies). Thermophoresis was measured at different MST power (20, 40, and 80%), with 80% giving the best results. The MST data was analysed and the K_D was calculated using the NTAnalysis software (NanoTemper Technologies).

3.2.6 Ligand binding on D1 Lipodisq samples

The determination of the amount of active receptor was carried out by radioligand binding assays on HEK293f D1 membrane samples and D1 contained Lipodisq. The D1 selective antagonist *N*-methyl-[^{3}H]-SCH 23390 was used as radioligand (81.9 Ci/mmol, PerkinElmer). For saturation studies, 5 different concentrations of radioligand (in duplicates or triplicates) were used within the 0.2-5 nM range, in 50 mM NaH_2PO_4, 2 mM $MgCl_2$, 100 mM NaCl buffer at pH 7.4 (avoiding $MgCl_2$ for Lipodisq samples). Protein amount used was 5 μg total protein per sample. Non-specific binding was assayed by competition with excess (10 μM) of unlabelled D1 selective antagonist (+)-butaclamol. All samples were incubated for 1 hour at room temperature for maximum receptor saturation. For the membrane assays, the bound ligand was separated from the free radioligand by rapid vacuum filtration through GF/B or GF/C glass microfiber filters presoaked in polyethyleneimine (PEI) 0.3% for 1 hour to reduce non-specific binding, and the filters were washed 4 times with 2 mL ice-cold 50 mM NaH_2PO_4 buffer pH 7.4. For Lipodisq samples, the separation was carried out using pre-equilibrated P-30 spin columns (Bio-Rad). Scintillation

liquid (3 mL) (ScintiSafe 3 Liquid Scintillation Cocktail, Fisher Scientific) was added to the bound sample and radioactivity was measured in dpm on a scintillation counter (1409 DSA Liquid Scintillation Counter, PerkinElmer). Specific binding was determined by subtracting the non-specific dpm from the total dpm.

3.2.7 Proteomics experiments

Bands observed on an InstantBlue (Expedeon) gels were excised and dehydrated with acetonitrile. TCEP and chloracetamide was used to reduce and alkylated cysteines before digestion by trypsin at 37°C overnight. Samples were sent to the Proteomics Facility in the Biochemistry Department (University of Oxford) for peptide analysis and identification of the proteins.

3.2.8 Western Blot

Proteins were separated by SDS-PAGE gel and transferred to a PVDF membrane (GE Healthcare) by semi-dry transfer (Trans-Blot, BioRad) following Western-Breeze Chromogenic protocol from *life technologies*. For D1 samples, anti-D1 Fab (1 mg/ml, UCB) was used as primary antibody at 1/3,000 dilution, and anti-rabbit IgG HRP (Thermo) was employed as the secondary antibody at 1/20,000 dilution. For EcMATE samples, monoclonal mouse anti-His (Sigma) and anti-GFP (Origene) antibodies and a secondary AP anti-mouse antibody solution (Invitrogen). Antibodies were diluted in blocking solution (1% BSA, 50 mM Tris buffer, 150 mM NaCl and 0.1% v/v Tween 20) and incubated for 1 hour at room temperature for primary antibody and secondary antibody incubation was at room temperature for 30 minutes. For EcMATE samples, bands were visualized by addition of Chromogenic solution (Invitrogen), for 1-2h. Afterwards, the solution was discarded, and the membrane was washed with water and dried at room temperature. For D1, chemilumiscence detection was used using chemilumiscent film (GE Healthcare) and the Pierce ECL kit (Thermo).

3.2.9 Native mass spectrometry

Native mass spectra were acquired using a Thermo Q-Exactive mass spectrometer (as described in [230]) in collaboration with the group of Prof. Carol Robinson (University of Oxford, UK). Experiments were performed using a gold coated needle (home-made) at high protein concentration (1-5 mg/mL) in a volatile buffer (usually ammonium acetate) and collisional energy voltage was applied in order to obtain protein signal (from 10 V to 200 V). Data was analysed and deconvoluted using the UniDec algorithm [256].

3.3 Results and discussion

3.3.1 Protein extraction and purification

The same procedure was followed for extraction and purification of both EcMATE and D1 (Figure 3.8).

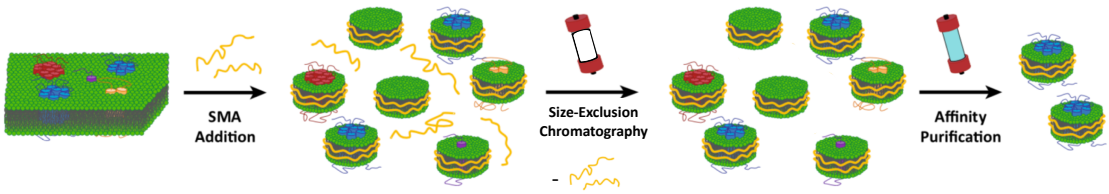


Figure 3.8: A quick overview of how to form Lipodisq from the membrane. First SMA is added to the membrane to form Lipodisq. Excess SMA is removed by SEC and protein-of-interest Lipodisq are pulled by IMAC (adapted from [213]).

First, solubilization of the membrane protein was performed by the addition of an excess of polymer to the membrane in a 1:1.5 weight-to-weight ratio as performed in the literature [195, 340]. The time of incubation of the polymer-membrane mixture was chosen to be 1-2 h at 4°C in order to keep protein folding intact during the extraction. Indeed, longer time of incubation or higher temperature could be used for solubilizing membrane proteins from membrane environment, but this could be detrimental to protein folding and activity as shown by [195, 214, 340]. A few cases in the literature carry out this solubilization step at room temperature for extended

time such as for chromatophore (1h at 20°C, [205]), complex IV (30 minutes at 25°C [208]) and for the A_{2a} model GPCR in yeast and HEK cells (20h at 20°C [214]). In our case, we did not follow the same experimental conditions of Jamshad and colleagues, as compared to A_{2a} for which ligand binding data suggests that the protein is still active at temperature higher than room temperature, no data is available for D1 about its stability at room temperature. Therefore, we opted to keep the temperature as low as possible and the SMA incubation time was increased up to 8 hours to maximize the formation of the Lipodisq at low temperature.

An important parameter to take into account is the buffer used during the solubilization. It should contain between 100-300 mM NaCl, which helps the polymer to deposit on the membrane and form Lipodisqs. It is especially important for protein expressed from bacterial sources, where negatively charged lipids (such as PG and cardiolipin) are more abundant than in other host expressions systems. This would ensure that the charges on the membrane are shielded and that electrostatic repulsion between the negative charges on the polymer and the membrane is impeded [195].

Once samples have been solubilized, removal of any non-solubilized materials and aggregates are removed by ultra-centrifugation. The supernatant is subjected to size-exclusion chromatography to remove the excess polymer present. At this point, assessment of the solubilisation process could be performed for the EcMATE-GFP samples. A strong yellow supernatant with colourless pellet would indicate a good solubilisation, whereas a green pellet would indicate a bad solubilization (protein is not solubilized by SMA).

Size-exclusion chromatography has been performed as previously presented in chapter 2 (Figure 2.8) to remove excess of polymer prior to IMAC purification (Figure 3.9). The SMA is removed for two main reasons, one being that the excess polymer would hinder the biophysical characterisation of the proteins once in Lipodisqs (for CD, for example) and the second and most important one being that the SMA, due to the maleic acid moiety, would like EDTA, chelate the metal ion present in the IMAC column. As the protein purification relies on the IMAC

purification, removal of SMA is necessary as SMA would compete in binding with the HisTag of the protein, producing a poor yield [340].

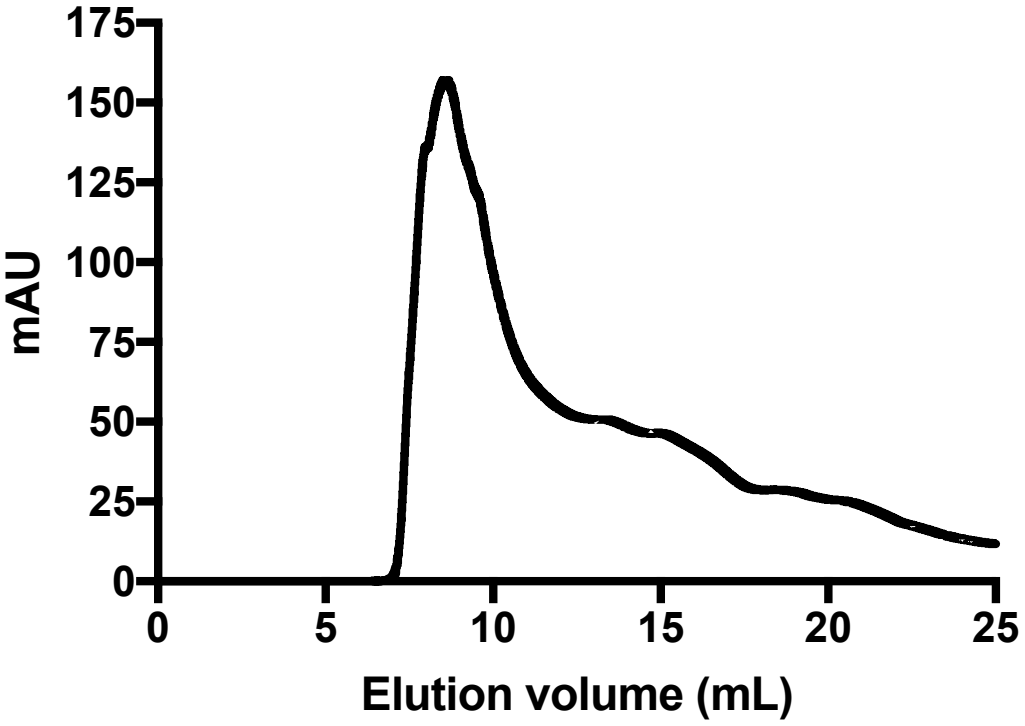


Figure 3.9: Typical size exclusion chromatogram of Lipodisq extracted from the membrane of *E.coli* or HEK before IMAC.

For SEC of both D1 and EcMATE, samilar elution profiles are observed as for bR-DMPC Lipodisqs (Figure 3.9). Here, the samples from the elution volumes from 8.5 mL to 13 mL are collected. No fractions are discarded at this point, except the late fractions containing SMA, as the protein could have any size as its oligomeric state is yet unknown. For EcMATE, monomeric proteins are usually observed in detergent but some studies in the literature for EmrE suggest some dimeric state could exist [315]. DRs have been observed in several different oligomeric state from monomer, dimer or tetramer. As a result, the oligomeric state would have an impact on the Lipodisq size and therefore we cannot exclude any fractions at this stage.

Once the excess polymer had been removed, the samples were purified by IMAC using a HisTrap column. Samples were recirculated in the column as a single passage

yields a low amount of receptor due to the large size of the Lipodisq, impeding the interaction between the metal ion and the HisTag [340]. Therefore, a low flow rate and several passes through the column favour the interaction between the ion metal and the HisTag as shown by Pollock and colleagues [340, 341]. The temperature at which the purification was performed (4°C) has been chosen to ensure protein stability. Elution of the protein is performed by increasing the imidazole concentration in steps of 25 mM, 50 mM, 100 mM and 250 mM (Figure 3.10). The 25 mM imidazole step is performed to elute the non-specific protein bound to the column as shown in SDS-PAGE. The 50 mM imidazole step is performed to start the elution of the protein, but still other proteins co-elute with the protein of interest. The last step at high imidazole shows the protein eluting with high purity as shown by the SDS-PAGE gels in Figure 3.10. Silver stain was used to ensure that the protein had not co-eluted with any impurities.

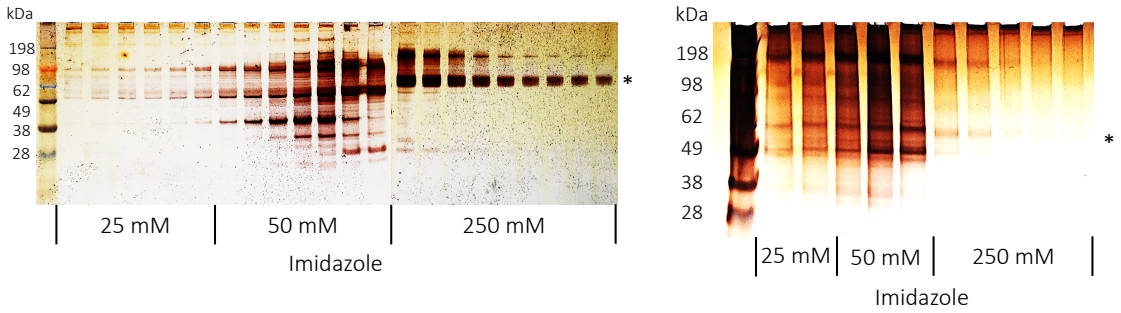


Figure 3.10: SDS-PAGE gels from IMAC purification. EcMATE (Left) and D1 (Right) Lipodisq gels are presented. Protein of interest (marked with *) is usually eluted at concentration higher than 50 mM imidazole.

The presence of the protein was verified by western blot analysis as shown in Figure 3.11. For the D1-LQ sample, enhanced chemiluminescence (ECL) was performed as the amount of purified receptor was low. Anti-His antibody and the D1 fragment antibody (Fab) shows a band at the expected molecular weight of the protein, confirming that the protein has been purified (Figure 3.11) .

Concerning EcMATE Lipodisqs, anti-His has been performed using chromogenic detection as the amount of receptor purified is greater than for the D1 samples. Two different bands (Figure 3.11), one at the expected molecular weight of the

protein and another band at a higher molecular weight than the receptor is observed. The higher molecular weight band could possibly be a contaminant from the Ni purification or a dimer of the protein.

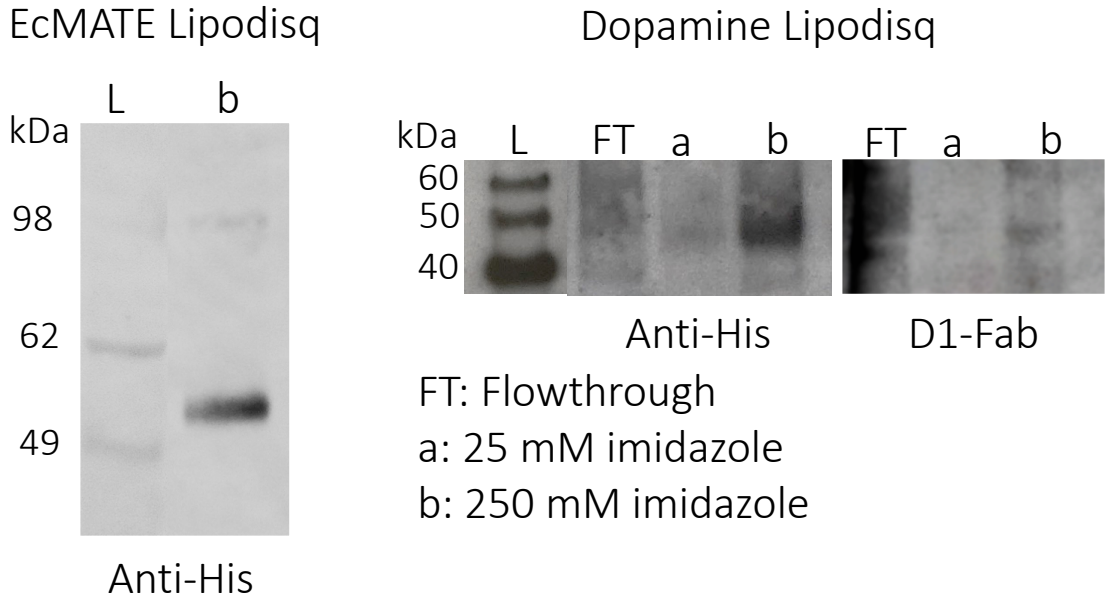


Figure 3.11: Western blots for EcMATE and D1 Lipodisq samples. Left: EcMATE sample is showing a band between 49 and 62 kDa as expected from the molecular weight of the protein. Right: D1 Lipodisq samples are presented (right). D1-Fab reveals the presence of the D1 receptor in the sample purified after IMAC.

3.3.2 Proteomics of D1

Due to the low amount of receptor purified and to ensure that D1 was present after the IMAC purification, proteomics experiments were performed (Table 3.1). Three peptide fragments have been assigned to D1, being from the C-terminus, the intracellular loop 3 and the extra-cellular loop 2 and therefore confirming that the dopamine receptor can be purified using SMA.

Table 3.1: Peptides identified from the proteomics experiments on D1 Lipodisq samples.

Unique peptides of D1 identified	
Peptides	**Location**
EEAAGIARPLEK	C-terminus
NCQTTTGNGKPVECSQPESSFK	Intracellular loop 3
AKPTSPSDGNATSLAETIDNCDSSLSR	Extracellular loop 2

3.3.3 Structural characterisation of the protein incorporated in Lipodisq

The crystal structures of pfMATE, suggest that when the protein changes its conformation from bent (PDB:3VVO) to straight (PDB:3VVN), a change in the secondary structure content is observed as an increase in α-helical content (81% in bent to 84% in straight). Changes in EcMATE secondary structure on binding a lipophilic drug (Doxorubicin, Dox) or a dye (rhodamine 6G, R6G) were followed by circular dichroism spectroscopy. CD is not sensitive to ligand binding to non-protein components (e.g. SMA and lipids). Indeed, both Dox and R6G, due to their positive charge, could interact non-specifically (electrostatic interaction) with the SMA belt of the Lipodisq, or with some negatively charged lipids present in the Lipodisq.

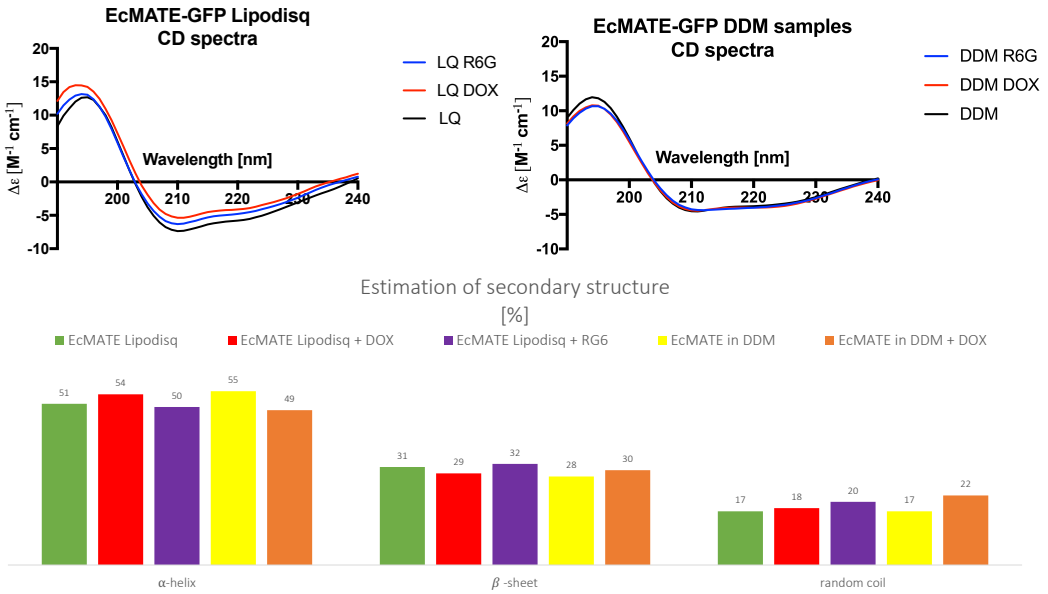


Figure 3.12: Top: Circular dichroism spectra from EcMATE in Lipodisq and in detergent (DDM) in absence or presence of the ligand. The CD spectra were measured in three analytical replicates and mean values were taken for representation. Bottom: Estimation of the secondary structure using CDSSTR method with reference set for membrane proteins.

CD spectra of EcMATE were acquired in Lipodisq and in detergent in the presence and absence of ligand (Figure 3.12). All the samples did have the expected α-helical folding for the EcMATE, as the 'double minima' are present between 205-225 nm and some β component as the sample still contains the GFP protein. Spectra of the detergent-solubilised samples share the same general shape as the Lipodisq sample and a slight change in their spectra with the addition of the ligands is observed.

For the Lipodisq samples, the doxorubicin (Dox) spectrum (Figure 3.12) is also slightly different than the other spectra presented, and the analysis of the α and β components of the protein shows a slight change in the α-helical content (see Figure 3.12). The addition of Dox to the DDM solubilized sample shows the opposite trend, as the α-helical content decreases upon addition of Dox to the protein. This change could be due to a different conformation being trapped during the SMA extraction compared to the DDM sample, as the secondary structure content is different for each of them. Very little change in the β content (contributed by GFP) is observed for the samples in DDM and Lipodisq. This suggests that the GFP does not interact with either of the ligands used in this study.

3.3.4 Radioactive and non-radioactive ligand binding assays

3.3.4.1 EcMATE Lipodisq

Microscale Thermophoresis (Figure 3.7) has been used to calculate the affinity constant (K_D) between the ligand (doxorubicin) and the protein using low concentrations of both sample and ligand.

Prior to MST experiments, EcMATE-GFP was cleaved by the TeV protease to remove the GFP tag, since doxorubicin and GFP have similar excitation and emission spectra. MST experiments require a single fluorescent probe, and doxorubicin was chosen here as it would report better the binding to the protein compared to the GFP protein, which is far from the binding site. TeV cleavage of GFP was performed overnight at 4°C and cleavage is confirmed by SDS-PAGE (Figure 3.13). The GFP

protein and the TeV protease were removed by spin concentrator using a molecular weight cut-off of 100 kDa, which retains the EcMATE-Lipodisqs. Unfortunately, the cleavage was not complete (78% cleaved as calculated by UV-Vis before and after TeV), and some EcMATE-GFP was still observed in the gel.

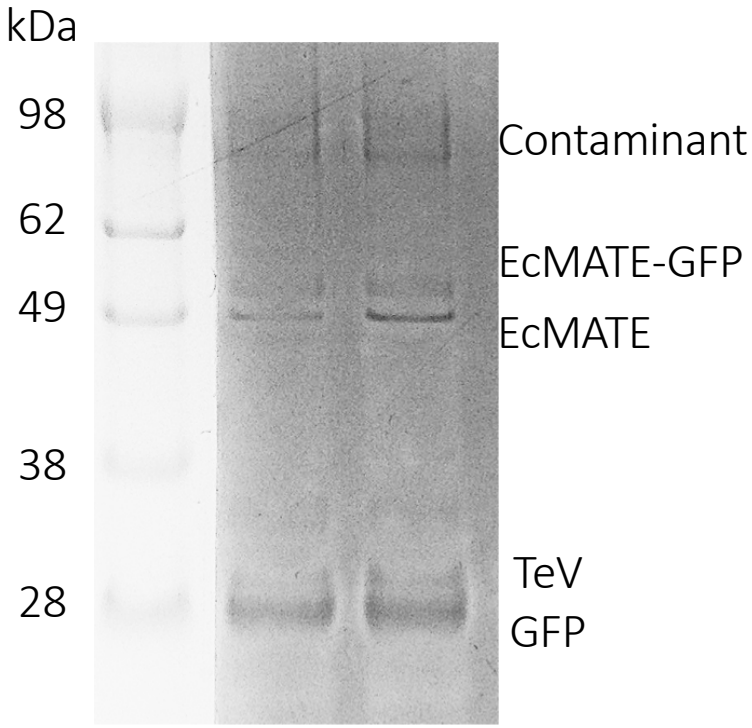


Figure 3.13: TeV cleavage of the EcMATE protein in Lipodisq

MST was performed to determine the affinity constant for the binding of Dox to EcMATE. The EcMATE in Lipodisq was concentrated and titrated from 25 nM to 1 μM, whereas doxorubicin was used as the fluorescent probe and its concentration was kept constant for the experiment. The affinity constant was calculated from the NTAnalysis using the law of mass action and the equilibrium dissociation constant estimated as described by Seidel and colleagues [342].

The affinity constant calculated (Figure 3.14) for doxorubicin, (K_D of 105 $\pm$ 2 nM) is in accordance with the literature data for NorM, which falls in the high nanomolar range (600 nM in [343, 344]). This implies that the EcMATE in Lipodisq can bind once in the Lipodisq, and EcMATE is properly folded as the CD data

suggest (Figure 3.12). The shift in the K_D observed between NorM and EcMATE could be due to the low concentration of Na^+ used in our experiments. It has been suggested that sodium has an effect on ligand binding by inducing slight structural changes at low concentrations (70 mM) in NorM [343], but unfortunately, no study has revealed a direct effect of the sodium concentration on ligand binding [344].

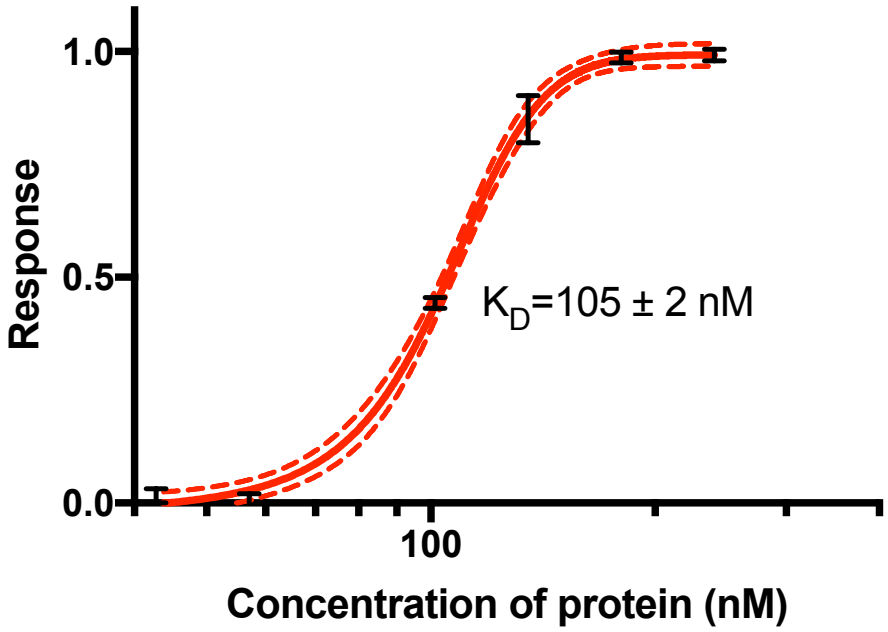


Figure 3.14: MST binding data of the doxorubicin with EcMATE Lipodisq yields a K_D of 105 ± 2 nM. Error bars represent the standard error of n=3 measurements.

3.3.4.2 D1 Lipodisq

The activity of the D1 protein reconstituted into LQ was demonstrated by radio-ligand binding (Figure 3.15). First, the activity of the protein in HEK cell membranes was performed by using a D1 antagonist, SCH23390 and the non-specific binding was assessed by (+)-butaclamol, which was used as a displacer molecule as described in the literature [345]. The data (Figure 3.15)reveals that the protein is able to bind ligands in both the membrane and in Lipodisqs. The K_D value for the Lipodisq sample (11.6 ± 3.8 nM) is similar to the value obtained from the protein in the HEK membrane (1.8 ± 0.2 nM). This reveals that the protein activity is maintained by SMA from the membrane. A shift for the K_D and the B_{max} values could be

explained by a change of conditions during the experiments, as no magnesium is present for the Lipodisq binding assay. Another possibility would be the change of oligomeric state from the membrane to the Lipodisq. It has been shown for D2 that a change of the oligomeric state of the receptor or a change in the salt concentration could shift the B_{max} and the K_D values [328]. A dimer formation would result in a lower affinity constant and slight reduction of the B_{max} as the binding of a second molecule to the dimer exerts a strong negative cooperativity as shown by Armstrong and colleagues [328]. This correlates well with our binding data, where a decrease of the binding affinity from the membrane to the Lipodisq is observed and it would suggest that D1 dimers are present in the Lipodisq samples.

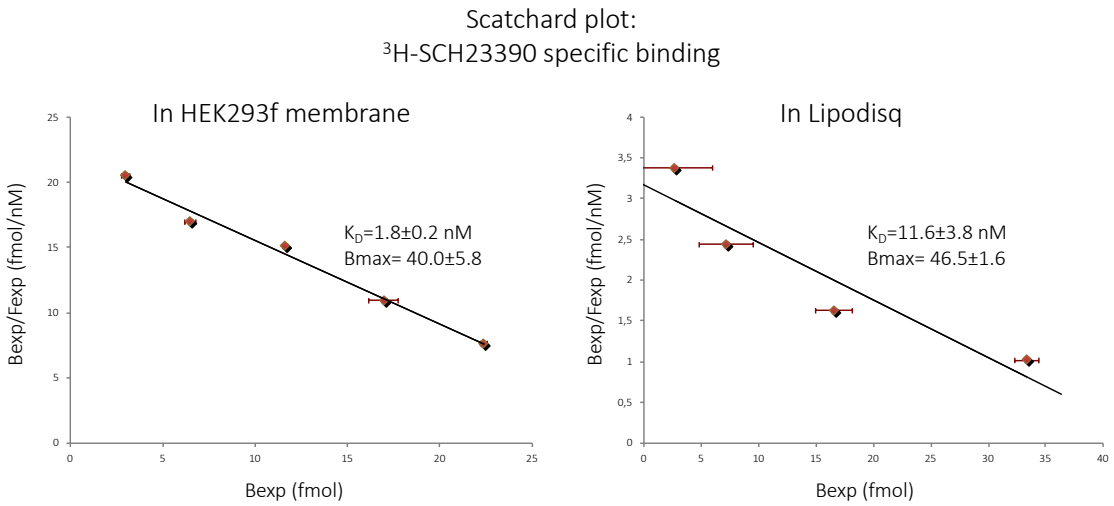


Figure 3.15: Radio-ligand binding data from the HEK membrane and from Lipodisq. Error bars represent the standard error of n=3 measurements.

Similar results have been observed for the adenosine receptor (A_{2a}) [214], which was extracted from HEK cells using SMA and the receptor shows similar activity in the HEK membrane and in SMALPs. This observation confirms that SMA is a suitable new alternative for membrane protein purification, and enables the study of the different GPCR signalling pathways in a native environment compared to the traditional use of detergent. Indeed, it has been demonstrated that dopamine receptors, upon interaction with some drugs such as cocaine, are able to translocate

in a different lipid environment, therefore demonstrating how crucial the protein-lipid environment is for ligand binding or protein signalling [346, 347].

3.3.5 Native mass spectrometry

3.3.5.1 EcMATE Lipodisq

So far we have shown that both EcMATE and D1 are able to be extracted and purified from the membrane using SMA and that EcMATE and D1 are able to bind ligands once in Lipodisqs. Unfortunately, we have not been able to obtain sufficient data concerning their oligomeric state, their possible PTMs or lipid environment. To elucidate these questions, native mass spectrometry was used, similarly to what described for bR in Chapter 2, where identification of the oligomeric state, PTMs, ligands and lipids was demonstrated for bacteriorhodopsin.

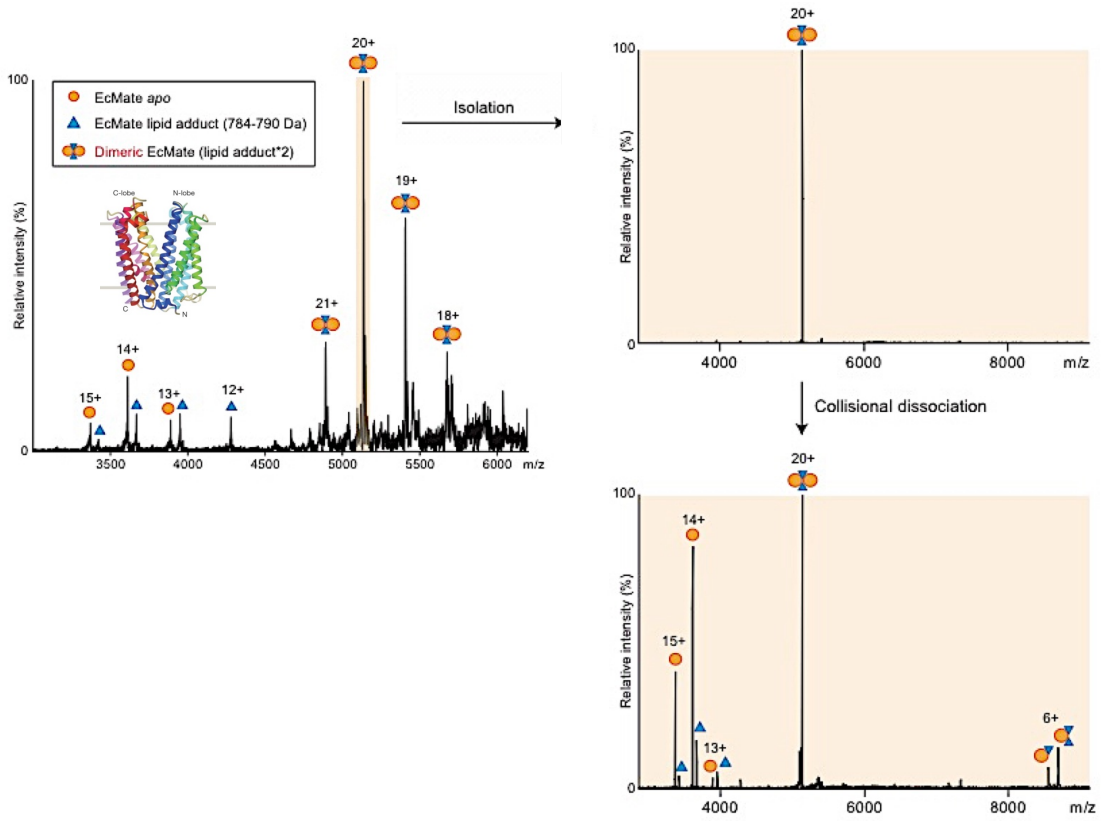


Figure 3.16: nMS spectra of EcMATE Lipodisq from membrane. Tandem-MS is performed to show that the protein is dimeric and possesses a lipid adduct.

The nMS spectrum shown in Figure 3.16 was recorded at collisional energy of 80 V, which is a similar voltage used for the bR DMPC Lipodisq (Chap. 2). Here, we observe two different species, corresponding to a monomeric and dimeric EcMATE protein without and with adduct. Due to the low voltage used for the nMS experiment in Figure 3.16, tandem MS was used to help in the identification of the mass of the individual component of the Lipodisq. The higher mass has been identified as a dimer of the EcMATE protein and it reveals that the 102.68 kDa mass dissociates into monomer, monomer plus one lipid, monomer plus two lipids and dimer plus one lipid. The mass for the monomer corresponds to the mass of the EcMATE protein and a dimeric oligomeric state has not been observed in detergent (Dr Hsin-Yung Yen, personal communication). It is suggested that MATE proteins are usually found as monomers, but other multidrug resistance proteins, such as EmrE, Sav1886 and YdaH have been determined to function as dimers and have been crystallized in a dimeric assembly [348, 349]. The dimer observed here is unlikely to be an artefact from the SMA extraction, as the lipid or molecule adduct identified looks to be important for maintaining such assembly as the different monomer and dimer adduct suggest. It has been shown by nMS and MD that some lipids can stabilize some protein oligomers by mediating interactions at their interface [73]. We therefore attempted the identification of the lipid adduct species.

A first attempt to disrupt the oligomeric state of the protein was performed by adding an equal amount in weight of a lipid, DMPC, to the membrane prior to SMA addition to the membrane. Purification was performed as described previously and SDS-PAGE gel reveals a double band around the expected protein molecular weight and another band around 100 kDa, similar to our previous purification without any added lipid (Figure 3.17).

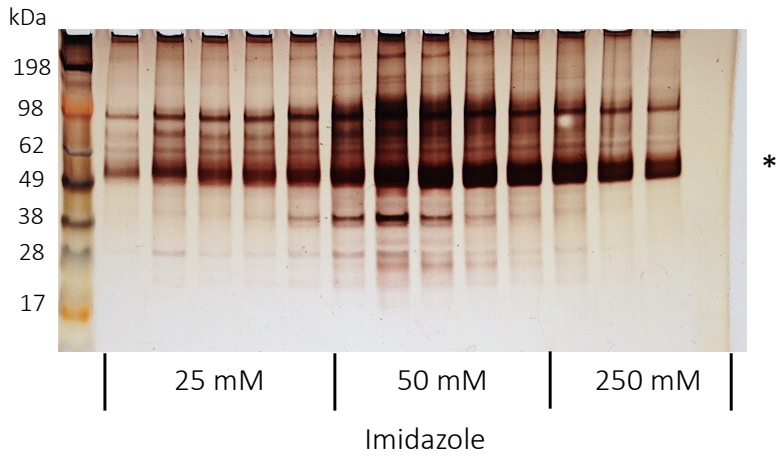


Figure 3.17: SDS-PAGE gel after IMAC purification of the EcMATE Lipodisq supplemented with DMPC lipid. Protein is marked with *.

This sample (Figure 3.17) was analysed by nMS and shows that two species are present (Figure 3.18) as suggested by the SDS-PAGE gel (Figure 3.17). We obtained the same dissociation pattern for the EcMATE dimer and we observed another protein with a different mass, which is thought to be a contaminant protein from the IMAC purification [350] as its monomer mass is different from the EcMATE protein. Unfortunately, the mass of the lipid (785-789 Da) did not enable its identification as the mass range obtained is too broad.

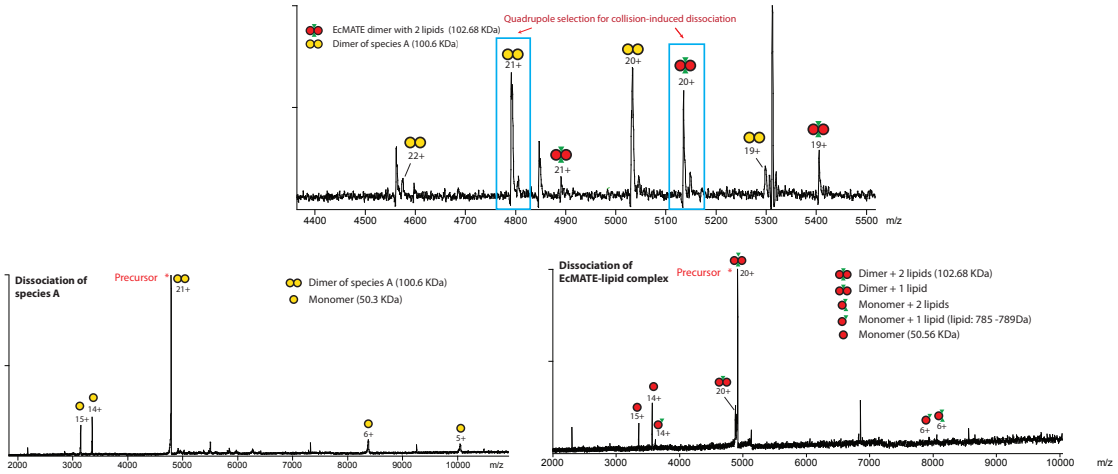


Figure 3.18: DMPC supplemented EcMATE Lipodisq nMS spectra. Dimeric specie and the lipid adduct are still present.

Since the bacterial membrane is mainly composed by PG and PE lipids (Table 1.1), protein expression was performed in a bacterial strain which lacks PG lipids. After expression and before adding the SMA to the membrane, an equal amount of DMPC was added to the membrane to compensate the lack of PG, as an excess of PE lipid is detrimental to the formation of Lipodisq [195, 198]. Purification of the protein was performed as previously, and the SDS-PAGE gel shows the same pattern as for the DMPC added membrane purification (Figure 3.19), with two bands one at the expected molecular weight of the protein and one band around 100 kDa.

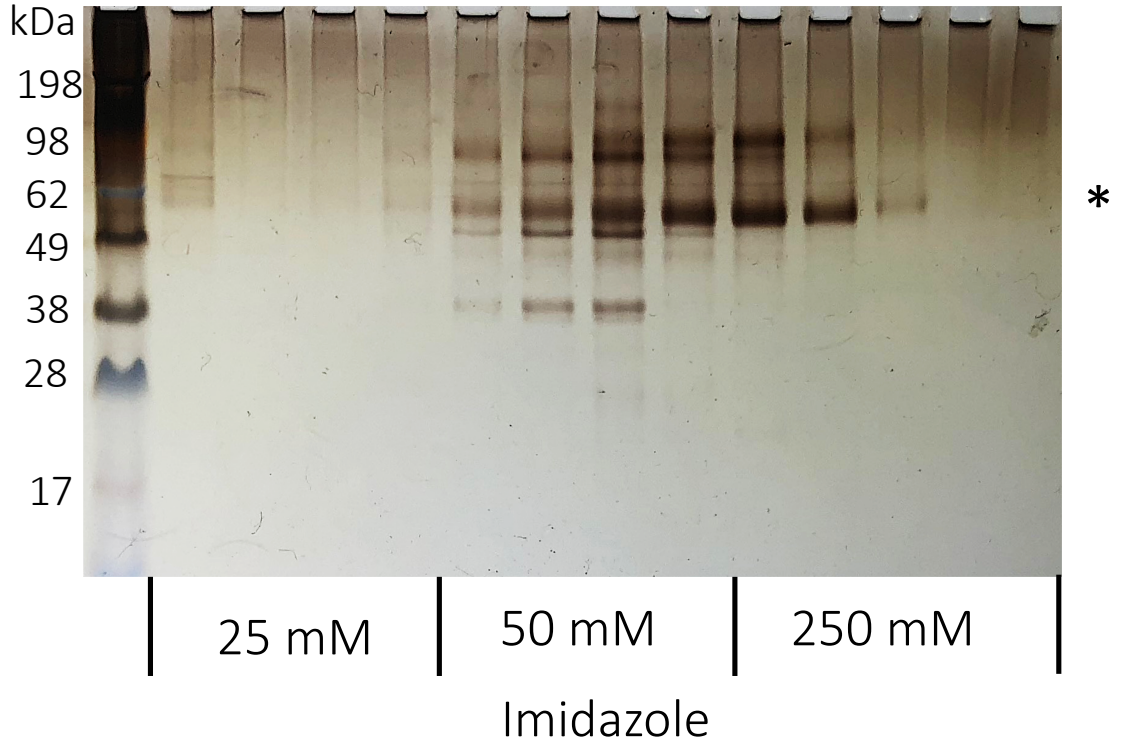


Figure 3.19: SDS-PAGE gel from the EcMATE PG deficient membrane Lipodisq purification. Protein is marked with *.

nMS spectra show the same results as for DMPC added membranes (Figure 3.20). Therefore, a different approach was performed to attempt the identification of the adduct.

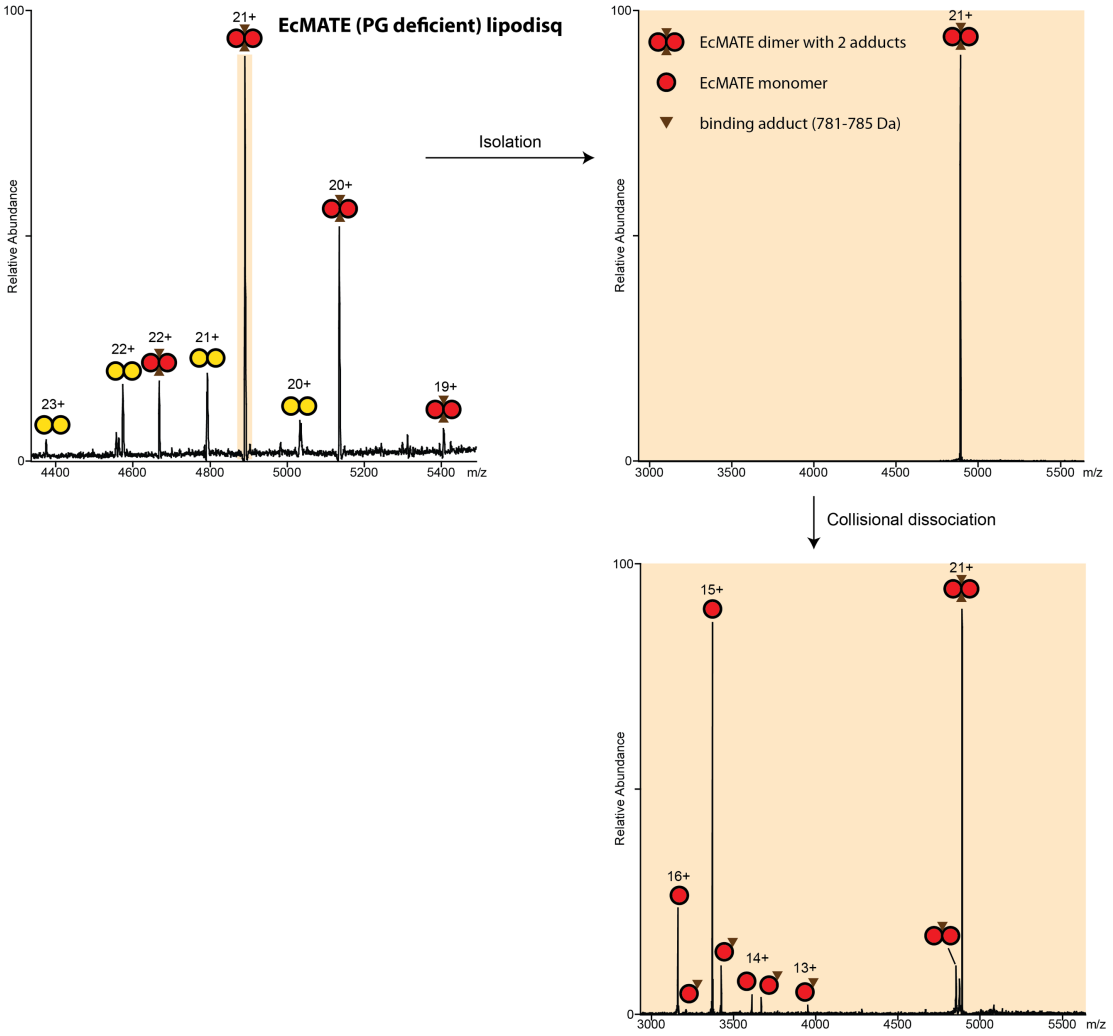


Figure 3.20: EcMATE PG deficient membrane Lipodisq nMS spectra. EcMATE is still dimeric and the lipid adduct is still present.

We decided to try the identification of the lipid by lipidomics, but unfortunately at the stage where this thesis has been submitted, the analysis of the results has not been performed. It is still uncertain if the adduct identified is a lipid as it could also be a molecule which is in close contact with the protein and important for the dimer assembly.

The importance of the identification of the adduct could help in the elucidation of the dimer interface. Therefore, the study of the interface by mutations at key amino acids or by nMS with lipid titration in detergent-solubilized EcMATE sample could help to understand its biological significance. Other multidrug transporters have

shown to be active as dimers and even as antiparallel dimers [314, 315], similarly to our MST data with doxorubicin. It is still a debate in the literature, wherever the dimer is an artefact from protein reconstitution in liposomes, crystallization artefact or over-expression of protein in the membrane or if it has a real role in regulating transport of molecule across the membrane.

3.3.5.2 D1 Lipodisq

For D1 Lipodisq, nMS spectra were recorded at a CE of 120 V showing two different mass peaks corresponding to 101 kDa and 108 kDa (Figure 3.21). This spectrum was obtained at a higher CE compared to the other proteins studied and the peaks are not as intense as for bR or EcMATE in Lipodisq spectra acquired (Figure 3.16 and 3.18) previously. This is demonstrated by the fact that the peaks are just above the noise level (Figure 3.21). As a result of the low intensity, no tandem mass spectrometry could be performed.

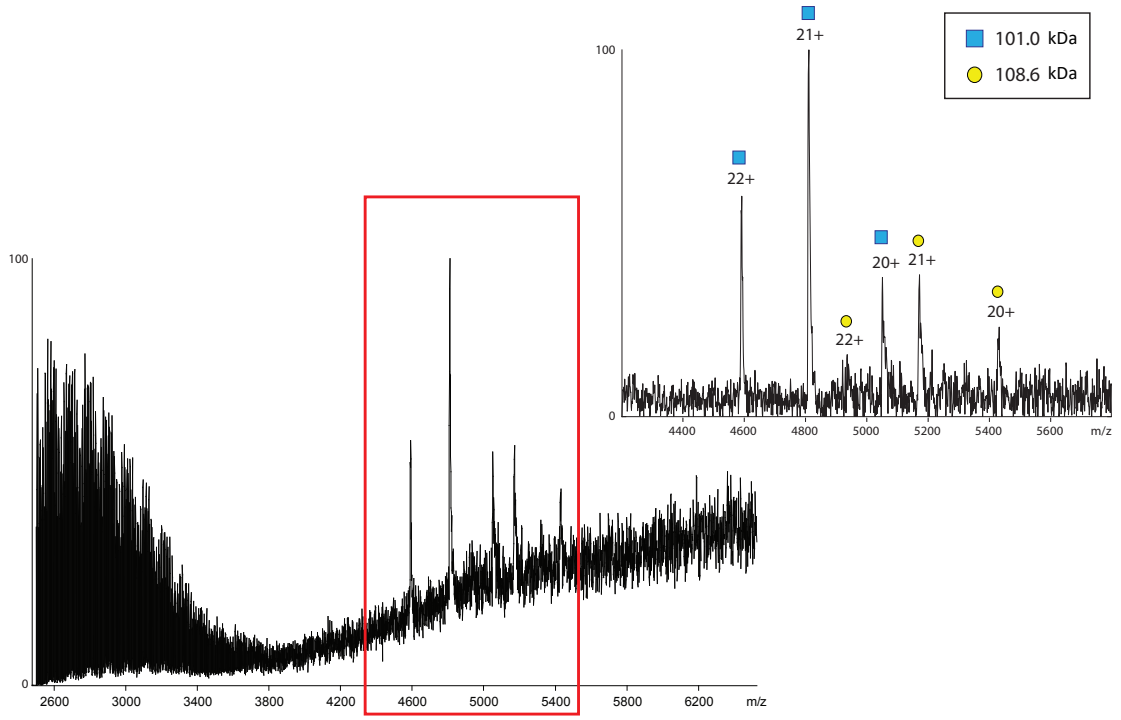


Figure 3.21: D1 Lipodisq nMS spectra showing that two different species with masses of 101 kDa and 108.6 kDa can be observed. The peaks are just above the noise level, which signifies that protein concentration is low.

From the sequence of the dopamine receptor 1 (Figure 3.22), we can deduce the mass of the protein, which is 50.1 kDa. It has been suggested that the receptor could be palmitoylated at two different cysteine residues (C347 and C351) when expressed in insect cells [325, 351] and in HEK [326, 352] cells for D1 and other dopamine receptors. Palmitoylation has been shown to stabilize the receptor as well as for the regulation of dopamine receptor functions. It has also been shown to be a prerequisite for the dimerization of other GPCRs such as rhodopsin [353], the β_2-AR, which was crystallized as a dimer in presence of cholesterol and a post-translational palmitoylation [354] and the μ-opioid receptor, which reveals a complex interaction between palmitoylation, dimer formation and cholesterol [355].

Palmitoylation on the protein would add approximately 239 Da to the mass of the protein per site, increasing the mass of the protein up to 50.6 kDa. Dopamine receptors are found in different oligomeric states in mammalian membranes, such as monomers, dimers or tetramers and they can also be interacting with neurotensin or cannabinoid receptors forming hetero-oligomers [331–333]. The mass obtained (101 kDa) in the nMS experiment would imply that we have isolated a D1 dimer in Lipodisq as already suggested from the radioligand binding data obtained (Figure 3.15). To confirm the existence of the dimer, higher collisional energy was applied but unfortunately due to the low signal observed, the dissociation of the suggested dimer was not achieved, impeding the correct attribution of the protein mass. We therefore cannot conclude that the 101 kDa peaks observed here are D1 dimers.

A second set of peaks corresponding to a mass of 108 kDa is observed in the spectra (Figure 3.21). The peaks observed could be from a contaminant protein from the IMAC purification, as a band around 100 kDa could be observed in the SDS-PAGE gel (Figure 3.10). Kaur and colleagues [356] have shown that TGF-β protein could non-specifically co-purify with proteins expressed in HEK cells as well as interacting with GPCRs internalization [357]. The TGF-β is a 55 kDa protein which dimerizes directly after its synthesis and would match the mass obtained in the nMS experiment. As the molecular weight of the TGF-β protein is similar to

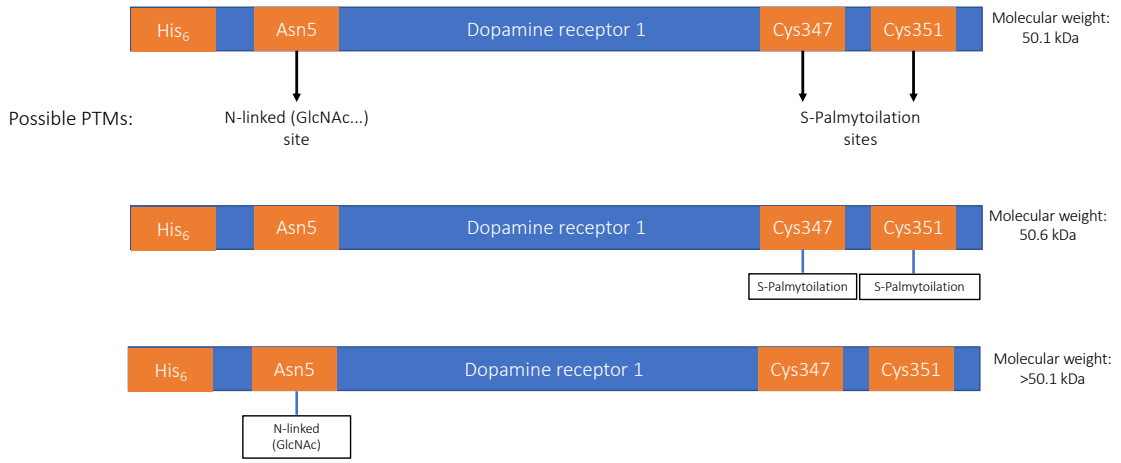


Figure 3.22: Sequence of D1 with possible post-translational modifications. D1 possesses 2 different sites for palmitoylation and 1 site for glycosylation. The mass of the post-translational modified protein is shown.

D1, it would appear in the gel at the same molecular weight of D1. TGF could therefore be one of the contaminant bands on the SDS-PAGE gel in Figure 3.10.

Another possibility would be that the 108 kDa mass corresponds to a highly glycosylated D1 protein, but no characteristic smear is observed on the SDS-PAGE and western blots, which suggests that the receptor is not glycosylated. Lastly, another possibility could be the formation of a heterodimer between D1 and another GPCR naturally present in the HEK membranes, and would correspond to one of the contaminant bands observed in the SDS-PAGE gel in Figure 3.10.

3.4 Conclusions

For the EcMATE protein, we have demonstrated that we can form Lipodisq from the *E. coli* membrane and purify the receptor using IMAC in high yield and purity (Figure 3.10). We have shown that the protein is folded by CD (Figure 3.12) and that the addition of doxorubicin induces slight changes in its secondary structure, suggesting an interaction between the doxorubicin and the transporter. MST experiments (Figure 3.14) have demonstrated that doxorubicin was able to bind to the EcMATE protein. The protein-ligand affinity was calculated and falls in the

nanomolar range similar to previous experiments in the literature and implies that the Lipodisq environment is not perturbing ligand-binding assays.

Lastly, native mass spectrometry (Figure 3.16), with the possibility of performing tandem mass spectrometry experiments, imply that we have isolated a dimeric EcMATE protein with a lipid adduct, which looks to be important for the formation of the dimer. The use of tandem mass spectrometry (Figure 3.16) for Lipodisq enables the protein complex to be dissociated in the gas phase. Tandem MS has not been performed on protein Nanodiscs as the collisional voltage required to observe protein peaks is already very high (personal communication Dr Hsin-Yung Yen) and make the Lipodisq the only lipid-based platform to allow tandem MS to be performed. The identification of the lipid adduct is still under investigation by lipidomics, since the various attempts to disrupt the dimer were unsuccessful.

For the D1 Lipodisq sample, we have shown that we can extract and purify a human GPCR from its native environment as proteomics (Table 3.1) and western blots experiments (Figure 3.11) confirm the presence of the receptor after IMAC (Figure 3.10). Moreover, ligand binding for the D1 Lipodisq sample (Figure 3.15) suggests a different oligomeric state than in the membrane. The nMS data (Figure 3.21) acquired would suggest that we have isolated a palmitoylated dimeric D1. Unfortunately, due to the low intensity of the nMS data acquired and due to the impossibility of disrupting the protein oligomer at high collisional energy and to perform tandem mass spectrometry, we cannot conclude that the protein peaks corresponds to a D1 dimer.

4

Structure of archaerhodopsin 3 in a detergent-free environment. From expression to high resolution crystal structure.

4.1 Introduction

4.1.1 Archaerhodopsin 3 (AR3)

Archaerhodopsin 3 (AR3) is expressed in the light-harvesting membrane of *Halorubrum sodomense* from a distinct archaeal organism to bacteriorhodopsin (*Halobacterium salinarum*). The protein shares 59% sequence identity with bR and over 90% sequence identity to archaerhodopsin proteins AR1 and AR2 (Figure 4.1). Its oligomeric state in the membrane is still unknown, but bR, AR2 and AR4 have been observed as trimers in their native membranes [358, 359].

Compared to bR, the AR proteins are usually co-purified with bacterioruberin, an additional chromophore, which is present in the claret membrane of the ARs but absent in the bR purple membrane [295]. Bacterioruberin and other carotenoids have been shown to be present in the membrane of *H. sodomense* and are responsible of the red-orange colour of the cells [360]. Bacterioruberin has been suggested to have a structural role in the formation of the trimer for archaerhodopsin proteins,

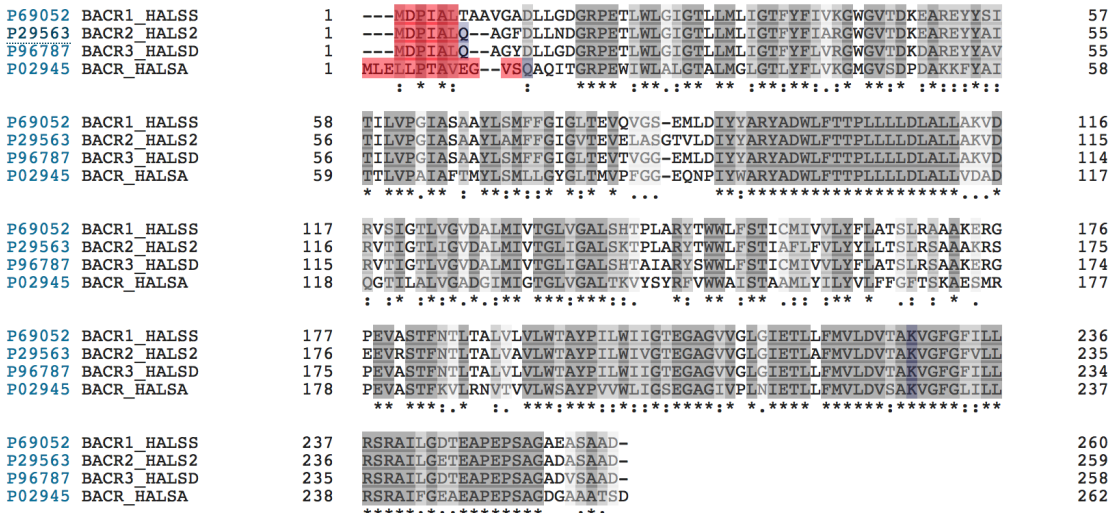


Figure 4.1: Sequence alignment of archaerhodopsin 1, 2, 3 and bacteriorhodopsin. Colour code is grey for similar amino acids, red for signal peptide and blue for modified amino acids (here Q and K).

as it has been resolved binding to clefts between monomers in the trimer in the AR2 trimeric crystal structure [358] (Figure 4.2). Bacterioruberin has been shown to modulate the photocycle kinetics and ATP formation in *H. sp xz515* [361, 362]. It is also suggested that bacterioruberin could also protect against photobleaching [363] and that prolonged sunlight exposure enhances bacterioruberin biosynthesis [364].

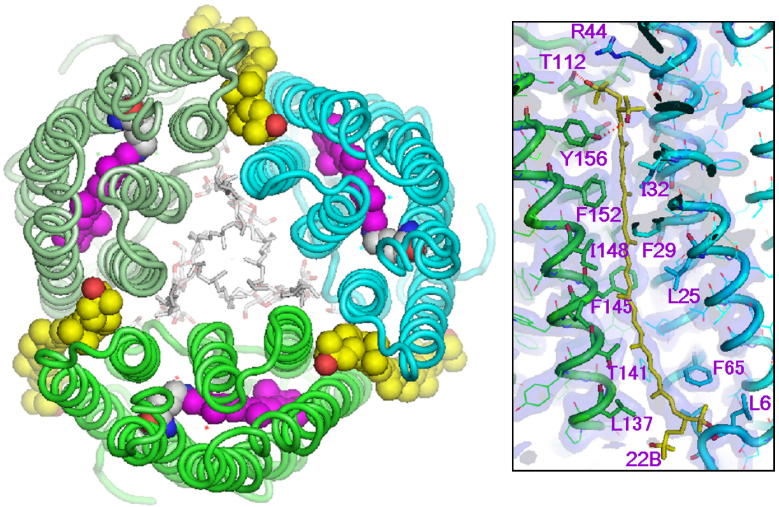


Figure 4.2: Left panel: Structure of the trimeric AR2 (PDB:2Z55, 2.5 Å resolution) with bacterioruberin coloured in yellow, retinal in magenta and other lipids in grey. Right panel: Bacterioruberin (yellow) is interacting with some amino acids between subunits (adapted from [358]).

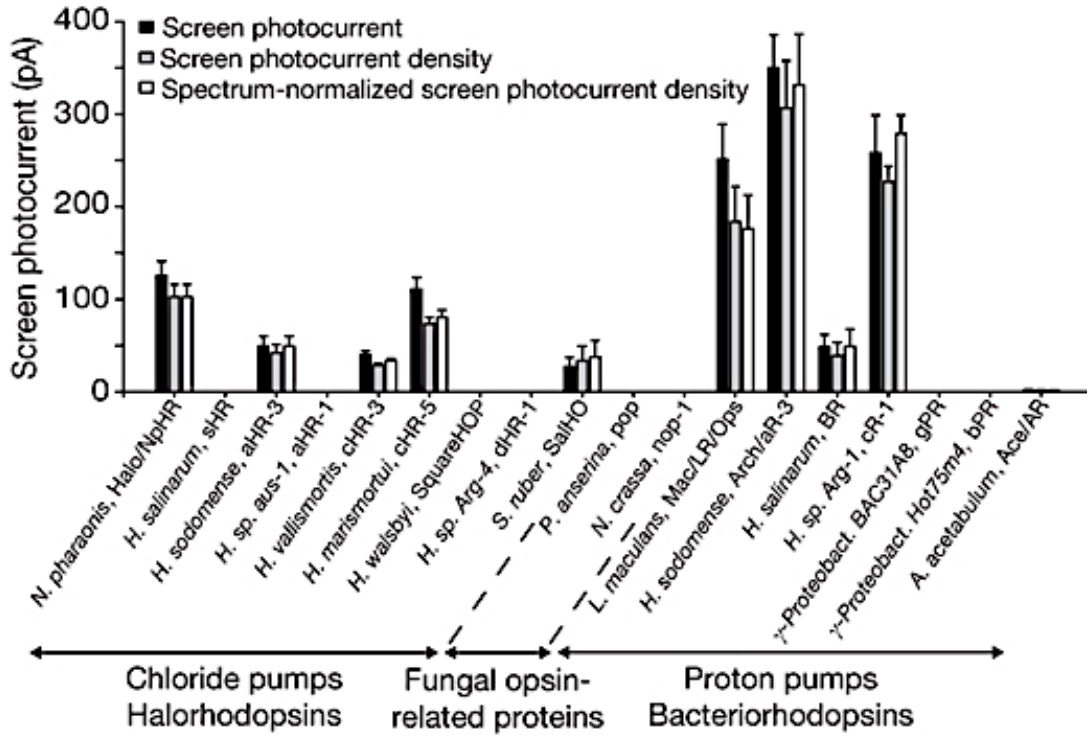


Figure 4.3: Photocurrent generated by different rhodopsins. AR3 is generating the highest current as depicted in this graph (reproduced from [131]).

Of all the known archaerhodopsin proteins, AR3 is of particular interest, firstly, because of its absorption spectrum, which is the most red-shifted, due to its hydrophobic retinal pocket, and secondly, because it is able to generate a 7 to 8-fold higher photocurrent than bR despite its close homology [131] (Figure 4.3). AR3 has therefore been used as an optogenetic tool to silence neural activity using visible light [365]. Optogenetics takes advantage of these light-sensitive proteins (especially microbial rhodopsins, Figure 4.4) to take the control of cells by simply shining light onto them (especially neuronal cells) and in living organisms [130, 366].

Optogenetic tools are usually genetically modified light-sensitive microbial rhodopsins and are chosen due to their high stability against pH, temperature, light exposure and their ability to produce high photocurrents under low illumination [368]. Such proteins are halorhodopsin, channelrhodopsin and archaerhodopsin. AR3, which is commonly called Arch in the optogenetics field, has been engineered to

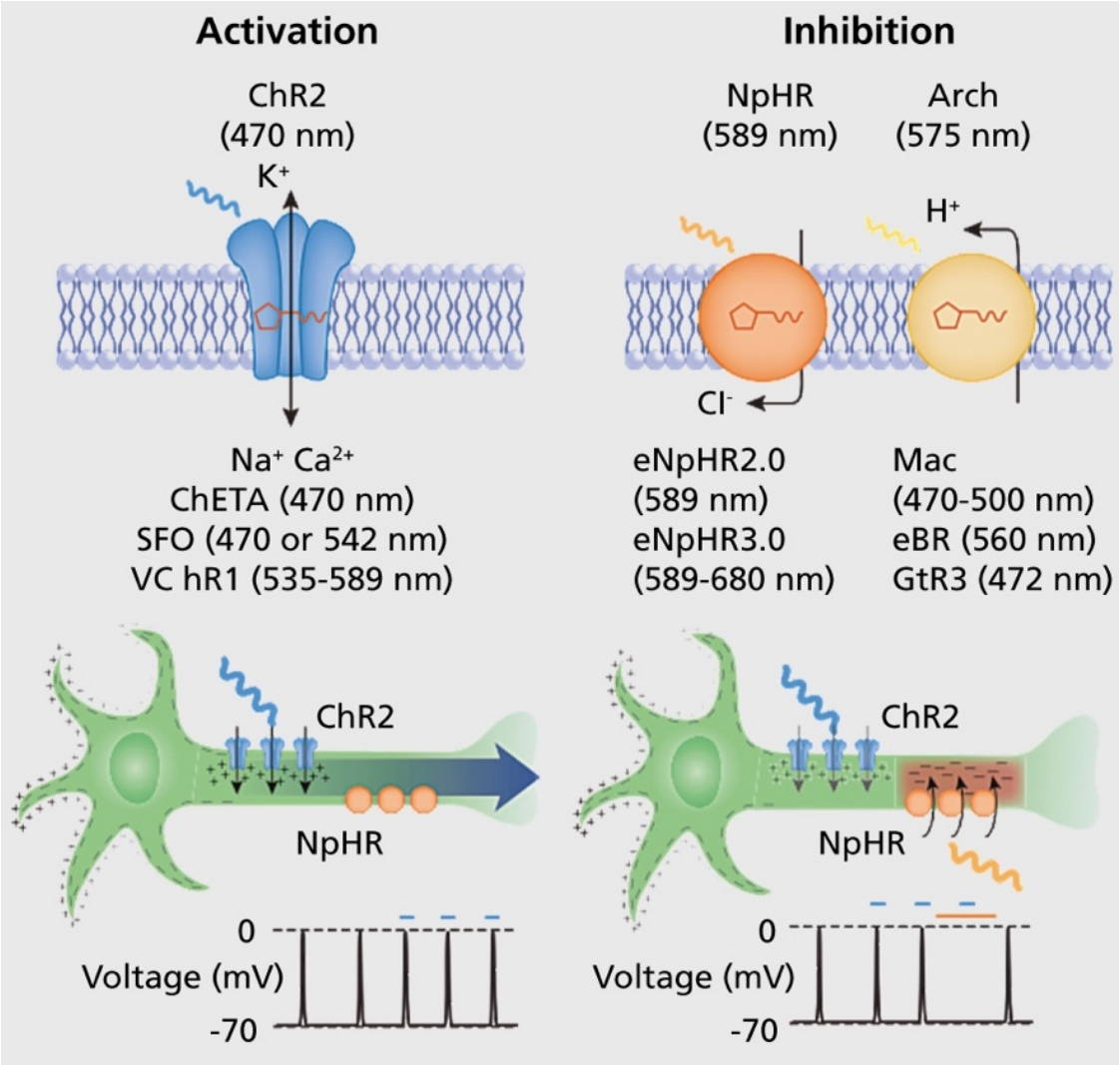


Figure 4.4: Proteins such as channelrhodopsin (ChR2), halorhodopsin(HR) and archaerhodopsin (Arch) are used in neurones to modulate membrane voltage potential since these proteins respond to specific light. Here the blue light activates channelrhodopsin while the orange light activates halorhodopsin. Application of simultaneous blue and orange light results in unmodified membrane potential (bottom right corner) (reproduced from [367], SFO: step function opsins; ChETA: channelrhodopsin mutant; eBR: modified bacteriorhodopsin construct; GtR3: *G. theta* rhodopsin 3; Mac: *L. maculans* rhodopsin; eNpHR: *Natronomonas pharaonis* halorhodopsin variants; VChR1: *Volvox carteri* channelrhodopsin).

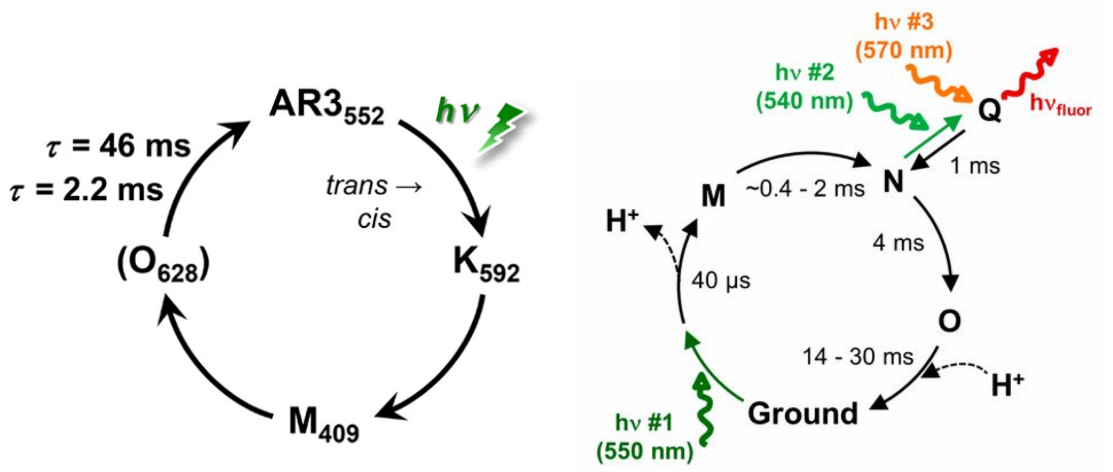


Figure 4.5: AR3 photocycle. Left: Model of the AR3 photocycle showing that only K, M and O state can be observed from flash photolysis experiments (reproduced from [374]). Right: AR3 photocycle derived from the different transient absorption and fluorescence data from [373].

produce higher currents, enabling 100% of neurons to be silenced, preventing their excitation [369] (Figure 4.4). Compared to other rhodopsins, such as halorohodopsins, which remain inactive for a few minutes after illumination, AR3 spontaneously recovers within seconds after illumination, due to a faster photocycling rate [131].

The photocycles of archaerhodopsin proteins are not well studied (Figure 4.5), but are thought to have similar photointermediates to bR but with a shorter cycling time in archaerhodopsin (as shown by Lukashev and colleagues for AR1 and AR2 from *Halobacterium sp. aus-1* and *aus-2* [370]), despite the fact that 27 of the 30 residues involved in the proton translocation and 20 of 21 residues from the retinal pocket are conserved [370]. For AR2, although the cycling time is shorter, the transition from the K to L state transition is slower compared to bR due to a difference of one amino acid in the retinal binding pocket ($M145^{bR}$ is replaced by $F145^{AR2}$) [371]. The proton release mechanism of AR4 is reversed [372] and the cycling time is shorter than for bR [362].

Although the AR3 retinal-binding pocket and proton channel are similar to bR, Fourier-transform infrared difference spectroscopy (FT-IR) suggests that there are significant differences in the network of hydrogen bonds to internal water molecules

between the ground states of the two proteins, which could be the reason of the higher current produced by AR3 [375]. Despite the fact that there is no crystal structure currently available for AR3, mutagenesis of key residues located in the proton channel and in proximity to the retinal Schiff base, has led to different mutants sensitive to different wavelengths and capable of performing the photocycle faster than the wild type protein by converting the proton pump into a light-gated proton channel [374] (Figure 4.6).

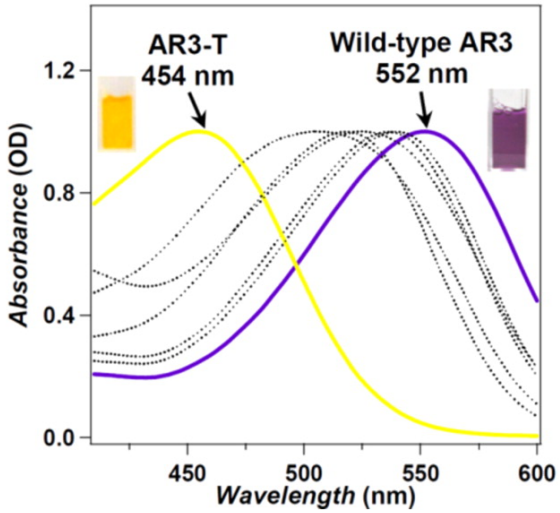


Figure 4.6: Tuning of the absorption spectra of AR3 via point-mutation in the retinal pocket. AR3-T is a triple mutant (M128A, G132V, A225T) which blue-shift the absorbance of the protein and converts the pump into a channel (adapted from [374]).

The photointermediates of bR have been characterised by spectroscopy (mainly FT-IR, Raman spectroscopy and NMR) and crystallography. For their studies, key mutations have been introduced, which 'lock' the protein in a certain photointermediate, have permitted crystallisation and structural characterisation. Unfortunately, the expression of bR mutants in *E. coli* leads to misfolded proteins and reduced yields, which hinders their study [376, 377]. Expression of the mutants in the *H. salinarum* is difficult and takes considerable time compared to *E. coli* expression (from 1-2 days to several weeks) and the archaeal expression pathway is not well understood.

4.1.2 Membrane protein crystallography

The number of membrane protein crystal structures deposited in the protein databank (PDB) has increased exponentially in recent years and this is due in part to the development of several techniques in the past decades such as lipidic cubic phase (LCP), which has proven an invaluable methodology for obtaining high-resolution structural data for a large number of polytopic membrane protein families from small membrane proteins such as microbial rhodopsins and GPCRs up to huge macromolecular complexes such as LHCII [46]. LCP consists of a single lipid bilayer bent into a highly organized three-dimensional hydrated lattice, which is more ordered than a liquid but less ordered than a solid, into which membrane proteins can be incorporated.

Protein crystal formation requires interactions that are specific, highly directional and organized in a manner that is appropriate for the formation of a three-dimensional crystal lattice, where LCP provides extensive contacts in the hydrophobic protein regions compared to the vapour diffusion method [378]. However, dehydration of the crystals during their extraction from crystallization plates (fishing and mounting of crystals onto diffraction loops) may result in a reduction in long-range order through the lattice or a phase change in the lipid from cubic phase to sponge phase, diminishing the crystal packing and therefore the diffraction of the crystals. LCP crystals are usually frozen in liquid nitrogen to protect them against radiation damage, which may lock the protein into a non-physiological conformation and prevent the protein from undergoing conformational changes which are accessible at room temperature. Novel room-temperature techniques such as serial millisecond crystallography (SMX) permit the acquisition of data at room temperature with reduced [379] or no radiation damage [380] as the exposure time per crystal is reduced relative to conventional methods.

4.1.3 XFEL and time-resolved serial femtosecond crystallography

The development of microfocus beamlines nearly 20 years ago marked a step-change in the development of methods for membrane protein crystallography. X-ray free electron lasers (XFEL) offer a further step change in the methods for obtaining high-resolution membrane protein structures [381]. XFEL has recently attracted a lot of interest due to the possibility of obtaining radiation damage-free crystal structures [382].

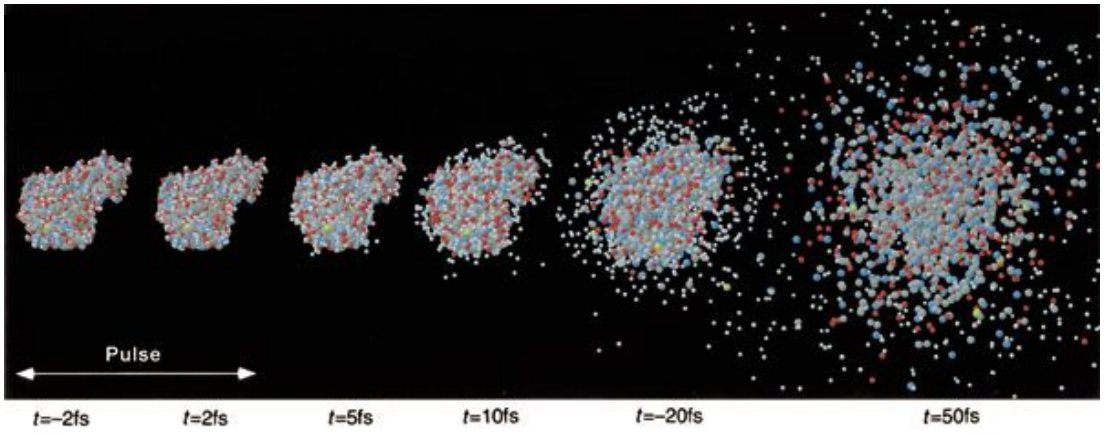


Figure 4.7: Molecular dynamics simulating an XFEL pulse on a lysozyme showing disintegration followed in time (adapted from [380]).

The main differences between synchrotron and XFEL beamlines are the peak brilliance, which is up to ten orders of magnitude higher than synchrotrons [383], the level of coherent light delivered and the very short duration of the light pulses (femtoseconds) [384]. Due to the higher energy peak, it is therefore possible to achieve a submicron focus within tens of femtoseconds, opening the way of using smaller and more weakly diffracting crystals [381, 384]. High-resolution radiation damage-free diffraction data may be obtained at room temperature due to the diffraction-before-destruction principle [380] (Figure 4.7). As the crystal is hit by the intense x-ray beam, it vaporizes within few femtoseconds but as the scattering occurs before its destruction, the diffraction pattern can be recorded [380, 385, 386]. Therefore, the use of serial femtosecond crystallography (SFX, Figure 4.8), where several hundreds

to thousands of crystals are needed to obtain a full dataset was implemented in a 'one crystal, one shot' approach [143, 387]. This methodology opens the way for multiple applications including time-resolved studies [388], challenging proteins such as membrane proteins [389] (and particularly GPCRs [143]), the determination of radiation-sensitive protein structures [382] and the possibility of obtaining crystal structures close to physiological temperatures [390].

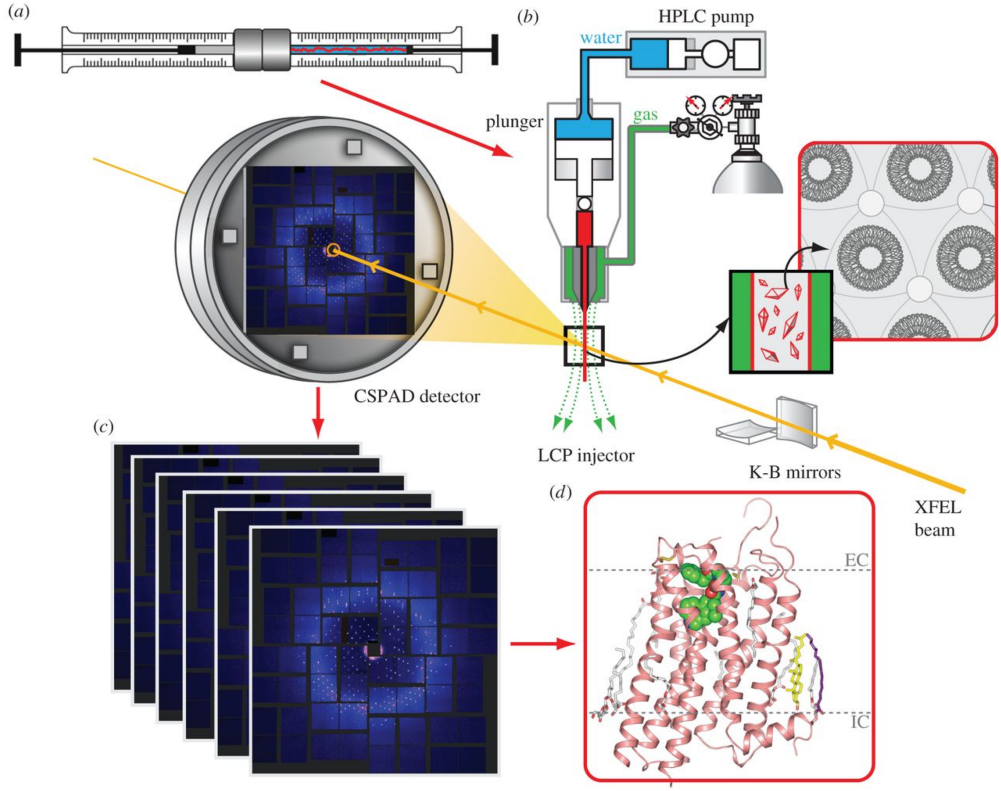


Figure 4.8: Schematic showing the LCP injector for SFX experiments. (a) Protein is mixed with the monoolein to form the LCP (b) Microcrystals of proteins are loaded into the LCP injector. The stream of crystals intersects with an XFEL beam and diffractions patterns are recorded (c) A few thousands of diffraction patterns are processed for structure determination (d) The structure of the protein is refined and solved (reproduced from [389]).

Recently, time-resolved serial femtosecond crystallography (TR-SFX) at XFEL sources using crystals of wild type bacteriorhodopsin has produced a three-dimensional movie of the bR photocycle, where movements of water molecules within the channel and changes in the conformations of several amino acids are observed

at room temperature [268, 269]. Moreover, using XFEL, which uses a very intense short x-ray pulses that enable the collection of diffraction data before the sample is destroyed [380], Nango and colleagues were able to obtain radiation damage-free crystal structures, opening the possibility of observing some lipids or small molecules in close proximity to the protein, which are usually damaged using synchrotron radiation. These methods also open the way to perform room temperature measurements [391, 392].

Furthermore, serial femtosecond crystallography (SFX) allows the study of sub-micrometre crystals, which are usually too small for synchrotron [383, 387, 391], opening the door to the study of several membrane proteins usually yielding small and fragile crystals such as GPCRs [143] (Figure 4.8).

4.1.4 Aims

The AR3 photointermediates have been primarily characterized by spectroscopic measurement involving FT-IR and flash photolysis and no high-resolution structure is available. We aim to use synchrotron and XFEL radiation to obtain high-resolution structures of the protein and its different photointermediates.

The aims of this chapter are therefore to express the wild-type protein in the native organism and to purify it without detergent to conserve all the native lipids and chromophore required for the photocycle. This contrasts with previous studies which rely on the expression and purification of the recombinant protein from bacterial sources with different mutations, and also require solubilisation and purification using detergents.

We aim to crystallize and solve the structure of the protein, directly from the claret membrane and from Lipodisq using first synchrotron radiation crystallography. Then using TR-SFX XFEL, we aim to elucidate the photocycle of the protein and to record a three-dimensional molecular movie of how water and amino acids side-chains move within the channel as performed for bR [268]. We also propose to use native mass spectrometry and Lipodisq to identify the natural ligands present in the crystal structure.

4.2 Materials and methods

4.2.1 Expression and purification of AR3

Halorubrum sodomense strain RD-26 (ATCC-33755) cells were purchased from LGC Standards Ltd (Teddington, UK) and were grown according to the manufacturer's protocol with some minor modifications. Initially cells were grown in 20-25 mL of liquid culture media with high salt concentration (125 g NaCl, 160g $MgCl_2$, 0.13 g $CaCl_2$, 5 g K_2SO_4, 1 g bacteriological peptone (LP72, Oxoid), 1 g yeast extract, 2 g soluble starch) pH 7.4 at 45°C and 170 rpm shaking for 5-7 days (until the OD_{600} reached 1.2). Flasks containing 1 L of fresh culture medium were inoculated from the 25 mL cultures and incubated at 45°C and 170 rpm shaking for at least 12 days. Cells were harvested by centrifugation after the OD_{600} had reached 1.7-1.9 (8000g; 30 min; 4°C) and the pellets were resuspended in 4 M NaCl, mixed together, stirred for 2 hours or manually homogenized, and then 5 mg of DNAse (Sigma) was added for 30 min at 4°C. The preparation was dialysed overnight in 0.1 M NaCl, and centrifuged (70,000g; 45 min; 4°C). Sucrose density gradient ultracentrifugation was used to isolate the AR3-rich claret membrane, using a step gradient of 35%, 40%, 45% and 50% w/v, centrifuged (110,000g, 15 hours, 15°C). The bottom band with a pink/purple colour was collected. Dialysis was performed against MilliQ water overnight in order to remove the sucrose. The sample was then further centrifuged (70,000g, 45 min, 4°C), and the pellet was resuspended in ddH_2O to a final concentration of 20 mg/ml and stored at 4°C prior to spectroscopic experiments and crystallisation.

4.2.2 Delipidation of the protein

Proteins were delipidated following the protocol from [267, 393]. The protein-containing membranes were pelleted by centrifugation (70,000g, 30 min, 4°C), and resuspended in 6 mL of 25 mM NaH_2PO_4, pH 6.9. Detergent (n-octyl-β-D-glucoside (OG), Glycon) was added to the sample (2 mL of 10% w/v OG in ddH_2O pH 7) and the preparation was sonicated for 1 min in a bath sonicator at room temperature.

The sample was incubated at 22°C overnight without stirring. The solution was adjusted to pH 5.5, and centrifuged (100,000g, 45 min, 15°C) to remove aggregates and any non-solubilized material. The supernatant was applied to a preparative gel column (Hi-Load 16/600, Superdex 200 pg) pre-equilibrated in 25 mM NaH_2PO_4, 1.2% w/v OG at pH 5.5. Fractions were collected from chromatogram peaks and further analysed. Coloured fractions are further concentrated using a VivaSpin concentrator to 9 mg/mL and stored at 4°C.

4.2.3 UV-Vis spectroscopy

Spectra were recorded on a Jasco V-630 instrument at different wavelengths in the visible range using a 1 cm quartz cuvette and blanked against buffer.

4.2.4 Dynamic light scattering

Particle size was measured using a Malvern Zetasizer Nano S instrument (Malvern, UK) with a disposable cuvette at 633 nm. The data was processed using Malvern Zetasizer software.

4.2.5 Electron microscopy (EM)

Images were recorded at the Institut de Biologie Structurale (Grenoble, France) using negative stain at different magnifications 30,000x, 49,000x and 68,000x. Images were analysed using Fiji/ImageJ in order to determine size of the particles.

4.2.6 Circular dichroism (CD)

CD spectra were acquired with a Jasco J-815 Spectropolarimeter using a 1 mm cuvette. A wavelength range (185-240 nm) was selected to monitor secondary structure of the proteins at ambient temperature. Concentration range used for measurements was adjusted between 0.01-0.1 mg/mL and the protein was diluted in low salt buffer in order to perform experiments. The data was analysed, and baseline corrected using the Spectra Manager software from Jasco. α, β and random coil content was calculated from the Dichroweb website [276] using the CDSSTR analysis programme [277] and the reference set SMP180 for membrane proteins [278].

4.2.7 Lipodisq preparation

Archaerhodopsin 3 (4 mg) was pelleted (70,000g, 30 min, 15°C) and resuspended in 1 mL of 20 mM sodium phosphate and 250 mM NaCl buffer containing 20 mg of 1-palmitoyl-2-oleoyl-*sn*-glycero-3-phosphocholine (POPC) small unilamellar vesicles (SUVs) produced after the freeze/thaw cycles followed by extrusion in a final protein/lipid molar ratio of 1:172. The solution was sonicated for 30 minutes in a warm bath sonicator (40-45°C). SMA (added as a solution in 1:1.5 w/w) was added to the vesicle membrane sample, and the solution incubated (42°C for 1 h). Samples were centrifuged (100,000g, 30 min, 10°C) in order to remove non-solubilized membranes and the supernatant collected.

4.2.8 Native mass spectrometry

Native mass spectra were acquired using a Thermo Q-Exactive mass spectrometer (as described in [230]) in collaboration with the group of Prof. Carol Robinson (University of Oxford, UK). Experiments were performed using a gold coated needle (home-made) at high protein concentration (1-5 mg/mL) in a volatile buffer (usually ammonium acetate) and collisional energy voltage was applied in order to obtain protein signal (from 10 V to 200 V). Data was analysed and deconvoluted using the UniDec algorithm [256].

4.2.9 LCP preparation and crystallization screens

Lipidic cubic phase (LCP) was prepared by mixing the non-delipidated protein sample with monoolein (Nu-Check) in a 40:60 volume ratio using Hamilton syringes and a syringe coupler [394]. For synchrotron, the syringe is coupled to the crystallisation robot and the LCP is dispensed into the plates. Several plates were used to screen conditions for crystal growth. For XFEL experiments, up to 20 μL of the LCP was injected into a 100 μL Hamilton syringe filled with precipitant solution. For AR3 the precipitant solution giving rise to crystals contains 30% v/v polyethylene glycol 600 (Fluka Analytical), 100 mM MES buffer pH 5.5, 150

mM NaCl, 150 mM $CaCl_2$. A shower of small crystals appeared within a few days at room temperature.

4.2.10 Data collection on synchrotron radiation experiments at Diamond and XFEL experiment

This can be found in the appendix.

4.3 Results and discussion

4.3.1 Expression and purification

Purification of AR3-rich membrane, named the claret membrane, was performed via sucrose gradient ultracentrifugation (Figure 4.9). Using similar sucrose gradients density layers used for bR purification leads to a non-pure sample, where multiple bands appears on an SDS-PAGE (Figure 4.9). Similar sucrose gradient layer for AR4 [362] produces a purple-pink band between 45%-50% sucrose density with high purity as assessed by SDS-PAGE, where a single band appeared around 17-20 kDa (Figure 4.9). This difference has been attributed to the fact that the claret membrane contains bacterioruberin, and the resulting proteoliposomes formed are smaller than those obtained from the purple membrane [361, 395].

Expression of archaerhodopsin 3 yields about 10 to 15 mg of pure protein per litre culture of *Halorubrum sodomense*. The required temperature for growth is higher (45°C vs 37°C) than for *H. salinarum* and the media has a higher concentration of magnesium than for bR reflecting the origin of the archaea (the Dead Sea in Israel), which has a similar concentration of magnesium, sodium chloride and high temperature [396].

4.3.2 Characterization of the claret membrane

Dynamic light scattering and electron microscopy were performed to compare the size of the proteoliposomes formed from the AR3 claret membrane and the bR purple membrane. The claret membrane is approximately 100 nm smaller in radius compared to the purple membrane when measured using DLS (Table 4.1) which is

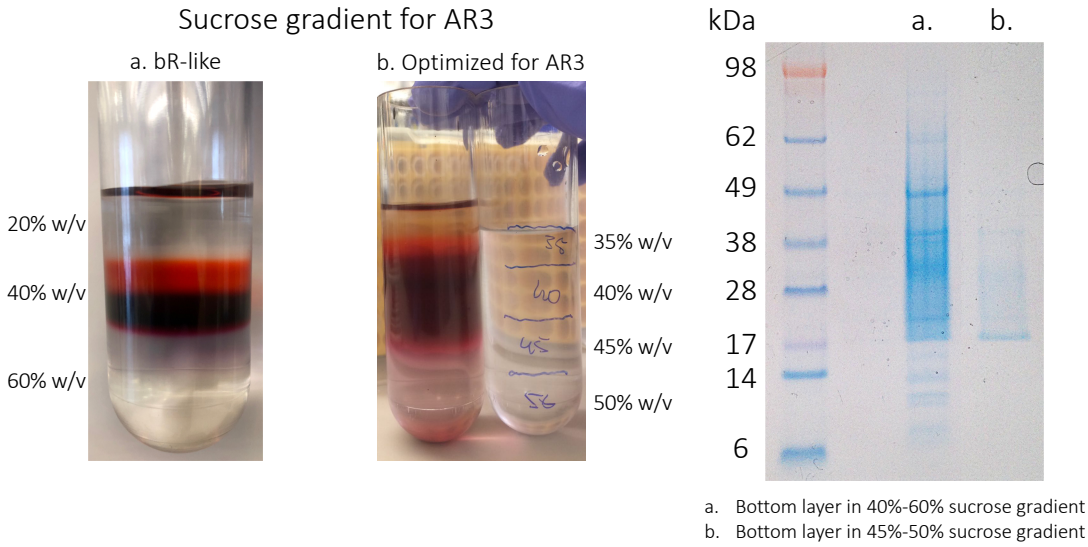


Figure 4.9: AR3 is purified via sucrose gradient ultracentrifugation. Same density layer of sucrose from bR yields a non-pure sample. Tuning the sucrose density layers yields a pure AR3 sample.

Table 4.1: DLS measurement of the claret membrane proteoliposomes of AR3 and the purple membrane proteoliposomes of bR

Dynamic light scattering	**Radius [nm]**
Purple membrane proteoliposomes (bR)	290 ± 129.3
Claret membrane proteoliposomes (AR3)	193.7 ± 101.3

consistent with EM (Figure 4.10), in which patches of approximately 150-200 nm radius are observed. The smaller size observed is similar to the size observed for other AR proteins (AR4 [362, 395]) and AR1 [397]) suggesting a greater curvature for AR proteoliposomes compared to bR proteoliposomes. Recent data on AR4, where the bacterioruberin was absent, shows an increase of the size of the particles [361]. This is well correlated with the fact that the bacterioruberin plays an important structural role for the archaerhodopsin 1, 2 and 4 as it helps in the trimerization of several microbial rhodopsins [358, 361] by contracting the protein assembly.

UV-Vis absorption spectroscopy confirms the presence of bacterioruberin in AR3 proteoliposomes since the AR3 sample exhibits the characteristic 'three-finger' pattern for this chromophore (Figure 4.11). Unfortunately, due to the

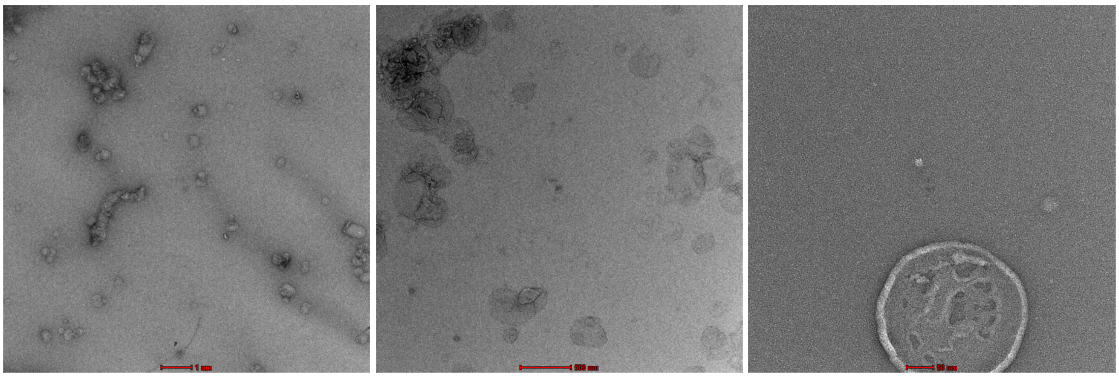


Figure 4.10: EM picture showing the proteoliposomes from *H. sodomense* at different magnification with scale bar of 1 μm, 500 nm and 50 nm.

presence of this peak, it is not possible to observe the protein absorbance peak, as in bacteriorhodopsin. Therefore, delipidation of the sample was performed to remove the lipid and other carotenoids present in the claret membrane which hinder the determination of the absorption maximum of the protein. Size-exclusion chromatography was used to separate micelles containing carotenoids and lipids from protein micelles aggregates as shown in Figure 4.11. Protein micelles (peak b in Figure 4.11) are bigger than lipid/carotenoid micelles (peak c in Figure 4.11) and therefore elute earlier. Aggregated protein or remaining claret membrane proteoliposomes elute in the void volume (peak a in Figure 4.11).

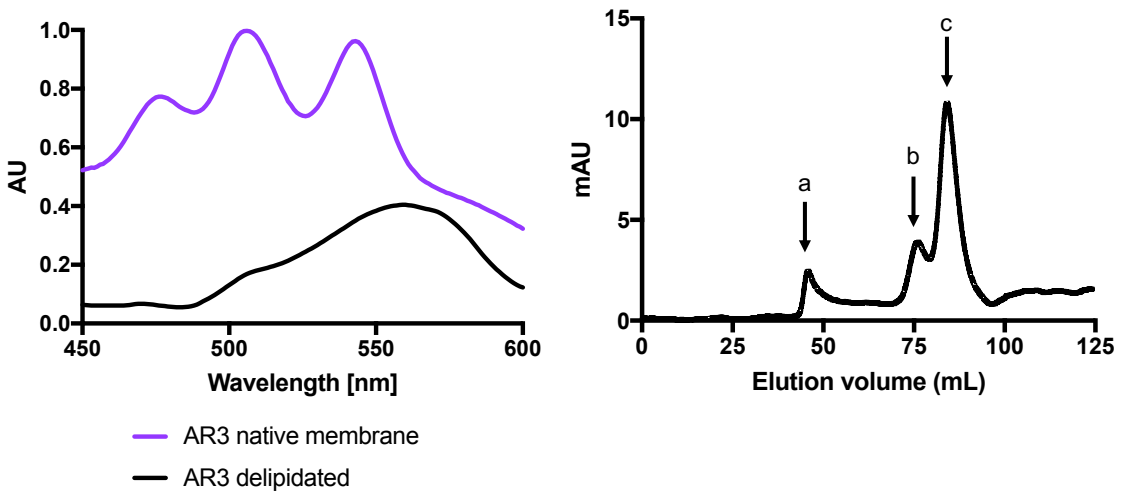


Figure 4.11: Left: Absorption spectra of AR3 from the claret membrane and delipidated. Right: Size-exclusion chromatogram of the delipidated AR3.

The UV-Vis spectrum (Figure 4.11) shows that the absorbance peak is around 566 nm, is slightly red-shifted relative to AR3 expressed and purified previously from *E. coli* (552 nm in DDM at pH 7.4, [374]). The shift observed could be due to the different conditions of solubilization used here compared to the literature, as the detergent and the pH have strong effect on the absorbance of the protein. As an example, the acidification of the solution yields a bathochromic shift due to the protonation of residue D85 (purple-to-blue transition, a shift from approximately 12 nm from pH 8 to pH 2) in bR from *H. salinarum* [398] and *H. walsabi* [399]. Different detergents, such as OG (557 nm, [400]), Triton X-100 (555 nm, [400]) or DDM (550 nm, [401]), also affect the absorption spectra of bR. The shift observed between recombinant AR3 expressed in bacteria and the archaeal AR3 from the native organism, which is greater than 14 nm, is simply a combination of different pH and detergent, which is still red-shifted compared to bR.

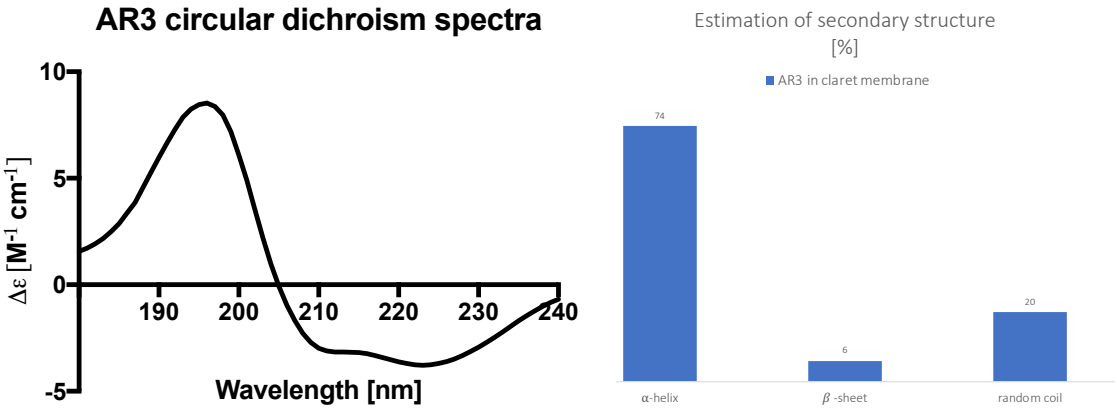


Figure 4.12: Left: CD spectra of AR3. Right: Estimation of the secondary structure of AR3.

The secondary structure of AR3 was characterised by circular dichroism (CD) spectroscopy (Figure 4.12). The CD spectrum shows the typical shape of an α-helical protein as the characteristic 'double minima' is observed between 205-225 nm. Secondary structure content was performed by CDSSTR and the reference set for membrane proteins gives 74% α helicity, 6% β-sheet character and 20% random coil [276–278]. These values are similar to those obtained for bR in Chapter

2 (Figure 2.10) and from the archaerhodopsin protein structures in the PDB. For AR2 (PDB ID: 1VGO), the DSSP algorithm estimates 68% α-helicity and 3 % β sheet and for AR1 (PDB ID: 1UAZ), 65 % helical and 4 % β sheet. Together with the UV-Vis absorption data, the CD spectra suggest that AR3 purified by this method is correctly folded.

Lastly, the activity of the protein has been assessed using droplet interface bilayer experiments (in collaboration with the group of Prof. Hagan Bayley, University of Oxford, UK). The protein has shown to be able to produce currents in the order of 8-12 pA when illuminated (data not shown, Dr Vanessa Restrepo-Schild and Dr Javier Viñals Camallonga, personal communication) confirming that the protein is still able to respond to light after the purification.

4.3.3 nMS of AR3 Lipodisq

Ligands and lipids are poorly resolved in X-ray crystallography in part due to radiation damage. In order to help in the identification of such ligands, we propose to combine Lipodisq and native mass spectrometry, which we have shown to be able to co-extract lipids and other ligands which are in close proximity to the protein.

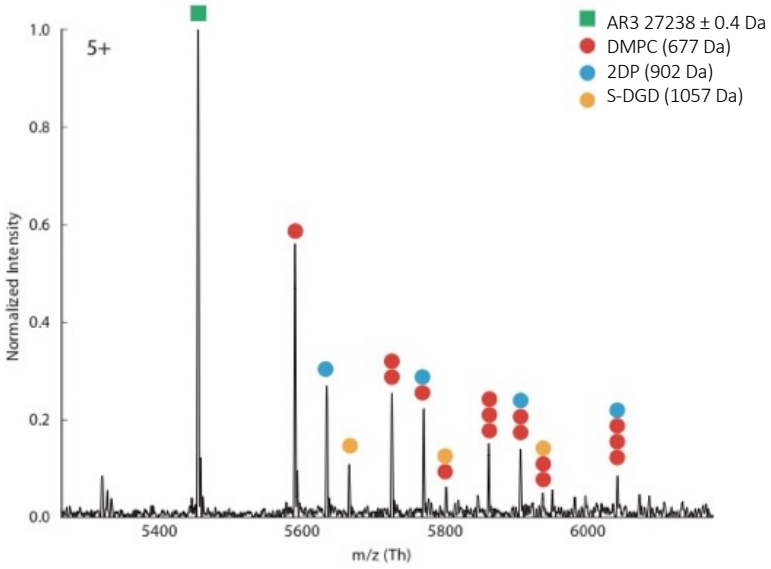


Figure 4.13: AR3 nMS spectra showing two endogenous lipid adducts, 2DP and S-DGD. The mass of the protein is 27,238 Da.

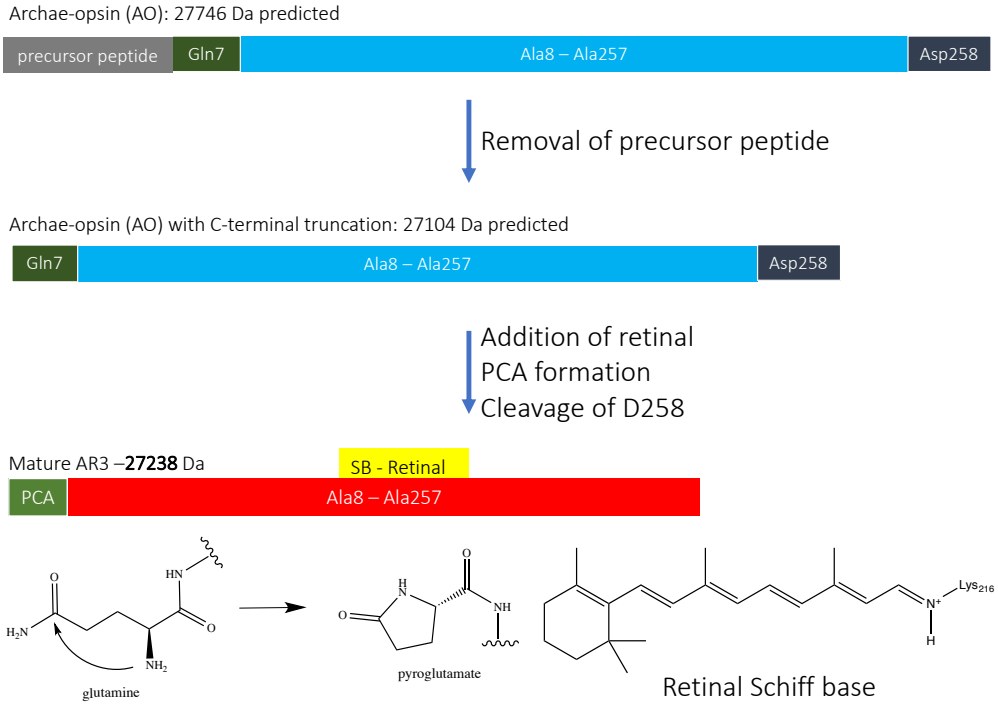


Figure 4.14: The proposed AR3 maturation pathway is presented here. First the signal peptide is removed giving rise to the archae-opsin. Afterwards, three post-translational modifications are carried out. The formation of the retinal Schiff base, the cyclization of the glutamine residue to a pyroglutamate and the cleavage of the last amino acid, Asp258. These modifications yields the same mass as in the nMS experiments 27,238 Da.

Here we have used the same methodology applied for DMPC-bR Lipodisq (Chap. 2) to DMPC-AR3 Lipodisq. The spectrum in Figure 4.13, shows that the protein mass corresponds to an AR3 protein bearing several post-translational modifications. As for bR in *H. salinarum*, the removal of the signal peptide and some post-translational modifications are performed in *H. sodomense*, since the mass reported here corresponds to a protein bearing a pyroglutamate at the N-terminus, a retinal Schiff base linked to a lysine, the removal of residue D258 at the C-terminus (Figure 4.14). Compared to bR, the signal peptide in AR3 is shorter (6 residues compared to 13 residues), giving rise to heavier protein (27.2 kDa for AR3) compared to 27.0 kDa for bR.

Moreover, two different archaeal lipids are identified in Figure 4.13. The lipid 2DP, a PGP-Me lipid, which has been already observed in our previous bR experiment and in some crystal structures, and a S-DGD lipid. Both lipids

can be found in *Halorubrum* archaeal species as demonstrated by Gonzalez and colleagues by ESI-MS [402, 403]. S-DGD lipids are involved in stabilization of the lipid bilayer during changes in osmolarity [298, 404], and some authors have speculated that they could be involved as a proton donor for bR [405]. Indeed, it has been demonstrated that the presence of these C20 (and C25) lipid chains could make the bilayer thicker and more resilient against changes in pH and salt concentration [262]. Therefore, it is not surprising to find these lipids in close contact with the protein as they are part of the claret membrane.

Unfortunately, no bacterioruberin was observed in our mass spectrometry experiments. This could be due to the short lipid chain length used in this study compared to the lipid found in the claret membrane (C20, C20 chain [403, 406]), but this is unlikely to happen as we just have observed the presence of such lipids. Another possibility is that the bacterioruberin only binds to the trimer, such as in AR2 [358], AR4 [361] and Halorhodopsin [121, 407] and would therefore not be present in our monomeric sample.

4.3.4 AR3 crystallisation from the claret membrane

The crystallization of AR3 was achieved directly from the claret membrane in the presence of MO without the use of detergent (Figure 4.15). This method has previously been used for bR, but no coordinates have been deposited in the PDB [408]. The authors claim that the diffraction of such crystals is of the same quality and space group as detergent-solubilized bR, therefore concluding that detergents are not required for the crystallisation of naturally enriched protein [408].

The claret membrane-LCP mix was prepared and spotted onto crystallization plates containing several crystallization conditions for a first screen. After several days, red crystals (size of approximately 20 μm) appeared on a few crystallization conditions, which were then optimized by varying the pH, the salt concentration and the PEG content. After several screening rounds, the best crystallization condition was obtained (see Materials and methods 4.2.9). Crystals were fished and mounted onto crystallization loops and flash-frozen in liquid nitrogen before

diffraction experiments at the I24 beamline in Diamond Light Source (UK). Crystal symmetry, unit cell parameter, orientation and resolution limit are ascertained by rotating the crystal and recording several diffraction patterns.

Afterwards, a data collection strategy was determined in order to maximize the resolution and completeness of the data set. Sometimes, one crystal could be enough for obtaining a full data set, but in our case, three different crystals were needed to obtain a full data set. The structure was solved at 1.3 Å resolution by molecular replacement, which involves the fitting of the coordinates of a homologue (in our case AR1, PDB ID: 1UAZ) to the experimental data. The structure was refined using Refmac [410] and Phenix [411]. The data collection and the structure solving were performed with Dr Isabel Moraes (National Physical Laboratory, UK) with PDB ID 6GUX.

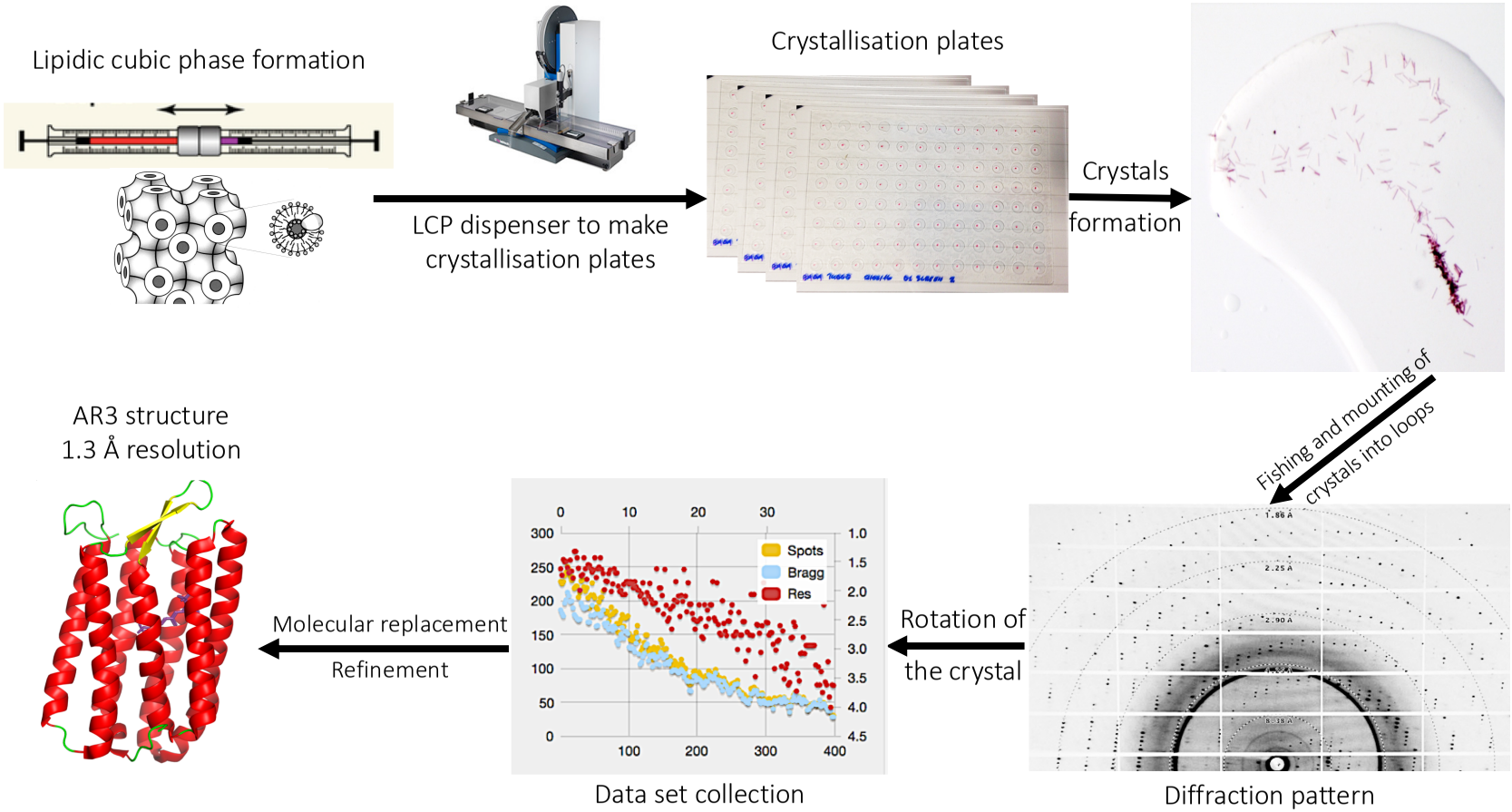
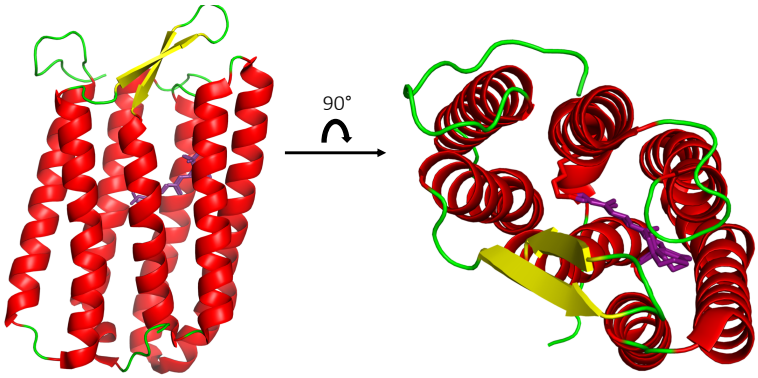


Figure 4.15: Detergent-free crystallization of AR3. LCP is formed by mixing the claret membrane with the monoolein. Crystallization plates are produced and in some of them some crystals appeared. The crystals are mounted onto crystallization loops for diffraction. Several rounds of optimization were performed until obtaining high-resolution data on different data set. Molecular replacement and refinement were performed to finally obtain the 1.3 Å resolution crystal structure. Picture from syringes and cubic phase adapted from [393, 409].

4.3.5 Crystal structure analysis

The structure of AR3 (Figure 4.16) reveals the expected 7 transmembrane helices with an extracellular two-stranded β-sheet. The N-terminus is fully resolved, unlike other microbial rhodopsins (Figure 4.16).



Data Collection	
Space group	$P2_12_12_1$
Temperature	100 K
Number of crystals	2
Cell dimensions a, b, c (Å) α, β, γ, (°)	 46.70, 47.52, 104.42 90, 90, 90
Wavelength (Å)	0.9686
$CC_{1/2}$	0.994 (0.057)
Mean *I/σ(I)*	7.0 (0.6)
Refinement	
Resolution range (Å)	43.26 - 1.3 (1.35-1.30)
Completeness (%)	96.4 (81.46)
R_{work}/R_{free} (%)	14.5/17.8
Average *B* all atoms (Å^2)	20.38
R.m.s. deviations	
Bond lengths (Å)	0.008
Bond angles (°)	1.016
Ramachandran plot	
outliers (%)	0.0
allowed (%)	1.27
favoured (%)	98.73

Figure 4.16: Crystal structure of AR3. As expected from the CD data, it is similar to bacteriorhodopsin, with 7TM and a β-sheet. The retinal is shown in purple. Statistics on data collection and refinement can be found in the table.

A pyroglutamate (PCA) instead of Gln is observed at the N-terminus (Figure 4.17), as predicted from the nMS experiment (Figure 4.13). This post-translational modification has been shown to be present in bacteriorhodopsin by denaturing MS [412, 413], but is not resolved in any previously deposited crystal structure for bR or any other archaerhodopsin protein. For bR, it is involved in protein maturation as shown in chapter 2, where the signal peptide and the last aspartate residues are removed, and the glutamate is cyclized into PCA. It has been identified to block Edman degradation in bR [412–414] and some studies in AR show the same trend [397, 415]. Its role is not clear in archaea, but it is commonly found in β-amyloid [416] and in some hormones such as neurotensin [417] or gastrin [418] and its primarily role is to stabilize and protect from aminopeptidase enzymes [419] and helps in the aggregation and formation of amyloid plaques [420].

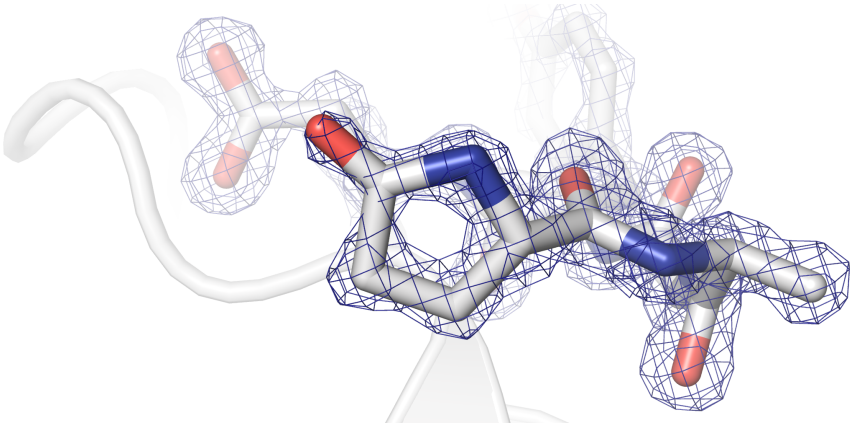


Figure 4.17: Pyroglutamate (PCA) is shown here with the electron density (contoured at $\sigma_{2F_o\text{-}Fc}$=1.5). It is the first time the PCA has been observed in a microbial rhodopsin.

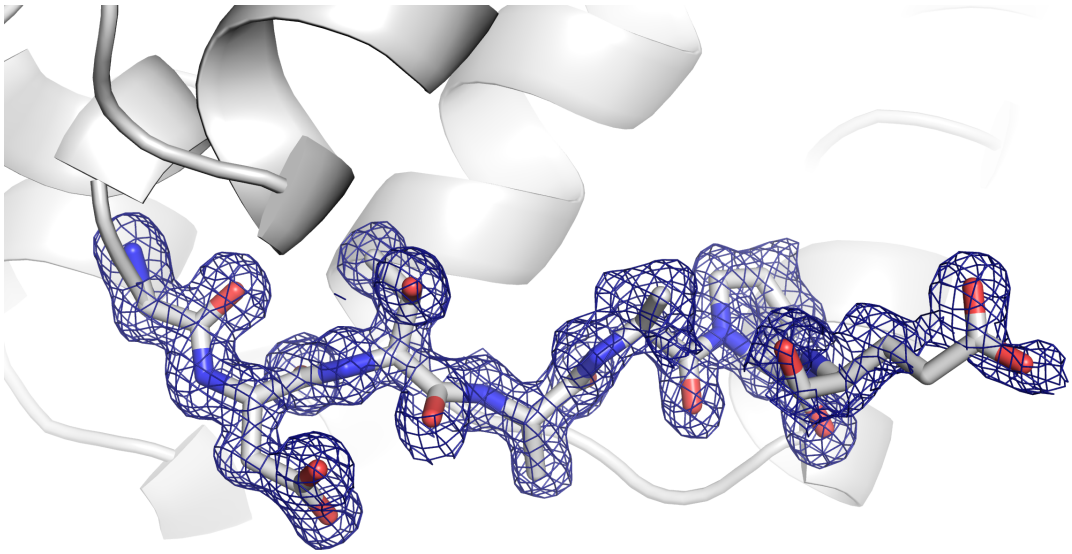


Figure 4.18: C-terminus (with electron density shown (contoured at $\sigma_{2F_o\text{-}Fc}$=1.5)) is unresolved from Glu247 and we are unable to see the deletion of D258 the last amino acid.

Unfortunately, the C-terminus is unresolved from E247 and we are unable to see the deletion of Asp258 expected from the nMS experiment (Figure 4.18).

The retinal moiety is seen in two different conformations in the AR3 structure, with a *cis*- and *trans*-retinal form in a ratio of 70:30 respectively (Figure 4.19 a-b). This ratio has been obtained only by refinement methods since no experimental data are available for AR3. Figure 4.19 c-f shows the retinal and the corresponding

difference map (Figure 4.19 (c-d) $F_{70\%cis\text{-}30\%trans}$-$F_{100\%trans}$ and Figure 4.19 (e-f) $F_{70\%cis\text{-}30\%trans}$-$F_{100\%cis}$), where some residual density can be observed, especially for the all-*trans* isomer around the Schiff base lysine and the β-ionone ring, suggesting that the second isomer (*cis*) is present and confirming that the ratio fitted for the two isomers of the retinal has been modelled correctly.

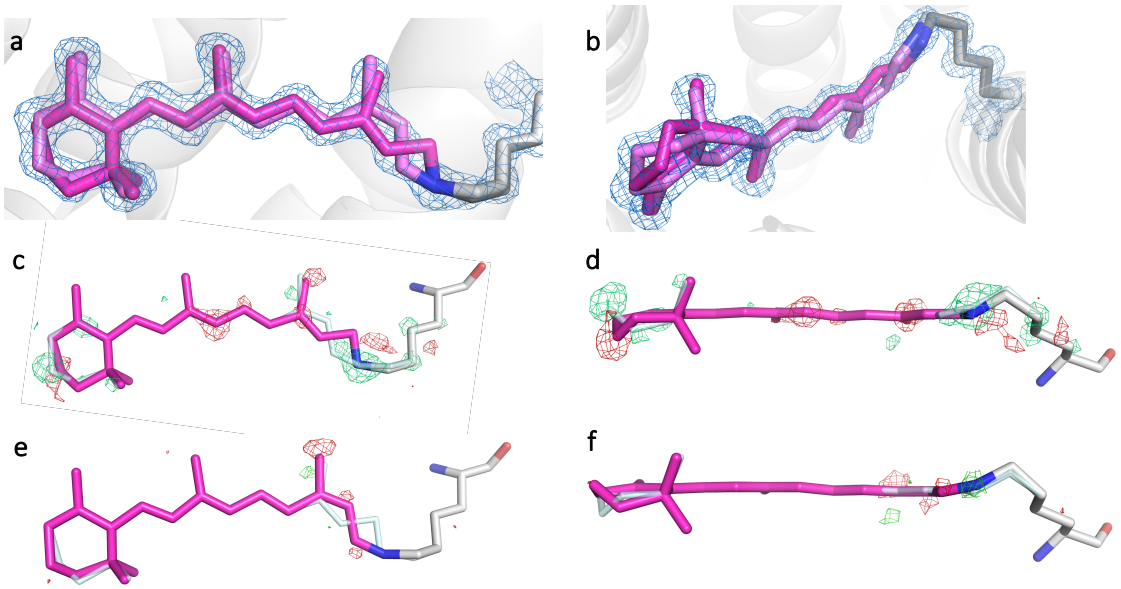


Figure 4.19: The retinal Schiff base in different isomers configuration is observed. a and b show the electron density with both conformation fitted (contoured at $\sigma_{2F_o\text{-}Fc}$=1.5) of the retinal. c and d show the difference map between the $F_{70\%cis\text{-}30\%trans}$-$F_{100\%trans}$, (contoured at σ=3) with *trans* isomer in pink and *cis* in green. e and f show the difference map between the $F_{70\%cis\text{-}30\%trans}$-$F_{100\%cis}$, (contoured at σ=3) with *cis* isomer in pink and *trans* in green. Positive and negative density are shown in green and red respectively.

The ratio observed for AR3 would suggest that the dark-adapted state has been obtained as a similar ratio is reported for bR (67:33 [421]), and that the light-adapted state shows more than 95% of all-*trans* configuration in bR and other archaerhodopsin [421]. The ratio of both *cis* and all-*trans* isomers has been suggested to change when large pressure (such as in a crystal protein) or high viscosity media are used as well by change of temperature, pH or hydration [422, 423]. Moreover, when large pressure is applied to bacteriorhodopsin, the equilibrium balance is shifted in favour of the *cis* isomer as shown in [422, 424].

No large structural changes have been observed for bR using SANS [425] and crystallography [426] for the dark-adapted state. Some differences in the internal orientation of the side-chains have been observed for some amino acids such as R82 as well as the distance between the E194 and E204 pair and the distance between the retinal and a few amino acids (D212, D85 and W86) [426, 427] (Table 4.2 and Figure A.2). The distance observed in the AR3 crystal structure for the *trans* isomer correlates well with the data obtained for bR by crystallography but minor deviations are observed for the *cis* isomer for AR3 compared to bR. It shows that the distances between the retinal and the different amino acids are bigger by 0.2 to 0.3 Å for each amino acid. It has been suggested that these side-chains are more flexible and therefore, during light-adaption, are more prone to move within the protein [426].

Table 4.2: Comparison of the distances between the retinal and a few amino acids obtained by X-ray crystallography and NMR (adapted from [426])

	bR$_{trans}$		**bR$_{cis}$**		**AR3$_{trans}$**	**AR3$_{cis}$**
	X-ray	**NMR**	**X-ray**	**NMR**	**X-ray**	
Retinal-C14-W86-N$^{\epsilon}$	3.6	3.8	4.4	4.6	3.8	4.8
Retinal-C14-D85-C$^{\gamma}$	5.8	>6.0	6.3	>6.0	5.7	6.5
Retinal-C14-D212-C$^{\gamma}$	4.6	4.4	4.9	>6.0	4.6	5.2

The pentameric arrangement of amino acid side-chains and water molecules (Figure 4.20 a-c), which is observed in ground state bR (light- and dark-adapted Figure 4.20 b and c respectively), is conserved in AR3 but with one subtle difference, being that water 401 (W401) is observed at two different positions (with different occupancy, Figure 4.20 a), slightly altering the distance between the water 406 (W406) and D85.

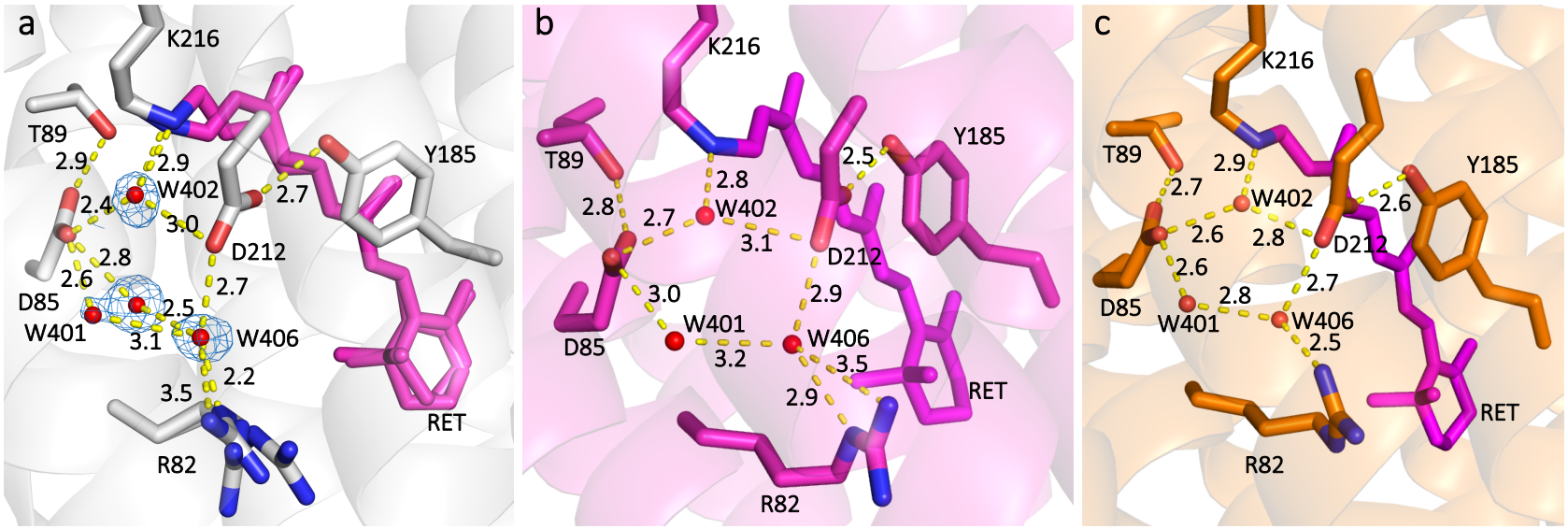


Figure 4.20: The pentameric arrangement of hydrogen bonds in AR3 (a), bR in the dark-adapted (DA) (b, PDB:1X0S) and bR light-adapted (LA) state (c, PDB:1C3W) are shown. Differences arise in the AR3 structures for the W401 which is seen in different positions (different occupancies, electron density contoured at $\sigma_{2F_o\text{-}Fc}$=1) and the distance (and orientation) of the R82 (3 conformations for AR3).

This has already been suggested from FT-IR experiments [375] that the hydrogen bonding network is weaker when compared to bR. This is confirmed in our structure as water 401 is seen in different positions at partial occupancies as shown in Figure 4.20 a), therefore destabilising this network. It has been suggested that R82 and water 406 are not interacting strongly [375] in the ground state but the distances and orientation obtained in our structure are fairly similar to the dark-adapted bR structure (Figure 4.20), whereas the orientation of the side-chain and the distances observed in our structure are different from the light-adapted bacteriorhodopsin (Figure 4.20 and 4.21).

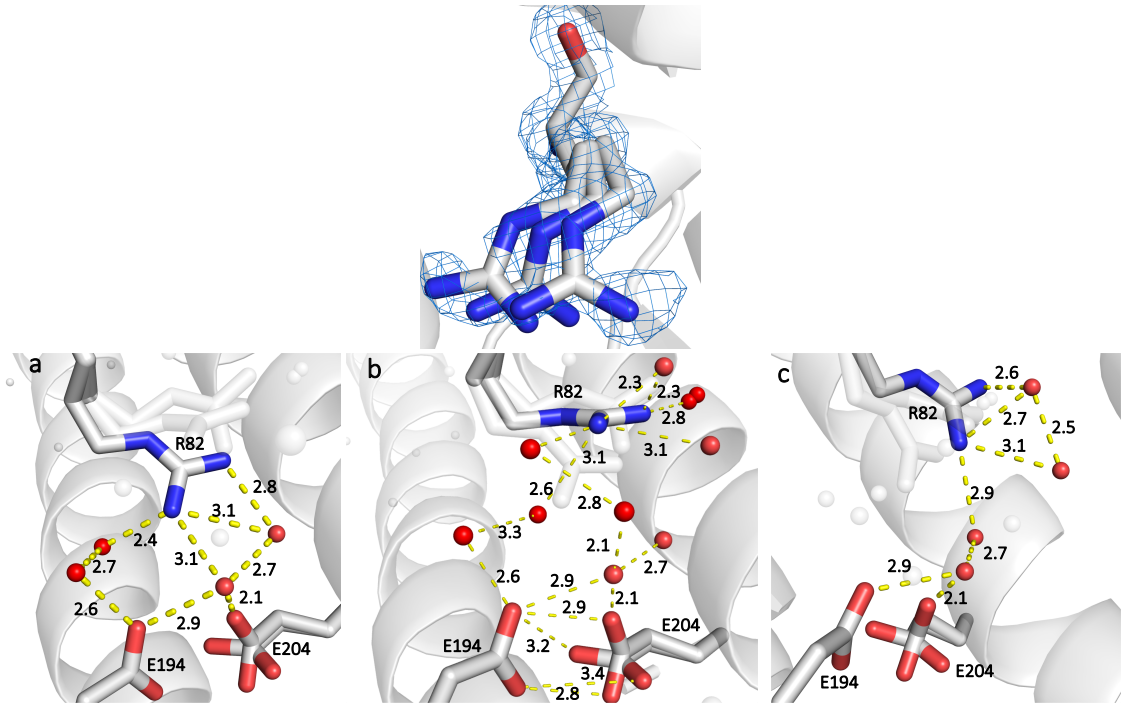


Figure 4.21: Top: R82 is seen in three different conformations and has been refined with an occupancy of 0.33 for each conformation (electron density contoured at $\sigma_{2F_o\text{-}Fc}$=1). Bottom: Extracellular side of the protein where an extensive hydrogen bonding network is observed. R82, which can be fitted in three different conformations is shown and the different hydrogen bonding network in between water molecules with each of the possible conformations of R82 are presented in panel a-c. Water molecules are coloured as red spheres, distances in Å.

Several water molecules, forming a complex hydrogen bonding network, are observed between R82, E194 and E204 on the extracellular face of AR3, which

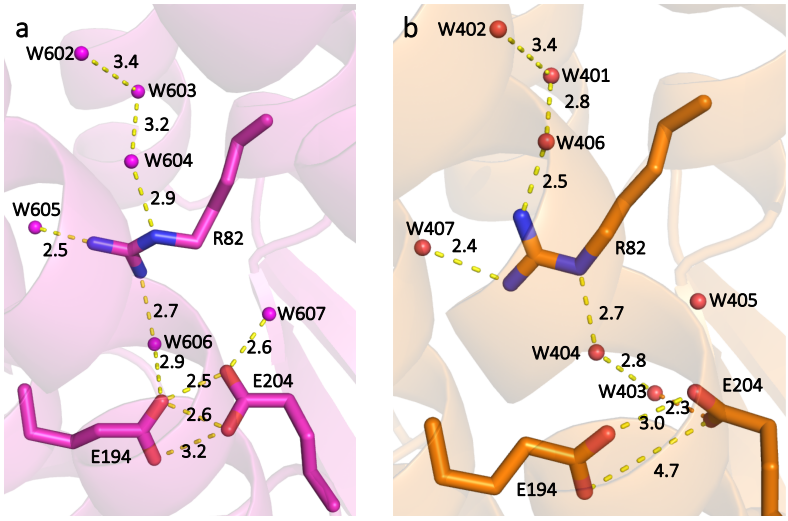


Figure 4.22: Light-(pink) and dark-adapted (orange) structure of bacteriorhodopsin, where the distance between the E194/E204 is closer in the dark state compared to the light-adapted state.

enhances the hydrogen bonding network between the residues (Figure 4.21). Also, the distance between the pair E194/E204 is closer (2-3 Å) in the dark-adapted state of bR compared to the light-adapted state (> 3 Å, Figure 4.21). Similarly to the DA state, the AR3 structure exhibits the same distance between the residues, therefore confirming that the AR3 dark-adapted structure has been obtained.

The arrangement of water molecules near the pair of E194 and E204 suggests a similar proton release mechanism as suggested from the FT-IR experiments [375]. The distribution and number of water molecules are different in AR3 compared to any other archaerhodopsin and bacteriorhodopsin structures. There are nine water molecules in the extracellular side compared to the 2-3 water molecules usually observed in other structures (Figure 4.21 and 4.22). Figure 4.21 shows the different hydrogen bonding network with each of the possible Arg82 conformation. These water molecules in the region of the E194/204 form a larger cavity compared to bR. We postulate that this extensive water molecules network could be one of the reasons for the faster photocycle observed for AR3 compared to other microbial rhodopsins.

Residues identified by Henderson [264] in the retinal-binding pocket and the proton channel are mainly conserved, the only exception being F42 which is replaced by Y42, enabling the hydrogen bond network in the proton channel to expand due to

Table 4.3: Amino acid in the retinal pocket in bacteriorhodopsin and archaerhodopsin 3

Amino acids in the retinal pocket		Grand average of hydropathicity (GRAVY) [428, 429]
Bacteriorhodopsin	WTTLMGWSTMWYPWDAK	-0.459
Archaerhodopsin 3	**VY**WTTLM**I**GWSTMWYPW**F**DAK	0.114

the addition of the hydroxyl group of the tyrosine. Indeed, the retinal pocket contains four more hydrophobic amino acids than in bR (V, Y, I and F amino acids) (Table 4.3), causing the retinal pocket to be more hydrophobic (as calculated by the grand average of hydropathicity (GRAVY) [428, 429])) as shown in Table 4.3, red-shifting the protein absorbance compared to bR, as confirmed by our UV-Vis measurement (Figure 4.11) and described in the literature for other rhodopsins [368, 430].

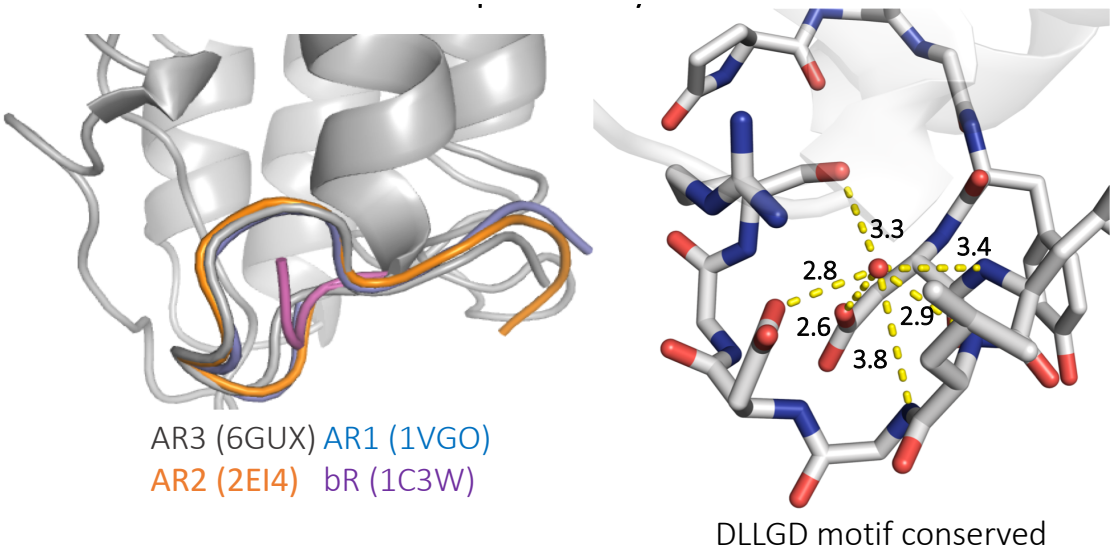


Figure 4.23: Omega loop of Archaerhodopsin proteins. The DLLGD motif is conserved in archaerhodopsins: shown here is AR3 where a water molecule appears to stabilize the conformation of the omega loop.

Unlike bR, AR proteins have an omega loop, located close to the N-terminus (Figure 4.23). This omega loop has been suggested to play a role in bacterioruberin binding, but unfortunately, the chromophore could not be fitted to the electron density in this region (Figure 4.24). Moreover, some water molecules form hydrogen bonds to maintain the omega loop as shown in Figure 4.23.

Lastly, electron density (Figure 4.25) corresponding to lipid fragments is observed in the grooves of the structures, but the chromophore could not be identified.

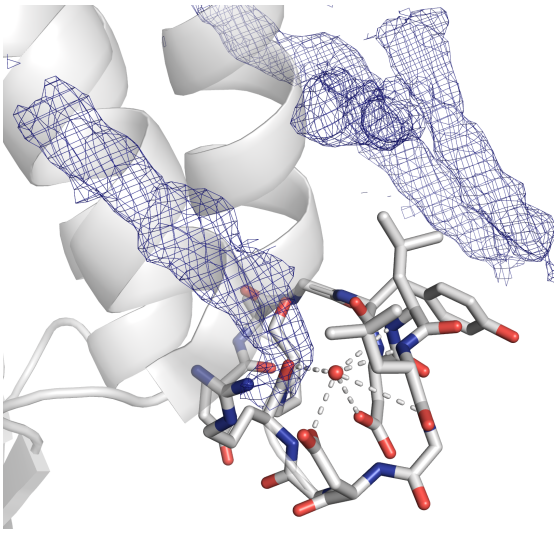


Figure 4.24: Omega loop of AR3. Some electron density (contoured at $\sigma_{2F_o\text{-}Fc}$=0.5) can be found next to the omega loop, which could be lipid or the bacterioruberin.

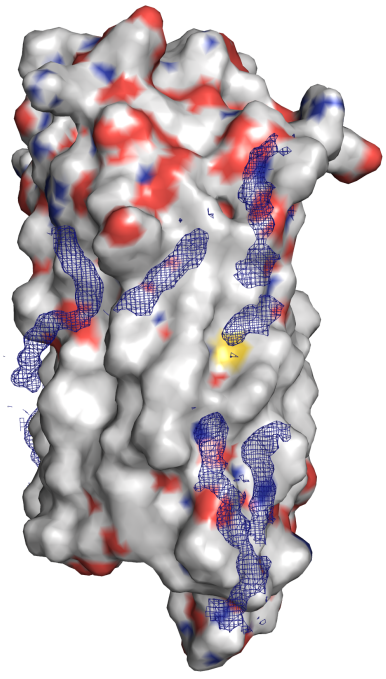


Figure 4.25: Side-view of the AR3 structure (represented in surface, coloured by elements), where some electron density (coloured in blue, contoured at $\sigma_{2F_o\text{-}Fc}$=0.5), corresponding to lipid fragments, is observed.

4.3.6 Crystallisation of AR3 from Lipodisq nanoparticles

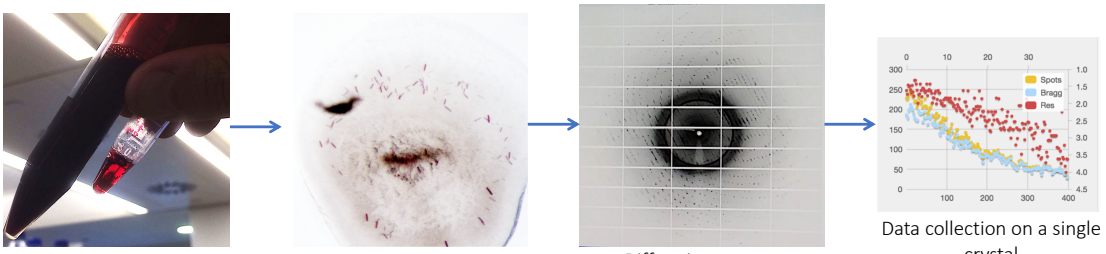


Figure 4.26: Crystallization of AR3 from AR3 DMPC Lipodisq. Crystals appear after a few days and diffract up to 1.5 Å. Several data set have been acquired.

An AR3 Lipodisq sample was prepared following the protocol established for bR-DMPC Lipodisq [285]. Here, we decided to choose POPC, as POPC has a melting temperature below 0°C and is therefore fluid at room temperature. This is to ensure that the monoolein and the Lipodisq would efficiently mix to form LCP. This is in contrast with the bR SMALPs crystal structure, which used DMPC as a scaffold lipid and for which, crystal formation takes months at 20°C. The same reconstitution ratio was used (1:172 protein to lipid ratio), but a higher temperature was used due to the more rigid packing observed for the claret membrane [361, 362, 395]. Afterwards, SMA was added at the same ratio (1:1.5 w/w lipid:SMA) and was removed by size-exclusion chromatography as performed in Chapter 2 (Figure 2.8).

The sample was concentrated (up to 10-20 mg/mL) and several crystallisation plates were prepared, one of them containing the same crystallization condition for the claret membrane. After a few days, crystals appeared. These crystals were fished and mounted into crystallization loops for diffraction. A typical diffraction pattern is shown in Figure 4.26. The crystals diffracted to 1.5 Å (slightly worse than for the claret membrane in terms of resolution) but have similar decay after rotation. Therefore, in order to obtain a full data set, several crystals were diffracted with some spots observed up to 1.4-1.5 Å. Unfortunately, at the time of this thesis, no refined

structure is available (data is being analysed) and therefore no direct comparison can be made with the structure modelled from the claret membrane diffraction data.

4.3.7 Time-resolved serial femtosecond crystallography

Motivation to pursue the study of the AR3 photocycle by TR-SFX is driven by FT-IR experiments that suggest similar structural changes than in bR, but with a different internal distribution of water molecules [375]. We have already observed some differences in the AR3 ground state compared to bR in that the pentameric arrangement and the residues in the extracellular part have a complex hydrogen bonding network. One way to directly observe the movement of these water molecules is to use time-resolved crystallography. Similar experiments with photosystem II [431–433] and bR have been carried out by Nango and colleagues [268] for the structural determination of the K, L and M state (nanosecond to millisecond timescale) (Figure 4.28) and more recently by Nogly and colleagues [269] to study the retinal isomerization on the femto- to picosecond timescales.

The crystal growth conditions used in this experiment were optimized to obtain a higher density and smaller crystals, than those used for our synchrotron experiments, which are unsuitable for this injector [434, 435]. To do so, crystals were grown in Hamilton syringes [389] and glass vials as shown in Figure 4.27. Before being loaded into the injector, crystals were illuminated for 5 minutes under a yellow light to facilitate the transition from the dark-adapted to the light-adapted state.

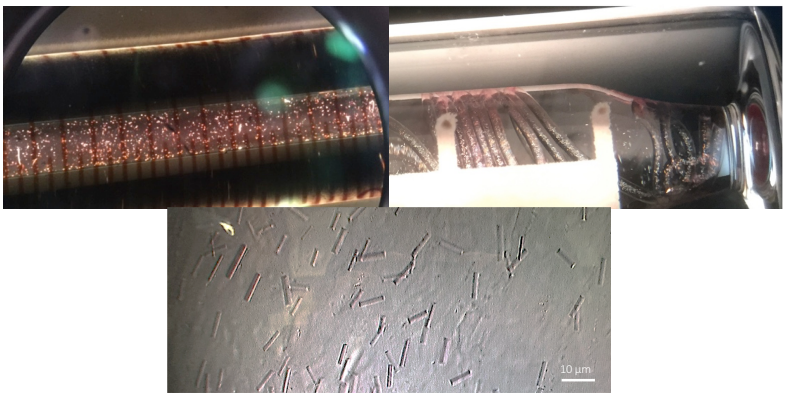


Figure 4.27: Crystals grown for the XFEL experiment in syringes and vials. Microscope picture showing the crystal shape before being loaded into the LCP-injector.

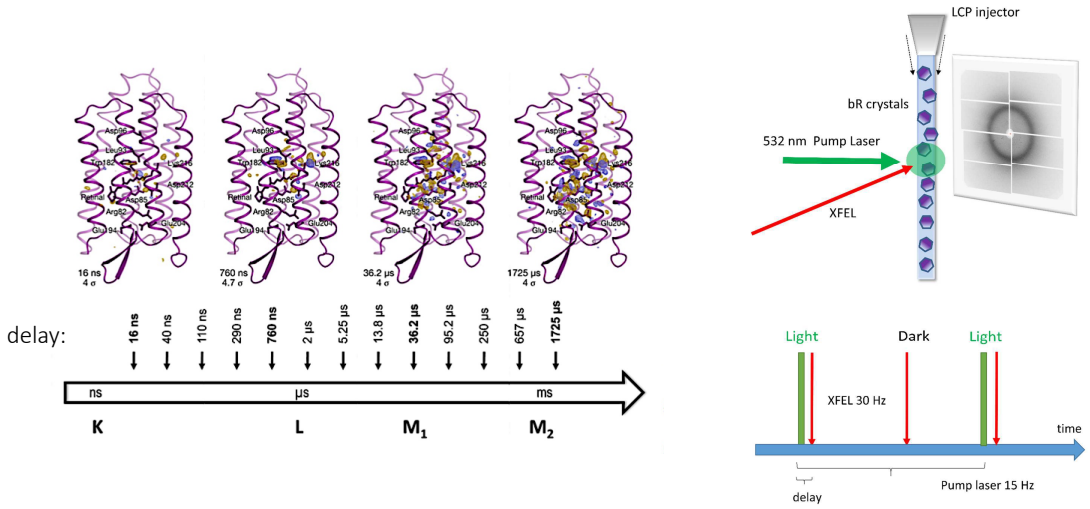


Figure 4.28: Left: The different time points collected by Nango and colleagues are shown. Right: Setup used for the XFEL experiments depicted here. Adapted from [268].

To first obtain a global picture of the photocycle, we decided to perform the same timesteps (Figure 4.28) as performed by Nango and colleagues (from 40 ns to 1.7 ms [268]). Fortunately, we have been able to use the same apparatus (Figure 4.29) as their experiment to obtain a direct comparison, by using the high-viscosity LCP injector (from the Iwata consortium) as well as the two-way excitation laser pump-probe configuration (Figure 4.29), which has two lasers to illuminate both sides of the crystal stream in order to maximize light penetration inside the lipid stream [436]. The pump probe laser wavelength was tuned to 570 nm (instead of 532 nm in [268]) due to the red-shift in the maximum absorbance observed for AR3 compared to bR.

The LCP crystals were loaded into the injector and the flow rate was adjusted with the pump-probe laser delay time. The frequency of the pump-probe laser was set at 15 Hz, while the XFEL pulse was 30 Hz, enabling collection of the ground state data (no pump-probe laser flash) in between every pump-probe laser flash (Figure 4.28). Cheetah and CrystFEL were used to monitor the hit rate, which indicates the proportion of XFEL flashes that result in a recorded diffraction pattern is recorded, the resolution and help to merge, index and scale the data collected. As before, molecular replacement was used to solve the phase problem using the AR1 structure (PDB:1UAZ).

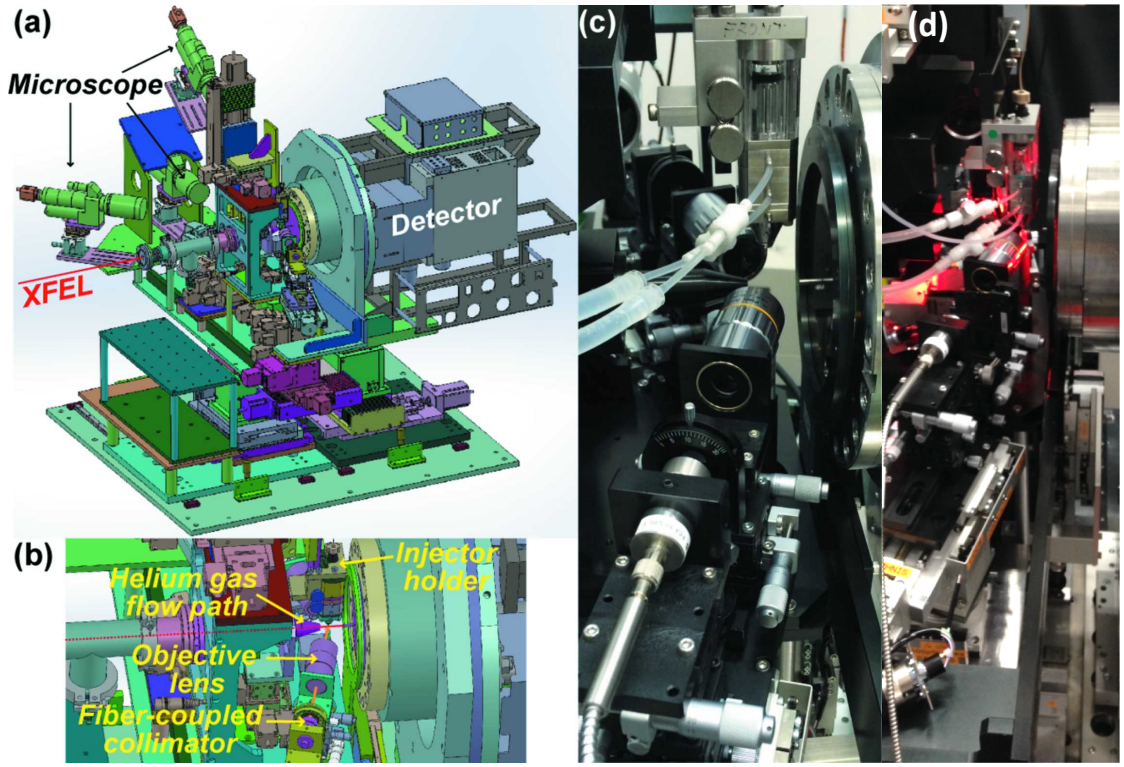


Figure 4.29: Time-resolved setup used for our experiment in SACLA. In a schematic representation in (a) and a detailed zoom around the injector is shown in (b). Two photographs are shown with the pump-probe laser off (c) and on (d). Adapted from [436].

Preliminary electron density maps were calculated for the pump-probe laser-off structure and the 5 μs delay time and the difference map between the 5 μs map and laser off is shown in Figure 4.30. A water molecule (W402) close to D85 is shown to be moving as the water occupancy changes and the D85 rotates, demonstrating that the protein is able to perform the photocycle. This has been already observed for the K and L states where the hydrogen bonding network is rearranged and water 402 as well as D85 move closer to the retinal [111, 437]. Unfortunately, no crystal structures are available yet as the data collected during the XFEL experiment are still under refinement.

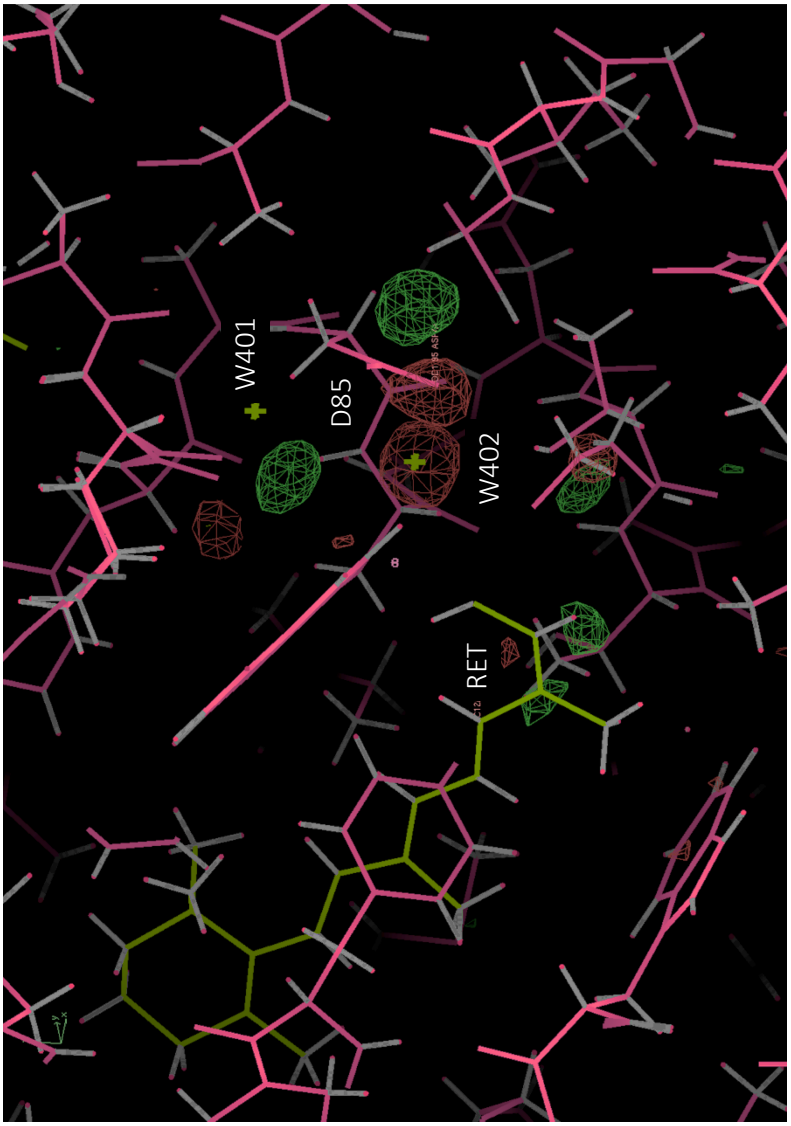


Figure 4.30: D85 and water (W402 shown in non-bonded representation) movement are observed after a delay time of 5 μs as reflected by the positive (green) and negative density (red).

4.4 Conclusions

In this chapter, we have obtained a dark-adapted high-resolution crystal structure of AR3 (Figure 4.16) expressed and purified from the native organism without detergent (Figure 4.9). The DLS (Figure 4.1) and EM data (Figure 4.10) correlates well with what it is observed in the literature for ARs, in which the claret membrane patches are smaller than the bR purple membrane patches. The UV-Vis experiment (Figure 4.11) and the environment of the retinal observed in the crystal structure explains why the absorption spectrum is red-shifted compared to the other AR proteins and bR.

The nMS experiments (Figure 4.13) correlates well with what we observe in the crystal structure as the post-translational modifications deduced from the mass spectrometry experiment (Figure 4.14) are present in the structure (Figure 4.16), with the exception of the deletion of D258 at the C-terminus which is not resolved enough to observe it (Figure 4.18). Unfortunately, the lipid fragments were not resolved in the cryo structure, but we hope to be able to assign them in the XFEL models.

More importantly, we have been able to crystallize a membrane protein from the Lipodisq within days compared to the bR SMALPs which took significantly longer, providing a new way to obtain membrane protein crystal structures in near-native environments in which possible ligands and lipids may be identified.

Concerning the structure, we have demonstrated that it is in its dark-adapted state, mainly due to the cis-trans ratio obtained, (Figure 4.19) and the distance between certain amino acids and the retinal (Table 4.2). We have also show that the pentameric arrangement (Figure 4.20) and the proton release mechanism (Figure 4.21) differ from bR (in both dark and light-adapted state due to the presence of the water 401 in two different conformations, Figure 4.22 and 4.20) and that the proton release mechanism is similar in both rhodopsins, but a larger hydrogen bonding network is observed in AR3 (Figure 4.21 and 4.22). This is consistent with the FT-IR experiments performed by Saint Clair and colleagues [375].

Lastly, we have demonstrated the capability of performing TR-SFX on AR3 crystals, and we have observed some water and amino acids residues involved in the proton translocation mechanism that move in response to light exposure (Figure 4.30). We expect to obtain a full three-dimensional movie and to be able to compare AR3 with bR, in order to understand how the protein is able to produce a higher current and perform a faster photocycle.

5

SMA as a complementary tool to study of the protein and lipid composition of the cuticle of *C. elegans*

5.1 Introduction

5.1.1 *C. elegans*

C. elegans has been a successful model organism for more than 50 years as it permits the study of both animal development and behaviour [438, 439]. It is a small transparent nematode worm from about 1 mm long with a three day life-cycle, which feeds on bacteria and is easily cultivated in the laboratory (Figure 5.1). The *C. elegans* genome was the first of a multicellular organism to be sequenced [440]. These nematodes have a fixed number of cells, nearly invariant from one to another. Their simplicity makes them a perfect model system for studies of gene expression, ageing, development and the nervous system [441].

Surprisingly, although, *C. elegans* has been studied for many years, its 'exoskeleton' [444], the cuticle, which forms a barrier between the external environment and the worm epidermis is poorly characterized. The cuticle (Figure 5.2) has an important role in *C. elegans* biology as it maintains body shape whilst permitting locomotion, nutrition and offers protection against bacterial and fungal parasites

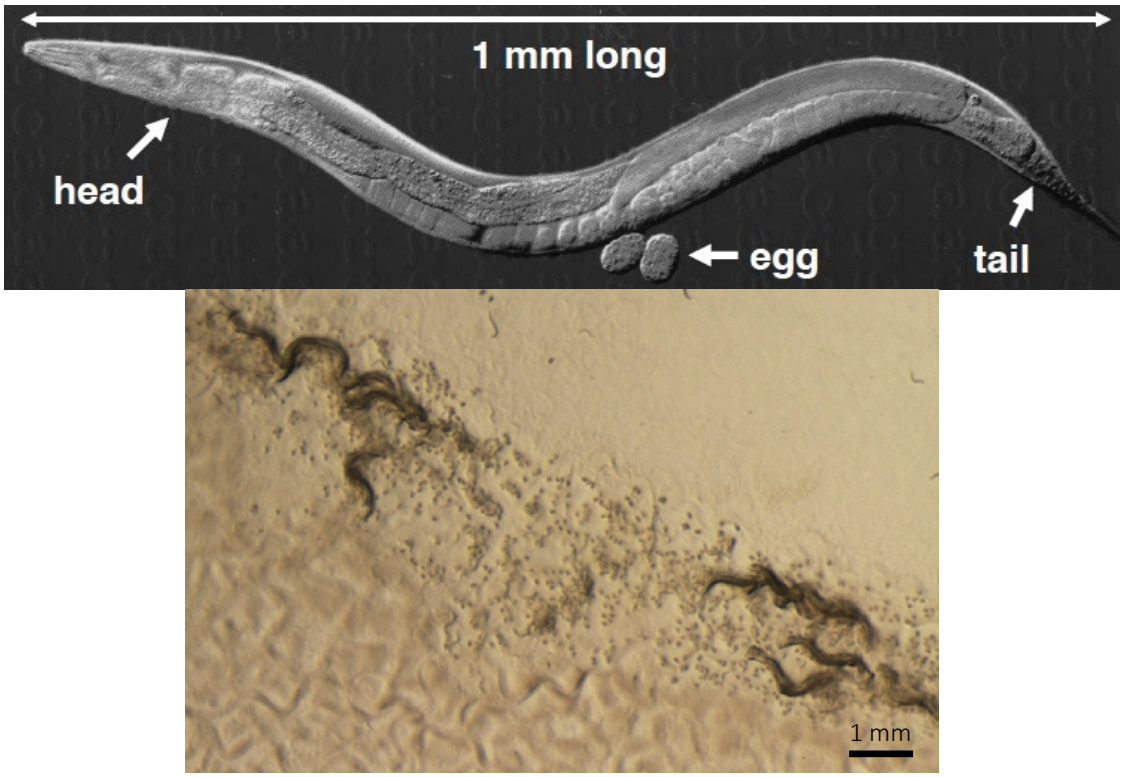


Figure 5.1: Top: *C. elegans* nematode Bottom: *C. elegans* feeding on *E. coli* on nematode growth media plates (NGM) plates. Adapted from [442, 443]

[445]. The post cuticle is secreted by the underlying epithelial cells and is regenerated entirely following molting at four larval growth stages (L1-4). It is thought that the protein and lipid composition as well as thickness changes at every larval stage and that it may vary in response to changes in its environment [441, 444].

The cuticle consists of several layers, the outermost being the surface coat, which is covered by glycoprotein and has a net negative charge at neutral pH, due to the sugar-sulphate moieties [445]. This outermost layer is likely to play an important role in the locomotion and prevention of adhesion of microbes to the nematodes surface [444]. Evidence for this role comes from the observation that *C. elegans srf* mutants have been identified, which have different surface carbohydrate epitope expression, a weakened cuticle, modified bacterial adherence and a different surface glycoprotein expression [444]. Other additional *bus* (*Bacterially UnSwollen*) mutants shows similar phenotypes and modified surface lectin binding [446].

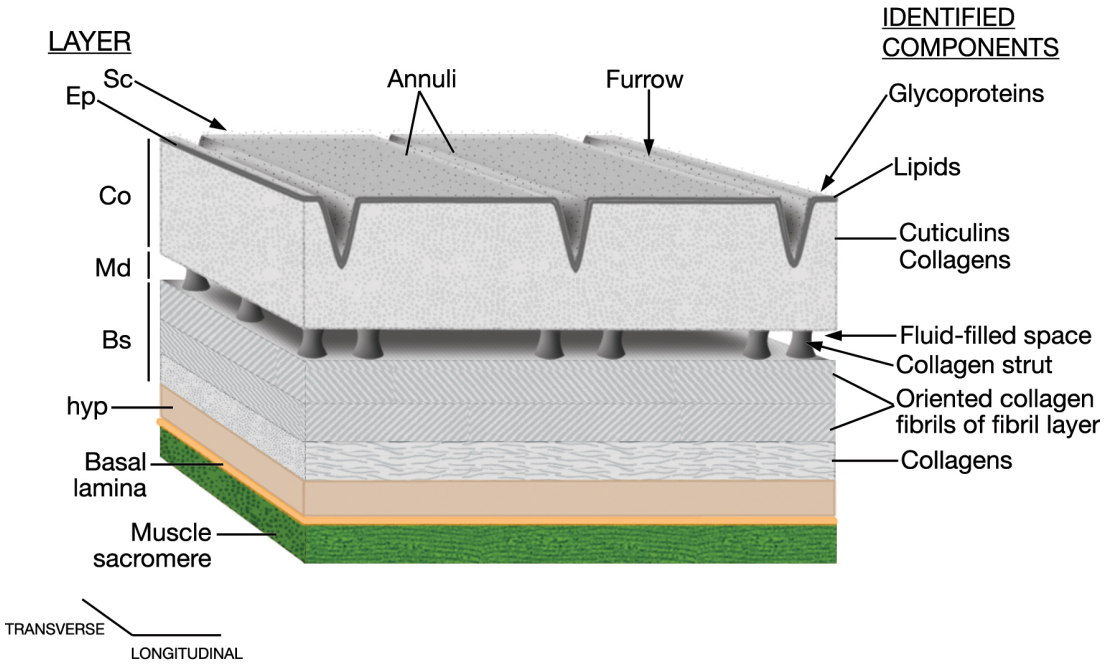


Figure 5.2: The different components of the *C. elegans* surface coat. (Sc) Surface coat; (Ep) epicuticle; (Co) cortical zone; (Md) medial zone; (Bs) basal zone. Adapted from [444]

Below the hydrophilic surface coat, lipids and glycoprotein are found in the epicuticle. Some of these lipids have been identified by TLC by Blaxter and colleagues and they include non-polar species such as steroids (particularly cholesterol), polar lipids such as PC and PE and some glycolipids, which have important role in immune response [445, 447]. With the exception of the epicuticle and the surface coat, the cuticle is predominantly made of collagen and its derivatives (cross-linked and collagen-like molecules) [448].

While the total lipidome of the *C. elegans* has been studied by biochemical, genetic and imaging techniques [449–451], characterization of the cuticle lipid and protein content has been limited [445]. Some lipid analyses have been performed on the parasitic nematodes such as *Trichinella spiralis* and speculate that the epicuticle is mainly composed of PC, PE and PG and can form an inverted cylindrical configuration [452]. It has been demonstrated from several different species of nematodes that the lipid mobility is restricted compared to a typical

plasma membrane [441, 453]. The presence of lipids in the epicuticle of other nematodes has been assessed by fluorescent probes and lipase treatment [441, 444, 451, 454] and the flexibility and resistance to chemical and physical stress of the cuticle have been attributed to the presence of some waxes and/or glycolipids (ascarosides, [454]). Lastly, proteins in the epicuticle have been shown to quickly diffuse within the membrane, which is attributed to weak ionic interactions with lipids or due to their partition into lipid domains containing neutral lipids in which they can diffuse freely [441, 453].

We wished to exploit the properties of SMA to extract the surface lipids and proteins from the wild-type and mutant strains of *C. elegans* for biochemical characterization using MALDI-TOF-MS. Our aim is to identify the surface biochemical differences underpinning the different phenotypes of the wild-type and surface mutants.

5.1.2 Matrix-Assisted Laser Desorption/Ionization time-of-flight mass spectrometry (MALDI-TOF-MS)

One ion source mainly used in proteomics is the Matrix-Assisted Laser Desorption/Ionization (MALDI) (Figure 5.3), where the protein of interest (or a mixture of proteins) is mixed with a small organic molecule (the matrix) and is then deposited on a plate where the mixture is left to evaporate to form crystals of matrix and protein [455]. Molecules such as dihydroxybenzoic acid (DHB) or dihydroxyacetophenone (DHAP) are usually used for proteins as they easily transfer or accept (depending on the mode of detection) protons permitting the ionization of the protein. The matrix is usually mixed with water for soluble proteins or acetonitrile for membrane proteins to ensure protein solubilisation before the deposition on the plate. The protein is therefore denatured in the process of deposition onto the surface. Laser pulses occur once the plate is placed under vacuum and the energy can be absorbed by the matrix and accumulated to finally induce desorption of not only the matrix, but also of the buried sample molecules/ions inside the matrix. The exact mode of generation of ions is not yet well understood and several mechanisms have been

suggested over the years [456]. After desorption and generation of multi-charged ions, radicals, and electrons, in-plume reactions can occur and by collision with each other, the final ions are generated, generally $[M+H]^+$, $[M+Na]^+$ or $[M-H]^-$, depending on the mode chosen and analysed. MALDI experiments generate mainly singly charged ions compared to other ionization techniques such as ESI, for which multiple charged species can be observed. The major drawback of the MALDI MS experiments is that the matrix can give rise to noise signals below 1000 Da which can impede the correct identification of molecules or peptides in that range [455]. Inorganic salt present in some proteins or sometimes in buffer used for protein purification can impede ionization of the protein and must be carefully removed prior to MS experiments. As the spots where proteins and matrix are deposited are larger than the beam of the laser, several laser shots must be done on different places to ensure enough protein signals to be collected. Laser wavelength or intensity, composition of the matrix mixes or the addition of an organic acid to help ionization, influence the quality and the reproducibility of the MALDI experiment.

Nowadays MALDI is used to study proteins present in tissues or whole cell extracts isolated by SDS-PAGE before sequencing using either in-source fragmentation in which the laser induces peptide bonds to break, producing peptides of different lengths or by prior incubation with protease such as trypsin or pepsin which specifically cleave the protein at amino acid residues producing specific peptides with a specific mass called peptide mass fingerprint (PMF) [457] . The protein sequence is then deduced from PMFs using bioinformatics tools such as MASCOT [458] or FindPept [459]. Post-translational modifications carried by the protein can also be identified using this technique.

The typical mass analyser used for MALDI-MS experiment is a time-of-flight instrument in which a voltage between the conductive plate and the detector is applied after irradiation by the laser. The separation of the ions is directly related to the applied electric field and the kinetic energy of the ions generated. The strong electric field applied accelerates the ions until a field-free drift range where the ions are not accelerated anymore, and they travel at a speed which is proportional

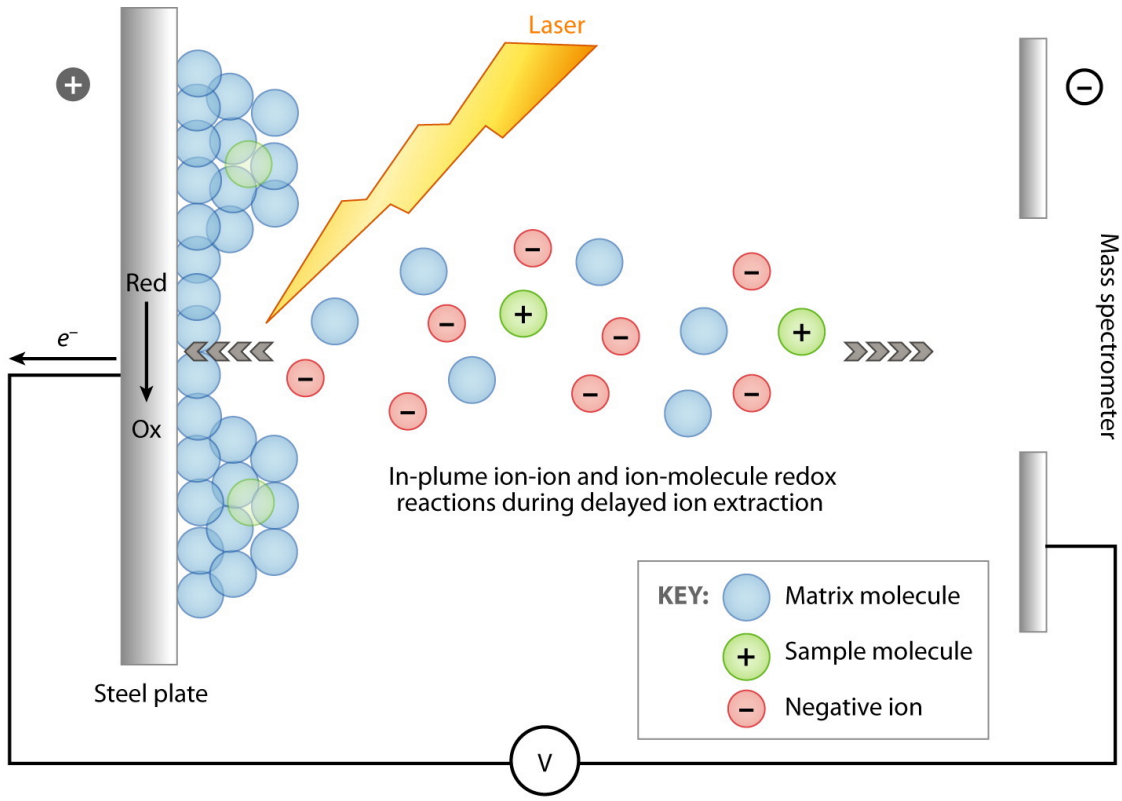


Figure 5.3: Illustration of MALDI-MS process in positive mode. Ions are formed after laser flash which ionizes proteins and matrix. Adapted from [455]

to the mass and the charge of the ions. The lighter and the more highly charged the ions, the faster they will fly (Figure 5.4).

$$E_{kin} \cdot z = \frac{mv^2}{2}$$

and

$$v = \sqrt{\frac{2 \cdot E \cdot z}{m}}$$

$$\frac{m}{z} = \frac{2E}{v^2}$$

where

$$v^2 = \frac{L^2}{t^2}$$

The time of flight is then deduced from the fact that:

$$v = \frac{L}{t}$$

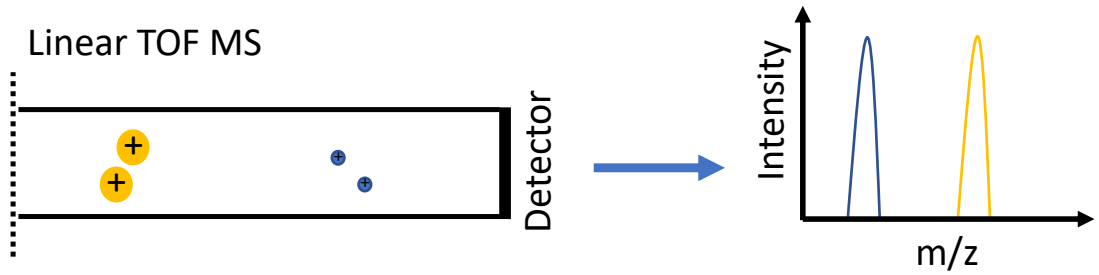


Figure 5.4: Linear TOF mass analyser. Smaller and more charged ions travel faster. Peak is broad due to the uneven energy distribution (different velocities of the same ions).

then

$$t = \frac{L}{v}$$

L being the length of the tube and t the drift time.

Two different modes of TOF can be used depending on the mass of the molecules of interest (Figure 5.4 and 5.5). The linear mode is mostly used for large molecules because the pathway is short and therefore they can still be detected with a reasonable sensitivity. The main drawback is due to the small distance towards the detector, for which ions reach the detector with only small delay, leading to low resolution (the peak broadening). The reason for peak broadening is due to the ions bearing the same charge but not the same initial velocity due to the uneven energy distribution of the laser pulse.

Resolution may be increased with reflectron mode and delayed extraction (Figure 5.5). For smaller molecules, a longer pathway allows better separation of ions, leading to better resolution, but lower sensitivity. The delayed extraction technique relies on applying an electric field after the desorption, thus accelerating the slower ions with higher potential energy. This will lead to narrower peak, as all ions with the same mass to charge ratio will arrive at the same time at the detector. One of the advantages of the reflectron mode is the ability to focus ions with the same mass to charge ratio, adjusting the energy for all ions so that they will hit together the detector. A second advantage is that the flight path

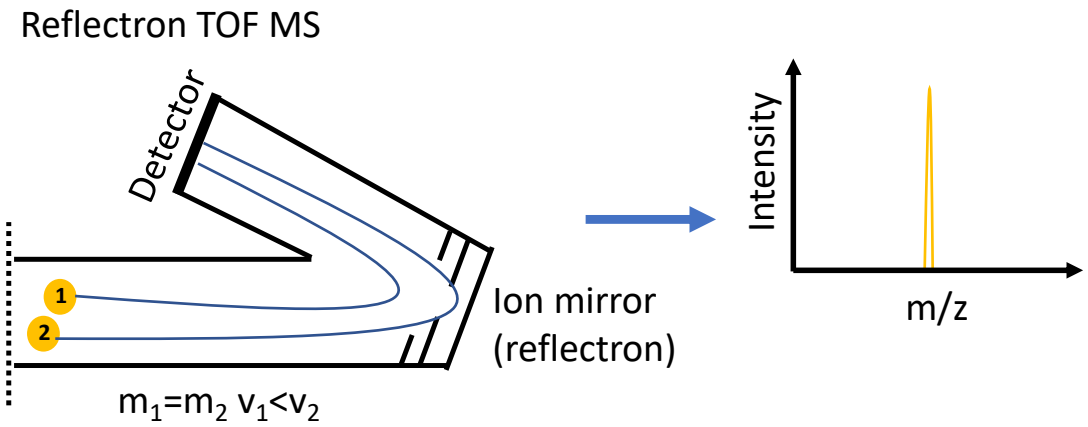


Figure 5.5: Reflectron TOF mass analyser. Ions with the same mass to charge ratio but with different potential energy are focused in the ion mirror and a narrower peak compared to linear TOF mass analyser is obtained.

is twice as long and will thus increase the distance between peaks and improve the readability of the mass spectrum.

Detection of the ions is mainly performed by a microchannel plate, which is used to detect and amplify the signal of the ions. The mechanism of detection of ions is as follows: as an ion collides within the wall of the microchannel, the emission of several electrons is triggered. This process is repeated across several layers and leads to signal amplification, as one electron can produce up to 100,000 electrons at the end of the process. This flux of electrons generates an electric current which is detected [460]. Therefore, the more ions arriving at the detector, the strongest is the current generated. In combination with the time of arrival on the detector, the mass spectrum can be generated with intensities of the peaks proportional to the current generated of the ions.

5.1.3 Aims

Here the lipid and protein composition of the cuticle was explored using the *C. elegans* N2 wild-type strain and the *agmo-1* mutant, which lacks alkylglycerol monooxygenase (AGMO), a metabolic enzyme responsible for the degradation of the ether-linked lipid species [461, 462]. Loss of the enzyme alters the sensitivity

towards bacterial pathogens and destabilizes the cuticle, by affecting the metabolic pathways responsible for lipid synthesis [462]. SMA polymer will be used as a new tool to simultaneously extract the lipid and proteins present in the nematode cuticle, which is not possible for standard organic extractions. The advantage of using SMA is its ability to extract lipids, non-selectively and to preserve protein structure and activity [195, 198, 201, 392, 463]. Previous proteomics and lipidomics experiments using SMALPs have been performed in the literature by hydrogen-deuterium exchange mass spectrometry and using LC-MS/MS [215, 464].

5.2 Materials and methods

5.2.1 *C. elegans* culture

The N2 and *agmo-1* nematodes were grown by Dr Delia O'Rourke in the laboratory of Prof. J. Hodgkin (Department of Biochemistry, University of Oxford). Worms were synchronized in order to obtain a homogeneous population prior to SMA addition.

5.2.2 Formation of Lipodisq

Synchronised populations of worms were washed off bacteria on Nematode growth media plates after a few wash with 10 mM Tris 5 mM NaCl pH 8 by three round of centrifugation (2500g, 2 minutes, 4°C). A SMA solution (25% w/v in 50 mM Tris buffer pH 8) was added to the washed worms at a final concentration of 5% v/v in 50 mM Tris buffer pH 8 and were incubated (30 minutes, 40°C). The sample was centrifuged, and the supernatant was kept for further analysis.

5.2.3 Proteomics

Proteins bands were extracted from the SDS-PAGE gels, treated with PNGase (to remove possible glycosylation) and FASP protocol was followed. Briefly, the Lipodisq samples were solubilised by 50% acetonitrile, 0.1% trifluoroacetic acid and transferred to an 10,000 MWCO Vivaspin concentrator and centrifuged (14,000g, 15 minutes) until all material has passed through. The flowthrough was discarded and 200 μL of 100 mM TEAB, 8 M urea, 10 mM TCEP pH 8 was added to the filter

and left to incubate for 30 minutes with gentle shaking. Afterwards, the filter was centrifuged (14,000g, 30 minutes) until dried and the flowthrough was discarded. A 200 μL of 100 mM TEAB, 8 M urea, 20 mM chloro-iodoacetamide buffer was added to the filter and left to incubate for 30 minutes with gentle shaking. Afterwards, the filter was centrifuged (14,000g, 30 minutes) and the flowthrough was discarded. Filter was washed with 1 M urea, 50 mM TEAB pH 8 by two centrifugation steps and the flowthrough was discarded. Trypsin was added in a ratio of 1:20 w/w (enzyme to protein) and incubated overnight at 37°C. The tube was centrifuged (14,000g, 30 minutes) and the flowtrough was kept. The membrane was washed with 0.1% trifluoroacetic acid (TFA), centrifuged (14,000g, 30 minutes) and the flowthrough was collected. The membrane was washed with 50% acetonitrile in 0.1% TFA, centrifuged (14,000g, 30 minutes) and the flowthrough was collected, pulled together with previous flowthroughs and dried under vacuum. Peptides were then ready to be analysed by mass spectrometry.

5.2.4 Lipids extraction from Lipodisq

Lipids were extracted from the Lipodisq samples according to the method of Bligh and Dyer [302]. Briefly, 200 μL Lipodisq-containing sample was mixed vigorously for 1 h, with 2 mL chloroform/methanol (2:1 v/v). Phase separation was achieved by adding 1 mL of MilliQ water. The extract was left for 10 min at room temperature and then centrifuged (1,000g,10 min) and the lower phase was retrieved washed twice with a methanol/water mix (1:1 v/v) and dried under a stream of N_2 gas.

5.2.5 Thin layer chromatography

The lipids were spotted onto a TLC silica gel (Merck). Plates were developed with a methanol/chloroform/ammonium hydroxide (65:25:4 v/v/v) solvent mixture [280]. Lipid bands were visualized by spraying the plates with molybdenum blue (Sigma) and charred at 200°C. Retention factors (R_f) were calculated.

5.2.6 Matrix assisted laser desorption ionization mass spectrometry (MALDI-MS)

Water and DHB matrix were spotted onto a MALDI plate (MTP 384 Polished Steel TF Targets) and allowed to dry at room temperature. Lipids were resuspended in chloroform/methanol mixture (2:1 v/v), deposited above the dried matrix and allowed to dry at room temperature. MALDI TOF mass spectra were acquired using a Bruker Ultraflex TOF/TOF operating in linear positive ion mode. MALDI laser intensity was selected to provide optimal intensity and resolution of acquired mass spectra. External calibration was performed using protein standards and some lipids standards, which were analysed under identical conditions. The identification of lipid was performed using LIPID MAPS online searching tools [465] and data analysis was performed using the Thermo XCalibur (ThermoFisher) processing software.

5.3 Results and discussion

Both the time of incubation and temperature were adjusted to ensure that both wild-type and mutant worms recovered after the SMA treatment as shown in Figure 5.6. The best conditions for the SMA extraction of the nematode surface was found to be a temperature of between 30°C and 40°C and an incubation time of 30 to 60 minutes. After incubation, the SMA-worm solution was pelleted, the supernatant was collected and DLS measurements were performed to verify Lipodisq formation. A viability test was performed and more than 95% of the worms survived the SMA incubation.

DLS data show that Lipodisqs were present in the supernatant (peak at 4-6 nm) and that some excess of SMA is still present in the sample (peak at 1.3 nm), especially for the N2 strain (Figure 5.7 and Table 5.1). The mutant strain did not contain any excess SMA, despite the fact that the same number of worms were used to perform this experiment. This would suggest that the cuticle from the N2 strain is more resistant to the SMA treatment than to the mutant cuticle, which is more easily disrupted by the SMA. This correlates well with the literature which suggests that the *agmo-1* mutant has a more fragile cuticle than the wild-type strain [462].

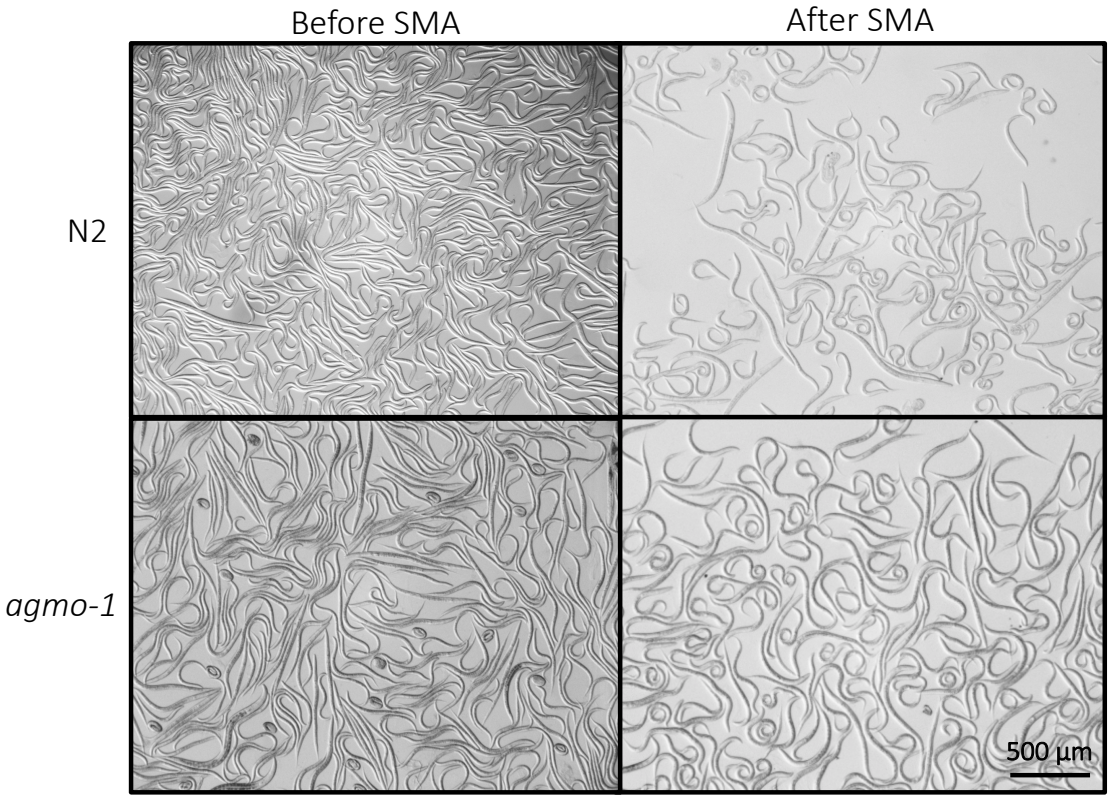


Figure 5.6: Synchronised worms before and after addition to SMA. The viability of the worms was not affected.

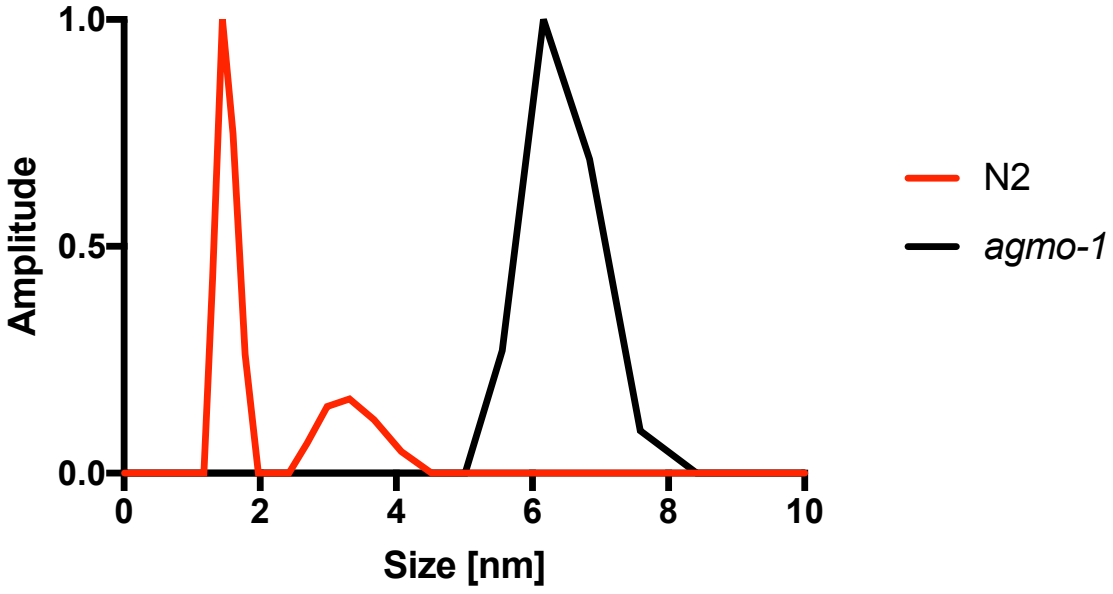


Figure 5.7: DLS data showing the different size obtained using the wild-type and mutant strain.

Table 5.1: DLS data of the Lipodisq from the wild-type and mutant strain.

DLS data radius [nm]	N2	*agmo-1*
Peak 1	1.5±0.1	6.38±0.44
Peak 2	3.3±0.4	-

The difference in sizes of Lipodisqs observed here may also indicate the presence of different proteins in the two strains, as the size of a lipid-only Lipodisq is about 2-3 nm radius and the sizes observed here are larger than the lipid-only Lipodisqs. SDS-PAGE was performed to demonstrate that some proteins have been incorporated (Figure 5.8). A low amount of protein was solubilized for N2 compared to the *agmo-1* Lipodisq sample, which appears to have a far greater diversity of proteins in its cuticle. Or as mentionned earlier, *agmo-1* mutant strain is much more fragile and susceptible to SMA, therefore proteins from lower levels of the worms surface are extracted with the SMA. A few bands (marked with * on Figure 5.8), appear to be conserved between the mutant and the wild-type strain.

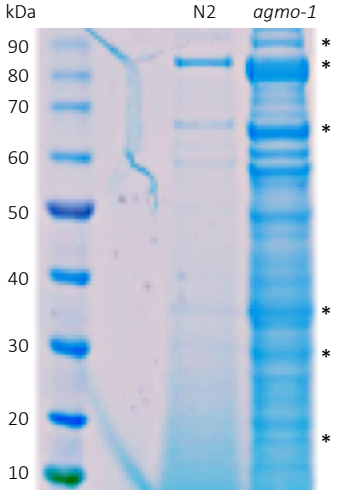


Figure 5.8: SDS-PAGE showing the different protein extracted from the *C. elegans* using SMA. A few bands have been marked with * to show conserved protein bands between the N2 and the mutant strain.

To further assess and identify the different proteins extracted, we decided to perform a proteomics analysis using the filter-aided sample preparation (FASP)

method, which requires the formation of tryptic peptides from crude lysate for LC-MS. The FASP method has been shown to be suitable with a high concentration of detergent and is suitable for the study of membrane proteins [466, 467].

Additionally, an in-gel tryptic digest of the proteins present in the gel was also performed. Lipodisq extracts from N2 and *agmo-1* worms were directly loaded onto SDS-PAGE, total proteins were stained (see method) and chopped from the gel before being digested with trypsin and then analysed by LC-MS/MS. A control experiment was performed to identify possible bacterial contamination from the OP50 *E. coli* strain used for feeding the nematodes. To do so, similar conditions for the SMA addition were performed on plates containing the *E. coli* strain without the nematodes and the supernatant was collected and analysed by the same proteomics methods.

So far, we have been able to identify more than a hundred proteins for each *C. elegans* strain and we are working on the identification of these proteins, trying to assess if any proteins isolated are unique to *agmo-1* or shared between both strains.

After the proteomics analysis, we decided to analyse the lipid composition of the Lipodisq formed from both nematodes (Figure 5.9). As the *agmo-1* mutant lacks alkylglycerol monooxygenase (AGMO), which cleaves the ether bond of alkylglycerols, we expect to observe some differences in the abundance of ether-linked lipids in the mutant strain. Lipids were extracted by following the method of Bligh and Dyer [302] and were analysed by thin layer chromatography (TLC), as performed in the literature for the lipidomics analysis in SMALPs [213, 215].

Lipids headgroups were identified by their retention factor values (Table 5.2). Present in both the mutant and the wild-type worm were ceramides (CE), cerebrosides (Cb) and lyso-phosphatidylcholine (LPC). For the N2 strain, lipids such as phosphoethanolamine (PE), lyso-phosphatydilglycerol (LPG), sphingosine/sphingomyelin (SM) and lyso-phosphatydilserine (LPS) were found, whereas in the mutant *agmo-1*, PMME, cardiolipin (CL) and PG were found. Also, some lipid species are not able to migrate in the chosen solvent mixture, and this might indicate the presence of highly charged species as speculated by Blaxter and colleagues [445]. Some of

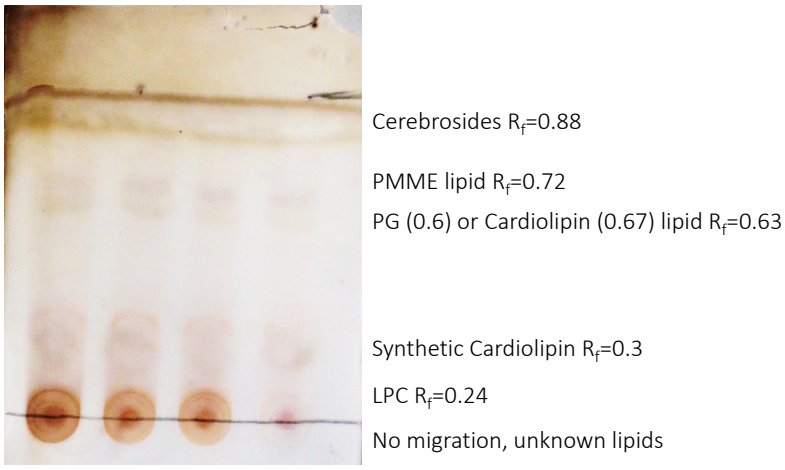


Figure 5.9: Thin layer chromatography experiments. The *agmo-1* lipid extraction is shown here where different concentration of lipids were spotted on the plate.

Table 5.2: The different lipids identified (with their retention factors in brackets) by TLC and compared to the literature. ND, unidentified lipids.

N2	***agmo-1***	**N2 from Blaxter[445]**
PE (0.79)	PMME (0.71)	PI (0.09)
LPG (0.54)	CL (0.67)	ND (0.24)
SM (0.28)	PG (0.6)	PC (0.38)
LPS (0.18)	-	PE (0.5)
CE (1)		ND (0.61)
Cb (0.94)		Sterol (0.9)
LPG (0.22)		ND (1)

the lipids found in the Lipodisq extraction were also identified by Blaxter and colleagues, such as PE and ceramides, but in comparison no PC or PI can be found in our TLC data (Table 5.2). Some retention factors present in the Blaxter paper are similar to our TLC data and can be identified using the lipid table found on the Avanti website [280], as the solvent system used is similar to the one performed for the Lipodisq experiment. Therefore, the R_f=0.24 could be some LPC lipids and the R_f=0.61, could be some PG lipids. All of the lipids identified by the TLC analysis are lipid species expected from genetic studies on *C. elegans* as revealed by Witing and colleagues [451].

Unfortunately, the TLC experiments are not able to distinguish between ester-

and ether-linked lipids with the same headgroup. Therefore, MALDI-TOF MS was used to identify some of the lipid present in both strains. As some of these lipids have a mass below 1 kDa, we decided to calibrate the instrument with the standard low molecular weight protein standard in addition to lipids such as DMPC, POPC, DOPC and POPG, to ensure that the mass measured by MALDI would be as accurate as possible. Moreover, as the 500 Da to 1000 Da mass range is difficult to study due to the noise peaks produced by the matrix, a control experiment including the recording of mass spectra of matrix-only spots was performed. The peaks of this matrix-only experiment were subtracted from the Lipodisq sample experiments. Another control was performed which includes the removal of the peaks coming the OP50 bacterial source lipids extracted using SMA. As for the matrix-only peaks, they were removed from the mass spectra of N2 and *agmo-1*. The mass spectra for the N2 and *agmo-1* after removal of both the matrix and OP50 lipids peaks are shown in Figure 5.10.

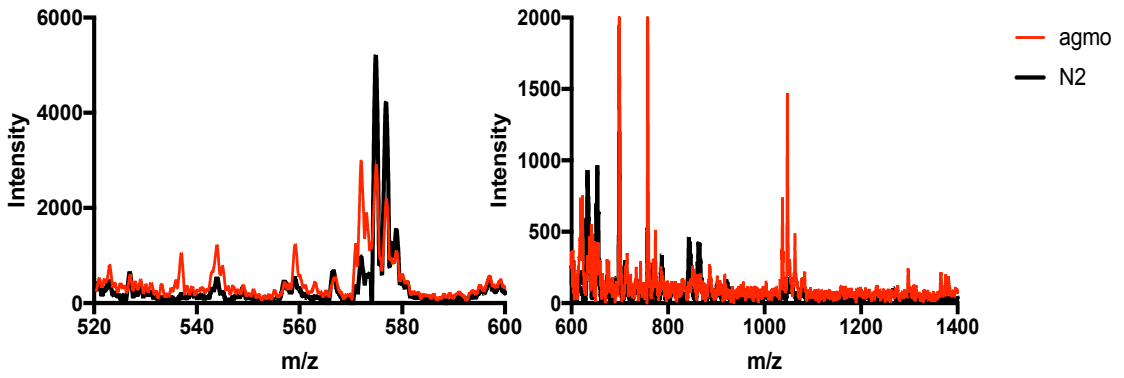


Figure 5.10: MALDI-MS spectra at different range exhibiting different peaks.In red the *agmo-1* mutant and in dark the wild-type. Some differences are observed especially in the 600-1200 m/z region.

Lipid peaks were determined with an intensity above 500 (signal-to-noise ratio > 2) and peaks were assigned. Identification of lipid was performed using the LipidMAPS website [465] with a mass tolerance of $\pm$ 0.1 m/z. All peaks were considered as possible ion adducts with potassium, sodium, with a possible loss of water and singly and doubly charged, as MALDI primarily generates sodium

and potassium adducts of singly or doubly charged species [455]. The results are presented in Table 5.3.

Some lipid species (in green in Table 5.3) are observed in both the N2 and *agmo-1* samples, including PA, sulfoquinovosyldiacylglycerol (SQDG), mannosyl-PI-ceramide (MIPC) and lyso-phosphatidylinositol-monophosphate (LPIP). The presence of SQDG and ceramide-type lipids is consistent with our TLC experiment (Figure 5.9 and Table 5.2) and the literature, especially for the sulfonated lipids, which are responsible for the negative charge on the cuticle. In addition to these lipids, the N2 strain has some additional lipid types such as PC, PE or PS, which could not be discriminated by mass. From the TLC experiment and the literature, PC and PE are both possible candidates and fragmentation of the lipid was attempted for its identification, but due to its low intensity, no fragmentation peaks were observed. The literature suggest that sulfatides, PE and PI have the lowest detectability threshold [468]. Therefore, their identification, in this experiment may mean that the sample contains high amount of these lipids, which is not surprising as PI and sulfatides lipids have been suggested to regulate the cuticle surface charge [445].

Compared to the wild-type strain, more lipids were observed and identified for the *agmo-1*mutant, as seen by the TLC (Figure 5.9 and Table 5.2). The lipids highlighted (in red Table 5.3) are ether-linked lipid species, which have been speculated to accumulate at the cuticle surface due to the lack of the AGMO enzyme. Taken together, these results show that there is an accumulation of some ether-linked lipids at the cuticle surface of the mutant, which may prevent bacterial adherence by masking binding targets on the worm surface. This is also in agreement with the experimental observation that the *agmo-1* nematodes float on aqueous buffer (unlike the wild-type worms) since the presence of some ether-linked lipids and waxes could affect buoyancy [469]. The accumulation of other lipid species could be due to a compensation mechanism, which would involve the upregulation of other lipases to compensate for the lack of ether-linked cleavage, which would explain the heterogeneous lipid composition found in the mutant.

Table 5.3: The different lipids identified in SMA extracts using the LipidMAPS website [465]. In red the lipids which have been identified as ether-linked lipids and in green lipids which are shared between the wild-type and mutant strain.

Mass (Da)	*agmo-1*	N2	OP50
1539.587	TG	-	-
1411.581	-	-	Present
1389.593	-	-	Present
1385.993	DGDG	-	-
1369.024	PIP	-	-
1366.886	CL	-	-
1338.589	-	-	Present
1290.895	PI	-	-
1279.758	PIP	-	-
1277.554	$M(IP)_2C$	-	-
1165.738	SQDG	-	-
1158.823	PE	-	-
1148.848	SQDG	-	-
1141.55	$M(IP)_2C$	-	-
1134.746	PS	-	-
1120.828	PS	-	-
1112.506	-	-	Present
1107.787	PS	-	-
1106.841	LacCer or PC	-	-
1090.528	-	-	Present
1087.602	MIPC	-	-
1061.485	-	-	Present
1039.509	-	-	Present
1006.738	DGDG	-	-
996.704	-	PS or PE or PC	-
947.71	PG (P)	-	-
946.785	TG	-	-
888.844	DG or TG(O) or TG(P)	-	-
850.358	PIP	-	-
837.42	SQDG	-	-
824.388	LPIP	-	-
811.422	LPIP		-
760.465	ShexCer	-	-
760.332	MIPC		-
751.324	PS	-	-
741.407	-	-	Present
703.549	PE (O) OR PE (P)	-	-
699.037	-	-	Present
698.689	CE OR WE	-	-
659.284	-	-	Present
655.376	PA		-
653.3	SQDG		-
647.558	-	-	Present
637.291	-	-	Present
619.525	-	-	Present

Table 5.4: Abbreviations used for the lipids

Glycerophosphocholines	PC (LPC for lyso species)
Glycerophosphoethanolamines	PE (LPE for lyso species)
Glycerophosphoserines	PS (LPS for lyso species)
Glycerophosphoglycerols	PG (LPG for lyso species)
Glycerophosphates	PA (LPA for lyso species)
Glycerophosphoinositols	PI (LPI for lyso species)
Glycerophosphoglycerophosphoglycerols (Cardiolipins)	CL
Monoradylglycerolipids	MG
Diradylglycerolipids	DG
Triradylglycerolipids	TG
Digalactosyldiacylgylcerols	DGDG
Sulfoquinovosyldiacylglycerols	SQDG
Ceramides/Sphingoid bases	Cer/Sph
Hexosyl ceramides	HexCer
Mannosyl-PI-ceramides	MIPC
Mannosyl-di-PI-ceramides	$M(IP)_2C$
Lactosyl ceramides	LacCer
Sulfatides	SHexCer
Wax esters	WE
Cholesteryl esters	CE
Fatty acids	FA
Lyso-phosphatidylinositol-monophosphate	LPIP

5.4 Conclusions

We have demonstrated that SMA may be used as an effective tool to study the proteome (Figure 5.8) and the lipidome (Figure 5.9) of the *C. elegans* cuticle. We have shown that SMA can be used on living organisms without affecting their viability compared to harsh lipid extraction using organic mixture (Figure 5.6).

Here we have performed a concise analysis to demonstrate that some ether lipids are present (Table 5.3) in the cuticle of the mutant worm lacking the specific enzyme to cleave ether bonds in alkylglycerol. The presence of additional ether-linked lipids on the *agmo-1* mutant nematode surface changes the interaction with surface adherent bacteria [462] compared to the wild-type N2 worm and makes the cuticle of *agmo-1* more fragile [462]. The increased fragility is supported here as more lipids and proteins have been solubilized from *agmo-1* compared to the wild-type N2 worms using SMA (Table 5.2 and 5.3). Moreover, we have observed some negatively

charged lipids (SQDG, PA, PS, PG), which are involved in maintaining the surface charge as suggested by Blaxter and Witting [445, 451].

Additionally, a standard protocol for lipid MALDI-MS has been performed as suggested by Fuchs and colleagues [468]. We expect to try other matrices and additives such as lithium salts or TFA, which could help in the identification of the different other lipid component of the *C. elegans* cuticle. Also, a more thorough analysis would require the use of other mass spectrometry techniques such as LC-MS/MS as similarly performed in the literature [215]. The use of such MS techniques would help in a more accurate identification of the lipids present as some lipid species may not been have observed and identified due to their low intensity in the MALDI experiment.

Similarly, the protein composition appears to be altered at the surface of the worm between the two strains (Figure 5.8). We anticipate that the protein composition differs due to the lack of the AGMO enzyme and to be compensated by the presence of other proteins, especially by lipases. It would be interesting to observe what types of protein can be identified and their origin in the nematode, as this will ascertain that the SMA is actually only acting on the cuticle and not from other organs of the nematode.

6

Lipodisq nanoparticles as a new drug delivery platform

6.1 Introduction

The hydrophobicity of novel therapeutic compounds is a major problem for drug development. Strategies to increase solubility and bioavailability of drugs include increasing hydrophilicity by chemical modification (e.g. fluorination), addition of bulky molecules such as PEG to increase the half-time of the molecule in the body or the development of prodrugs [470]. Unfortunately, chemical modifications of the active compound generally decrease effectiveness. In order to maintain their efficacy, delivery systems have been developed [471] including nanoparticles (e.g. quantum dots, ferromagnetic complexes [472] or dendrimers [473]), liposome-based formulations (e.g. Doxil) [474], carbon nanotubes (CNT) [475] and drug conjugates (e.g. PEG-drug derivatives). The drawbacks of these delivery systems are their large size (diameter larger than 50 nm for a quantum dots for example), their stability in the body [476], their unknown long-term toxicity (e.g. detoxification of quantum dots once in the body) and their poor Enhanced Permeability and Retention (EPR) effect [471].

Lipid-based drug delivery systems are of interest since lipids can be easily metabolized in the body and they provide a unique amphipathic environment with

the ability to carry non-polar molecules in aqueous solutions (both inside and outside of cells). Liposomes, micelles or nanodiscs can be used to achieve the delivery of hydrophobic drug molecules to the target tissue [476]. Doxil (used for cancer therapy) [474], Marqibo (liposomes containing Vincristine, another anti-cancer drug) [477] or Epaxal (used as vaccine for Hepatitis C)[478] are examples of liposomal drug formulations that are currently commercially available. The large size ($>$ 50 nm diameter) of lipid-based delivery systems hinders penetration of the drug into cells and their stability in the body may be low [476] (e.g. phospholipids are rapidly degraded by enzymes [479]).

It is also important for drugs to be delivered to a specific organ or tumour. Therefore, drug release from lipid-based delivery systems can be stimulated by changes in temperature [480], pH [481] or UV light exposition [482] near the target site. The thermo-controlled release is an interesting technique as by applying localised heat the drug will be released specifically at the tumour site and not in other parts of the body [483]. Introducing photoswitchable lipids (e.g. cyanine-type dyes) in order to trigger a change in morphology once illuminated with an UV lamp [484] or using pH-sensitive compounds, using the fact that the internal environment of cancer cells is more acidic than that of healthy cells [485], have also been be able to show a drug release because of change in shape or size of the carrier.

6.1.1 Doxorubicin as a model drug for lipid-based drug-delivery

Doxorubicin belongs to the anthracyclin family and was first used as an antibiotic (Figure 6.1). Farmitalia first discovered daunorubicin, a similar molecule, in the 1950s, extracted from *Streptomyces* bacteria, which has shown to be active against mouse tumors [486]. Doxorubicin, which was discovered later, was shown to be active against a broad spectrum of tumors including multiple myeloma, some types of leukaemia, ovarian, pancreatic, prostate or cervical cancers [487]. So far, several hypotheses have emerged about the mechanism of action of doxorubicin, the most relevant being the intercalation of doxorubicin between DNA base pairs,

inhibiting the actions of topoisomerase II and therefore blocking the process of DNA replication, leading to cell death [488] (Figure 6.1). Due to its highly conjugated aromatic ring system, doxorubicin has low solubility in water (LogP=1.27 [489]), rendering its administration to patients difficult.

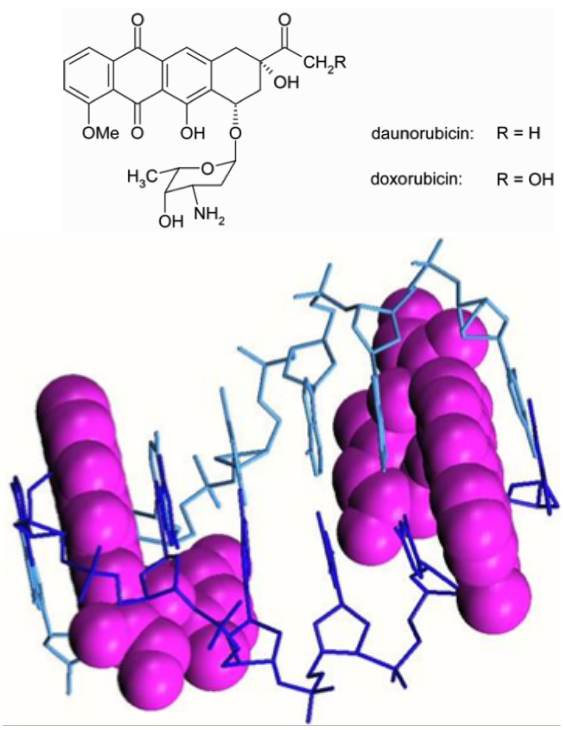


Figure 6.1: Top: chemical structure of the doxorubicin molecule. Bottom: doxorubicin (in pink) intercalates into DNA (blue) and thus stops the process of replication (reproduced from[490]).

Several side effects are observed in patients treated with doxorubicin, such as nausea, skin irritation or fever but the most dramatic one being heart failure (cardiomyopathy) [487]. Reduction of the side effects and a decrease in the toxicity to non-cancerous cells are key goals and some alternative formulations of doxorubicin have been developed. Doxil (Caelyx) [474], a liposomal formulation of doxorubicin, is now used clinically for the treatment of different types of cancer due to its lower cardiotoxicity (Figure 6.2).

Lipid-based formulations offer a protective environment against the degradation of the drug, increases its lifetime in the body and delays its release into cells. Non-SMA-based Lipodisqs have been already used as for the delivery of inhibitors

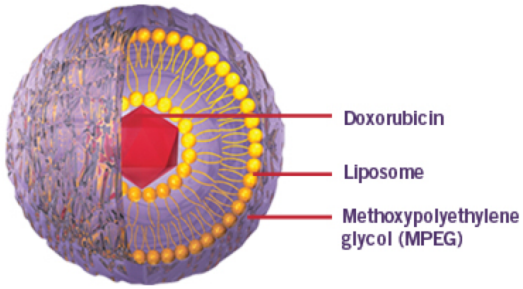


Figure 6.2: Doxil, a liposomal formulation of doxorubicin, which is now used clinically for the treatment of different types of cancer [474] (reproduced from [491]).

of cannabinoid receptors (CB_2), for different nonsteroidal anti-inflammatory drugs (NSAIDs) and for a skin-toning agent that is commercially available in Singapore, Japan and Vietnam for example [492].

Previous work has demonstrated that Lipodisqs can enter cells by phagocytosis, are non-cytotoxic when not loaded with drugs, and can kill cancer cells when loaded with doxorubicin and that the half maximal inhibitory concentration (IC_{50}) of doxorubicin in Lipodisqs (930 nM) is lower than the drug in solution (2.05 μM) and in liposomal formulation (Doxil, 7.2 μM-258 μM) [493]. Lipodisqs may provide a delivery system which maintains anti-tumour efficacy at a lower administered dose of doxorubicin, minimising the undesirable side effects (principally the cardiotoxicity).

6.1.2 Aims

The aim of this chapter is to show that SMA-Lipodisq nanoparticles can also be used as a novel drug delivery carrier. Here we propose to evaluate the potential of using the Lipodisq, loaded with doxorubicin, a powerful chemotherapy drug, as a new nanovehicle for drug delivery.

The identification of the location of doxorubicin in Lipodisqs has been studied (located in the region of the lipid headgroup) [494], but the mechanism of enhancing bioavailability remains unclear. Here we will conjugate a dye to the polymer and use some lipid-dye conjugate to estimate the location of the doxorubicin and compared it with the previous data obtained and study the biodistribution of the SMA, the drug and the lipids once administered to animal models.

6.2 Materials and methods

6.2.1 Drug incorporation to Lipodisq

Lipid (as a dry powder) and doxorubicin were mixed in a chloroform/methanol solution and evaporated under a N_2 stream and the resulting lipid film was allowed to dry under vacuum overnight in a desiccator. The film was rehydrated using 50 mM PBS and the solution was sonicated for 5 min. Afterwards, 5-10 freeze thaw cycles (in liquid nitrogen and water bath at 42°C) were applied. Extrusion was performed using a Mini-Extruder (Avanti) and two 1000 μL syringes. The solution was extruded first using a 0.4 μm filter and then a 0.1 μm filter (Whatman) at a temperature always 5° higher than the phase transition temperature of the lipid when hydrated. Between ten to twenty passages of the mixture through each type of filter were necessary to obtain a clear red suspension. Finally, SMA polymer was added in a 1:1.25 w/w lipid-to-SMA ratio. The mixture was then vortexed for a few seconds and maintained at 42°C for 1 hour. The sample was then centrifuged (14,000g, 5 min, RT) and the supernatant was kept for further characterization.

6.2.2 Synthesis of SMA-SH

SMAnh polymer was conjugated to cysteamine using a method adapted from [202]. Starting from 1 g of styrene maleic anhydride (SMAnh, 3:1 ratio), cysteamine (15 mg) was added and mixed in DMF. A volume of 700 μL of trimethylamine was added and the mixture stirred (30 min, RT). SMAnh-SH was precipitated by addition of approximately 30 mL of 1 M of acetic acid and the pellet was recovered after centrifugation (4000g, 5-10 min, RT). Several washes with water (between 5 to 10) were necessary to remove DMF and the sample was lyophilized. Hydrolysis of polymer was performed by dissolving SMAnh-SH powder in 0.1 M borate buffer 100 mM DTT pH 8.5 (100°C, 4 h). Once cool, the solution was dialysed overnight (MWCO 3.5 kDa, 30 mL cassette Thermo) against 1 mM DTT, pH 8. The SMA-SH polymer was finally lyophilized and re-suspend in either PBS

pH 7.4 for further dye conjugation or in 1 mM DTT, pH 8 for long-term use at a SMA-SH concentration of 125 mg/mL.

6.2.3 Conjugation of fluorescent dye to SMA-SH (SMA-SH-A)

Alexa dye (1 mg) was dissolved in 20 μL DMSO and added directly to the SMA-SH previously dissolved in phosphate buffer pH 7.4 supplemented with 5 mM TCEP. The mixture was left to stir (2 h, in the dark, room temperature). Afterwards, the polymer was extensively dialysed against 1 mM DTT pH 8 to remove any non-conjugated dye.

6.2.4 Purification of SMA-SH-A

To remove any possible excess of dye and SMA-SH, the sample was purified by TLC using a mobile phase of chloroform/methanol/water (5:5:1 v/v/v). Free dye was used as a control. SMA-SH-A migrates with a retention factor (R_f) between 0.4-0.7 and the free dye with an R_f=0.9. SMA-SH-A was extracted from the TLC plate and extracted from the silica using methanol. Silica was removed by centrifugation (4000g, 5 min, R.T.) and the supernatant was recovered and dried using a rotary evaporator. Once dried, SMA-SH-A was solubilized in PBS supplemented with 1 mM DTT, pH 8.

6.2.5 Size exclusion chromatography

The Lipodisq-Dox sample was concentrated prior to size exclusion chromatography experiments using Vivaspin (MWCO 100 kDa, Millipore) and applied to a 5 mL HiTrap column prior equilibrated with PBS buffer. Coloured fractions were collected, concentrated and kept at 4°C for further experiments.

6.2.6 UV-Vis spectroscopy

Samples were applied to a 1 mL plastic cuvette in PBS buffer for UV-Vis spectroscopy. A wavelength range from 400 nm to 700 nm was used to check for the presence of

the absorption peak corresponding to Alexa 647 dye (at 650 nm) and doxorubicin (500 nm) at a scanning speed of 50 nm/s.

6.2.7 Fluorescence quenching experiments

For the fluorescence quenching experiment, two samples are required for each lipid preparation: one was prepared containing potassium iodide (100 mM, Sigma) in phosphate buffer and the other set was prepared with potassium chloride (100 mM, Sigma) in phosphate buffer. These buffers were added at the beginning of the preparation of Lipodisqs (addition of stock solution of 1 M KCl/KI to the Lipodisq-Dox sample).

The fluorescence measurements were performed on a LS50B Luminescence Spectrometer from Perkin Elmer. The excitation wavelength used was 480 nm and the emission spectra were recorded from 500 nm to 650 nm. Every measurement was done using a 500 μL cuvette and the sample was diluted ten times. The temperature was regulated using a water bath (Haake) and the temperature was maintained at 20°C.

6.2.8 Size determination using dynamic light scattering

Particle size of the Lipodisqs was measured using a Malvern Zetasizer Nano S instrument in a disposable cuvette at 633 nm. The data was processed using Malvern Zetasizer software.

6.2.9 Biodistribution experiments in mice

The biodistribution of Lipodisq were performed by the Sandvig group in Oslo University Hospital (Norway). Brielfy, a suspension of fluorescently labelled Lipodisq nanoparticles were injected into the tail veins of wild-type ddY mice. Mice were killed by bleeding, and their organs were collected and analysed at the different time intervals (1h, 4h and 24h).

6.3 Results and discussion

Previous work has demonstrated that doxorubicin can be incorporated in Lipodisq nanoparticles by mixing the drug with lipid prior to the formation of liposomes [493]. It has also been demonstrated that the doxorubicin is monomeric in the Lipodisq, while at similar concentrations in solution, it is dimeric [494]. Here we want to use a fluorescently labelled SMA, to enable the tracking of the polymer in different organs once administered into an animal. Therefore, the first step here is to synthesize the polymer, characterize the Dox environment and observe if any changes happen between the fluorescent and non-fluorescent Lipodisq-Dox formulation and then to apply these samples to xenograft-mice and observe the biodistribution of the fluorescent Lipodisq.

6.3.1 Synthesis and purification of SMA-SH-A

The SMA was conjugated to a dye following a protocol from the literature [202], where the SMA is first derivatized with a cysteamine, which introduces a thiol group to the SMA (Figure 6.3). The reaction was performed in presence of triethylamine, which acts as a strong base to activate the amino group (on the cysteamine molecule) to permit the attack towards the carbonyl group present on the polymer. This reaction opens the anhydride group and produce a carboxylic group on one end and the cysteamine conjugates (amide bond formation) to the other end. This conjugation adds a thiol group to the polymer, enabling fast and efficient labelling with maleimide dyes. A 1:1 molar ratio was chosen and a low yield was observed as in literature [202]. This has been attributed to the heterogeneity (maleic acid to styrene ratio) and the molecular weight polydispersity of the polymer.

A few differences were observed compared to the typical SMA hydrolysis performed previously. A few more washing steps using water and acetic acid are required to wash the polymer from any DMF solvent left after the reaction. Also, the use of sodium hydroxide at pH 12 was replaced by borate buffer at pH 8.5, to prevent non-reversible oxidation of the thiol group [202].

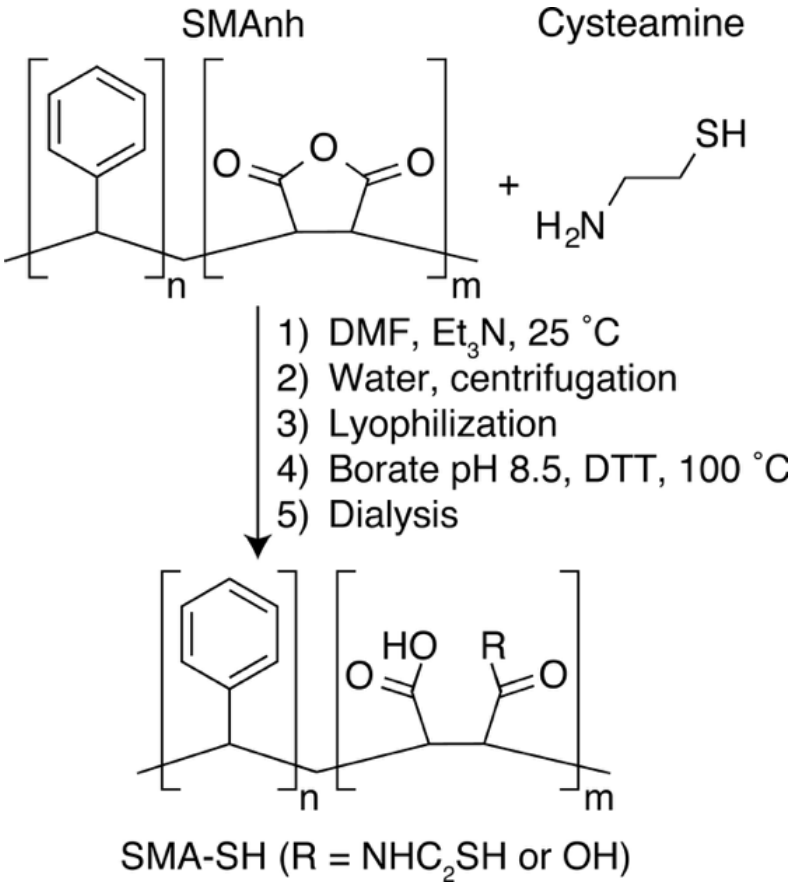


Figure 6.3: Chemical reaction scheme from SMAnh to SMA-SH (adapted from [202]).

Once lyophilized, the Alexa-647 dye was conjugated following the manufacturer's protocol [495]. This is in contrast with Lindhoud and colleagues [202] as they conjugate the dye after forming the Lipodisq with the SMA-SH polymer. Here, we decided to conjugate first the dye to the polymer prior to Lipodisq formation to prevent competing reaction with the lipid and the doxorubicin. Therefore, TCEP was added in phosphate buffer at pH 7 to ensure the reduction of the thiol groups and the ratio used was 1:10 molar ratio (dye:SMA-SH) to prevent over conjugation. Removal of excess dye was performed by dialysis and verified by TLC (Figure 6.4).

The large smear with retention factors between 0.4-0.7 (Figure 6.4) is most likely due to the varying SMA hydrophobicities, or due to the different level of dye conjugation. The free dye was spotted next to the SMA-SH-A and the R_f of the dye was 1 (Figure 6.4). Using TLC, we have demonstrated that the free dye is

not present but unfortunately, it was not possible to separate the SMA-SH from the SMA-SH-A, as they possess similar elution properties.

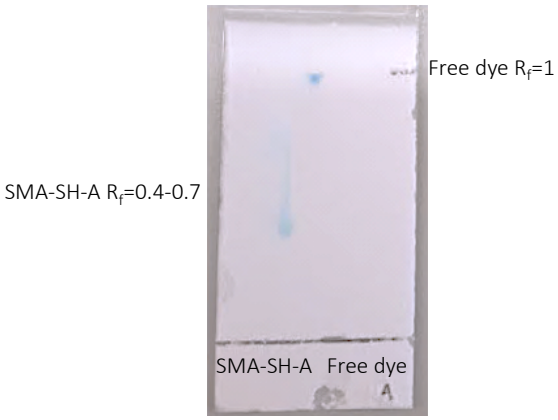


Figure 6.4: Thin layer chromatography of the SMA-SH-A and the free dye. A smear can be observed in the SMA-SH-A sample.

6.3.2 Incorporation of doxorubicin in SMA-SH-A Lipodisq

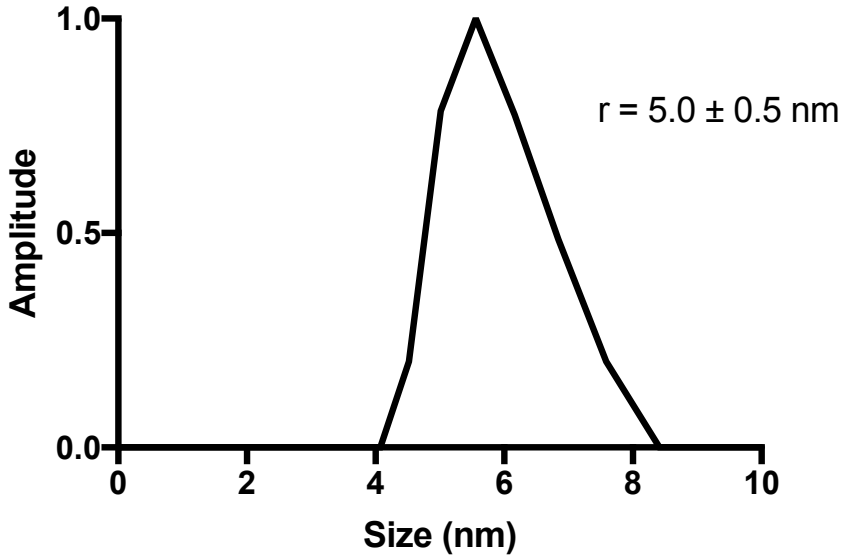


Figure 6.5: DLS of the plain SMA-SH-A DMPC Lipodisq exhibiting a larger size compared to SMA DMPC Lipodisq.

After the purification of the SMA-SH-A polymer, Lipodisq formation was attempted, by solubilizing a suspension of DMPC liposomes using the same lipid-to-polymer ratio as performed previously in Chapter 2 and 3 and in the literature [124]. DLS

was used to assess the formation of the Lipodisq. As seen in figure 6.5, the size of SMA-SH-A Lipodisq observed is similar to SMA Lipodisq, indicating the dye conjugation does not affect the ability of the SMA to form Lipodisq. Also, a slight increase in SMA-SH-A Lipodisq size is observed due to the dye, which is a bulky molecule and contributes to the increase of the hydrodynamic radius of the particles.

As the SMA-SH-A shows the ability to form Lipodisq similarly to SMA, doxorubicin was incorporated at different ratio (1%, 5% and 10% mol/mol doxorubicin-to-lipid ratio) and the particles size was measured by DLS (Figure 6.6).

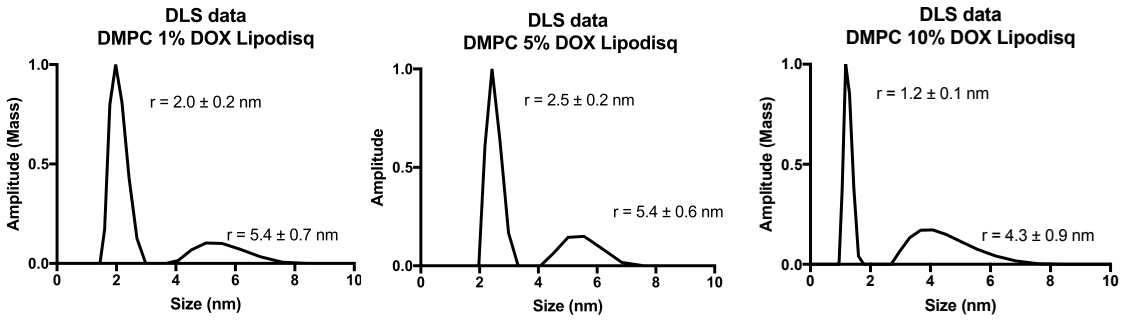


Figure 6.6: DLS of the different SMA-SH-A DMPC doxorubicin Lipodisq samples.

As observed (Figure 6.6), two different populations of peaks are observed in every sample, one being around 2 nm and another peak around 4 to 5 nm. The peak between 1-2 nm is the free SMA-SH-A which was not removed for this experiment. A similar peak (around 1.7 nm) is usually observed in the SMA Lipodisq when the excess of SMA is not removed. The slight change observed here is consistent with the fact that the SMA is now conjugated to the Alexa dye, which produces a bulkier SMA. Similar observations were made for SMA Dox Lipodisq nanoparticles [494].

The second peak, between 4 to 5 nm, are the Lipodisq nanoparticles loaded with doxorubicin. As observed, an increase in size is observed when the doxorubicin is incorporated, with the exception of the 10% Dox samples, for which a decrease in size is observed. These differences in size may be attributable to the different locations of the doxorubicin once incorporated in the Lipodisq. It has been demonstrated that the doxorubicin can be located in different parts of the Lipodisq, superficially, inside

the bilayer or at the edge of the Lipodisq [494]. To investigate the location of the doxorubicin in the Lipodisq, fluorescence quenching experiments were performed.

Prior to the fluorescence experiments, excess SMA-SH-A and doxorubicin were removed using concentrator with a high molecular weight cutoff (MWCO) of 100 kDa. The 100 kDa MWCO ensure that the fluorescence observed in the sample belonged only to the Dox present in the Lipodisq as the SMA (approximately 7-10 kDa) and doxorubicin (543 Da) are removed during the concentration step. The method used here was preferred to size-exclusion chromatography as it offers a quick way to separate the Lipodisq from the small molecule and polymer without diluting the sample.

6.3.3 Fluorescence quenching

The sensitivity of the fluorescence spectrum of doxorubicin to the polarity of its microenvironment was used to investigate how the drug interacts with the Lipodisq (Figure 6.7). It has been demonstrated that above a concentration of 30 μM, the doxorubicin self-quenches in solution [494, 496]. Iodide ions can quench solvent-accessible doxorubicin however when protected by the Lipodisq, doxorubicin fluorescence is less affected by the presence of iodide ions [493, 494] with only a minor decrease in fluorescence.

Here we performed the same experiment with SMA-SH-A and similar results were observed (Figure 6.8). Between 10% to 20% percent of the doxorubicin fluorescence is quenched compared to the doxorubicin in solution, in which fluorescence is quenched by 66% when exposed to iodide ions (Figure 6.8). Therefore, the doxorubicin fluorescence is slightly affected by the presence of iodide, meaning that the doxorubicin has been incorporated into the Lipodisq and is no longer accessible to the solution. For the 1% Dox sample, more quenching is observed compared to the other two samples (Figure 6.8), and this could be due to a different location of the doxorubicin in the Lipodisq. The ratio of fluorescence at 555 nm/588 nm and 630 nm/588 nm can be used to determine in which type of environment the molecule lies [497] (Figure 6.7). Using various solvents with different dielectric constants, a

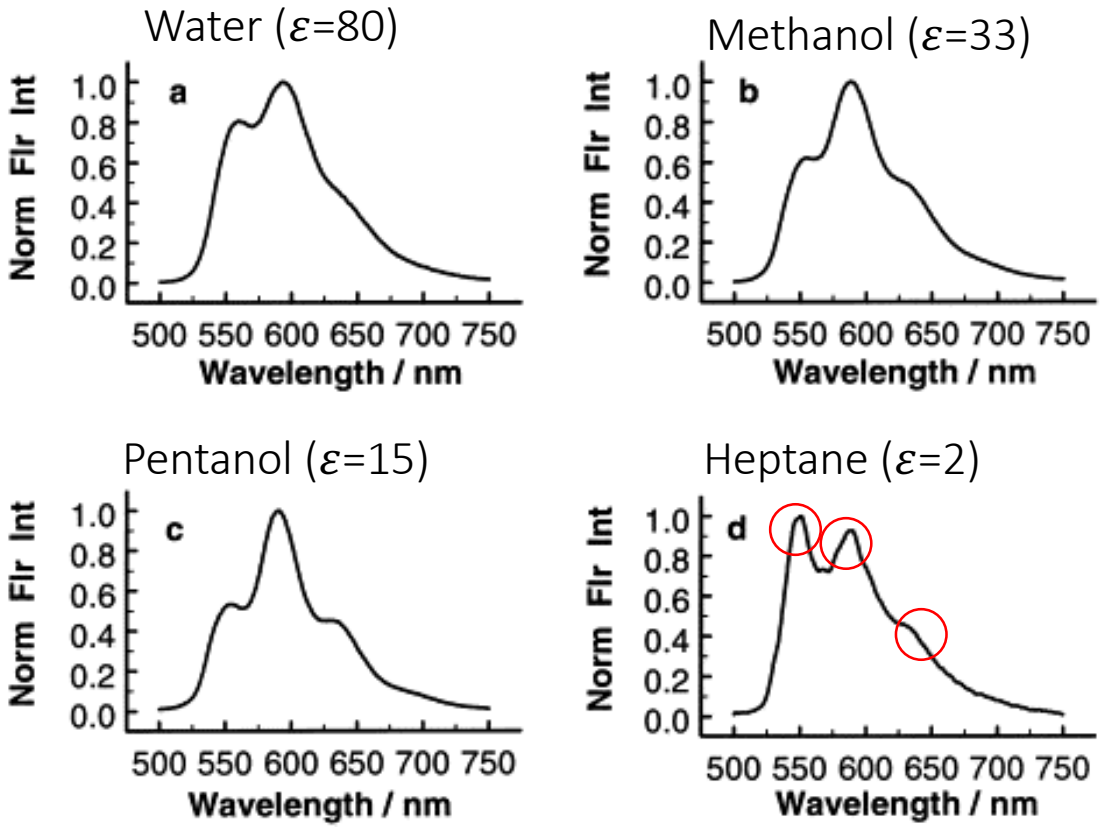


Figure 6.7: Doxorubicin fluorescence is affected by solvent dielectric constant. Different example of doxorubicin fluorescence spectra are shown here in different organic solvent. The appearance of a peak at 630 nm is characteristic of a highly hydrophobic environment (adapted from [497]).

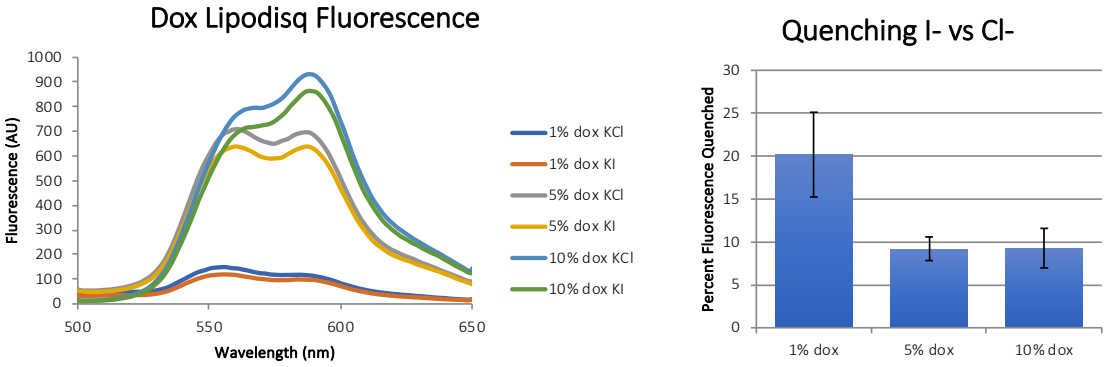


Figure 6.8: Doxorubicin quenching fluorescence in SMA-SH-A DMPC Lipodisq with the different loading of doxorubicin. The fluorescence spectra was measured in five analytical replicates and mean values were taken for representation. Error bars represent standard error of n=5 measurements

calibration curve may be generated to study the location of the doxorubicin in the Lipodisq. Using the data on the bilayer dielectric constant calculated by molecular dynamics simulations [498], the doxorubicin location can be determined (Figure 6.9).

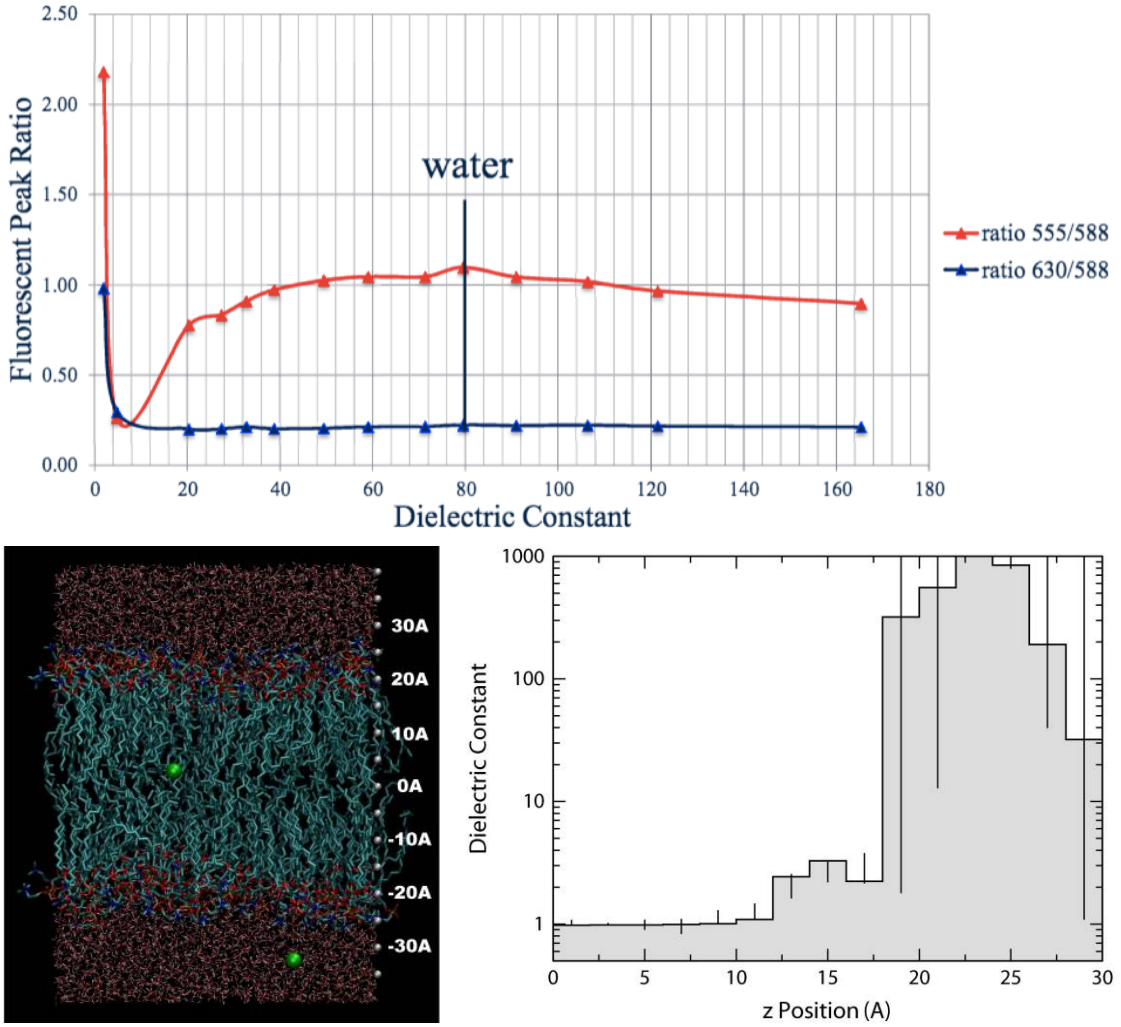


Figure 6.9: Top: Doxorubicin fluorescence peak ratio in different solvent is plotted. The 630/588 ratio is only changing in highly hydrophobic environment (reproduced from [494]). Bottom: A plot of a simulated dielectric constant in a lipid bilayer (adapted from [498]).

The fluorescence ratio (table 6.1) observed for 5% Dox suggests that the dielectric constant around the doxorubicin fluorophore is around 20, meaning that the molecule is likely to be in close proximity to the glycerol moieties of the phospholipids [498]. This would indicate that the Dox is either at the surface or at the edge of Lipodisq, therefore accounting for an increase in size of the Lipodisq as observed by DLS

Table 6.1: Fluorescence ratio for the Dox SMA-SH-A Lipodisqs nanoparticles.

Ratio fluorescence peak	1% Dox DMPC Lipodisq	5% Dox DMPC Lipodisq	10% Dox DMPC Lipodisq
555/588	1.26	0.98	0.73
630/588	0.27	0.25	0.27
Estimated dielectric constant	<20	~20	<20

(Figure 6.6). For the 1% and 10% Dox containing samples (Table 6.1), the dielectric constant observed would be below 20, indicating that the molecule is inserted in the lipid bilayer. The size observed by DLS for the 10% Dox suggests that a smaller Lipodisq is formed, probably due to a tighter lipid packing when doxorubicin is incorporated in Lipodisqs, which is not observed for the 1% and 5% Dox containing Lipodisq, which have similar size (5.4 nm approximately, Figure 6.6) but are still larger than empty Lipodisqs (5 nm, Figure 6.5).

The data reported here from the fluorescence ratio experiments indicates that the doxorubicin molecule is located around the glycerol moieties region, since the mean local dielectric constant of doxorubicin observed was around 20. Importantly, the doxorubicin bears a positively charged moiety (with a pK_a around 8.2), meaning that in the experimental conditions the doxorubicin was charged (pH 7.4), preventing deep penetration into the bilayer. In addition, it was observed by Dupou-Cezanne and colleagues [499] that a high lateral pressure of bilayers hinders the penetration of doxorubicin. In conclusion, the location of doxorubicin is likely to be around the glycerol moieties of the phospholipids, the positive charge either interacting with the phosphate group or protruding from the Lipodisq to allow solvation.

6.3.4 Biodistribution experiments

Once the Dox-Lipodisqs were characterized, the fluorescently labelled SMA-SH-A DMPC Lipodisq were administered to mice as a first control experiment. Previous *in vitro* experiments have shown that Lipodisq nanoparticles (without any Dox) were not toxic to cells [493] and recently Tanaka and colleagues have performed a biodistribution study of SMA nanoparticles using radiolabelled probes showing a similar effect *in vivo* [500].

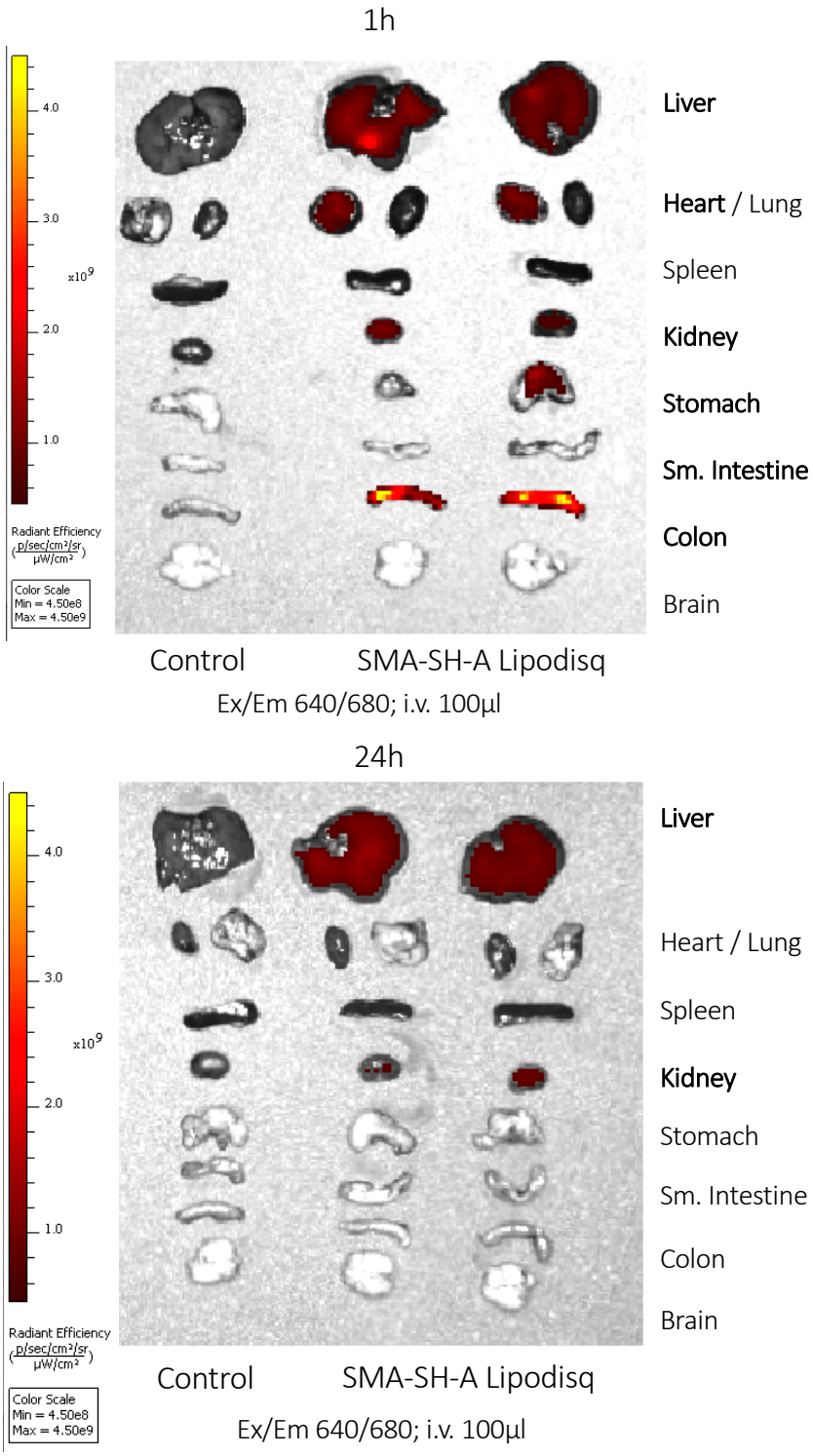


Figure 6.10: Fluorescence imaging of the organs of the sacrificed mice after 1h and 24h. Major concentration of SMA-SH-A polymer are marked in bold.

After being sacrificed, the biodistribution of the SMA-SH-A Lipodisqs was

assessed by measuring the fluorescence of the polymer in the different organs of the mice at different time points (1h, 4h and 24h) (Figure 6.10).

After 1h, we can observe that the fluorescence has spread to nearly all the organs, except the spleen, the lung and the brain. It is especially interesting to note that there is a high fluorescence signal in the colon, which implies that there is a rapid excretion of the Lipodisqs. After 4h and 24h, only low fluorescence of the SMA-SH-A can be observed in the kidney and liver, suggesting a very fast excretion of the Lipodisq once administered. MSP nanodiscs have shown a similar accumulation in the kidney, whereas liposomes only accumulate in the liver and spleen [501]. No accumulation can be observed in the lungs, consistent with previous observation for nanodiscs and liposomes. No fluorescence is detectable in the spleen in contrast to liposomes and other polymer-based nanoparticles, indicating that the Lipodisqs have not stimulated an immune response. Similar observations for SMA nanoparticles have been noted from Tanaka and colleagues [500].

The data presented here suggest that the Lipodisq could be used as a new drug delivery carrier due to their fast excretion, low toxicity and non-interaction with other organs such as lungs or heart. Also, to note that the Lipodisqs did not trigger any immune response (no spleen accumulation), but this has to be confirmed in future experiment with the doxorubicin molecule loaded in Lipodisq.

6.3.5 Conclusions

Here, we have been able to synthesize a fluorescent SMA derivative (Figure 6.3) which retains the properties of the SMA as demonstrated by DLS experiments (Figure 6.5). Synthesis of several other fluorescent SMA polymers could help not only in drug delivery but also in structural biology such as in ligand-binding assays similarly performed by us, with the fluorescent tagged MSP Nanodiscs [502].

Using the fluorescently labelled SMA, we have been able to incorporate doxorubicin into Lipodisq nanoparticles (Figure 6.6), which is an anti-cancer drug and shown that the Doxorubicin is incorporated in the Lipodisq as revealed by fluorescence quenching experiments (Figure 6.8). We have determined its

approximate location in the Lipodisq by using its fluorescence peak ratio to measure the dielectric constant and conclude that the doxorubicin location is likely to be located around the glycerol moieties of the phospholipids (Table 6.1).

Lastly, we have shown that the Lipodisqs can be used as a new drug delivery carrier as they present some advantages such as low toxicity, fast excretion and can become disrupted in low pH environments such as the cytoplasm of tumour cells, permitting drug release (Figure 6.10). Other potential applications could include the use of specific biomarker for cancer cells such as folate [503], which could be incorporated into Lipodisqs enhancing the specificity towards cancer cells and thus reducing the risk of their uptake by normal cells.

7 Conclusions

It has been demonstrated that the local environment of a protein affects both its structure and function, especially membrane proteins where lipids and other small molecules (such as cholesterol) have shown to influence protein activity and conformation [504]. Although detergents have contributed significantly to experimental advances in understanding membrane protein structure and dynamics, they may remove or perturb bound lipids, which can have a direct influence on protein activity [158, 159, 505]. Alternative methods for extracting and solubilising membrane proteins, including lipid-based platforms such as MSP-Nanodiscs or liposomes offer a more realistic membrane environment but they all rely on detergent-solubilized proteins and artificial lipid environment [171, 173, 188, 193]. It is also important to note that the approaches shown in this thesis are important for resolving functionally relevant lipid-protein interactions [17, 18, 40, 70, 75, 76], rather than just finding lipids in crystal structures, many of which are wrongly modelled [40, 80, 81], or by spiking complexes which may or may not have any relevance to the natural lipid component [18, 25, 26, 75, 76]. Here, we have demonstrated, that the Lipodisq method can explore lipid-protein interactions as well as protein-protein interactions without affecting the protein folding and activity avoiding detergents, therefore permitting a more realistic study of the natural membrane protein environment as already demonstrated in a few studies [198, 201, 340, 341, 506].

In this thesis, we have used a detergent-free approach to extract membrane proteins from their native environment with SMA. The resulting Lipodisq nanoparticles, in which the proteins are embedded, do not perturb its function and structure as demonstrated in Chapters 2 and 3 by biophysical methods including CD, MST and radio-ligand binding. The use of a non-thermostabilised GPCR and a transporter demonstrate, that this technique can be used for any type of membrane protein as it allows easy purification with a high yield and purity. Lipodisq nanoparticles are a complimentary tool to other existing platforms such as MSP-Nanodiscs, but have the advantage of that the embedded protein has never been in contact with detergent.

We have also implemented the use of native mass spectrometry for Lipodisqs, being able to observe proteins peaks at lower voltage (for bR in Chapter 2, EcMATE and D1 in Chapter 3 and AR3 in Chapter 4) than MSP-Nanodiscs and detergents [235, 255]. For microbial rhodopsins (bR and AR3), we have been able to observe several endogenous lipids present in the purple and claret membranes and to identify them using the LipidMAPS online database [465]. Moreover, the exact mass obtained has enabled the identification of the different post-translational modifications carried by the different proteins. As an example, the pyroglutamate (PCA) at the N-terminus of AR3, first identified by MS, was then fitted to the electron density of the AR3 crystal structure. We also hope to use the AR3 native mass spectrometry data in combination with the XFEL data obtained to try to identify the different lipids present in the crystal structures, as in the synchrotron data obtained here, lipids are significantly damaged by radiation [378, 507].

For EcMATE, we have observed by nMS an unexpected oligomeric state (dimer) compared to the monomeric state usually observed for detergent-solubilised MATE proteins [305, 306, 508]. Moreover, the different experiments performed in Chapter 3 suggest, due to the mass obtained, that a lipid (or small molecule) is responsible for stabilizing this dimer. A similar case for a transporter has been observed recently [250] and the dimer interface has been solved by strategic point mutations on the protein. We are still performing several experiments and expect to be able to assess the identity of the ligands using mainly lipidomics and a similar approach used by

Pyle and colleagues [250]. Using MST and CD, we have shown that doxorubicin binds to EcMATE with a similar affinity as for other MATE transporters and appears to undergo a similar change of conformation. In future experiments, we aim to use the EcMATE Lipodisq with native mass spectrometry to assess if a molecule is able to interact with a protein (ligand-binding by mass spectrometry) as performed for detergent-solubilized samples [251]. This can open the way to use Lipodisq as a screening platform for ligand binding. Using Lipodisq can also inform us about the lipid environment of the protein and help us to understand how, in certain cases, lipids or other small molecules may impact on protein function or/and structure.

Studies of human non-thermostabilised GPCRs are complicated by the low amount of receptor present in the host expression system and low stability, especially in detergent [505, 509]. Here we have used Lipodisq to extract, purify and characterize the human dopamine receptor 1 from HEK cells with some promising results as the receptor extracted was shown to be active by radio-ligand binding. Native mass spectrometry experiments and radio-ligand binding assays suggest that a dimer has been purified. It is difficult to observe ligands or lipids by nMS due to the low amount of receptor purified and we expect similar experiments at much higher concentrations to be able to observe ligands, small molecules (such as cholesterol) or lipids. Indeed, it has been suggested that some GPCR dimerization can be induced by cholesterol or similar molecules [355, 510–512] and native mass spectrometry is an excellent method to demonstrate this behaviour.

We have obtained the structure of the dark-adapted state of AR3 at 1.3 Å resolution without the use of detergent. We hope to solve the structure of the protein crystallized from Lipodisq samples and intend to try to crystallize other membrane proteins in this way. This could open the way, in combination with native mass spectrometry, to identify the location of some important lipids and ligands and to assign post-translational modifications.

The AR3 structure obtained in this thesis shows the retinal Schiff base in two conformations with a majority of *cis* isomer and with the orientation of some amino acids such as Arg82 and the glutamate pair (E194 and E204), similar to

the bR dark-adapted structure. Unfortunately, no experimental data on the ratio of *cis* to *trans* isomer of the dark-adapted AR3 is available and therefore no direct comparison can be performed but the presence of the methionine (instead of phenylalanine) in the retinal pocket suggest that the ratio fitted for the dark-adapted state is similar to bR and differs from the other AR proteins [421]. Some specific features such as the pyroglutamate group or the omega loop, a characteristic structural motif at the N-terminus of archaerhodopsin proteins, are observed at very high resolution. Unfortunately, the bacterioruberin chromophore could not be fitted in any of the crystal structure or identified in the native mass spectrometry experiments, suggesting that it may only bind tightly to AR3 in the trimeric assembly as in AR2 and Halorhodopsin [121, 358]. Obtaining the native oligomeric state for crystallography and native mass spectrometry should be explored and would reveal if the bacterioruberin carotenoid is present in the trimer as in the AR2 structure [358] or merely present in excess in the claret membrane. Atomic Force Microscopy or cryo-EM could help in the assessment of the oligomeric state of AR3 as performed for bR and other microbial rhodopsins [513]. Moreover, a light-adapted structure of AR3 (from XFEL or synchrotron radiation) would be helpful in order to observe the change in the *cis* to *trans* isomer light-adaption and in amino acid side chain re-orientation.

Using XFEL, the study of the AR3 photocycle is still under investigation but we have already been able to observe that the protein is functional in the crystal environment since we have observed the movement of water molecules and the re-orientation of fundamental amino acids involved in proton translocation. We hope to be able to collect several timepoints for the AR3 photocycle and to be able to compare them directly with the recent literature [268, 269]. We have already observed several water molecules present in the proton-release side of the protein, but we have not seen any change in the proton uptake side, and we hope, with the XFEL experiments, to unravel the reason for the faster photocycle kinetics of AR3 compared to other archaerhodopsins and to bacteriorhodopsin.

In chapter 5, we have demonstrated that the SMA polymer can be used for exploring the lipidome and membrane proteome of the *C. elegans*. We have shown that the lipid composition of a mutant lacking an important enzyme involved in lipid biosynthesis is altered to the wild-type. This has been demonstrated by MALDI-MS but a more thorough analysis would require the use of LC-MS/MS which is more sensitive and would enable the identification of all the lipids present [215, 253] as some lipid species have poor detectability in MALDI due to their low ionization [456, 468]. Moreover, proteomics is still under investigation to complement the lipidomics data and to observe if protein expression is affected by the lack of the AGMO enzyme.

Lastly, the Lipodisq nanoparticles have been used as a new drug delivery platform for the hydrophobic anti-cancer drug, doxorubicin, which when administered as a solution induces serious side effects [514]. Previous studies from our lab have shown that Lipodisq nanoparticles are non-toxic and that Lipodisq loaded with doxorubicin have a lower IC_{50} than the drug itself in solution and in other formulations. Unfortunately, *in vitro* experiments provide poor information regarding the biodistribution of the polymer once *in vivo*, which can accumulate and be toxic for certain organs. In order to study the biodistribution of the SMA once injected *in vivo*, we have conjugated a dye to the SMA polymer following the protocol established in the literature [202] with slight changes and form Lipodisq with the dye-conjugated SMA (SMA-SH-A). Following successful formation of the Lipodisqs, as assessed by DLS and size-exclusion chromatography, doxorubicin has been incorporated and its location has been examined by fluorescence quenching experiments.

The biodistribution of the Lipodisq nanoparticles has been studied by collaborators and has shown rapid excretion and no accumulation in key organs, in contrast to MSP-Nanodiscs, which accumulates in the spleen [188]. Even though the SMA is non-toxic to cells and does not affect key organs, the doxorubicin-Lipodisqs are distributed among all cells and increasing the specificity for cancer cells doping the Lipodisq for example with folate [503] or with specific lipids reacting in changes of temperature [515] or light [482, 484] could be of benefit.

Appendices

A Appendix

A.1 SDS-PAGE

SDS-PAGE was performed on a X-cell Surelock minicell and pre-cast NuPAGE Bis-Tris 12% (or 4-12%) gel following the protocol from *life technologies*. Samples were prepared as stands in the protocol [516] using NuPAGE LDS Sample Buffer (4x) and denatured at 60°C - 70°C. The gel was run for 40 minutes at 180 V at room temperature in MES running buffer. Different staining methods have been used either silver stain to assess purity or Coomassie for proteomics experiments.

A.2 Western Blot

SDS-PAGE gels were transferred to an activated PVDF membrane (previously incubated with methanol, GE Healthcare) using a semi-dry transfer method (Trans-Blot from BioRad) for 2 h at 150 mA. Transfer was assessed by Ponceau staining (Sigma).

A.3 Silver stain

Silver-stain was performed using the Silver Stain Plus kit from Bio-Rad to stain proteins in the gel following the manufacturer's protocol.

A.4 Coomassie staining

InstantBlue (C.B.S. Scientific Company, San Diego, USA) was incubated with the gel at least 30 minutes at room temperature.

A.5 BCA assay

The Pierce BCA Protein Assay Kit from Thermo was used to measure the protein concentration following manufacturer's protocol.

A.6 Calibration curve for size-exclusion chromatography

High molecular weight kit from GE healthcare has been used in order to calibrate the column. The kit contains a series of proteins from very high molecular weight to low molecular (from 670 kDa to 1.35 kDa). Dextran Blue (2000 kDa) is used to determine the void volume of the column. Briefly, each protein is solubilized in 50 mM PBS buffer and all proteins are mixed accordingly to the manufacturer's protocol. Samples is then injected in the column and flow rate is kept constant at 0.2 ml/min. Elution volume is then recorded for each protein and a calibration curve can be produced by plotting Stokes radius (R_{st}) vs the root mean square of the gel phase distribution coefficient ($(-\log(K_{av}))^{0.5}$) as performed in the manufacturer's protocol [517]. Linear regression is performed and an estimate of the radius of the nanoparticle can be calculated.

A.7 Trace metal solution

The trace metal solution was prepared using 65 mg of $ZnSO_4$, 15 mg of $MnSO_4$, 27 mg of $FeCl_2$ and 7.5 mg of $CuSO_4$ dissolved in 100 mL 0.001 M HCl.

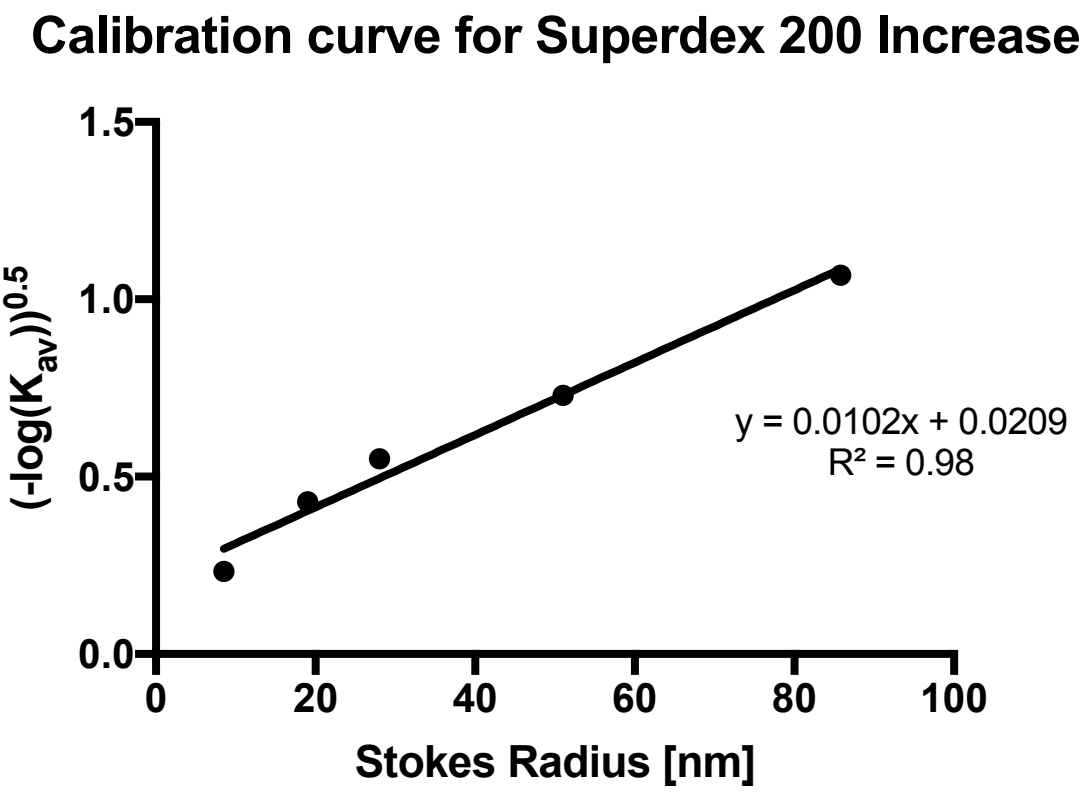


Figure A.1: Calibration curve for the Superdex 200 Increase 10/300 GL.

A.8 Data collection at synchrotron

Crystallographic data collected at 100 K was recorded on the I24 microfocus beamline at Diamond Light Source (Harwell, UK). Crystals were flash-cooled in liquid nitrogen and maintained at 100 K under N_2 gas. Diffraction patterns from multiple crystals were combined using the BLEND analysis software [518]. Phases for AR3 were obtained by Molecular Replacement using the Phaser software [519] using the deposited structure for AR1 (PDB ID 1UAZ, [397]). The initial electron density maps were inspected and the model was built using Coot [520] and model refinement was performed using PHENIX [411].

A.9 Data collection for XFEL

TR-SFX experiments were performed at BL3 of SACLA in November 2017 using the same setup as Nango and colleagues [268]. The only difference with the Nango

setup is the laser wavelength (570 nm vs 532 nm) because of the red-shift in absorbance of AR3 compared to bR. Data collection was assisted by Cheetah [521] and by the data processing pipeline developed at SACLA [522]. CrystFEL [523] was used for further processing of diffraction data. Phases for AR3 were obtained by molecular replacement using the Phaser software [519] using the deposited structure for AR1 (PDB ID 1UAZ, [397]). The initial electron density maps were inspected and the model was built using Coot [520] and model refinement was performed using PHENIX [411].

A.10 Distances between the retinal Schiff base and several amino acids

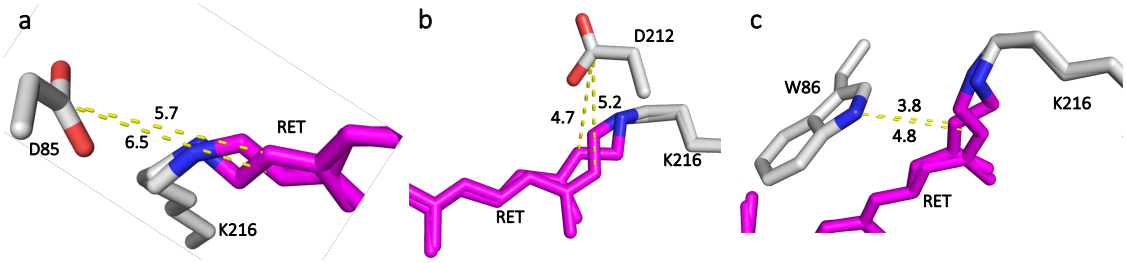


Figure A.2: Distances between the retinal Schiff base and (a) D85, (b) D212 and (c) W86. Retinal coloured in purple.

References

[1] J. T. Hannich, K. Umebayashi, and H. Riezman. "Distribution and functions of sterols and sphingolipids." In: *Cold Spring Harbor Perspectives in Biology* (2011), pp. 1–14.

[2] A. Yamashita et al. "Acyltransferases and transacylases that determine the fatty acid composition of glycerolipids and the metabolism of bioactive lipid mediators in mammalian cells and model organisms". In: *Progress in Lipid Research* 53.1 (2014), pp. 18–81.

[3] J. T. Hannich et al. "Structure and conserved function of iso-branched sphingoid bases from the nematode: Caenorhabditis elegans". In: *Chemical Science* 8.5 (2017), pp. 3676–3686.

[4] S. Grösch, S. Schiffmann, and G. Geisslinger. "Chain length-specific properties of ceramides". In: *Progress in Lipid Research* 51.1 (2012), pp. 50–62.

[5] T. Harayama et al. "Lysophospholipid acyltransferases mediate phosphatidylcholine diversification to achieve the physical properties required in vivo". In: *Cell Metabolism* 20.2 (2014), pp. 295–305.

[6] G. Van Meer, D. R. Voelker, and G. W. Feigenson. "Membrane lipids: Where they are and how they behave". In: *Nature Reviews Molecular Cell Biology* 9.2 (2008), pp. 112–124.

[7] B. Antonny et al. "From zero to six double bonds: Phospholipid unsaturation and organelle function". In: *Trends in Cell Biology* 25.7 (2015), pp. 427–436.

[8] M. Sud et al. "LMSD: LIPID MAPS structure database". In: *Nucleic Acids Research* 35.SUPPL. 1 (2007), pp. 527–532.

[9] G. Von Heijne. "Membrane-protein topology". In: *Nature Reviews Molecular Cell Biology* 7.12 (2006), pp. 909–918.

[10] A. Bruce et al. *Molecular Biology of the Cell*. Garland Science, 2015.

[11] T. Harayama and H. Riezman. "Understanding the diversity of membrane lipid composition". In: *Nature Reviews Molecular Cell Biology* 19.5 (2018), pp. 281–296.

[12] S. J. Singer and G. L. Nicolson. "The fluid mosaic model of the structure of cell membranes". In: *Science. AAAS* 175.4023 (1972), pp. 720–731.

[13] R. Ernst, C. S. Ejsing, and B. Antonny. "Homeoviscous Adaptation and the Regulation of Membrane Lipids". In: *Journal of Molecular Biology* 428.24 (2016), pp. 4776–4791.

[14] B. Antonny. “Mechanisms of Membrane Curvature Sensing”. In: *Annual Review of Biochemistry* 80.1 (2011), pp. 101–123.

[15] H. T. McMahon and J. L. Gallop. “Membrane curvature and mechanisms of dynamic cell membrane remodelling”. In: *Nature* 438.7068 (2005), pp. 590–596.

[16] L. S. Brown and O. P. Ernst. “Recent advances in biophysical studies of rhodopsins – Oligomerization, folding, and structure”. In: *Biochimica et Biophysica Acta - Proteins and Proteomics* 1865.11 (2017), pp. 1512–1521.

[17] A. G. Lee. “Biological membranes: The importance of molecular detail”. In: *Trends in Biochemical Sciences* 36.9 (2011), pp. 493–500.

[18] C. Hunte. “Specific protein-lipid interactions in membrane proteins”. In: *Biochemical Society Transactions* 33.Pt 5 (2005), pp. 938–942.

[19] M. T. Nakamura, B. E. Yudell, and J. J. Loor. “Regulation of energy metabolism by long-chain fatty acids”. In: *Progress in Lipid Research* 53.1 (2014), pp. 124–144.

[20] T. Shimizu. “Lipid Mediators in Health and Disease: Enzymes and Receptors as Therapeutic Targets for the Regulation of Immunity and Inflammation”. In: *Annual Review of Pharmacology and Toxicology* 49.1 (2009), pp. 123–150.

[21] M. D. Resh. “Fatty Acylation of Proteins: The Long and the Short of it”. In: *Progress in Lipid Research* 63 (2016), pp. 120–131.

[22] T. Magee and M. C. Seabra. “Fatty acylation and prenylation of proteins: What’s hot in fat”. In: *Current Opinion in Cell Biology* 17.2 (2005), pp. 190–196.

[23] E. Sezgin et al. “The mystery of membrane organization: Composition, regulation and roles of lipid rafts”. In: *Nature Reviews Molecular Cell Biology* 18.6 (2017), pp. 361–374.

[24] J. O. De Craene et al. “Phosphoinositides, major actors in membrane trafficking and lipid signaling pathways”. In: *International Journal of Molecular Sciences* 18.3 (2017).

[25] D. Russo, S. Parashuraman, and G. D’Angelo. “Glycosphingolipid–protein interaction in signal transduction”. In: *International Journal of Molecular Sciences* 17.10 (2016), pp. 1–21.

[26] F. X. Contreras et al. “Specificity of intramembrane protein-lipid interactions”. In: *Cold Spring Harbor Perspectives in Biology* 3.6 (2011), pp. 1–18.

[27] A. G. Lee. “How lipids affect the activities of integral membrane proteins”. In: *Biochimica et Biophysica Acta - Biomembranes* 1666.1-2 (2004), pp. 62–87.

[28] J. Suzuki et al. “Calcium-dependent phospholipid scrambling by TMEM16F”. In: *Nature* 468.7325 (2010), pp. 834–840.

[29] J. Suzuki et al. “Xk-related protein 8 and CED-8 promote phosphatidylserine exposure in apoptotic cells”. In: *Science* 341.6144 (2013), pp. 403–406.

[30] J. M. Boggs. “Intermolecular hydrogen bonding between lipids: influence on organization and function of lipids in membranes”. In: *Canadian Journal of Biochemistry* 58.10 (1980), pp. 755–770.

[31] B. Ramstedt and J. P. Slotte. “Sphingolipids and the formation of sterol-enriched ordered membrane domains”. In: *Biochimica et Biophysica Acta - Biomembranes* 1758.12 (2006), pp. 1945–1956.

[32] D. A. Brown and E. London. “Structure and function of sphingolipid- and cholesterol-rich membrane rafts”. In: *Journal of Biological Chemistry* 275.23 (2000), pp. 17221–17224.

[33] A. A. Spector and M. A. Yorek. “Membrane lipid composition and cellular function”. In: *Journal of lipid research* 26.9 (1985), pp. 1015–1035.

[34] H. Guillou et al. “The key roles of elongases and desaturases in mammalian fatty acid metabolism: Insights from transgenic mice”. In: *Progress in Lipid Research* 49.2 (2010), pp. 186–199.

[35] R. Dawaliby et al. “Phosphatidylethanolamine is a key regulator of membrane fluidity in eukaryotic cells”. In: *Journal of Biological Chemistry* 291.7 (2016), pp. 3658–3667.

[36] K. Marheineke et al. “Lipid composition of Spodoptera frugiperda (Sf9) and Trichoplusia ni (Tn) insect cells used for baculovirus infection”. In: *FEBS Letters* 441.1 (1998), pp. 49–52.

[37] X. Shi et al. “Regulation of lipid droplet size and phospholipid composition by stearoyl-CoA desaturase”. In: *Journal of Lipid Research* 54.9 (2013), pp. 2504–2514.

[38] G. W. Feigenson. “Phase behavior of lipid mixtures”. In: *Nature Chemical Biology* 2.11 (2006), pp. 560–563.

[39] A. G. Lee. “Lipid phase transitions and phase diagrams I. Lipid phase transitions”. In: *BBA - Reviews on Biomembranes* 472.2 (1977), pp. 237–281.

[40] M. F. Brown. “Curvature forces in membrane lipid-protein interactions”. In: *Biochemistry* 51.49 (Dec. 2012), pp. 9782–95.

[41] C. M. Rosetti, A. Mangiarotti, and N. Wilke. “Sizes of lipid domains: What do we know from artificial lipid membranes? What are the possible shared features with membrane rafts in cells?” In: *Biochimica et Biophysica Acta - Biomembranes* 1859.5 (2017), pp. 789–802.

[42] R. Raghupathy et al. “Transbilayer lipid interactions mediate nanoclustering of lipid-anchored proteins”. In: *Cell* 161.3 (2015), pp. 581–594.

[43] V. Cherezov, H. Fersi, and M. Caffrey. “Crystallization screens: Compatibility with the lipidic cubic phase for in meso crystallization of membrane proteins”. In: *Biophysical Journal* 81.1 (2001), pp. 225–242.

[44] M. Caffrey. “On the Mechanism of Membrane Protein Crystallization in Lipidic Mesophases”. In: *Cryst Growth Des* 8.12 (2008), pp. 4244–4254.

[45] N. Johner et al. “Protein and lipid interactions driving molecular mechanisms of in meso crystallization”. In: *Journal of the American Chemical Society* 136.8 (2014), pp. 3271–3284.

[46] M. Caffrey. “A comprehensive review of the lipid cubic phase or in meso method for crystallizing membrane and soluble proteins and complexes”. In: *Acta Crystallographica Section F:Structural Biology Communications* 71 (2015), pp. 3–18.

[47] K. Balasubramanian and A. J. Schroit. “Aminophospholipid Asymmetry: A Matter of Life and Death”. In: *Annual Review of Physiology* 65.1 (2003), pp. 701–734.

[48] S. Manno, Y. Takakuwa, and N. Mohandas. “Identification of a functional role for lipid asymmetry in biological membranes: Phosphatidylserine-skeletal protein interactions modulate membrane stability”. In: *Proceedings of the National Academy of Sciences* 99.4 (2002), pp. 1943–1948.

[49] A. A. Gurtovenko and I. Vattulainen. “Lipid transmembrane asymmetry and intrinsic membrane potential: Two sides of the same coin”. In: *Journal of the American Chemical Society* 129.17 (2007), pp. 5358–5359.

[50] M. Nakano et al. “Flip-Flop of Phospholipids in Vesicles : Kinetic Analysis with Time-Resolved Small-Angle Neutron Scattering Flip-Flop of Phospholipids in Vesicles : Kinetic Analysis with Time-Resolved Small-Angle”. In: *Journal of Physical Chemistry B* 113 (2009), pp. 6745–6748.

[51] J. C. M. Holthuis and T. P. Levine. “Lipid traffic: floppy drives and a superhighway”. In: *Nature Reviews Molecular Cell Biology* 6.3 (Mar. 2005), pp. 209–220.

[52] D. L. Daleke. “Phospholipid flippases”. In: *J Biol Chem* 282.2 (Jan. 2007), pp. 821–5.

[53] R. F. Zwaal and A. J. Schroit. “Pathophysiologic implications of membrane phospholipid asymmetry in blood cells”. In: *Blood* 89.4 (Feb. 1997), pp. 1121–32.

[54] S. Garg et al. “Noninvasive neutron scattering measurements reveal slower cholesterol transport in model lipid membranes”. In: *Biophys J* 101.2 (July 2011), pp. 370–7.

[55] B. Frey and U. S. Gaipl. “The immune functions of phosphatidylserine in membranes of dying cells and microvesicles.” In: *Seminars in immunopathology* 33.5 (2011), pp. 497–516.

[56] H. Zhao et al. “Regulation of zinc homeostasis in yeast by binding of the ZAP1 transcriptional activator to zinc-responsive promoter elements”. In: *Journal of Biological Chemistry* 273.44 (1998), pp. 28713–28720.

[57] L. A. Woon et al. “Calcium sensitivity of phospholipid scrambling in human red cell ghosts”. In: *Cell Calcium* 25.4 (1999), pp. 313–320.

[58] P. Devaux. “Protein Involvement in Transmembrane Lipid Asymmetry”. In: *Annual Review of Biophysics and Biomolecular Structure* 21.1 (1992), pp. 417–439.

[59] M. Ikeda, A. Kihara, and Y. Igarashi. “Lipid asymmetry of the eukaryotic plasma membrane: functions and related enzymes.” In: *Biological & pharmaceutical bulletin* 29.8 (2006), pp. 1542–1546.

[60] P. Williamson. “Phospholipid Scramblases.” In: *Lipid insights* 8.Suppl 1 (2015), pp. 41–4.

[61] H. T. Cheng and E. London. “Preparation and properties of asymmetric vesicles that mimic cell membranes. Effect upon lipid raft formation and transmembrane helix orientation”. In: *Journal of Biological Chemistry* 284.10 (2009), pp. 6079–6092.

[62] R. F. A. Zwaal, P. Comfurius, and E. M. Bevers. “Surface exposure of phosphatidylserine in pathological cells”. In: *Cellular and Molecular Life Sciences* 62.9 (2005), pp. 971–988.

[63] A. Gassama-Diagne et al. “Phosphatidylinositol-3,4,5-trisphosphate regulates the formation of the basolateral plasma membrane in epithelial cells”. In: *Nature Cell Biology* 8.9 (2006), pp. 963–970.

[64] R. M. Epand. “Features of the Phosphatidylinositol Cycle and its Role in Signal Transduction”. In: *Journal of Membrane Biology* 250.4 (2017), pp. 353–366.

[65] A. Grall et al. “PNPLA1 mutations cause autosomal recessive congenital ichthyosis in golden retriever dogs and humans”. In: *Nature Genetics* 44.2 (2012), pp. 140–147.

[66] S. Grond et al. “PNPLA1 Deficiency in Mice and Humans Leads to a Defect in the Synthesis of Omega-O-Acylceramides”. In: *Journal of Investigative Dermatology* 137.2 (2017), pp. 394–402.

[67] T. Hirabayashi et al. “PNPLA1 has a crucial role in skin barrier function by directing acylceramide biosynthesis”. In: *Nature Communications* 8 (2017).

[68] M. A. Lemmon. “Membrane recognition by phospholipid-binding domains”. In: *Nature Reviews Molecular Cell Biology* 9.2 (2008), pp. 99–111.

[69] URL: `http://www.cellsignallingbiology.org/csb/002/csb002fig2_localized_inositol_lipid_signalling.htm?resolution=HIGH)`.

[70] D. Marsh and A. Watts. “Spin-labeling and lipid-protein interactions in membranes”. In: *Lipid-protein interactions* 2 (1982), pp. 53–126.

[71] O. Soubias et al. “Rhodopsin/lipid hydrophobic matching - Rhodopsin oligomerization and function”. In: *Biophysical Journal* 108.5 (2015), pp. 1125–1132.

[72] A. V. Botelho et al. “Curvature and Hydrophobic forces drive oligomerization and modulate activity of rhodopsin in membranes”. In: *Biophysical Journal* 91.12 (2006), pp. 4464–4477.

[73] K. Gupta et al. “The role of interfacial lipids in stabilizing membrane protein oligomers”. In: *Nature* 541.7637 (2017), pp. 421–424.

[74] A. Laganowsky et al. “Membrane proteins bind lipids selectively to modulate their structure and function”. In: *Nature* 510.7503 (2014), pp. 172–175.

[75] A. G. Lee. “Lipid–protein interactions”. In: *Biochemical Society Transactions* 39.3 (2011), pp. 761–766.

[76] D. Marsh. “Energetics of hydrophobic matching in lipid-protein interactions”. In: *Biophysical Journal* 94.10 (2008), pp. 3996–4013.

[77] M. Svensson et al. “Lipids as cofactors in protein folding: stereo-specific lipid-protein interactions are required to form HAMLET (human alpha-lactalbumin made lethal to tumor cells).” In: *Protein science : a publication of the Protein Society* 12.12 (2003), pp. 2805–2814.

[78] M. T. Marty, K. K. Hoi, and C. V. Robinson. “Interfacing Membrane Mimetics with Mass Spectrometry”. In: *Accounts of Chemical Research* 49.11 (2016), pp. 2459–2467.

[79] E. Park and T. A. Rapoport. “Mechanisms of Sec61/SecY-Mediated Protein Translocation Across Membranes”. In: *Annual Review of Biophysics* 41.1 (2012), pp. 21–40.

[80] D. Marsh and T. Páli. “The protein-lipid interface: perspectives from magnetic resonance and crystal structures”. In: *Biochim Biophys Acta* 1666.1-2 (Nov. 2004), pp. 118–41.

[81] D. Marsh and T. Páli. “Orientation and conformation of lipids in crystals of transmembrane proteins”. In: *European Biophysics Journal* 42.2-3 (Mar. 2013), pp. 119–46.

[82] F. A. Heberle et al. “Bilayer thickness mismatch controls domain size in model membranes”. In: *Journal of the American Chemical Society* 135.18 (2013), pp. 6853–6859.

[83] M. R. R. de Planque et al. “Interfacial anchor properties of tryptophan residues in transmembrane peptides can dominate over hydrophobic matching effects in peptide-lipid interactions”. In: *Biochemistry* 42.18 (May 2003), pp. 5341–8.

[84] E. Perozo et al. “Physical principles underlying the transduction of bilayer deformation forces during mechanosensitive channel gating”. In: *Nature Structural Biology* 9.9 (2002), pp. 696–703.

[85] R. Phillips et al. “Emerging roles for lipids in shaping membrane-protein function”. In: *Nature* 459.7245 (2009), pp. 379–385.

[86] H. I. Petrache, S. W. Dodd, and M. F. Brown. “Area per lipid and acyl length distributions in fluid phosphatidylcholines determined by 2H NMR spectroscopy”. In: *Biophysical Journal* 79.6 (2000), pp. 3172–3192.

[87] K. Nakahara et al. “The Sjögren-Larsson Syndrome Gene Encodes a Hexadecenal Dehydrogenase of the Sphingosine 1-Phosphate Degradation Pathway”. In: *Molecular Cell* 46.4 (2012), pp. 461–471.

[88] L. Wigger et al. “Plasma Dihydroceramides Are Diabetes Susceptibility Biomarker Candidates in Mice and Humans”. In: *Cell Reports* 18.9 (2017), pp. 2269–2279.

[89] F. Perrotti et al. “Advances in lipidomics for cancer biomarkers discovery”. In: *International Journal of Molecular Sciences* 17.12 (2016).

[90] L. Fagerberg et al. “Prediction of the human membrane proteome”. In: *Proteomics* 10.6 (2010), pp. 1141–1149.

[91] M. A. Yildirim et al. “Drug-target network”. In: *Nature Biotechnology* 25.10 (2007), pp. 1119–1126.

[92] A. Engel and H. E. Gaub. “Structure and Mechanics of Membrane Proteins”. In: *Annual Review of Biochemistry* 77.1 (2008), pp. 127–148.

[93] Ø. Halskau, A. Muga, and A. Martínez. “Linking new paradigms in protein chemistry to reversible membrane-protein interactions.” In: *Current protein & peptide science* 10 (2009), pp. 339–359.

[94] E. G. Govorunova et al. “Microbial Rhodopsins: Diversity, Mechanisms, and Optogenetic Applications”. In: *Annu. Rev. Biochem.* (2017).

[95] O. P. Ernst et al. “Microbial and animal rhodopsins: Structures, functions, and molecular mechanisms”. In: *Chemical Reviews* 114.1 (2014), pp. 126–163.

[96] T. Kottke et al. “Photoreceptors Take Charge: Emerging Principles for Light Sensing”. In: *Annual Review of Biophysics* 47.1 (2018).

[97] I. Gushchin and V. Gordeliy. “Microbial Rhodopsins”. In: *Subcell Biochem* 87 (2018), pp. 19–56.

[98] P. Orekhov et al. “Sensory Rhodopsin I and Sensory Rhodopsin II Form Trimers of Dimers in Complex with their Cognate Transducers”. In: *Photochemistry and Photobiology* 93.3 (2017), pp. 796–804.

[99] J. K. Lanyi and H. Luecke. “Bacteriorhodopsin”. In: *Current Opinion in Structural Biology* 11.4 (2001), pp. 415–419.

[100] S. Hussain et al. “Functional consequences of the oligomeric assembly of proteorhodopsin”. In: *Journal of Molecular Biology* 427.6 (2015), pp. 1278–1290.

[101] J. L. Spudich and R. A. Bogomolni. “Mechanism of colour discrimination by a bacterial sensory rhodopsin”. In: *Nature* 312.5994 (1984), pp. 509–13.

[102] K. H. Jung, V. D. Trivedi, and J. L. Spudich. “Demonstration of a sensory rhodopsin in eubacteria”. In: *Molecular Microbiology* 47.6 (2003), pp. 1513–1522.

[103] J. L. Spudich et al. “Retinylidene Proteins: Structures and Functions from Archaea to Humans”. In: *Annual Review of Cell and Developmental Biology* 16.1 (2000), pp. 365–392.

[104] P. J. Booth. “A successful change of circumstance: A transition state for membrane protein folding”. In: *Current Opinion in Structural Biology* 22.4 (2012), pp. 469–475.

[105] H. Kandori. “Ion-pumping microbial rhodopsins”. In: *Frontiers in Molecular Biosciences* 2.September (2015).

[106] H. Luecke et al. “Coupling photoisomerization of retinal to directional transport in bacteriorhodopsin”. In: *Journal of Molecular Biology* 300.5 (2000), pp. 1237–1255.

[107] S. P. Balashov et al. “Glutamate-194 to cysteine mutation inhibits fast light-induced proton release in bacteriorhodopsin”. In: *Biochemistry* 36.29 (1997), pp. 8671–8676.

[108] M. S. Hutson et al. “Evidence for a perturbation of arginine-82 in the bacteriorhodopsin photocycle from time-resolved infrared spectra”. In: *Biochemistry* 39.43 (2000), pp. 13189–13200.

[109] H. Otto et al. “Substitution of amino acids Asp-85, Asp-212, and Arg-82 in bacteriorhodopsin affects the proton release phase of the pump and the pK of the Schiff base.” In: *Proceedings of the National Academy of Sciences of the United States of America* 87.3 (1990), pp. 1018–1022.

[110] J. Tittor et al. “Chloride and proton transport in bacteriorhodopsin mutant D85T: Different modes of ion translocation in a retinal protein”. In: *Journal of Molecular Biology* 271.3 (1997), pp. 405–416.

[111] H Kandori. “Role of internal water molecules in bacteriorhodopsin”. In: *Biochim Biophys Acta* 1460.1 (Aug. 2000), pp. 177–91.

[112] J. Heberle. “A local area network of protonated water molecules”. In: *Biophysical Journal* 87.4 (Oct. 2004), pp. 2105–6.

[113] S. Wolf, E. Freier, and K. Gerwert. “How does a membrane protein achieve a vectorial proton transfer via water molecules?” In: *ChemPhysChem* 9.18 (2008), pp. 2772–2778.

[114] K Gerwert, E. Freier, and S. Wolf. “The role of protein-bound water molecules in microbial rhodopsins”. In: *Biochimica et Biophysica Acta - Bioenergetics* 1837.5 (2014), pp. 606–613.

[115] H Luecke et al. “Structure of bacteriorhodopsin at 1.55 A resolution”. In: *Journal of Molecular Biology* 291.4 (Aug. 1999), pp. 899–911.

[116] T. P. Sakmar et al. “Rhodopsin: Insights from Recent Structural Studies”. In: *Annual Review of Biophysics and Biomolecular Structure* 31.1 (2002), pp. 443–484.

[117] M. Hoffmann et al. “Color tuning in rhodopsins: the mechanism for the spectral shift between bacteriorhodopsin and sensory rhodopsin II”. In: *Journal of the American Chemical Society* 128.33 (2006), pp. 10808–18.

[118] J. K. Lanyi. “Proton transfers in the bacteriorhodopsin photocycle”. In: *Biochimica et Biophysica Acta - Bioenergetics* 1757.8 (2006), pp. 1012–1018.

[119] C. Wickstrand et al. “Bacteriorhodopsin: Would the real structural intermediates please stand up?” In: *Biochimica et Biophysica Acta - General Subjects* 1850.3 (2015), pp. 536–553.

[120] T. Hirai, S. Subramaniam, and J. K. Lanyi. “Structural snapshots of conformational changes in a seven-helix membrane protein: lessons from bacteriorhodopsin”. In: *Current Opinion in Structural Biology* 19.4 (2009), pp. 433–439.

[121] T. Kouyama et al. “Crystal Structure of the Light-Driven Chloride Pump Halorhodopsin from Natronomonas pharaonis”. In: *Journal of Molecular Biology* 396.3 (2010), pp. 564–579.

[122] D. Oesterhelt and W. Stoeckenius. “Rhodopsin-like Protein from the Purple Membrane of Halobacterium halobium”. In: *Nature New Biology* 233.39 (1971), pp. 149–152.

[123] T. H. Bayburt and S. G. Sligar. “Membrane protein assembly into Nanodiscs”. In: *FEBS Letters* 584.9 (2010), pp. 1721–1727.

[124] M. C. Orwick et al. “Detergent-free formation and physicochemical characterization of nanosized lipid-polymer complexes: Lipodisq”. In: *Angewandte Chemie - International Edition* 51.19 (2012), pp. 4653–7.

[125] Y. T. Li et al. “A review on bacteriorhodopsin-based bioelectronic devices”. In: *Sensors (Switzerland)* 18.5 (2018), pp. 1–21.

[126] M. Zocher et al. “Single-molecule force spectroscopy from nanodiscs: An assay to quantify folding, stability, and interactions of native membrane proteins”. In: *ACS Nano* 6.1 (2012), pp. 961–971.

[127] R. Ashwini, S. Vijayanand, and J. Hemapriya. “Photonic Potential of Haloarchaeal Pigment Bacteriorhodopsin for Future Electronics: A Review”. In: *Current Microbiology* 74.8 (2017), pp. 996–1002.

[128] G. Miesenböck. “Optogenetic Control of Cells and Circuits”. In: *Annual Review of Cell and Developmental Biology* 27.1 (2011), pp. 731–758.

[129] E. S. Boyden. “Optogenetics and the future of neuroscience”. In: *Nature Neuroscience* 18.9 (2015), pp. 1200–1201.

[130] K. Deisseroth. “Optogenetics: 10 years of microbial opsins in neuroscience”. In: *Nature Neuroscience* 18.9 (2015), pp. 1213–1225.

[131] B. Y. Chow et al. “High-performance genetically targetable optical neural silencing by light-driven proton pumps”. In: *Nature* 463.7277 (2010), pp. 98–102.

[132] D. R. Hochbaum et al. “All-optical electrophysiology in mammalian neurons using engineered microbial rhodopsins”. In: *Nature Methods* 11.8 (2014), pp. 825–833.

[133] L. Buchen. “Neuroscience: Illuminating the brain”. In: *Nature* 465.7294 (2010), pp. 26–28.

[134] D. M. Rosenbaum, S. G. F. Rasmussen, and B. K. Kobilka. "The structure and function of G-protein-coupled receptors". In: *Nature* 459.7245 (2009), pp. 356–363.

[135] R. J. Lefkowitz and S. K. Shenoy. "Transduction of receptor signals by β-arrestins". In: *Science* 308.5721 (2005), pp. 512–517.

[136] Q. Al-Awqati. "One hundred years of membrane permeability: does Overton still rule?" In: *Nature Cell Biology* 1 (1999), pp. 201–202.

[137] R. J. Poole. "Energy coupling for membrane transport". In: *Annual Review Plant Physiology* 29 (1978), pp. 437–460.

[138] H. Lodish, A. Beck, and C. A. Kaiser. *Molecular Cell Biology*. W.H.Freeman, 2008.

[139] R. Wayne Albers. *Basic Neurochemistry*. Academic Press, 2012.

[140] P. Borst and R. O. Elferink. "Mammalian ABC Transporters in Health and Disease". In: *Annual Review of Biochemistry* 71.1 (2002), pp. 537–592.

[141] F. J. Sharom. "The P-glycoprotein multidrug transporter". In: *Essays Biochem* 50.1 (Sept. 2011), pp. 161–78.

[142] W. Lim, B. Mayer, and T. Pawson. *Cell signalling Principles and mechanisms*. Garland Science, 2015.

[143] B. Stauch and V. Cherezov. "Serial Femtosecond Crystallography of G Protein–Coupled Receptors". In: *Annual Review of Biophysics* 47.1 (2018).

[144] W.J. Thomsen and D.P. Behan. "2.20 - G Protein-Coupled Receptors". In: *Comprehensive Medicinal Chemistry II*. Ed. by John B. Taylor and David J. Triggle. Oxford: Elsevier, 2007, pp. 771–826.

[145] R. B. Clark. "Profile of Brian K. Kobilka and Robert J. Lefkowitz, 2012 Nobel Laureates in Chemistry". In: *Proceedings of the National Academy of Sciences* 110.14 (Feb. 2013), pp. 5274–5275.

[146] T. Schöneberg et al. "Mutant G-protein-coupled receptors as a cause of human diseases". In: *Pharmacol Ther* 104.3 (Dec. 2004), pp. 173–206.

[147] P. Geppetti et al. "G Protein-Coupled Receptors: Dynamic Machines for Signaling Pain and Itch". In: *Neuron* 88.4 (Nov. 2015), pp. 635–649.

[148] R. Fredriksson and H. B. Schiöth. "The repertoire of G-protein-coupled receptors in fully sequenced genomes". In: *Molecular Pharmacology* 67.5 (May 2005), pp. 1414–25.

[149] I. S. Moreira. "Structural features of the G-protein/GPCR interactions". In: *Biochimica et Biophysica Acta (BBA) - General Subjects* 1840.1 (Jan. 2014), pp. 16–33.

[150] N. Kresge, R. D. Simoni, and R. L. Hill. "The regulation of adenyl cyclase by G-protein: the work of Alfred Gilman". In: *The Journal of Biological Chemistry* 280.44 (2005).

[151] W. M. Oldham and H. E. Hamm. “Heterotrimeric G protein activation by G-protein-coupled receptors”. In: *Nature Reviews Molecular Cell Biology* 9.1 (2008), pp. 60–71.

[152] N. M. Duc, H. R. Kim, and K. Y. Chung. “Recent Progress in Understanding the Conformational Mechanism of Heterotrimeric G Protein Activation”. In: *Biomol Ther (Seoul)* 25.1 (2017), pp. 4–11.

[153] E. Ghosh et al. “Methodological advances: the unsung heroes of the GPCR structural revolution”. In: *Nature Reviews Molecular Cell Biology* 16.2 (2015), pp. 69–81.

[154] B. Jastrzebska et al. “Isolation and functional characterization of a stable complex between photoactivated rhodopsin and the G protein, transducin”. In: *The FASEB Journal* 23.2 (Feb. 2009), pp. 371–381.

[155] N. Van Eps et al. “Gi- and Gs-coupled GPCRs show different modes of G-protein binding”. In: *Proceedings of the National Academy of Sciences of the United States of America* 115.10 (2018), pp. 2383–2388.

[156] S. Ferré. “The GPCR heterotetramer: challenging classical pharmacology”. In: *Trends Pharmacol Sci* 36.3 (Mar. 2015), pp. 145–52.

[157] K. Duquesne and J. N Sturgis. “Membrane protein solubilization”. In: *Methods in Molecular Biology* 601 (2010), pp. 205–17.

[158] D. Linke. “Explanatory chapter: choosing the right detergent”. In: *Methods Enzymol* 541 (2014), pp. 141–8.

[159] A. M. Seddon, P. Curnow, and P. J. Booth. “Membrane proteins, lipids and detergents: Not just a soap opera”. In: *Biochimica et Biophysica Acta - Biomembranes* 1666.1-2 (2004), pp. 105–117.

[160] T. Arnold and D. Linke. “Phase separation in the isolation and purification of membrane proteins”. In: *BioTechniques* 43.4 (2007), pp. 427–440.

[161] D. Linke. *Chapter 34 Detergents. An Overview*. 1st ed. Vol. 463. C. Elsevier Inc., 2009.

[162] M. Orwick-Rydmark, T. Arnold, and D. Linke. “The use of detergents to purify membrane proteins”. In: *Current Protocol in Protein Science* (2016).

[163] R. Pain. “Determining the CD spectrum of a protein”. In: *Curr Protoc Protein Sci* Chapter 7 (Jan. 2005), Unit 7.6.

[164] C. Fernández and K. Wüthrich. “NMR solution structure determination of membrane proteins reconstituted in detergent micelles”. In: *FEBS Lett* 555.1 (Nov. 2003), pp. 144–50.

[165] V. Breukels et al. “Overview on the use of NMR to examine protein structure”. In: *Current Protocol in Protein Science* Chapter 17 (2011).

[166] T. J. Barnard, J. L. Wally, and S. K. Buchanan. “Crystallization of integral membrane proteins”. In: *Current Protocol in Protein Science* Chapter 17 (2007).

[167] R. S. Cantor. “Lipid composition and the lateral pressure profile in bilayers”. In: *Biophysical Journal* 76.5 (1999), pp. 2625–2639.

[168] K. Charalambous et al. “Lipid bilayer composition influences small multidrug transporters”. In: *BMC Biochemistry* 9.1 (2008), pp. 1–12.

[169] D. A. P. Gutmann et al. “A high-throughput method for membrane protein solubility screening: the ultracentrifugation dispersity sedimentation assay”. In: *Protein Science* 16.7 (2007), pp. 1422–8.

[170] O. P. Ernst et al. “Monomeric G protein-coupled receptor rhodopsin in solution activates its G protein transducin at the diffusion limit”. In: *Proceedings of the National Academy of Sciences of the United States of America* 104.26 (2007), pp. 10859–64.

[171] A. Akbarzadeh et al. “Liposome: classification, preparation, and applications”. In: *Nanoscale Res Lett* 8.1 (Feb. 2013), p. 102.

[172] M. C. Woodle and D. Papahadjopoulos. “Liposome preparation and size characterization”. In: *Methods Enzymol* 171 (1989), pp. 193–217.

[173] J.L. Rigaud and D. Lévy. “Reconstitution of membrane proteins into liposomes”. In: *Methods Enzymol* 372 (2003), pp. 65–86.

[174] B. Mui and M. J. Hope. “Formation of Large Unilamellar Vesicles by Extrusion”. In: *Liposome Technology* (2006).

[175] C. Indiveri. “Studying amino acid transport using liposomes”. In: *Methods in Molecular Biology* 606 (2010), pp. 55–68.

[176] F. J. Morera et al. “Ion-channel reconstitution”. In: *Methods in Molecular Biology* 400 (2007), pp. 571–85.

[177] I. L. Jørgensen, Gerdi Christine Kemmer, and Thomas Günther Pomorski. “Membrane protein reconstitution into giant unilamellar vesicles: a review on current techniques”. In: *European Biophysics Journal* 46.2 (2017), pp. 103–119.

[178] C. Tribet, R. Audebert, and J.-L. Popot. “Amphipols: Polymers that keep membrane proteins soluble in aqueous solutions”. In: *Proceedings of the National Academy of Sciences* 93.26 (1996), pp. 15047–15050.

[179] J.-L. Popot et al. “Amphipols From A to Z”. In: *Annual Review of Biophysics* 40.1 (2011), pp. 379–408.

[180] V. Polovinkin et al. “High-Resolution Structure of a Membrane Protein Transferred from Amphipol to a Lipidic Mesophase”. In: *Journal of Membrane Biology* 247.9-10 (2014), pp. 997–1004.

[181] C R Sanders and J H Prestegard. “Magnetically orientable phospholipid bilayers containing small amounts of a bile salt analogue, CHAPSO”. In: *Biophysical Journal* 58.2 (1990), pp. 447–60.

[182] P. Gourdon et al. “HiLiDe—Systematic Approach to Membrane Protein Crystallization in Lipid and Detergent”. In: *Crystal Growth and Design* (2011).

[183] S. Poulos et al. *Bicelles coming of age: An empirical approach to bicelle crystallization*. 1st ed. Vol. 557. Elsevier Inc., 2015.

[184] L Czerski and C R Sanders. "Functionality of a membrane protein in bicelles". In: *Anal Biochem* 284.2 (Sept. 2000), pp. 327–33.

[185] E. A. Morrison and K. A. Henzler-Wildman. "Reconstitution of integral membrane proteins into isotropic bicelles with improved sample stability and expanded lipid composition profile". In: *Biochim Biophys Acta* 1818.3 (Mar. 2012), pp. 814–20.

[186] T. H. Bayburt and S. G. Sligar. "Single-molecule height measurements on microsomal cytochrome P450 in nanometer-scale phospholipid bilayer disks". In: *Proceedings of the National Academy of Sciences of the United States of America* 99.10 (2002), pp. 6725–30.

[187] T. K. Ritchie et al. "Chapter 11 Reconstitution of Membrane Proteins in Phospholipid Bilayer Nanodiscs". In: *Methods in Enzymology* 464 (2009).

[188] I. G. Denisov and S. G. Sligar. "Nanodiscs in Membrane Biochemistry and Biophysics". In: *Chemical Reviews* 117.6 (2017), pp. 4669–4713.

[189] J. E. Rouck et al. "Recent advances in nanodisc technology for membrane protein studies (2012-2017)". In: *FEBS Lett* 591.14 (July 2017), pp. 2057–2088.

[190] N. R. Civjan et al. "Direct solubilization of heterologously expressed membrane proteins by incorporation into nanoscale lipid bilayers". In: *Biotechniques* 35.3 (Sept. 2003), pp. 556–60, 562–3.

[191] M. L. Nasr and G. Wagner. "Covalently circularized nanodiscs; challenges and applications". In: *Current Opinion in Structural Biology* 51 (2018), pp. 129–134.

[192] J. A. Lyons et al. "Saposin-Lipoprotein Scaffolds for Structure Determination of Membrane Transporters". In: *Methods in Enzymology* 594 (2017), pp. 85–99.

[193] J. Frauenfeld et al. "A saposin-lipoprotein nanoparticle system for membrane proteins". In: *Nature Methods* 13.4 (2016), pp. 345–351.

[194] A. Flayhan et al. "Saposin Lipid Nanoparticles: A Highly Versatile and Modular Tool for Membrane Protein Research". In: *Structure* 26.2 (2018), pp. 345–355.

[195] S. Scheidelaar et al. "Molecular Model for the solubilization of membranes into nanodisks by styrene maleic acid copolymers". In: *Biophysical Journal* 108.2 (2015), pp. 279–290.

[196] S R Tonge and B J Tighe. "Responsive hydrophobically associating polymers: a review of structure and properties". In: *Advanced Drug Delivery Reviews* 53.1 (2001), pp. 109–22.

[197] T. J. Knowles et al. “Membrane proteins solubilized intact in lipid containing nanoparticles bounded by styrene maleic acid copolymer”. In: *Journal of the American Chemical Society* 131.22 (2009), pp. 7484–7485.

[198] J. M. Dörr et al. “The styrene–maleic acid copolymer: a versatile tool in membrane research”. In: *European Biophysics Journal* 45.1 (2016), pp. 3–21.

[199] H. Maeda. “SMANCS and polymer-conjugated macromolecular drugs: Advantages in cancer chemotherapy”. In: *Advanced Drug Delivery Reviews* 46.1-3 (2001), pp. 169–185.

[200] S. Tonge. *Compositions Comprising a Lipid and Copolymer of Styrene and Maleic Acid*. 2006.

[201] M. Esmaili and M. Overduin. “Membrane biology visualized in nanometer-sized discs formed by styrene maleic acid polymers”. In: *Biochimica et Biophysica Acta - Biomembranes* 1860.2 (2018), pp. 257–263.

[202] S. Lindhoud et al. “SMA-SH: Modified Styrene-Maleic Acid Copolymer for Functionalization of Lipid Nanodiscs”. In: *Biomacromolecules* 17.4 (2016), pp. 1516–1522.

[203] T. Ravula et al. “Formation of pH-Resistant Monodispersed Polymer–Lipid Nanodiscs”. In: *Angewandte Chemie - International Edition* 57.5 (2018), pp. 1342–1345.

[204] A. O. Oluwole et al. “Formation of Lipid-Bilayer Nanodiscs by Diisobutylene/Maleic Acid (DIBMA) Copolymer”. In: *Langmuir* 33.50 (2017), pp. 14378–14388.

[205] D. J. K. Swainsbury et al. “Probing the local lipid environment of the Rhodobacter sphaeroides cytochrome bc1and Synechocystis sp. PCC 6803 cytochrome b6f complexes with styrene maleic acid”. In: *Biochimica et Biophysica Acta - Bioenergetics* 1859.3 (2018), pp. 215–225.

[206] V. Postis et al. “The use of SMALPs as a novel membrane protein scaffold for structure study by negative stain electron microscopy”. In: *Biochim Biophys Acta* 1848.2 (2015), pp. 496–501.

[207] D. J. K. Swainsbury et al. “Bacterial reaction centers purified with styrene maleic acid copolymer retain native membrane functional properties and display enhanced stability”. In: *Angewandte Chemie - International Edition* 53.44 (2014), pp. 11803–11807.

[208] A. R. Long et al. “A detergent-free strategy for the reconstitution of active enzyme complexes from native biological membranes into nanoscale discs”. In: *BMC Biotechnology* 13 (2013), p. 41.

[209] S. Gulati et al. “Detergent-free purification of ABC (ATP-binding-cassette) transporters”. In: *Biochemical Journal* 461.2 (2014), pp. 269–278.

[210] J. Komar et al. “Membrane protein insertion and assembly by the bacterial holo-translocon SecYEG-SecDF-YajC-YidC”. In: *Biochemical Journal* 473.19 (2016), pp. 3341–3354.

[211] S. Rehan, V. O. Paavilainen, and V. P. Jaakola. “Functional reconstitution of human equilibrative nucleoside transporter-1 into styrene maleic acid copolymer lipid particles”. In: *Biochimica et Biophysica Acta - Biomembranes* 1859.5 (2017), pp. 1059–1065.

[212] M. Jamshad et al. “G-protein coupled receptor solubilization and purification for biophysical analysis and functional studies, in the total absence of detergent”. In: *Bioscience Reports* 35.2 (2015), pp. 1–10.

[213] J. M. Dörr et al. “Detergent-free isolation, characterization, and functional reconstitution of a tetrameric potassium channel: The power of native nanodiscs”. In: *Proceedings of the National Academy of Sciences* 111.52 (2014), pp. 18607–18612.

[214] M. Jamshad et al. “Structural analysis of a nanoparticle containing a lipid bilayer used for detergent-free extraction of membrane proteins”. In: *Nano Research* 8.3 (2015), pp. 774–789.

[215] E. Reading. “Structural mass spectrometry of membrane protein within their native lipid environments”. In: *Chemistry* (2018).

[216] I. D. Sahu et al. “DEER EPR measurements for membrane protein structures via bifunctional spin labels and lipodisq nanoparticles”. In: *Biochemistry* 52.38 (2013), pp. 6627–6632.

[217] C. Logez et al. “Detergent-free Isolation of Functional G Protein-Coupled Receptors into Nanometric Lipid Particles”. In: *Biochemistry* 55.1 (2016), pp. 38–48.

[218] J. Broecker, B. T. Eger, and O. P. Ernst. “Crystallogenesis of Membrane Proteins Mediated by Polymer-Bounded Lipid Nanodiscs”. In: *Structure* 25.2 (2017), pp. 384–392.

[219] M. Parmar et al. “Using a SMALP platform to determine a sub-nm single particle cryo-EM membrane protein structure”. In: *Biochimica et Biophysica Acta - Biomembranes* 1860.2 (2018), pp. 378–383.

[220] C. Sun et al. “Structure of the alternative complex III in a supercomplex with cytochrome oxidase”. In: *Nature* 557.7703 (2018), pp. 123–126.

[221] S E Stein and D R Scott. “Optimization and testing of mass spectral library search algorithms for compound identification”. In: *Journal American Society Mass Spectrometry* 5.9 (1994), pp. 859–66.

[222] P. Lössl, M. van de Waterbeemd, and A. J. R. Heck. “The diverse and expanding role of mass spectrometry in structural and molecular biology”. In: *The EMBO Journal* 35.24 (2016), pp. 2634–2657.

[223] I. V. Chernushevich, W. Ens, and K. G. Standing. “Peer Reviewed: Orthogonal-Injection TOFMS for Analyzing Biomolecules”. In: *Analytical Chemistry* 71.13 (1999), 452A–61A.

[224] A. G. Marshall and C. L. Hendrickson. “High-resolution mass spectrometers”. In: *Annual Review of Analytical Chemistry* 1 (2008), pp. 579–99.

[225] S. Mehmood, T. M. Allison, and C. V. Robinson. “Mass Spectrometry of Protein Complexes: From Origins to Applications”. In: *Annual Review of Physical Chemistry* 66.1 (2015), pp. 453–474.

[226] M. Scigelova and A. Makarov. “Orbitrap mass analyzer - Overview and applications in proteomics”. In: *Proteomics* 1.1-2 SUPPL. (2006), pp. 16–21.

[227] B. T. Ruotolo et al. “Evidence for macromolecular protein rings in the absence of bulk water”. In: *Science* 310.5754 (Dec. 2005), pp. 1658–61.

[228] E. van Duijn. “Current limitations in native mass spectrometry based structural biology”. In: *Journal American Society Mass Spectrometry* 21.6 (June 2010), pp. 971–8.

[229] A. Konijnenberg et al. “Extending native mass spectrometry approaches to integral membrane proteins”. In: *Biological Chemistry* 396.9-10 (2015), pp. 991–1002.

[230] A. Laganowsky et al. “Mass spectrometry of intact membrane protein complexes”. In: *Nature Protocols* 8.4 (2013), pp. 639–651.

[231] J. L. P. Benesch. “Collisional activation of protein complexes: picking up the pieces”. In: *Journal American Society Mass Spectrometry* 20.3 (2009), pp. 341–8.

[232] K. R. Jennings. “The changing impact of the collision-induced decomposition of ions on mass spectrometry”. In: *International Journal of Mass Spectrometry* 200.1 (2000), pp. 479–493.

[233] A. Makarov. “Electrostatic axially harmonic orbital trapping: a high-performance technique of mass analysis”. In: *Analytical Chemistry* 72.6 (2000), pp. 1156–62.

[234] R. A. Zubarev and A. Makarov. “Orbitrap mass spectrometry”. In: *Analytical Chemistry* 85.11 (June 2013), pp. 5288–96.

[235] J. T. S. Hopper et al. “Detergent-free mass spectrometry of membrane protein complexes”. In: *Nature Methods* 10.12 (2013), pp. 1206–1208.

[236] L. Lin et al. “Types, principle, and characteristics of tandem high-resolution mass spectrometry and its applications”. In: *RSC Advances* 5.130 (2015), pp. 107623–107636.

[237] T. M. Annesley. “Ion suppression in mass spectrometry”. In: *Clinical chemistry* 49.7 (2003), pp. 1041–4.

[238] N. P. Barrera et al. “Micelles protect membrane complexes from solution to vacuum”. In: *Science* 321.5886 (2008), pp. 243–246.

[239] A. J Borysik and C. V. Robinson. “Formation and dissociation processes of gas-phase detergent micelles”. In: *Langmuir* 28.18 (May 2012), pp. 7160–7.

[240] P. Lössl, J. Snijder, and A. J. R. Heck. “Boundaries of mass resolution in native mass spectrometry”. In: *Journal American Society Mass Spectrometry* 25.6 (2014), pp. 906–17.

[241] F. Sobott et al. “The flight of macromolecular complexes in a mass spectrometer”. In: *Philosophical transactions. Series A, Mathematical, physical, and engineering sciences* 363.1827 (2005), pp. 379–91.

[242] N. P. Barrera and C. V. Robinson. “Advances in the Mass Spectrometry of Membrane Proteins: From Individual Proteins to Intact Complexes”. In: *Annual Review of Biochemistry* 80.1 (2011), pp. 247–271.

[243] N. P. Barrera, M. Zhou, and C. V. Robinson. “The role of lipids in defining membrane protein interactions: insights from mass spectrometry”. In: *Trends Cell Biol* 23.1 (Jan. 2013), pp. 1–8.

[244] A. Konijnenberg, A. Butterer, and F. Sobott. “Native ion mobility-mass spectrometry and related methods in structural biology”. In: *Biochim Biophys Acta* 1834.6 (June 2013), pp. 1239–56.

[245] J. Marcoux et al. “Mass spectrometry reveals synergistic effects of nucleotides, lipids, and drugs binding to a multidrug resistance efflux pump”. In: *Proceedings of the National Academy of Sciences of the United States of America* 110.24 (2013), pp. 9704–9.

[246] F. Lanucara et al. “The power of ion mobility-mass spectrometry for structural characterization and the study of conformational dynamics”. In: *Nature Chemistry* 6.4 (2014), pp. 281–94.

[247] A. Konijnenberg et al. “Global structural changes of an ion channel during its gating are followed by ion mobility mass spectrometry”. In: *Proceedings of the National Academy of Sciences of the United States of America* 111.48 (Dec. 2014), pp. 17170–5.

[248] M. Göth and K. Pagel. “Ion mobility–mass spectrometry as a tool to investigate protein–ligand interactions”. In: *Analytical and Bioanalytical Chemistry* 409.18 (2017), pp. 4305–4310.

[249] M. T. Marty et al. “Probing the Lipid Annular Belt by Gas-Phase Dissociation of Membrane Proteins in Nanodiscs”. In: *Angewandte Chemie - International Edition* 55.2 (2016), pp. 550–554.

[250] E. Pyle et al. “Structural Lipids Enable the Formation of Functional Oligomers of the Eukaryotic Purine Symporter UapA”. In: *Cell Chemical Biology* (2018), pp. 1–9.

[251] H.-Y. Yen et al. “Ligand binding to a G protein–coupled receptor captured in a mass spectrometer”. In: *Science Advances* 3.6 (2017), e1701016.

[252] J. W. Patrick et al. “Allostery revealed within lipid binding events to membrane proteins”. In: *Proceedings of the National Academy of Sciences* (2018), p. 201719813.

[253] K. Gupta et al. “Identifying key membrane protein lipid interactions using mass spectrometry”. In: *Nature Protocols* 13.5 (2018), pp. 1106–1120.

[254] M. Landreh et al. “Effects of Detergent Micelles on Lipid Binding to Proteins in Electrospray Ionization Mass Spectrometry”. In: *Analytical Chemistry* 89.14 (2017), pp. 7425–7430.

[255] M. T. Marty et al. “Native mass spectrometry characterization of intact nanodisc lipoprotein complexes”. In: *Analytical Chemistry* 84.21 (Nov. 2012), pp. 8957–60.

[256] M. T. Marty et al. “Bayesian deconvolution of mass and ion mobility spectra: from binary interactions to polydisperse ensembles”. In: *Anal Chem* 87.8 (2015), pp. 4370–6.

[257] URL: `https://elviajero.elpais.com/elviajero/imagenes/2015/10/22/actualidad/1445523532_424526_1445944877_sumario_grande.jpg`.

[258] URL: `http://www.biochem.mpg.de/5686208/%20and%20http://www.ks.uiuc.edu/Research/newbr/heptamer_big.jpg`.

[259] H. Belrhali et al. “Protein, lipid and water organization in bacteriorhodopsin crystals: A molecular view of the purple membrane at 1.9 Å resolution”. In: *Structure* 7.8 (1999), pp. 909–917.

[260] J. Muller, C. Munster, and T. Salditt. “Thermal denaturing of bacteriorhodopsin by X-Ray scattering from oriented purple membranes”. In: *Biophys J* 78.6 (2000), pp. 3208–17.

[261] I. Domonkos, M. Kis, and Z. Gombos. “Versatile roles of lipids and carotenoids in membranes”. In: *Acta Biologica Szegediensis* 59.2013 (2015), pp. 83–104.

[262] R. Angelini et al. “Novel ether lipid cardiolipins in archaeal membranes of extreme haloalkaliphiles”. In: *Biochimica et Biophysica Acta - Biomembranes* 1818.5 (2012), pp. 1365–1373.

[263] R. Henderson and P. N. Unwin. “Three-dimensional model of purple membrane obtained by electron microscopy”. In: *Nature* 257.5521 (1975), pp. 28–32.

[264] R. Henderson et al. “Model for the structure of bacteriorhodopsin based on high-resolution electron cryo-microscopy”. In: *Journal of Molecular Biology* 213.4 (1990), pp. 899–929.

[265] S. Faham and J. U. Bowie. “Bicelle crystallization: a new method for crystallizing membrane proteins yields a monomeric bacteriorhodopsin structure”. In: *J Mol Biol* 316.1 (Feb. 2002), pp. 1–6.

[266] G. Rummel et al. “Lipidic Cubic Phases: New Matrices for the Three-Dimensional Crystallization of Membrane Proteins”. In: *Journal of Structural Biology* 121.2 (1998), pp. 82–91.

[267] P. Nollert. “Lipidic cubic phases as matrices for membrane protein crystallization”. In: *Methods* 34.3 (Nov. 2004), pp. 348–53.

[268] E. Nango et al. “A three-dimensionalmovie of structural changes in bacteriorhodopsin”. In: *Science* 354.6319 (2016), pp. 1552–1557.

[269] P. Nogly et al. “Retinal isomerization in bacteriorhodopsin captured by a femtosecond x-ray laser”. In: *Science* 361.6398 (July 2018).

[270] J. Heberle et al. “Bacteriorhodopsin: the functional details of a molecular machine are being resolved”. In: *Biophysical Chemistry* 85.2-3 (2000), pp. 229–48.

[271] C. D. Heyes and M. A. El-Sayed. “The role of the native lipids and lattice structure in bacteriorhodopsin protein conformation and stability as studied by temperature-dependent Fourier transform-infrared spectroscopy”. In: *Journal of Biological Chemistry* 277.33 (2002), pp. 29437–43.

[272] B. Sternberg et al. “The essential role of specific Halobacterium halobium polar lipids in 2D-array formation of bacteriorhodopsin”. In: *Biochim Biophys Acta* 1108.1 (July 1992), pp. 21–30.

[273] D. J. Müller and A. Engel. “Atomic force microscopy and spectroscopy of native membrane proteins”. In: *Nature Protocols* 2.9 (2007), pp. 2191–2197.

[274] J. Wang et al. “Comparison of the dynamics of the primary events of bacteriorhodopsin in its trimeric and monomeric states”. In: *Biophysical Journal* 83.3 (2002), pp. 1557–66.

[275] S J Milder et al. “Effects of detergent environments on the photocycle of purified monomeric bacteriorhodopsin”. In: *Biochemistry* 30.7 (Feb. 1991), pp. 1751–61.

[276] L. Whitmore and B. A. Wallace. “Protein secondary structure analyses from circular dichroism spectroscopy: methods and reference databases”. In: *Biopolymers* 89.5 (May 2008), pp. 392–400.

[277] W C Johnson. “Analyzing protein circular dichroism spectra for accurate secondary structures”. In: *Proteins* 35.3 (May 1999), pp. 307–12.

[278] A. Abdul-Gader, A. J. Miles, and B. A. Wallace. “A reference dataset for the analyses of membrane protein secondary structures and transmembrane residues using circular dichroism spectroscopy”. In: *Bioinformatics* 27.12 (2011), pp. 1630–6.

[279] URL: `http://psldc.isis.rl.ac.uk/Psldc/`.

[280] URL: `https://avantilipids.com/tech-support/analytical-procedures/tlc-solvent-systems/`.

[281] R J Cherry and U Müller. “Temperature-dependent aggregation of bacteriorhodopsin in dipalmitoyl- and dimyristoylphosphatidylcholine vesicles”. In: *Journal of Molecular Biology* 121.2 (1978), pp. 283–98.

[282] B. Sternberg, A. Watts, and Z. Cejka. “Lipid-Induced Modulation of the Protein Packing in Two-Dimensional Crystals of Bacteriorhodopsin”. In: *Journal of Structural Biology* 110.3 (1993), pp. 196–204.

[283] M. P. Krebs and T. A. Isenbarger. “Structural determinants of purple membrane assembly”. In: *Biochimica et Biophysica Acta - Bioenergetics* 1460.1 (2000), pp. 15–26.

[284] M. C. Orwick et al. “Detergent-Free Formation and Physicochemical Characterization of Nanosized Lipid-Polymer Complexes: Lipodisq”. In: *Angewandte Chemie - International Edition* 51.19 (2012), pp. 4653–4657.

[285] M. Orwick-Rydmark et al. “Detergent-Free Incorporation of a Seven-Transmembrane Receptor Protein into Nanosized Bilayer Lipodisq Particles for Functional and Biophysical Studies”. In: *Nano Letters* 12.9 (2012), pp. 4687–4692.

[286] T. H. Bayburt et al. “Transducin activation by nanoscale lipid bilayers containing one and two rhodopsins”. In: *Journal of Biological Chemistry* 282.20 (2007), pp. 14875–14881.

[287] A. J. Miles and B. A. Wallace. “Circular dichroism spectroscopy of membrane proteins”. In: *Chemical Society Reviews* 45.18 (2016), pp. 4859–4872.

[288] A J Jackson. “Introduction to Small-Angle Neutron Scattering and Neutron Reflectometry”. In: *NIST Center for Neutron Research* May (2008), pp. 1–24.

[289] J. J. Dominguez Pardo et al. “Thermotropic properties of phosphatidylcholine nanodiscs bounded by styrene-maleic acid copolymers”. In: *Chemistry and Physics of Lipids* 208 (2017), pp. 58–64.

[290] N V Katre et al. “Attachment site(s) of retinal in bacteriorhodopsin”. In: *Proceedings of the National Academy of Sciences of the United States of America* 78.7 (1981), pp. 4068–72.

[291] L E Ball et al. “Mass spectrometric analysis of integral membrane proteins: application to complete mapping of bacteriorhodopsins and rhodopsin”. In: *Protein Science* 7.3 (1998), pp. 758–64.

[292] C. M. Ryan et al. “Post-translational Modifications of Integral Membrane Proteins Resolved by Top-down Fourier Transform Mass Spectrometry with Collisionally Activated Dissociation”. In: *Molecular & Cellular Proteomics* 9.5 (2010), pp. 791–803.

[293] P. J. Booth. “Unravelling the folding of bacteriorhodopsin”. In: *Biochimica et Biophysica Acta - Bioenergetics* 1460.1 (2000), pp. 4–14.

[294] D. Oesterhelt. “Bacteriorhodopsin”. In: *Methods in Enzymology* 88 (1982), pp. 10–17.

[295] A. M. Dummer et al. “Bacterioopsin-Mediated regulation of bacterioruberin biosynthesis in Halobacterium salinarum”. In: *Journal of Bacteriology* 193.20 (2011), pp. 5658–5667.

[296] J. A. Griffiths et al. “Calcium and Magnesium Binding in Native and Structurally Perturbed Purple Membrane”. In: *The Journal of Physical Chemistry* 100.3 (1996), pp. 929–933.

[297] R. Vreeland and L. Hochstein. *The biology of Halophillic bacteria*. CRC Press, 1992.

[298] S. Lobasso et al. “Osmotic shock induces the presence of glycocardiolipin in the purple membrane of Halobacterium salinarum”. In: *Journal of Lipid Research* 44.11 (2003), pp. 2120–2126.

[299] C. Renner, B. Kessler, and D. Oesterhelt. “Lipid composition of integral purple membrane by 1H and 31P NMR”. In: *Journal of Lipid Research* 46.8 (2005), pp. 1755–1764.

[300] R. Angelini et al. “MALDI-TOF/MS analysis of archaebacterial lipids in lyophilized membranes dry-mixed with 9-aminoacridine”. In: *Journal of Lipid Research* 51.9 (2010), pp. 2818–2825.

[301] URL: `https://avantilipids.com/tech-support/physical-properties/miscibility`.

[302] E.G. Bligh and W.J. Dyer. “Canadian Journal of Biochemistry and Physiology”. In: *Canadian Journal of Biochemistry and Physiology* 37.8 (1959), pp. 911–917.

[303] J. J. Mousa and S. D. Bruner. “Structural and mechanistic diversity of multidrug transporters”. In: *Natural Product Reports* 33.11 (2016), pp. 1255–1267.

[304] A. T. Nies et al. “Structure and function of multidrug and toxin extrusion proteins (MATEs) and their relevance to drug therapy and personalized medicine”. In: *Archives of Toxicology* 90.7 (2016), pp. 1555–1584.

[305] Y. Tanaka, S. Iwaki, and T. Tsukazaki. “Crystal Structure of a Plant Multidrug and Toxic Compound Extrusion Family Protein”. In: *Structure* 25.9 (2017), 1455–1460.e2.

[306] H. Miyauchi et al. “Structural basis for xenobiotic extrusion by eukaryotic MATE transporter”. In: *Nature Communications* 8.1 (2017).

[307] A. Yonezawa and K. I. Inui. “Organic cation transporter OCT/SLC22A and H+/organic cation antiporter MATE/SLC47A are key molecules for nephrotoxicity of platinum agents”. In: *Biochemical Pharmacology* 81.5 (2011), pp. 563–568.

[308] C. J. Hipolito, N. K. Bashiruddin, and H. Suga. “Protein cocrystallization molecules originating from in vitro selected macrocyclic peptides”. In: *Current Opinion in Structural Biology* 26.1 (2014), pp. 24–31.

[309] Y. Tanaka et al. “Structural basis for the drug extrusion mechanism by a MATE multidrug transporter”. In: *Nature* 496.7444 (2013), pp. 247–251.

[310] T. Terada and K. I. Inui. “Physiological and pharmacokinetic roles of H+/organic cation antiporters (MATE/SLC47A)”. In: *Biochemical Pharmacology* 75.9 (2008), pp. 1689–1696.

[311] M. Lu et al. “Structures of a Na+-coupled, substrate-bound MATE multidrug transporter”. In: *Proceedings of the National Academy of Sciences* 110.6 (2013), pp. 2099–2104.

[312] C. J. Hipolito et al. “A macrocyclic peptide that serves as a cocrystallization ligand and inhibits the function of a MATE family transporter”. In: *Molecules* 18.9 (2013), pp. 10514–10530.

[313] E. W. Yu, J. R. Aires, and H. Nikaido. "AcrB multidrug efflux pump of Escherichia coli: Composite substrate-binding cavity of exceptional flexibility generates its extremely wide substrate specificity". In: *Journal of Bacteriology* 185.19 (2003), pp. 5657–5664.

[314] Y.-J. Chen et al. "X-ray structure of EmrE supports dual topology model". In: *Proceedings of the National Academy of Sciences of the United States of America* 104.48 (2007), pp. 18999–19004.

[315] S. Dutta, E. A. Morrison, and K. A. Henzler-Wildman. "EmrE dimerization depends on membrane environment". In: *Biochimica et Biophysica Acta - Biomembranes* 1838.7 (2014), pp. 1817–1822.

[316] L. Brandstätter et al. "Analysis of AcrB and AcrB/DARPin ligand complexes by LILBID MS". In: *Biochim Biophys Acta* 1808.9 (Sept. 2011), pp. 2189–96.

[317] G. Pándy-Szekeres et al. "GPCRdb in 2018: adding GPCR structure models and ligands". In: *Nucleic Acids Res* 46.D1 (Jan. 2018), pp. D440–D446.

[318] V. V. Gurevich and E. V. Gurevich. "GPCRs and Signal Transducers: Interaction Stoichiometry". In: *Trends in Pharmacological Sciences* 0.0 (2018), pp. 1–13.

[319] R. Fredriksson et al. "The G-protein-coupled receptors in the human genome form five main families. Phylogenetic analysis, paralogon groups, and fingerprints". In: *Molecular Pharmacology* 63.6 (2003), pp. 1256–72.

[320] R. R. Gainetdinov et al. "Desensitization of G protein-coupled receptors and neuronal functions". In: *Annual Review Neuroscience* 27 (2004), pp. 107–44.

[321] R. P. Millar and C. L. Newton. "The Year In G Protein-Coupled Receptor Research". In: *Molecular Endocrinology* 24.1 (2010), pp. 261–274.

[322] N. L. Vekshina et al. "Dopamine D1–D2 receptor heterodimers: A literature review". In: *Biochemistry (Moscow), Supplement Series B: Biomedical Chemistry* 11.2 (2017), pp. 111–119.

[323] G. Y. K. Ng et al. "Desensitization, phosphorylation and palmitoylation of the human dopamine D1receptor". In: *European Journal of Pharmacology: Molecular Pharmacology* 267.1 (1994), pp. 7–19.

[324] J.-L. Cadet et al. "Dopamine D1 receptors, regulation of gene expression in the brain, and neurodegeneration". In: *CNS Neurol Disord Drug Targets* 9.5 (2010), pp. 526–538.

[325] G. Y. K. Ng et al. "Phosphorylation and Palmitoylation of the Human D2LDopamine Receptor in Sf9 Cells". In: *Journal of Neurochemistry* 63.5 (1994), pp. 1589–1595.

[326] B. Ebersole et al. "Effect of C-Terminal S-palmitoylation on D2 dopamine receptor trafficking and stability". In: *PLoS ONE* 10.11 (2015), pp. 1–23.

[327] C. Rangel-Barajas, I. Coronel, and B. Florán. "Dopamine Receptors and Neurodegeneration". In: *Aging Dis* 6.5 (2015), pp. 349–68.

[328] D. Armstrong and P. G. Strange. “Dopamine D2 receptor dimer formation. Evidence from ligand binding”. In: *Journal of Biological Chemistry* 276.25 (2001), pp. 22621–22629.

[329] K. Fuxe et al. “Diversity and bias through receptor-receptor interactions in GPCR heteroreceptor complexes. Focus on examples from dopamine D2 receptor heteromerization”. In: *Frontiers in Endocrinology* 5 (2014), pp. 1–11.

[330] S. R. George et al. *Dopamine receptor heteromeric complexes and their emerging functions*. 1st ed. Vol. 211. Elsevier B.V., 2014.

[331] K. Fuxe et al. “Intramembrane Interactions between Neurotensin Receptors and Dopamine D2Receptors as a Major Mechanism for the Neuroleptic-like Action of Neurotensin”. In: *Annals of the New York Academy of Sciences* 668.1 (1992), pp. 186–204.

[332] G Von Euler. “Biochemical characterization of the intramembrane interaction between neurotensin and dopamine D2 receptors in the rat brain”. In: *Brain Research* 561 (1991), pp. 93–98.

[333] A. M. Bagher et al. “Bidirectional allosteric interactions between cannabinoid receptor 1 (CB1) and dopamine receptor 2 long (D2L) heterotetramers”. In: *European Journal of Pharmacology* 813 (2017), pp. 66–83.

[334] E. Y. T. Chien et al. “Structure of the human dopamine D3 receptor in complex with a D2/D3 selective antagonist”. In: *Science* 330.6007 (2010), pp. 1091–5.

[335] S. Wang et al. “D4 dopamine receptor high-resolution structures enable the discovery of selective agonists”. In: *Science* 358.6361 (2017), pp. 381–386.

[336] S. Wang et al. “Structure of the D2 dopamine receptor bound to the atypical antipsychotic drug risperidone”. In: *Nature* 555 (2018), pp. 268–273.

[337] D. Milic and D. B. Veprintsev. “Large-scale production and protein engineering of G protein-coupled receptors for structural studies”. In: *Frontiers in Pharmacology* 6 (2015), pp. 1–24.

[338] URL: `https://www.biozentrum.unibas.ch/uploads/media/Microscale_Thermophoresis_Intro.pdf`.

[339] M. Jerabek-Willemsen et al. “MicroScale Thermophoresis: Interaction analysis and beyond”. In: *Journal of Molecular Structure* 1077 (2014), pp. 101–113.

[340] S. C. Lee et al. “A method for detergent-free isolation of membrane proteins in their local lipid environment”. In: *Nature Protocols* 11.7 (2016), pp. 1149–1162.

[341] N. L. Pollock et al. “Structure and function of membrane proteins encapsulated in a polymer-bound lipid bilayer”. In: *Biochimica et Biophysica Acta - Biomembranes* 1860.4 (2018), pp. 809–817.

[342] S. A. I. Seidel et al. “Microscale thermophoresis quantifies biomolecular interactions under previously challenging conditions”. In: *Methods* 59.3 (2013), pp. 301–315.

[343] P. Ryan Steed et al. “Na+-substrate coupling in the multidrug antiporter NorM probed with a spin-labeled substrate”. In: *Biochemistry* 52.34 (2013), pp. 5790–5799.

[344] F. Long et al. “Functional cloning and characterization of the multidrug efflux pumps NorM from Neisseria gonorrhoeae and YdhE from Escherichia coli”. In: *Antimicrobial Agents and Chemotherapy* 52.9 (2008), pp. 3052–3060.

[345] G. P. Kirillova et al. “Dopamine receptors in human lymphocytes: Radioligand binding and quantitative RT-PCR assays”. In: *Journal of Neuroscience Methods* 174.2 (2008), pp. 272–280.

[346] D. J. Luessen and R. Chen. “Psychostimulants, Brain Membrane Lipids and Dopamine Transmission”. In: *Journal of Biomolecular Research & Therapeutics* (2016).

[347] P. J. Voulalas, J. Schetz, and A. S. Undieh. “Differential subcellular distribution of rat brain dopamine receptors and subtype-specific redistribution induced by cocaine”. In: *Molecular Cell Neuroscience* 46.3 (2011), pp. 645–54.

[348] D. Du et al. “Structure, mechanism and cooperation of bacterial multidrug transporters”. In: *Current Opinion in Structural Biology* 33 (2015), pp. 76–91.

[349] J. Sun, Z. Deng, and A. Yan. “Bacterial multidrug efflux pumps: Mechanisms, physiology and pharmacological exploitations”. In: *Biochemical and Biophysical Research Communications* 453.2 (2014), pp. 254–267.

[350] V. M. Bolanos-Garcia and O. R. Davies. “Structural analysis and classification of native proteins from E. coli commonly co-purified by immobilised metal affinity chromatography”. In: *Biochim Biophys Acta* 1760.9 (2006), pp. 1304–13.

[351] H. Jin et al. “Palmitoylation occurs at cysteine 347 and cysteine 351 of the dopamine D1receptor”. In: *European Journal of Pharmacology* 386.2-3 (1999), pp. 305–312.

[352] X. Zhang et al. “Palmitoylation on the carboxyl terminus tail is required for the selective regulation of dopamine D2versus D3receptors”. In: *Biochimica et Biophysica Acta - Biomembranes* 1858.9 (2016), pp. 2152–2162.

[353] K. Seno and F. Hayashi. “Palmitoylation is a prerequisite for dimerization-dependent raftophilicity of rhodopsin”. In: *Journal of Biological Chemistry* 292.37 (2017), pp. 15321–15328.

[354] V. Cherezov et al. “High-resolution crystal structure of an engineered human beta2-adrenergic G protein-coupled receptor”. In: *Science* 318.5854 (2007), pp. 1258–65.

[355] H. Zheng et al. “Palmitoylation and membrane cholesterol stabilize μ-opioid receptor homodimerization and G protein coupling”. In: *BMC Cell Biol* 13 (2012), p. 6.

[356] J. Kaur and D. P. Reinhardt. “Immobilized Metal Affinity Chromatography Co-Purifies TGF-β1 with Histidine-Tagged Recombinant Extracellular Proteins”. In: *PLoS ONE* 7.10 (2012).

[357] M. Beinborn et al. “TGF-beta regulates T-cell neurokinin-1 receptor internalization and function.” In: *Proceedings of the National Academy of Sciences of the United States of America* 107.9 (2010), pp. 4293–8.

[358] K. Yoshimura and T. Kouyama. “Structural Role of Bacterioruberin in the Trimeric Structure of Archaerhodopsin-2”. In: *Journal of Molecular Biology* 375.5 (2008), pp. 1267–1281.

[359] L. Tang et al. “Imaging bacteriorhodopsinlike molecules of claretmembranes from Tibet halobacteria xz515 by atomic force microscope”. In: *Chinese Science Bulletin* 46.22 (2001), p. 1897.

[360] M. Rodrigo-Baños et al. “Carotenoids from Haloarchaea and their potential in biotechnology”. In: *Marine Drugs* 13.9 (2015), pp. 5508–5532.

[361] C. Sun et al. “In Situ Study of the Function of Bacterioruberin in the Dual-Chromophore Photoreceptor Archaerhodopsin-4”. In: *Angewandte Chemie* 130.29 (2018), pp. 9075–9079.

[362] Z. Cao et al. “Novel expression and characterization of a light driven proton pump archaerhodopsin 4 in a Halobacterium salinarum strain”. In: *Biochimica et Biophysica Acta - Bioenergetics* 1847.4-5 (2015), pp. 390–398.

[363] I. D. Dundas and H. Larsen. “The physiological role of the carotenoid pigments of halobacterium salinarium”. In: *Archiv für Mikrobiologie* 44.3 (1962), pp. 233–239.

[364] H. Okumura et al. “Morphological Change of the Higher Order Structure of Archaerhodopsin”. In: *Seibutsu Butsuri* 40.S41 (2000).

[365] D. Brinks et al. “Painting with Rainbows: Patterning Light in Space, Time, and Wavelength for Multiphoton Optogenetic Sensing and Control”. In: *Accounts of Chemical Research* 49.11 (2016), pp. 2518–2526.

[366] K. Deisseroth. “Optogenetics”. In: *Nature Methods* 8.1 (2011), pp. 26–29.

[367] E. Pastrana. “Optogenetics: Controlling cell function with light”. In: *Nature Methods* 8.1 (2011), pp. 24–25.

[368] R. S. McIsaac, Claire N Bedbrook, and Frances H Arnold. “Recent advances in engineering microbial rhodopsins for optogenetics”. In: *Current Opinion in Structural Biology* 33 (2015), pp. 8–15.

[369] X. Han et al. “A High-Light Sensitivity Optical Neural Silencer: Development and Application to Optogenetic Control of Non-Human Primate Cortex”. In: *Frontiers in Systems Neuroscience* 5 (2011).

[370] E. P. Lukashev et al. “pH dependence of the absorptionspectra and photochemical transformations of the archaerhodopsins”. In: *Photochemistry and Photobiology* 60.1 (1994), pp. 69–75.

[371] T. Kouyama et al. “Structure of archaerhodopsin-2 at 1.8Å resolution”. In: *Acta Crystallographica Section D: Biological Crystallography* 70.10 (2014), pp. 2692–2701.

[372] M. Ming et al. “Triton X-100 can alter the temporal sequence of the light-driven proton pump of archaerhodopsin 4”. In: *FEBS Letters* 580.28-29 (2006), pp. 6749–6753.

[373] D. MacLaurin et al. “Mechanism of voltage-sensitive fluorescence in a microbial rhodopsin”. In: *Proceedings of the National Academy of Sciences of the United States of America.* (2013).

[374] K. Inoue et al. “Converting a light-driven proton pump into a light-gated proton channel”. In: *Journal of the American Chemical Society* 137.9 (2015), pp. 3291–3299.

[375] E. C. Saint Clair et al. “Near-IR resonance Raman spectroscopy of archaerhodopsin 3: Effects of transmembrane potential”. In: *Journal of Physical Chemistry B* 116.50 (2012), pp. 14592–14601.

[376] S Karnik et al. “Expression of the archaebacterial bacterio-opsin gene with and without signal sequences in Escherichia coli: the expressed proteins are located in the membrane but bind retinal poorly”. In: *Proceedings of the National Academy of Sciences of the United States of America* 87.22 (1990), pp. 8955–9.

[377] R F Shand et al. “Wild-type and mutant bacterioopsins D85N, D96N, and R82Q: high-level expression in Escherichia coli”. In: *Biochemistry* 30.12 (Mar. 1991), pp. 3082–8.

[378] I. Moraes et al. “Membrane protein structure determination - The next generation”. In: *Biochimica et Biophysica Acta - Biomembranes* 1838 (2014), pp. 78–87.

[379] P. Nogly et al. “Lipidic cubic phase serial millisecond crystallography using synchrotron radiation”. In: *IUCrJ* 2 (2015), pp. 168–176.

[380] R Neutze et al. “Potential for biomolecular imaging with femtosecond X-ray pulses”. In: *Nature* 406.6797 (Aug. 2000), pp. 752–7.

[381] R. Neutze, G. Brändén, and G. F.X. Schertler. “Membrane protein structural biology using X-ray free electron lasers”. In: *Current Opinion in Structural Biology* 33 (2015), pp. 115–125.

[382] K. Hirata et al. “Determination of damage-free crystal structure of an X-ray-sensitive protein using an XFEL”. In: *Nature Methods* 11.7 (2014), pp. 734–6.

[383] A. Ishchenko, C. Gati, and V. Cherezov. “Structural biology of G protein-coupled receptors: new opportunities from XFELs and cryoEM”. In: *Current Opinion in Structural Biology* 51 (2018), pp. 44–52.

[384] J. M. Grimes et al. “Where is crystallography going?” In: *Acta Crystallographica Section D: Structural Biology* 74 (2018), pp. 152–166.

[385] H. N. Chapman et al. “Femtosecond X-ray protein nanocrystallography”. In: *Nature* 470.7332 (2011), pp. 73–7.

[386] H. N. Chapman, C. Caleman, and N. Timneanu. “Diffraction before destruction”. In: *Philosophical Transactions of the Royal Society B: Biological Sciences* 369.1647 (2014).

[387] L. C. Johansson et al. “A Bright Future for Serial Femtosecond Crystallography with XFELs”. In: *Trends in Biochemical Sciences* 42.9 (2017), pp. 749–762.

[388] M. Schmidt. “Time-Resolved Macromolecular Crystallography at Modern X-Ray Sources”. In: *Methods in Molecular Biology* 1607 (2017), pp. 273–294.

[389] W. Liu et al. “Femtosecond crystallography of membrane proteins in the lipidic cubic phase”. In: *Philosophical Transactions of the Royal Society B: Biological Sciences* 369.1647 (2014).

[390] H. van den Bedem and J. S. Fraser. “Integrative, dynamic structural biology at atomic resolution–it’s about time”. In: *Nature Methods* 12.4 (2015), pp. 307–18.

[391] J C H Spence. “XFELs for structure and dynamics in biology”. In: *IUCrJ* 4 (2017), pp. 322–339.

[392] J.-H. Lee, N. A. Zatsepin, and K. H. Kim. “Time-resolved serial femtosecond X-ray crystallography”. In: *Biodesign* 6.1 (2018), pp. 15–22.

[393] E. M. Landau and J. P. Rosenbusch. “Lipidic cubic phases: a novel concept for the crystallization of membrane proteins”. In: *Proceedings of the National Academy of Sciences of the United States of America.* 93.25 (1996), pp. 14532–5.

[394] M. Caffrey and V. Cherezov. “Crystallizing membrane proteins using lipidic mesophases”. In: *Nature Protocols* 4.5 (2009), pp. 706–31.

[395] X. Ding et al. “Functional roles of tyrosine 185 during the bacteriorhodopsin photocycle as revealed by in situ spectroscopic studies”. In: *Biochimica et Biophysica Acta - Bioenergetics* (2018).

[396] A. Oren. “Halobacterium sodomense sp. nov., a Dead Sea Halobacterium with an Extremely High Magnesium Requirement”. In: *International Journal of Systematic Bacteriology* 33.2 (1983), pp. 381–386.

[397] N. Enami et al. “Crystal Structures of Archaerhodopsin-1 and -2: Common Structural Motif in Archaeal Light-driven Proton Pumps”. In: *Journal of Molecular Biology* 358.3 (2006), pp. 675–685.

[398] S Subramaniam, T Marti, and H G Khorana. “Protonation state of Asp (Glu)-85 regulates the purple-to-blue transition in bacteriorhodopsin mutants Arg-82—-Ala and Asp-85—-Glu: the blue form is inactive in proton translocation”. In: *Proceedings of the National Academy of Sciences of the United States of America* 87.3 (1990), pp. 1013–7.

[399] M. F. Hsu et al. “Structural and functional studies of a newly grouped Haloquadratum walsbyi bacteriorhodopsin reveal the acid-resistant light-driven proton pumping activity”. In: *Journal of Biological Chemistry* 290.49 (2015), pp. 29567–29577.

[400] E Lam and L Packer. “Nonionic detergent effects on spectroscopic characteristics and the photocycle of bacteriorhodopsin in purple membranes”. In: *Archives of Biochemistry and Biophysics* 221.2 (Mar. 1983), pp. 557–64.

[401] M. Etzkorn et al. “Cell-free expressed bacteriorhodopsin in different soluble membrane mimetics: biophysical properties and NMR accessibility”. In: *Structure* 21.3 (2013), pp. 394–401.

[402] R. O. Gonzalez et al. “Archaeosomes made of Halorubrum tebenquichense total polar lipids: A new source of adjuvancy”. In: *BMC Biotechnology* 9 (2009), p. 71.

[403] A. Ventosa, A. Oren, and Y. Ma. *Halophiles and Hypersaline Environments*. Springer, 2011.

[404] P. Lopalco et al. “Osmotic shock stimulates de novo synthesis of two cardiolipins in an extreme halophilic archaeon”. In: *J Lipid Res* 45.1 (2004), pp. 194–201.

[405] M. Kamekura and M. Kates. “Structural Diversity of Membrane Lipids in Members of Halobacteriaceae”. In: *Bioscience, Biotechnology, and Biochemistry* 63.6 (1999), pp. 969–972.

[406] A. Corcelli et al. “Glycocardiolipin modulates the surface interaction of the proton pumped by bacteriorhodopsin in purple membrane preparations”. In: *Biochimica et Biophysica Acta - Biomembranes* 1768.9 (2007), pp. 2157–2163.

[407] T. Tsukamoto et al. “Thermal and spectroscopic characterization of a proton pumping rhodopsin from an extreme thermophile”. In: *Journal of Biological Chemistry* 288.30 (2013), pp. 21581–21592.

[408] P. Nollert et al. “Detergent-free membrane protein crystallization”. In: *FEBS Letters* 457 (1999).

[409] W. Liu, A. Ishchenko, and V. Cherezov. “Preparation of microcrystals in lipidic cubic phase for serial femtosecond crystallography”. In: *Nature protocols* 9.9 (2014), pp. 2123–34.

[410] A. A. Vagin et al. “REFMAC5 dictionary: organization of prior chemical knowledge and guidelines for its use”. In: *Acta Crystallogr D Biol Crystallogr* 60 (2004), pp. 2184–95.

[411] P. D. Adams et al. “PHENIX: a comprehensive Python-based system for macromolecular structure solution”. In: *Acta Crystallogr D Biol Crystallogr* 66 (2010), pp. 213–21.

[412] H G Khorana et al. “Amino acid sequence of bacteriorhodopsin”. In: *Proceedings of the National Academy of Sciences of the United States of America* 76.10 (Oct. 1979), pp. 5046–50.

[413] J S Seehra and H G Khorana. “Bacteriorhodopsin precursor. Characterization and its integration into the purple membrane”. In: *Journal of Biological Chemistry* 259.7 (Apr. 1984), pp. 4187–93.

[414] J. Mozdzanowski. “Deblocking of proteins containing N-terminal pyroglutamic acid”. In: *Methods Mol Biol* 211 (2003), pp. 365–9.

[415] K Uegaki, Y Sugiyama, and Y Mukohata. “Archaerhodopsin-2, from Halobacterium sp. aus-2 further reveals essential amino acid residues for light-driven proton pumps”. In: *Archives of Biochemistry and Biophysics* 286.1 (1991), pp. 107–10.

[416] S. Jawhar, O. Wirths, and T. A. Bayer. “Pyroglutamate amyloid- (A): a hatchet man in Alzheimer disease”. In: *Journal of Biological Chemistry* 286.45 (2011), pp. 38825–32.

[417] R. E. Morty et al. “Pyroglutamyl peptidase type I from Trypanosoma brucei: a new virulence factor from African trypanosomes that de-blocks regulatory peptides in the plasma of infected hosts”. In: *Biochemical Journal* 394 (2006), pp. 635–45.

[418] A M Smith and S A Watson. “Review article: gastrin and colorectal cancer”. In: *Aliment Pharmacol Ther* 14.10 (Oct. 2000), pp. 1231–47.

[419] R Rink et al. “To protect peptide pharmaceuticals against peptidases”. In: *Journal of Pharmacology Toxicology Methods* 61.2 (2010), pp. 210–8.

[420] S. Schilling et al. “On the seeding and oligomerization of pGlu-amyloid peptides (in vitro)”. In: *Biochemistry* 45.41 (2006), pp. 12393–9.

[421] K. Ihara et al. “Met-145 is a key residue in the dark adaptation of bacteriorhodopsin homologs”. In: *Biophysical Journal* 67.3 (1994), pp. 1187–1191.

[422] I Kovács et al. “Pressure effects on the dark-adaptation of bacteriorhodopsin”. In: *Biophysical Journal* 64.4 (1993), pp. 1187–93.

[423] T Kouyama, R A Bogomolni, and W Stoeckenius. “Photoconversion from the light-adapted to the dark-adapted state of bacteriorhodopsin”. In: *Biophysical Journal* 48.2 (1985), pp. 201–8.

[424] M Tsuda and T G Ebrey. “Effect of high pressure on the absorption spectrum and isomeric composition of bacteriorhodopsin”. In: *Biophysical Journal* 30.1 (1980), pp. 149–57.

[425] N A Dencher et al. “Light- and dark-adapted bacteriorhodopsin, a time-resolved neutron diffraction study”. In: *Biochim Biophys Acta* 1026.1 (July 1990), pp. 51–6.

[426] T. Nishikawa, M. Murakami, and T. Kouyama. “Crystal structure of the 13-cis isomer of bacteriorhodopsin in the dark-adapted state”. In: *Journal of Molecular Biology* 352.2 (2005), pp. 319–28.

[427] M. F. Brown et al. “Solid-state 2H NMR spectroscopy of retinal proteins in aligned membranes”. In: *Biochimica et Biophysica Acta (BBA) - General Subjects Biophys Acta* 1768.12 (Dec. 2007), pp. 2979–3000.

[428] J Kyte and R F Doolittle. “A simple method for displaying the hydropathic character of a protein”. In: *Journal of Molecular Biology* 157.1 (1982), pp. 105–32.

[429] URL: https://web.expasy.org/protparam/.

[430] R. S. McIsaac et al. “Directed evolution of a far-red fluorescent rhodopsin”. In: *Proceedings of the National Academy of Sciences* 111.36 (2014), pp. 13034–13039.

[431] C. Kupitz et al. “Serial time-resolved crystallography of photosystem II using a femtosecond X-ray laser”. In: *Nature* 513.7517 (2014), pp. 261–5.

[432] A. Aquila et al. “Time-resolved protein nanocrystallography using an X-ray free-electron laser”. In: *Opt Express* 20.3 (2012), pp. 2706–16.

[433] M. Suga et al. “Light-induced structural changes and the site of O=O bond formation in PSII caught by XFEL”. In: *Nature* 543.7643 (2017), pp. 131–135.

[434] A. Y. Lyubimov et al. “Advances in X-ray free electron laser (XFEL) diffraction data processing applied to the crystal structure of the synaptotagmin-1 / SNARE complex”. In: *eLife* 5 (2016).

[435] A. E. Cohen et al. “Goniometer-based femtosecond crystallography with X-ray free electron lasers”. In: *Proceedings of the National Academy of Sciences of the United States of America* 111.48 (2014), pp. 17122–7.

[436] M. Kubo et al. “Nanosecond pump-probe device for time-resolved serial femtosecond crystallography developed at SACLA”. In: *Journal of Synchrotron Radiation* 24.5 (2017), pp. 1086–1091.

[437] K Edman et al. “High-resolution X-ray structure of an early intermediate in the bacteriorhodopsin photocycle”. In: *Nature* 401.6755 (Oct. 1999), pp. 822–6.

[438] S. W. Brenner. “The genetics of behaviour”. In: *Br Med Bull* 29.3 (1973), pp. 269–71.

[439] S. W. Brenner. *The nematode Caenorhabditis elegans*. Cold Spring Harbor Laboratory, 1988.

[440] F E Bloom. “Staying afloat on the seas of data”. In: *Science* 282.5396 (Dec. 1998), p. 1989.

[441] D L Riddle, T Blumenthal, and B J Meyer. *C. elegans*. Cold Spring Harbor, 1997.

[442] A. Barrière and M.-A. Félix. “Isolation of C. elegans and related nematodes”. In: *WormBook* (2013).

[443] URL: https://sites.google.com/site/chioufenchuanglab/research/c-elegans.

[444] A. Page. “The cuticle”. In: *WormBook* (2007), pp. 1–15.

[445] M L Blaxter. “Cuticle surface proteins of wild type and mutant Caenorhabditis elegans.” In: *The Journal of biological chemistry* 268.9 (1993), pp. 6600–9.

[446] M. J. Gravato-Nobre et al. “Multiple genes affect sensitivity of Caenorhabditis elegans to the bacterial pathogen Microbacterium nematophilum”. In: *Genetics* 171.3 (2005), pp. 1033–45.

[447] A. D. Chisholm and S. Xu. “The Caenorhabditis elegans epidermis as a model skin. II: Differentiation and physiological roles”. In: *Wiley Interdisciplinary Reviews: Developmental Biology* 1.6 (2012), pp. 879–902.

[448] I. L. Johnstone. *The cuticle of the nematode Caenorhabditis elegans: A complex collagen structure*. 1994.

[449] S. Shi et al. “Activation of the caenorhabditis elegans degenerin channel by shear stress requires the MEC-10 subunit”. In: *Journal of Biological Chemistry* 291.27 (2016), pp. 14012–14022.

[450] R. Zhang and A. Hou. “Host-Microbe interactions in Caenorhabditis elegans”. In: *ISRN Microbiology* (2013), pp. 1–7.

[451] M. Witting and P. Schmitt-Kopplin. “The Caenorhabditis elegans lipidome: A primer for lipid analysis in Caenorhabditis elegans”. In: *Archives of Biochemistry and Biophysics* 589 (2016), pp. 27–37.

[452] K. Gounaris, V. P. Smith, and M. E. Selkirk. “Structural organisation and lipid composition of the epicuticular accessory layer of infective larvae of Trichinella spiralis”. In: *Biochimica et Biophysica Acta - Biomembranes* 1281.1 (1996), pp. 91–100.

[453] Proudfoot L, Smith H V Kusel J R, and Kennedy M W. “Biophysical properties of the nematode surface”. In: *Parasitic nematodes—Membranes, antigens and genes* (1991).

[454] D. L. Lee. *The Biology of Nematodes*. CRC Press, 2002.

[455] M. Abonnenc et al. “Electrochemical Aspects of Electrospray and Laser Desorption/Ionization for Mass Spectrometry”. In: *Annual Review of Analytical Chemistry* 3.1 (2010), pp. 231–254.

[456] M. Karas and R. Krüger. “Ion formation in MALDI: the cluster ionization mechanism”. In: *Chemical Reviews* 103.2 (2003), pp. 427–40.

[457] W. J. Henzel, C. Watanabe, and J. T. Stults. “Protein identification: the origins of peptide mass fingerprinting”. In: *Journal American Society Mass Spectrometry* 14.9 (2003), pp. 931–42.

[458] D N Perkins et al. “Probability-based protein identification by searching sequence databases using mass spectrometry data”. In: *Electrophoresis* 20.18 (Dec. 1999), pp. 3551–67.

[459] A. Gattiker et al. “FindPept, a tool to identify unmatched masses in peptide mass fingerprinting protein identification”. In: *Proteomics* 2.10 (2002), pp. 1435–44.

[460] T. Gys. “Micro-channel plates and vacuum detectors”. In: *Nuclear Instruments and Methods in Physics Research, Section A: Accelerators, Spectrometers, Detectors and Associated Equipment* 787 (2015), pp. 254–260.

[461] K. Watschinger and E. R. Werner. “Alkylglycerol monooxygenase”. In: *IUBMB Life* 65.4 (2013), pp. 366–72.

[462] C. M. Loer et al. “Cuticle integrity and biogenic amine synthesis in Caenorhabditis elegans require the cofactor tetrahydrobiopterin (BH4)”. In: *Genetics* 200.1 (2015), pp. 237–253.

[463] J. J. Dominguez Pardo et al. “Solubilization of lipids and lipid phases by the styrene–maleic acid copolymer”. In: *European Biophysics Journal* 46.1 (2017), pp. 91–101.

[464] E. Reading et al. “Interrogating Membrane Protein Conformational Dynamics within Native Lipid Compositions”. In: *Angewandte Chemie - International Edition* 56.49 (2017), pp. 15654–15657.

[465] URL: `http://www.lipidmaps.org`.

[466] J. R. Wiśniewski et al. “Brain phosphoproteome obtained by a FASP-based method reveals plasma membrane protein topology”. In: *J Proteome Res* 9.6 (2010), pp. 3280–9.

[467] O Vit and J Petrak. “Integral membrane proteins in proteomics. How to break open the black box?” In: *Journal of Proteomics* 153 (2017), pp. 8–20.

[468] B. Fuchs, R. Süss, and J. Schiller. “An update of MALDI-TOF mass spectrometry in lipid research”. In: *Progress in Lipid Research* 49.4 (2010), pp. 450–75.

[469] C. D. Magnusson and G. G. Haraldsson. “Ether lipids”. In: *Chemistry and Physics of Lipids* 164.5 (2011), pp. 315–40.

[470] L. Juillerat-Jeanneret and F. Schmitt. “Chemical modification of therapeutic drugs or drug vector systems to achieve targeted therapy: Looking for the grail”. In: *Medicinal Research Reviews* 27.4 (2007), pp. 574–590.

[471] S. Mashaghi et al. “Lipid nanotechnology”. In: *International journal of molecular sciences* 14.2 (2013).

[472] A. Valizadeh et al. “Quantum dots: synthesis, bioapplications, and toxicity”. In: *Nanoscale Research Letters* 7.1 (2012), p. 480.

[473] R. Kikkeri et al. *Carbohydrate-based nanoscience: metallo-glycodendrimers and quantum dots as multivalent probes*. Ed. by M. G. Hicks and C. Kettner. Berlin: Logos-Verlag, 2011.

[474] A. L. B. Seynhaeve et al. “Intact Doxil is taken up intracellularly and released doxorubicin sequesters in the lysosome: Evaluated by in vitro/in vivo live cell imaging”. In: *Journal of Controlled Release* 172.1 (2013), pp. 330–340.

[475] X. Zhang et al. “Targeted delivery and controlled release of doxorubicin to cancer cells using modified single wall carbon nanotubes”. In: *Biomaterials* 30.30 (2009), pp. 6041–6047.

[476] A. Arouri et al. “Lipases, liposomes and lipid-prodrugs”. In: *Current Opinion in Colloid and Interface Science* 18.5 (2013), pp. 419–431.

[477] J. A. Silverman and S. R. Deitcher. “Marqibo® (vincristine sulfate liposome injection) improves the pharmacokinetics and pharmacodynamics of vincristine”. In: *Cancer Chemother Pharmacol* 71.3 (2013), pp. 555–64.

[478] P. A. Bovier. "Epaxal: a virosomal vaccine to prevent hepatitis A infection". In: *Expert Rev Vaccines* 7.8 (2008), pp. 1141–50.

[479] E. A. Dennis et al. "Phospholipase A 2 Enzymes: Physical Structure, Biological Function, Disease Implication, Chemical Inhibition, and Therapeutic Intervention". In: *Chemical Reviews* 111.10 (2011), pp. 6130–6185.

[480] X.-Z. Zhang et al. "A novel thermo-responsive drug delivery system with positive controlled release". In: *International Journal of Pharmaceutics* 235.1–2 (2002), pp. 43–50.

[481] M. Oishi et al. "pH-Responsive PEGylated nanogels as targetable and low invasive endosomolytic agents to induce the enhanced transfection efficiency of nonviral gene vectors". In: *Biomacromolecules* 285.9 (2003), pp. 1055–1060.

[482] R. Tong et al. "Photoswitchable Nanoparticles for Triggered Tissue Penetration and Drug Delivery". In: *Journal of the American Chemical Society* 134.21 (2012), pp. 8848–8855.

[483] B. M. Dicheva et al. "Cationic Thermosensitive Liposomes: A Novel Dual Targeted Heat-Triggered Drug Delivery Approach for Endothelial and Tumor Cells". In: *Nano Letters* 13.6 (2013), pp. 2324–2331.

[484] R. Tong, H. H. Chiang, and D. S. Kohane. "Photoswitchable nanoparticles for in vivo cancer chemotherapy". In: *Proceedings of the National Academy of Sciences of the United States of America* 110.47 (2013), pp. 19048–53.

[485] Y. Kato et al. "Acidic extracellular microenvironment and cancer". In: *Cancer Cell International* 13.1 (2013), p. 89.

[486] URL: `http://cancerres.aacrjournals.org/content/42/3/local/front-matter.pdf`.

[487] C. Carvalho et al. "Doxorubicin: the good, the bad and the ugly effect". In: *Curr Med Chem* 16.25 (2009), pp. 3267–85.

[488] A. Bodley et al. "DNA Topoisomerase II-mediated Interaction of Doxorubicin and Daunorubicin Congeners with DNA". In: *Cancer Research* 49.21 (1989), pp. 5969–5978.

[489] C. Hansch and D. Hoekman Leo A. *Exploring QSAR - Hydrophobic, Electronic, and Steric Constants.* American Chemical Society, 1995.

[490] URL: `http://chemweb.bham.ac.uk/~hannonmj/Mike%20page/3wayjonction.html`.

[491] Doxil Website. *http://www.doxil.com*.

[492] URL: `http://malverncosmeceutics.com/development_pipeline.html`.

[493] Juan Francisco Bada Juarez. "Evaluation of novel nanosized lipid-based vehicles for delivery of amphipathic drug molecules". MA thesis. Ecole Polytechnique Fédérale de Lausanne, 2014.

[494] Charles Davies. "Engineering Lipid Nanoparticles for Structural Biology and Drug Delivery". MA thesis. University of Oxford, 2015.

[495] URL: https://assets.thermofisher.com/TFS-Assets/LSG/manuals/mp00003.pdf.

[496] P. Mohan and N. Rapoport. "Doxorubicin as a molecular nanotheranostic agent: effect of doxorubicin encapsulation in micelles or nanoemulsions on the ultrasound-mediated intracellular delivery and nuclear trafficking". In: *Molecular pharmaceutics* 7.6 (2010), pp. 1959–73.

[497] K. K. Karukstis et al. "Deciphering the fluorescence signature of daunomycin and doxorubicin". In: *Biophysical Chemistry* 73.3 (1998), pp. 249–263.

[498] H. Nymeyer and H. X. Zhou. "A method to determine dielectric constants in nonhomogeneous systems: Application to biological membranes". In: *Biophysical Journal* 94.4 (2008), pp. 1185–1193.

[499] L Dupou-Cézanne, A M Sautereau, and J F Tocanne. "Localization of adriamycin in model and natural membranes. Influence of lipid molecular packing". In: *European Journal of Biochemistry* 181.3 (1989), pp. 695–702.

[500] M. Tanaka, A. Hosotani, and T. Mukai. "Indium-111 labeling of high-density lipoprotein-mimicking phospholipid-styrene maleic acid copolymer complexes and its biodistribution in mice". In: *Journal of Labelled Compounds and Radiopharmaceuticals* (2018).

[501] N Oku et al. "Real-time analysis of liposomal trafficking in tumor-bearing mice by use of positron emission tomography". In: *Biochim Biophys Acta* 1238.1 (Aug. 1995), pp. 86–90.

[502] P. M. Dijkman and A. Watts. "Lipid modulation of early G protein-coupled receptor signalling events". In: *Biochim Biophys Acta* 1848.11 (2015), pp. 2889–97.

[503] J. M. Saul et al. "Controlled targeting of liposomal doxorubicin via the folate receptor in vitro". In: *Journal of Controlled Release* 92.1–2 (2003), pp. 49–67.

[504] T. A. Cross, D. T. Murray, and A. Watts. "Helical membrane protein conformations and their environment". In: *European Biophysics Journal* 42.10 (2013), pp. 731–755.

[505] S. Lee et al. "How Do Short Chain Nonionic Detergents Destabilize G-Protein-Coupled Receptors?" In: *Journal of the American Chemical Society* 138.47 (2016), pp. 15425–15433.

[506] S. C. Lee and N. L. Pollock. "Membrane proteins: is the future disc shaped?" In: *Biochemical Society Transactions* 44.4 (2016), pp. 1011–1018.

[507] V. Cherezov, K. M. Riedl, and M. Caffrey. "Too hot to handle? Synchrotron X-ray damage of lipid membranes and mesophases". In: *Journal of Synchrotron Radiation* 9 (2002), pp. 333–41.

[508] J. J. Mousa et al. "MATE transport of the E. Coli-derived genotoxin colibactin". In: *Nature Microbiology* 1.1 (2016).

[509] R. C. Stevens et al. “The GPCR Network: A large-scale collaboration to determine human GPCR structure and function”. In: *Nature Reviews Drug Discovery* 12.1 (2013), pp. 25–34.

[510] P. Mystek et al. “The role of cholesterol and sphingolipids in the dopamine D1receptor and G protein distribution in the plasma membrane”. In: *Biochimica et Biophysica Acta - Molecular and Cell Biology of Lipids* 1861.11 (2016), pp. 1775–1786.

[511] J. Oates et al. “The role of cholesterol on the activity and stability of neurotensin receptor 1”. In: *Biochimica et Biophysica Acta - Biomembranes* 1818.9 (2012), pp. 2228–2233.

[512] K. Pluhackova et al. “Dynamic Cholesterol-Conditioned Dimerization of the G Protein Coupled Chemokine Receptor Type 4”. In: *PLoS Computational Biology* 12.11 (2016).

[513] M. Shibata et al. “Oligomeric states of microbial rhodopsins determined by high-speed atomic force microscopy and circular dichroic spectroscopy”. In: *Scientific Reports* 8.1 (2018), pp. 1–11.

[514] O. Tacar, Pornsak Sriamornsak, and Crispin R. Dass. “Doxorubicin: An update on anticancer molecular action, toxicity and novel drug delivery systems”. In: *Journal of Pharmacy and Pharmacology* 65.2 (2013), pp. 157–170.

[515] Z. Zhang et al. “A brief review on the evolution of GPCR: conservation and diversification”. In: *Open Journal of Genetics* 02.04 (2012), pp. 11–17.

[516] Novex Bis-tris Gel. “NativePAGE ™ Novex Bis-Tris Gel”. In: 25 (2006), pp. 2–3.

[517] GE Healthcare. “Size exclusion chromatography: Principles and Methods”. In: *GE HealtCare Handbooks* (2012), p. 139.

[518] J. Foadi et al. “Clustering procedures for the optimal selection of data sets from multiple crystals in macromolecular crystallography”. In: *Acta Crystallogr D Biol Crystallogr* 69 (2013), pp. 1617–32.

[519] A. J. McCoy et al. “Phaser crystallographic software”. In: *Journal of Applied Crystallography* 40 (2007), pp. 658–674.

[520] P. Emsley and K. Cowtan. “Coot: model-building tools for molecular graphics”. In: *Acta Crystallogr D Biol Crystallogr* 60 (2004), pp. 2126–32.

[521] A. Barty et al. “Cheetah: software for high-throughput reduction and analysis of serial femtosecond X-ray diffraction data”. In: *Journal of Applied Crystallography* 47 (2014), pp. 1118–1131.

[522] T. Nakane et al. “Data processing pipeline for serial femtosecond crystallography at SACLA”. In: *Journal of Applied Crystallography* 49 (2016), pp. 1035–1041.

[523] T. A. White et al. “CrystFEL: a software suite for snapshot serial crystallography”. In: *Journal of Applied Crystallography* 45.2 (2012), pp. 335–341.